



HAL
open science

Identification, production et caractérisation de nanoplastiques environnementaux par l'utilisation d'outils géochimiques et de nanométrie

Florent Blancho

► **To cite this version:**

Florent Blancho. Identification, production et caractérisation de nanoplastiques environnementaux par l'utilisation d'outils géochimiques et de nanométrie. Sciences de la Terre. Université de Rennes, 2021. Français. NNT : 2021REN1B048 . tel-03890149

HAL Id: tel-03890149

<https://theses.hal.science/tel-03890149v1>

Submitted on 8 Dec 2022

HAL is a multi-disciplinary open access archive for the deposit and dissemination of scientific research documents, whether they are published or not. The documents may come from teaching and research institutions in France or abroad, or from public or private research centers.

L'archive ouverte pluridisciplinaire **HAL**, est destinée au dépôt et à la diffusion de documents scientifiques de niveau recherche, publiés ou non, émanant des établissements d'enseignement et de recherche français ou étrangers, des laboratoires publics ou privés.

Thèse de doctorat de

L'UNIVERSITE DE RENNES 1

ECOLE DOCTORALE N° 600

Ecole doctorale Ecologie, Géosciences, Agronomie et Alimentation

Spécialité : Sciences de la Terre et de l'Environnement

Par

Florent BLANCHO

Identification, production et caractérisation de nanoplastiques environnementaux par l'utilisation d'outils géochimiques et de nanométrie.

Thèse présentée et soutenue à Rennes, le 6 décembre 2021

Unité de recherche : UMR 6118

Rapporteurs avant soutenance :

Géraldine SARRET
Mohammed BAALOUSHA

Directrice de recherche, ISTerre, Université Grenoble Alpes
Professeur associé, Public Health Research Center, University of South Carolina

Composition du Jury :

Président :

Aline DIA

Directrice de recherche, Géosciences Rennes, Université Rennes 1

Examineurs :

Aline DIA
Mark WIESNER
Géraldine SARRET
Mohammed BAALOUSHA

Directrice de recherche, Géosciences Rennes, Université Rennes 1
Professeur, Civil & Environmental Engineering, Duke University
Directrice de recherche, ISTerre, Université Grenoble Alpes
Professeur associé, Public Health Research Center, University of South Carolina

Dir. de thèse :

Julien GIGAULT

Chargé de recherche, TAKUVIK, Université de Laval

Co-dir. de thèse :

Mélanie DAVRANCHE

Professeure, Géosciences Rennes, Université Rennes 1

**À ma sœur,
À mon beau-frère,
À tous les dépourvues de sort**

“Si l'on suivait les voies ferroviaires, qui aurait le pied marin?”

Je t'ai manqué, Alain Bashung

REMERCIEMENTS

Ce manuscrit parachève une péripétie scientifique d'un côté mais aussi humaine de l'autre. A cet effet, je tiens à remercier toutes les personnes qui ont participé aux deux versants de cette aventure, et qui m'ont permis surtout de réussir mon doctorat.

Tout d'abord, je tiens à remercier les deux personnes, sans qui ce projet n'aurait pas eu lieu : *ma directrice et mon directeur de thèse.*

Merci **Mélanie**, pour l'ensemble de nos échanges scientifiques et équités, ton soutien malgré des débuts difficiles, ta simplicité, ta rigueur, mais aussi et surtout ton honnêteté. Je te remercie énormément pour ta présence malgré ton emploi du temps très chargé.

Merci **Julien**, pour m'avoir fait confiance du début à la fin, pour toutes ces bonnes idées scientifiques que l'on a pu partager, nos échanges qu'ils soient professionnels ou personnels, et tes conseils pour l'avenir. Je te remercie aussi et surtout d'avoir toujours été présent lorsque j'en avais besoin.

*Je souhaite également remercier les membres de mon jury, **Aline Dia, Mark Weisner, Géraldine Sarret et Mohammed Baalousha.***

Je tiens à remercier toute l'équipe Nano-Bio-Géochimie (NBG). En effet, grâce à vos connaissances scientifiques, vous avez pu ensemble m'aider tout au long de mon doctorat.

Merci **Rémi**, pour tous les échanges scientifiques que l'on a eus. Merci pour tes conseils de modélisation et les bouts codes très précieux que tu nous as partagé.

Merci **Martine**, pour ton aide précieuse qui s'est étendue du premier jour de ma thèse jusqu'à sa fin. Je te suis très reconnaissant du temps que tu as passé à nous former que ce soit pour la salle blanche ou l'ICP-MS.

Merci **Charlotte**, pour les discussions scientifiques partagées, mais aussi tes conseils sur la rédaction, pour les présentations orales et l'après thèse.

Merci **Aline**, pour tes conseils de rédaction en fin de thèse, ils m'ont permis de l'achever dans les meilleures conditions.

Merci **Anne-Catherine**, pour tes conseils et échanges scientifiques mais aussi concernant les enseignements que j'ai effectués avec toi.

Merci **Mathieu Pédrot**, pour cette fameuse vidéo présentant les thématiques et sujets de recherches menés par l'équipe NBG, mes amis savent enfin ce que je fais !

Merci **Alice**, pour ton aide, ton soutien, ta joie de vivre. Tous deux doctorants : le même jour et dans le même bureau, j'ai apprécié d'avoir partagé avec toi tous ces moments qui font partie intégrante d'une thèse, à savoir : les certitudes, les doutes, les échecs, les réussites, les querelles et les embrassades. Je te remercie du fond du cœur et j'espère croiser ton chemin de nouveau !

Merci **Aurélie**, pour ton organisation infailible, qui m'a fortement aidé lors de mes dernières manipulations, même si je n'ai pu le copier qu'un court instant. A côté de ce clin d'œil, je te remercie pour l'énergie positive que tu dégages, la cohésion de groupe que tu apportes et la formidable décoration que tu as créé dans notre bureau.

Merci **Maxime**, sans toi, j'aurais dû gérer la catastrophe du micro-onde alors que je n'en avais pas le temps, ni l'énergie !

Merci **Patrice**, pour ton aide technique précieuse.

Merci à tous les doctorants, **Zélie, Elaheh, Anthony, Mara, Léa, Muqet, Yasaman** avec qui j'ai pu partager des expérimentations, des repas, des jeux de cartes mais aussi et surtout des fous rires.

Je tiens à remercier toutes les personnes ayant initiées et contribuées aux projets de recherches que nous avons menés, vous m'avez permis de bénéficier d'un soutien-scientifique et technique qui m'a énormément servi tout au long de ma thèse.

Merci plus particulièrement à **Stéphanie Reynaud, Hind El Hadri, Bruno Grassl, Antoine Aynard**.

Je tiens à remercier toutes les personnes avec qui j'ai pu échanger, travailler et être formé sur le campus de Beaulieu.

Merci à **Murielle Rabiller-Baudry**, pour ta formation sur l'ATR-FTIR, les analyses et les discussions scientifiques qui s'en sont suivies.

Merci à **Ronan Lebullenger**, pour ton aide concernant la quantification de la charge minérale de nos nanoplastiques, mais aussi et surtout les discussions que nous avons eu sur les utilisations possibles de l'ATG.

Merci à **Anthony Szymczyk**, pour avoir mis à disposition ton zétamètre.

Merci à **Ludivine Rault**, pour ta formation au MET mais aussi pour avoir toujours été présente et aidante lors de son utilisation.

Je tiens à remercier toutes les personnes avec qui j'ai pu échanger au Joint Research Center à Ispra.

Merci à **Francesco-Sirio Fumagalli et à Giacomo Ceccone**, pour toutes les analyses que vous avez effectuées ainsi que le support technique que vous nous avez apporté.

Merci à **Pascal Colpo**, pour ton aide lors de la préparation de mon voyage au JRC, qui fut malheureusement annulé.

Je tiens à remercier toutes les personnes de la fondation Ocean Clean up avec qui j'ai pu échanger.

Merci à **Boyan Slat, Laurent Lebreton, Fatimah Sulu Gambari, Matthias Egger et Gerianne Terlouw**. Je vous remercie tous énormément, les plastiques que vous m'avez

envoyés m'ont permis de mener à bien une grande partie des expérimentations que nous avons effectuées lors de ce travail de doctorat.

Je tiens à remercier les chercheurs avec qui j'ai collaboré et qui m'ont donné envie et aidé à poursuivre sur cette voie.

Merci **Lorenzo Spadini**, c'est en effet grâce à toi que j'ai commencé à faire de la recherche.

Merci, **Emilie Strady**, pour m'avoir formé à la recherche lors de mon stage de fin d'étude, mais aussi de m'avoir guidé à l'issu de ce dernier.

Merci **Laurent Charlet**, de m'avoir fait confiance pour finaliser l'étude de la pollution mercurielle en Suisse. Travailler à ISTerre fut très enrichissant pour moi et m'a aidé à trouver un laboratoire d'accueil au Canada.

Merci **Scott Mundle**, de m'avoir fait confiance pour t'aider à monter ton laboratoire. Cette expérience m'a permis de revenir au contact de la recherche mais m'a aussi motivé à postuler à des thèses.

Je tiens à remercier tous mes amis.

*Merci aux Frangins, **Violette et Amandine, Tiphaine et Thomas**, thèse ou pas, vous êtes tout simplement important pour moi ! Merci pour votre aide.*

Merci à **Gaël**, ça a été vraiment génial de passer ma première année de thèse en colocation avec toi. Merci de ton soutien au moment où j'en avais besoin et merci de m'avoir appris à brasser des bières.

*Merci à tous les Jacques, **Mathilde et Jean, Basil et Anaïs, Emelyne et Bastien, Armel et Apoline, Thomas et Constance, Christophe, Marcellin, Arnaud, Guillaume, Thomas, Pierre et Hugo**, ça m'a fait énormément plaisir de passer du temps avec vous.*

*Merci aux tontons, **Rémi, Luc, Mathilde, Martin, Jean-Baptiste, Pierre et Camille**, pour tous ces moments passés, les sorties, les belottes, les soirées et toutes ces discussions.*

*Merci à la connexion Grenobloise, **Jojo et Gwenn, Juliette et Charlie, Solène et Swann, et Marianne**, étudiants de la vie pour certains, en poste pour d'autres, on se voit moins souvent mais c'est avec grand plaisir que j'ai de vos nouvelles.*

*Merci à toute ma famille, ça m'a fait énormément de bien de vous avoir proche de moi pendant ces trois dernières années. Merci pour tout, *Je vous aime fort !**

Merci à Tiphaine, ma tendre et chère, ma muse, mon rayon de soleil, ma bouteille d'oxygène (toujours sur mon dos), je t'ai rencontré au début de cette aventure et fort est de constater que tu as été le facteur X de cette thèse réussie. Tu m'as apporté tout l'amour et le réconfort dont j'avais besoin. A l'heure actuelle, une toute autre aventure va commencer puisqu'un petit bout est bien au chaud à l'heure où j'écris ces lignes.

SOMMAIRE

	Page
REMERCIEMENTS	iii
SOMMAIRE	vi
INTRODUCTION GENERALE	1
CHAPITRE I. Identification des nanoplastiques dans des matrices environnementales: cas du polystyrène et du polypropylène	15
I.1 Introduction.....	18
I.2 Materials and methods	19
I.2.1 Samples	19
I.2.2. Nanoplastics preparation.....	20
I.2.3 Size and shape characterization	22
I.2.4 Nanoplastics molecular identification.....	23
I.3 Results and Discussions	24
I.3.1 Nanoscale effects on plastic pyrolysis	24
I.3.2 Natural organic matter contribution.....	30
I.4 Application to environmental NPs.....	33
CHAPITRE II. Production d'un modèle de nanoplastiques représentatif de l'environnement 39	
II.1. Introduction	42
II.2. Materials and methods.....	43
II.2.1. Environmental NPs production and organic matter degradation	43
II.2.2. Particle size, shape, and surface analysis	44
II.2.3. Characterization of e-NPs composition.....	46
II.3. Results and Discussion	50
II.3.1. Water extraction and purification of e-NPs.....	50
II.3.2. Environmental NPs polymer identification	53
II.3.3. Size characterization of e-NPs.....	54
II.3.4. Surface characterization of e-NPs and e-MPs	56
II.3.5. Implication for environmental NPs and protocol advantages	59
II.4. Conclusions	63
CHAPITRE III. Identification des mécanismes de sorption	64
III.1. Identification des complexes de surface : cas des terres rares	66
III.1.1 Introduction	67
III.1.2. Materials and methods	68
III.1.2.1. Nanoplastics models and characterization	68
III.1.2.2. Surface charge modelling.....	69
III.1.2.3. Adsorption experiments	70
III.1.2.4. Chemical Analysis.....	71
III.1.3. Results and discussion.....	71
III.1.3.1. Nanoplastics properties	71
III.1.3.2. PSL with surfactant, PSL _{surfactant}	74
III.1.3.3. PSL without surfactant, PSL _{free}	77
III.1.3.4. Environmentally relevant NPs, e-NPS	79

III.1.3.5. REE pattern deciphering	80
III.1.3.6. Implications for environmental NPs behavior	85
III.1.4. Conclusions	86
III.2. Modélisation thermodynamique de la sorption de Pb(II).....	87
III.2.1. Introduction	88
III.2.2. Materials and methods	90
III.2.2.1. NPs properties	90
III.2.2.2. Adsorption experiments	91
III.2.2.3. Chemical Analysis.....	92
III.2.2.4. Modeling	92
III.2.3. Results and Discussion.....	94
III.2.3.1. Nanoplastics characterization.....	94
III.2.3.2. Surface charge modeling and pKa extrapolation	95
III.2.3.3. Pb(II) adsorption by NPs.....	97
III.2.3.4. Pb(II) adsorption modeling	99
III.2.3.5. Impact of photo-oxidation on the NPs sorption capacity.....	102
III.2.3.6. Environmental implications	103
III.2.4. Conclusions	104
CONCLUSIONS ET PERSPECTIVES	105
IV.1 Conclusions	106
IV.1.1. Détection de nanoplastiques.....	106
IV.1.2. Production d'un modèle représentatif des NPs environnementaux	107
IV.1.3. Indentification des mécanismes d'adsorption des métaux par les e-NPS	107
IV.2. Perspectives.....	110
IV.2.1. Identification/détection des NPs	110
IV.2.2. Modèles de NPs	110
IV.2.3. Interaction entre métaux et NPs.....	112
IV.2.3. Caractérisation et transformation des NPs dans l'environnement	112
LISTE DES ABREVIATIONS, DES SIGLES ET DES ACRONYMES	115
LISTE DES FIGURES.....	118
LISTE DES TABLEAUX	124
REFERENCES	126

INTRODUCTION GENERALE

Les plastiques sont des polymères synthétiques aux propriétés inédites : faible densité, durabilité, propriété d'isolation thermique et électrique. Ces propriétés, associées à un faible coût de production, en font un matériel utilisé dans de nombreux domaines (e.g. médecine, construction, produits domestiques, emballages, etc.). Leur omniprésence est corroborée à l'évolution exponentielle de leur production mondiale depuis la seconde guerre mondiale (Figure 1). Depuis les années 2000, la croissance annuelle de leur production est la plus forte parmi tous les matériaux produits par l'humain (e.g. acier, ciment, etc.) (Kelly and Matos, 2005; Geyer et al., 2017). Sur ce point, les plastiques font partie intégrante de «la grande accélération» observée dans de nombreux domaines par Steffen et al., (2015) (e.g. production de CO₂, utilisation de l'eau, production de ciment, etc.). De telles évolutions posent désormais de nombreuses questions quant à leurs impacts sur l'environnement.

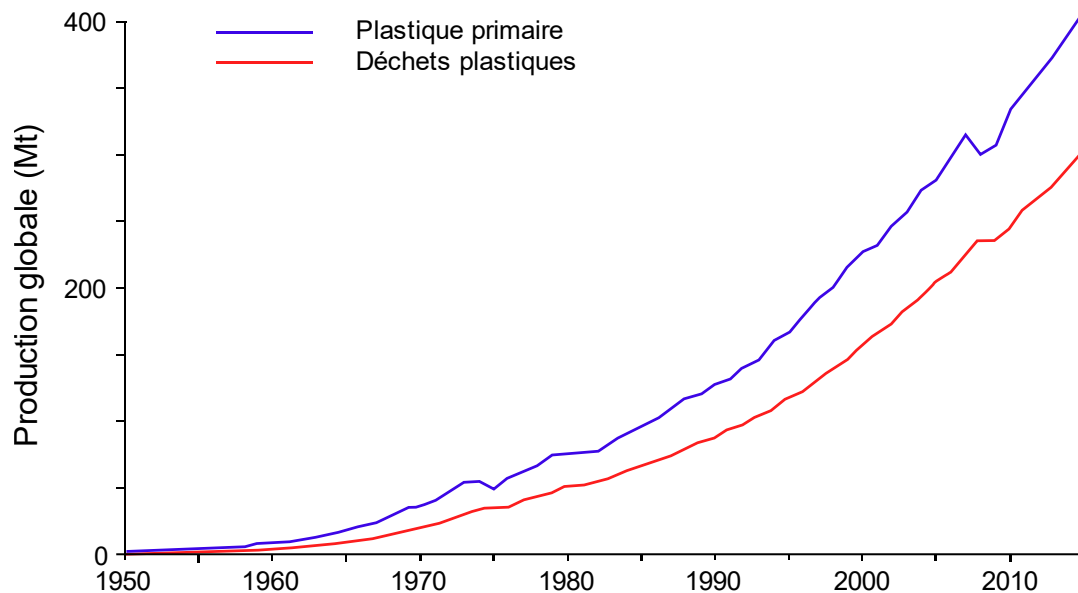


Figure 1. Production globale de plastique primaire et de déchets en millions de tonnes.

Adapté d'après Geyer et Al. 2017.

La quantité de déchets plastiques a suivi la même augmentation exponentielle. En 2010, 250 Mt de déchets plastiques ont été produits (Jambeck et al., 2015; Geyer et al., 2017) (Figure 1), dont une partie importante a été rejetée dans l'environnement. Dans les régions côtières, Jambeck et al. (2015) ont estimé ces rejets à 30 Mt, dont seuls 30% sont des déchets plastiques produits et utilisés sur place. Une conséquence majeure de ces rejets est l'omniprésence des plastiques dans l'environnement et notamment dans les gyres océaniques (Cozar et al., 2014) ; les fonds marins (Barnes et al., 2009), et même aux sommets des montagnes (Allen et al., 2019). Les plastiques sont conçus pour être durables, par conséquent, les déchets et débris issus de leur utilisation sont considérés comme persistants (Andrady, 2003; Worm et al., 2017) bien

qu'ils puissent dans une certaine mesure s'altérer dans l'environnement (Worm et al., 2017; Chamas et al., 2020). Cette dégradation est multifactorielle, abiotique et/ou biotique (Zettler et al., 2013; Gewert et al., 2015; Welden and Cowie, 2017; Min et al., 2020). Les cinétiques d'altération dépendent du milieu et de la composition des plastiques (Andrady, 2003; Chamas et al., 2020). L'oxydation UV est cependant considérée comme un des facteurs principaux de la dégradation environnementale des plastiques. Meides et al. (2021) ont montré que la dégradation se déroulait en deux phases. La première est une photooxydation de la couche de surface et la deuxième phase correspond à une fissuration de cette couche photo-oxydée, due à l'augmentation de la cristallinité de la matière (Ter Halle et al., 2017). Ces fissures fragilisent les plastiques et entraînent leur fragmentation (Scott, 1972). Ce processus n'est pas anecdotique puisqu'il a lieu à l'échelle de compartiments environnementaux entiers. En effet, dans les océans, l'augmentation du nombre de débris plastiques corrélée avec la diminution de leur taille est significative d'un processus de dégradation (Cozar et al., 2014; Ter Halle et al., 2016). Plus récemment, il a été montré que cette fragmentation s'étend jusqu'à atteindre des particules plastiques de taille nanométrique, et des chaînes polymériques (Lambert and Wagner, 2016; Ter Halle et al., 2017; Bianco et al., 2020). Dès lors, se pose la question du devenir de ce continuum de particules plastiques dans l'environnement.

Parmi ces débris plastiques, les nanoplastiques (NPs) soulèvent de nombreuses questions (i.e. effet, présence, comportement, etc.). Les particules de plastiques sont définies comme des NPs lorsqu'elles sont involontairement produites à partir de plastiques altérés dans l'environnement et par des processus industriels. S'ajoute à cela, le fait que les NPs ont une taille inférieure à 1000 nm et un comportement colloïdal, ils sont donc stables en solution (Gigault et al., 2018). Suite à la mise en évidence de leur présence dans l'environnement par Ter Halle et al. (2017), un nombre croissant d'études a été réalisé (Figure 2). Des NPs ont été depuis détectés dans de la neige, dans des lacs arctiques et dans un sol agricole contaminé en déchets plastiques (Materić et al., 2020, 2021; Wahl et al., 2021). L'engouement pour l'étude des NPs ne s'explique pas seulement par leur présence présumée ubiquiste, à l'instar des plastiques dans l'environnement, mais bien par leurs propriétés physico-chimiques. Besseling et al. (2019) ont suggéré que les concentrations en NPs seraient 10^{14} fois plus élevées que celles mesurées actuellement pour les microplastiques (MPs). Leur nombre augmente consécutivement à la fragmentation des macro/micro-plastiques accumulés dans l'environnement (Koelmans et al., 2015; Song et al., 2017). La fragmentation d'un plastique de 1mm en particules de 1000 nm conduit à la production de 10^9 particules. Par ailleurs, il existe un déséquilibre de l'ordre de 99% entre la masse de plastiques qui arrive jusqu'aux océans (e.g.

250 millions de tonnes) et celle observée à leur surface. La fragmentation des débris plastiques en NPs pourrait potentiellement et en partie expliquer ce bilan de masse (Cozar et al., 2014).

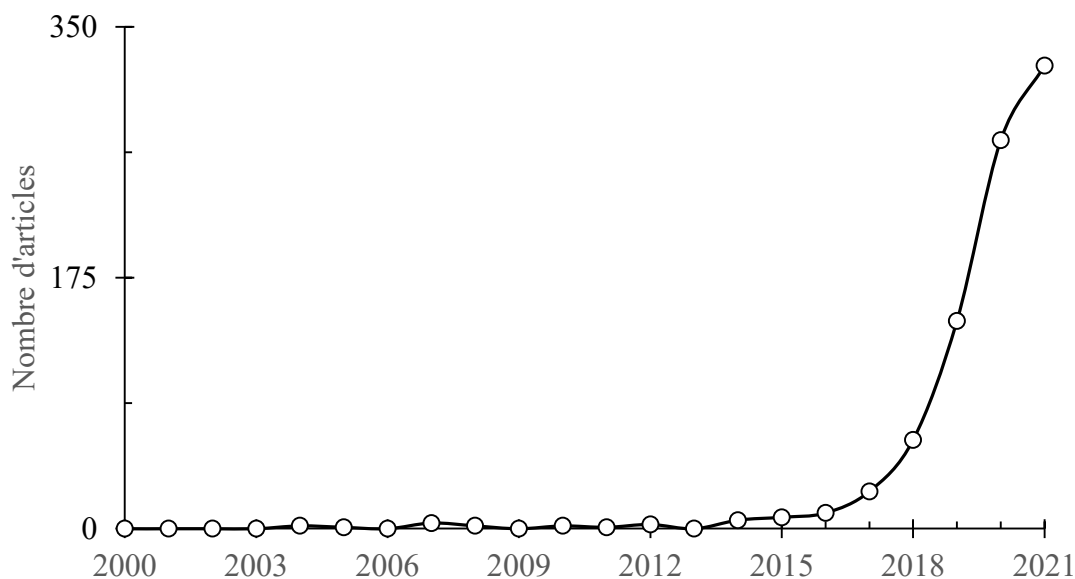


Figure 2. Nombre d'articles publiés par an traitant des NPs (recherche faite sous Scopus pour le terme "Nanoplastics" dans le titre, l'abstract et les mots clés).

La taille nanométrique des NPs leur confère des propriétés physico-chimiques uniques qui les distinguent des MPs. Les NPs sont des colloïdes stables en solution sous certaines conditions. Les mécanismes de transport des NPs sont donc très différents des MPs, qui eux, flottent ou non en fonction de leur densité. La surface d'échange entre les NPs et le milieu est de trois à quatre ordres de grandeur supérieure à celle des MPs. Leur grand rapport surface/taille leur confère une grande réactivité de surface, notamment vis-à-vis des micropolluants organiques et inorganiques. Besseling et al. (2019) estime ainsi que l'affinité des NPs pour les micro-polluants organiques persistants serait d'un à deux ordres supérieurs à celle des MPs. (Gigault et al., 2021) estime que cette forte réactivité chimique de surface diminuerait les cinétiques de libération des additifs contenus dans les NPs. Catrouillet et al., (2021) ont d'ailleurs suggéré que les métaux adsorbés dans la couche altérée des plastiques, elle-même à l'origine des NPs, auraient pour origine les métaux utilisés comme additifs dans la formulation des plastiques.

Enfin, la taille nanométrique des NPs leur permet également d'interagir avec les organismes vivants les plus petits, tels que les microorganismes qui constituent la base de la chaîne alimentaire, e.g., la taille des nano/micro-phytoplanctons est comprise entre 2 et 200 μm (Acevedo-Trejos et al., 2015). Les particules de taille nanométrique ont en effet la capacité de

pénétrer dans les cellules par endocytose, en franchissant directement la barrière intestinale vers la circulation sanguine et en traversant la barrière hémato-encéphalique (Koziara et al., 2003; Kashiwada, 2006; Browne et al., 2008). Bien que ces études écotoxicologiques permettent de définir des seuils de concentration en dessous duquel aucun effet négatif ne se distingue, il reste indispensable d'identifier et de quantifier la présence de NPs dans l'environnement.

Analyse in situ des NPs

Aujourd'hui, sur plus de ≈ 900 articles s'intéressant aux NPs, moins de 1% (soit 6 articles) ont mis en évidence la présence de NPs dans l'environnement, à partir d'échantillons naturels (Ter Halle et al., 2017; Davranche et al., 2020; Xu et al., 2020; Materić et al., 2020, 2021; Wahl et al., 2021). Ce très faible pourcentage met en évidence la difficulté de collecter et de détecter, voire d'analyser, les NPs en conditions environnementales. Il existe, en effet, dans ce domaine de véritables challenges.

1/ Les débris plastiques représentent un groupe hétérogène de polymères (i.e. PE, PP, PS, PVC, etc.). Leurs identifications/détections doivent donc être réalisées indépendamment et chaque polymère requiert un développement analytique spécifique.

2/ Les plastiques sont des composés carbonés à l'instar de la matière organique (MO) naturelle qu'elle soit particulaire, colloïdale ou dissoute. Une simple filtration ne permet pas d'isoler les NPs de la MO qui produit de nombreuses interférences avec les différentes techniques analytiques (Py-GCMS, TOC, etc.), limitant leur détection (Sullivan et al., 2020).

3/ Dans les échantillons naturels, le volume de NPs peut être faible par rapport à la MO même pour un nombre important de NPs, et cela est d'autant plus vrai que les NPs sont petits (Figure 3) (Gigault et al., 2021).

Afin de dépasser ces difficultés, des stratégies analytiques ont été développées (Cai et al., 2021). Les plus utilisées pour la détection des NPs en milieux naturels sont la spectrométrie de masse (Ter Halle et al., 2017; Materić et al., 2020, 2021; Wahl et al., 2021) et la spectroscopie UV (Xu et al., 2020). Les avantages de la spectrométrie de masse couplée à de la pyrolyse, de la thermogravimétrie ou de la désorption thermique sont multiples : (i) une faible quantité d'échantillon et (ii) la possibilité d'identifier plusieurs polymères simultanément. Néanmoins, de nombreuses interférences existent entre les NPs et la matière organique (Dümichen et al., 2015, 2017), comme celle entre la MO et le polystyrène (PS) dont la pyrolyse produit du styrène pour les deux éléments. Il semble possible d'identifier directement les NPs par l'intermédiaire d'autres pyrolyzates comme les dimères et trimères de styrène absents des produits de pyrolyse de la MO (Dümichen et al., 2015).

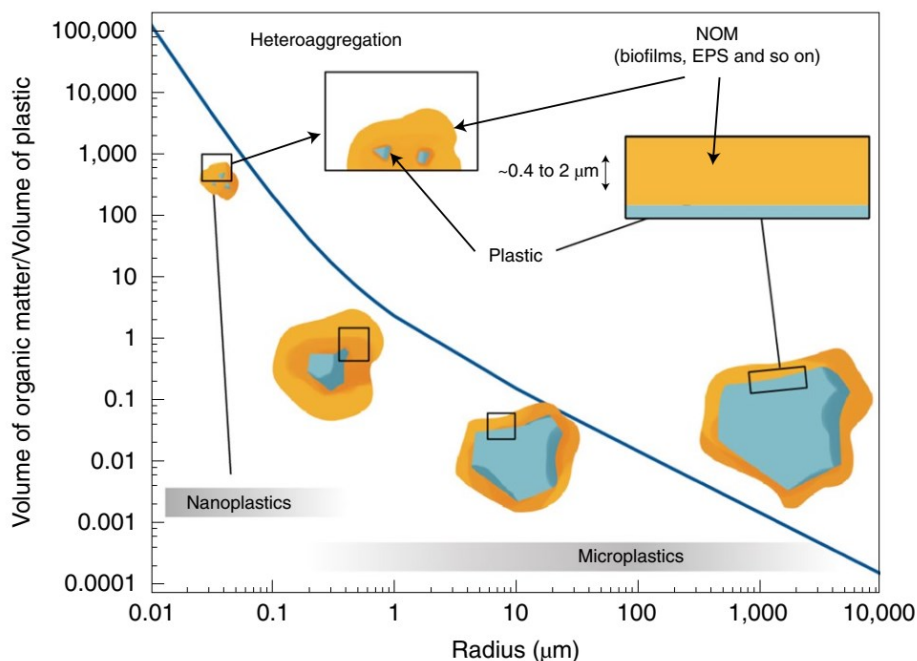


Figure 3. Rapport de volume MO/NPs en fonction du rayon des NPs pour une couche de MO constante (Gigault et al., 2021).

Certains auteurs identifient le PS via une approche indirecte basée sur le calcul de rapports, comme par exemple le rapport Toluène/Styrène (Dignac et al., 2005; Watteau et al., 2018). La détection des NPs de PS par Py-GCMS, peut donc être réalisée via diverses approches, la plus rapide et la plus simple étant l'identification directe du polymère. L'identification directe se doit d'être spécifique à chaque polymère, du fait d'interférences potentielles avec la MO. Or, les pyrogrammes disponibles dans la littérature ne sont pas toujours comparables à ceux obtenus par pyrolyse de NPs. Les proportions entre chaque pyrolyzates et les pyrolyzates eux-mêmes pourraient, en effet, varier. Ter Halle et al. (2017) utilise cette hypothèse afin d'expliquer l'absence de NPs de polypropylène (PP) dans leurs échantillons, qui contenaient pourtant des quantités importantes de MPs de PP. Pour résumer, la Py-GCMS nécessite encore d'importants développements pour détecter de façon optimale des NPs en milieu naturel. La première étape est de développer des méthodes et des stratégies analytiques spécifiques aux polymères composants les NPs.

De la nécessité de développer des modèles représentatifs des NPs environnementaux

Etudier les propriétés et le devenir des NPs environnementaux requière l'échantillonnage de quantités importantes de NPs à partir du milieu naturel, ce qui à l'heure actuelle, reste difficile en raison de leur faible concentration et de la présence simultanée de

nanoparticules naturelles et de MO (ex. colloïdes organiques, nano-oxydes de Fe, etc.). Une alternative est la production de modèles pertinents de ceux observés dans l'environnement (Ter Halle et al., 2017; Gigault et al., 2018). Les écotoxicologues ont été les premiers à utiliser comme modèle de NPs, des nanoparticules de latex de polystyrène (PSL), afin d'étudier les effets écotoxicologiques des NPs (Bhattacharya et al., 2010). Ce modèle est actuellement le plus utilisé en (éco)toxicologie mais aussi dans les études du comportement physico-chimiques des NPs (Della Torre et al., 2014; Alimi et al., 2018; Bergami et al., 2019; Bellingeri et al., 2019; Singh et al., 2019; Brachner et al., 2020; Shams et al., 2020; X. Wang et al., 2020; Liu et al., 2021).

Les PLS ont cependant des caractéristiques physico-chimiques bien différentes de celles définies pour les NPs. Les NPs sont polydispersés en taille et polymorphes avec une structure ouverte (Gigault et al., 2018) (Figure 4). Des fonctions de surface sont « naturellement » présentes à leur surface en réponse aux processus de photo-oxydation des polymères, subit lors de leur séjour dans le milieu naturel. Magrì et al., (2018) suggèrent que ces fonctions de surface sont majoritairement des fonctions carboxyliques. Au contraire, les PSL sont pour la plupart monodisperses, parfaitement rondes (Figure 4) et souvent recouvertes d'un seul type de fonction de surface : carboxyliques, hydroxyles, sulfate, etc. La densité de site COOH des PSL est définie a priori sans cohérence avec la densité des sites potentiellement présents à la surface des NPs environnementaux (Pessoni et al., 2019). Pourtant, cette densité est un facteur majeur de la réactivité et du comportement des NPs puisqu'elle contrôle leur stabilité colloïdale (Pessoni et al., 2019; Tallec et al., 2019; Liu et al., 2021).

La polymérisation des PSL est réalisée par l'intermédiaire de surfactants et d'initiateurs, comme par exemple pour les surfactants, le dodécylsulfate de sodium, SDS, et pour les initiateurs, le persulfate de potassium, KPS. Pikuda et al. (2018) ont montré que la toxicité des PSL peut être confondue avec celles des surfactants présents dans les suspensions de PSL. Les initiateurs de types sulfatés, quant à eux, produisent des groupements fonctionnels $-\text{SO}_4^{2-}$ et $-\text{SO}_3^-$ à la surface des PSLs (van den Hul and Vanderhoff, 1970; Tauer and Deckwer, 1998). Ces sites ont de faibles pKa ($\text{H}_2\text{SO}_4/\text{HSO}_4^- = -3$; $\text{pKa H}_2\text{SO}_3/\text{HSO}_3^- = 1.91$, Pankow, 2018) et sont donc ionisés à faible pH, ce qui stabilisent les PSLs en solution (Gong et al., 2001).

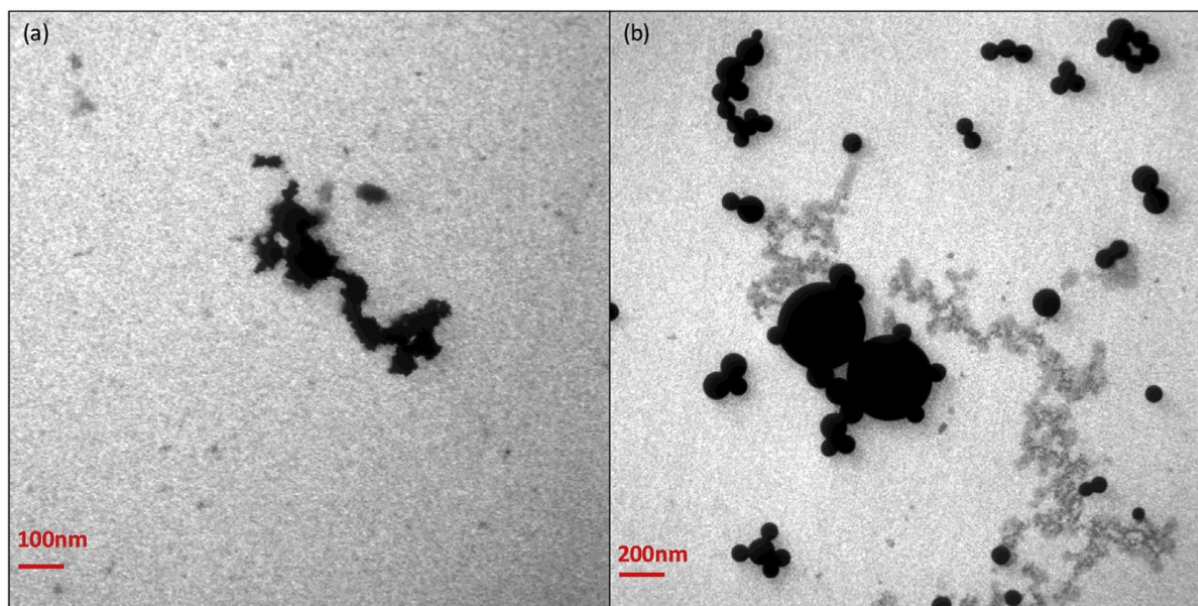


Figure 4. Image TEM de (a) Nanoplastiques environnementaux et (b) des modèles de NPs obtenus par polymérisation (Gigault et al., 2018).

L'utilisation des PSL comme modèles de NPs doit donc être remise en cause et de nouveaux modèles plus pertinents doivent être proposés. Ainsi, très récemment, Pessoni et al. (2019) ont développé une synthèse par polymérisation sans surfactant : le modèle « free soap emulsion ». Ce protocole utilise toutefois un initiateur sulfaté et des groupements SO_4/SO_3 peuvent être présents à la surface de ces modèles. Mitrano et al. (2019) ont développé un modèle de NPs composé d'un cœur de Pd pour faciliter leur détection et leur traçage, mais leur protocole utilise des surfactants et des initiateurs sulfatés. Ces nouveaux modèles PSLs restent, cependant, de forme sphérique avec une densité de groupement de surface COOH fixée a priori.

D'autres modèles de NPs sont produits par dégradation de polymères. Magri et al. (2018) ont utilisé l'ablation laser pour produire des suspensions de NPs polydispersés, de taille < 100 nm. L'ablation laser permet également d'oxyder la surface des NPs et de produire des groupements fonctionnels variés, e.g. hydroxyle, cétone, carboxyle, etc. Rodríguez-Hernández et al. (2019) et El Hadri et al. (2020) ont produit des modèles de NPs par broyage mécanique de polymères. Les NPs produits sont polydispersés de forme anisotrope et présentent une charge de surface. Davranche et al. (2019) ont produit des NPs à partir d'échantillons plastiques collectés dans l'environnement. La couche de surface de ces plastiques est très altérée et une simple sonication permet de produire une suspension d'environ 50 ppm de NPs. Ces NPs sont issus d'une photo-oxydation produite en conditions environnementales, et les groupes fonctionnels développés à leur surface sont représentatifs des NPs produits directement dans le milieu naturel. Cependant, Davranche et al. (2019) ne décrit pas en détail les propriétés de ce

modèle. Notons que la densité de site ionisable, i.e. sites nm^{-2} , demeure inconnue pour tous ces modèles obtenus par dégradation. Il est également très probable que la quantité de sites ionisables soit dépendante du protocole de production et des méthodes de production de ces NPs modèles (abrasion mécanique et/ou photo-oxydation).

Interactions entre micropolluants métalliques et NPs.

Peu d'informations existent sur les interactions NPs-métaux, cependant plus de données ont été produites pour les MPs. L'adsorption de métaux traces (tels que As, Ag, Cd, Co, Cr, Cu, Hg, Ni, Pb, Zn) par des granulés de MPs a en effet été mise en évidence (Turner and Holmes, 2015). Guo and Wang (2019) ont montré que l'adsorption de Sr^{2+} sur trois MPs (PE, PET, PVC) était contrôlée par un transfert de masse externe. L'As(III) serait adsorbé par des MPs de PS via des forces électrostatiques et des liaisons hydrogène (Dong et al., 2020). Très récemment, Tang et al. (2021) à partir de microplastiques de nylon collectés dans l'environnement ont montré que l'adsorption de Ni, Cu et Zn sur les MPs est contrôlée par la diffusion intra particulaire et la complexation de surface. Ils ont également souligné l'importance des fonctions de surface contenant un O dans l'adsorption des métaux. Récemment, de nombreuses données de sorption à la surface des MPs ont été traitées via un programme de « deep learning » (Guo and Wang, 2021). Ce programme a mis en avant que les MPs altérés ont une plus grande affinité pour les métaux que les MPs vierges, et que leur capacité de sorption dépend de la concentration initiale des métaux. Le modèle a également prédit que la capacité de sorption du Cd, du Pb et du Zn par les MPs était plus élevée dans les rivières que dans l'océan en réponse à sa forte salinité (Guo and Wang, 2021). Le piégeage des métaux par les MPs semble également être indépendant du type de polymère et augmenter avec le temps d'exposition (Rochman et al., 2014).

Tous ces résultats ne peuvent cependant pas être extrapolés aux NPs mais ils mettent en exergue le rôle joué par les fonctions de surface et notamment celles contenant de l'oxygène, créées suite à la photo-oxydation du plastique. La dégradation des plastiques produit en effet des radicaux libres initiant et propageant des réactions radicalaires dont les terminaisons insèrent des groupements fonctionnels oxygénés (Rabek, 1995; Magrì et al., 2018; Rodríguez-Hernández et al., 2019; Blanco et al., 2021a). Certains de ces groupements sont ionisables et à l'origine de la capacité de sorption des métaux par les NPs (Davranche et al., 2019).

Ces métaux peuvent provenir de l'environnement ou bien, comme l'a montré Catrouillet et al. (2021), des métaux utilisés comme additifs, libérés lors de la dégradation du plastique puis réadsorbés dans la couche d'altération à l'origine des NPs. Les métaux sont des éléments chimiques présents naturellement dans l'environnement. Ils sont généralement présents à l'état

de traces et utilisés par les organismes vivants (oligoéléments) mais peuvent atteindre des concentrations bien supérieures en réponse aux anomalies géogéniques ou aux activités humaines (Ahmad and Goni, 2010; Zhang et al., 2021). La plupart de ces métaux sont toxiques à fortes concentrations et posent un véritable problème de santé publique qui perdure depuis plusieurs décennies. Très récemment, une étude de Santé Publique France (SPF) a montré que la population française présentait des concentrations en métaux lourds (sang, cheveux, urine) inquiétantes et supérieures à celles des autres européens (Santé Publique France, 2021). La toxicité des métaux est contrôlée par leur spéciation, c'est-à-dire la distribution de leurs différentes espèces chimiques qui conditionne leur mobilité et leur biodisponibilité. Cette spéciation dépend des conditions physicochimiques du milieu et des ligands organiques, inorganiques, solubles ou solides présents. Une de leur grande particularité, par rapport aux autres éléments chimiques, est l'affinité qu'ils ont pour les surfaces solides, qu'elles soient particulaires ou colloïdales. Ainsi, dans les estuaires, lagons et rivières, 20 à 90% de ces micropolluants sont adsorbés aux colloïdes et particules (in)organiques (Martin et al., 1995; Vega and Weng, 2013; Luan and Vadas, 2015).

Ces processus d'adsorption des métaux par les colloïdes ou les particules se produisent grâce aux groupements fonctionnels développés à leur surface, essentiellement des -OH pour les surfaces minérales hydratées et -COOH ou ϕ -OH pour la MO (Lofts and Tipping, 1998; Stumm and Morgan, 2012). L'adsorption par les surfaces solides met en jeu différents processus tels que l'échange d'ion qui concerne essentiellement les alcalinoterreux (complexe de sphère externe, liaisons faibles) et la complexation de surface (complexe de sphère interne, liaisons fortes) pour les métaux notamment. Les fonctions de surface, les complexes de sphère interne et externe forment des couches plus ou moins denses à la surface du solide, qui créent une charge de surface attirant plus ou moins les ions de la solution, créant un potentiel de surface qui contrôle les quantités adsorbées : concept de la double couche (Figure 5).

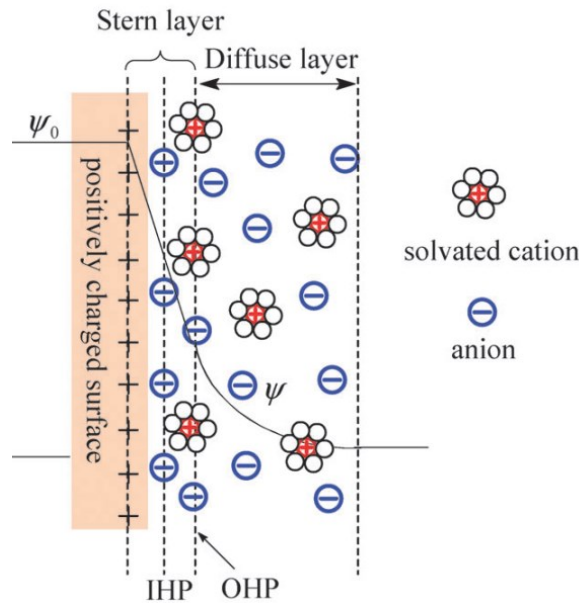


Figure 5. Modèle de Stern, décrivant l'évolution du potentiel de charge d'une surface, Ψ_0 , en fonction de la distance et des interactions avec les ions; IHP et OHP représentant, respectivement, les complexes de sphère interne et externe. Illustration d'après Zhang and Zhao (2009)

L'affinité des métaux pour les sites de surface est contrôlée par la stabilité du complexe formé, traduite par la valeur de la constante de stabilité, $\log K$, qui augmente avec la denticité du complexe, c'est-à-dire le nombre de liaisons formées entre le métal et la surface. A l'heure actuelle, ces connaissances ne sont pas disponibles pour les mécanismes d'adsorptions des métaux par les NPs. Ils ont uniquement été paramétrés à l'aide des modèles empiriques classiques d'adsorption (e.g. Freundlich, pseudo-second order) (Davranche et al., 2019). Si des hypothèses ont été émises quant aux processus physico-chimiques mis en jeu, ils n'ont jamais été validés.

L'étude des mécanismes de sorption des métaux par les surfaces est basée sur l'expérimentation qui permet de déterminer les capacités de sorption, et l'analyse, notamment par spectroscopie (RPE, XPS, XAS, EXAFS, XANES, etc.) qui, via l'étude de l'environnement atomique du métal considéré, permet de déterminer le type de complexes formés, sphère interne ou sphère externe, et sa denticité. Leur mise en œuvre est cependant lourde et l'accessibilité aux techniques limitée. La modélisation géochimique représente une alternative intéressante à ces techniques, elle permet notamment de tester différentes hypothèses mécanistiques et scénarii (variation des paramètres physico-chimiques, présence de ligands, etc.). La plupart de ces modèles sont basés sur un ensemble de réactions chimiques entre ions et sites de surface,

couplés à un modèle physico-chimique estimant le potentiel de surface du solide, e.g., Visual MINTEQ (Gustafsson, 2010), WHAM (Tipping, 1994), PHREEQC (Parkhurst and Appelo, 1999). Ces modèles requièrent, cependant, un certain nombre de données d'entrée telles que le pH, la force ionique (FI), les concentrations totales, la surface spécifique ($\text{m}^2 \text{g}^{-1}$), la densité de site, les constantes de déprotonation des sites (pKa) et les constantes de stabilité métaux-surface (log K). Or, la plupart de ces données n'existent pas ou uniquement partiellement pour les NPs modèles. Dans le Table 1 sont résumées les données disponibles. Aucune constante de stabilité, log K, n'a pour l'instant été produite et peu de jeu de données d'adsorption existent.

Table 1. Paramètres de surface nécessaires et disponibles pour la conception d'un modèle de complexation de surface métaux/NPs

NPs	Surface spécifique	Type de site	Denticité	pKa	Log K**	Données expérimentales	Références
PSL surfactant	X*	COOH	?	?	?	-	-
PSL sans surfactant	X*	COOH	?	?	?	X	Pessoni et al., 2019
PSL Pd	X*	COOH	?	?	?	-	Mitrano et al., 2019
m-NPs (PET)	?	?	?	?	?	-	Rodríguez-Hernández et al., 2019
m-NPs (PS)	?	?	?	?	?	-	El Hadri et al., 2020
e-NPs	?	?	?	?	?	X	Davranche et al., 2019

*Obtenue par calcul à partir de la taille des nanoparticules monodispersées.

** Extrapolées à partir de données expérimentales

Un autre outil, moins conventionnel et original pour accéder à certaines de ces informations, est la 'sonde' terres rares. Les terres rares sont un groupe de 14 éléments chimiques aux propriétés proches et cohérentes sur l'ensemble du groupe (de Baar et al., 1991; McLennan, 1994). Les réactions chimiques, auxquelles elles sont soumises, créent de légères différences entre elles, et notamment des fractionnements qui peuvent être exploités pour tracer des processus biogéochimiques (Davranche et al., 2011; Noack et al., 2014). Ces propriétés permettent d'étudier les terres rares comme un ensemble cohérent et d'exploiter leur fractionnement sous forme de spectre (pattern) qui correspond à la distribution de leur abondance en fonction de leur numéro atomique. Les variations du spectre des terres rares ont ainsi été utilisées pour étudier les processus de complexation de surface sur les colloïdes de MO (Tang, 2003; Takahashi et al., 2005; Pourret et al., 2007; Marsac et al., 2010). Il a ainsi été

montré que le spectre de terres rares varie en fonction de la charge en métaux adsorbés, de la nature des sites activés par la complexation et de la denticité (monodenté, chélate) des complexes formés (Figure 6).

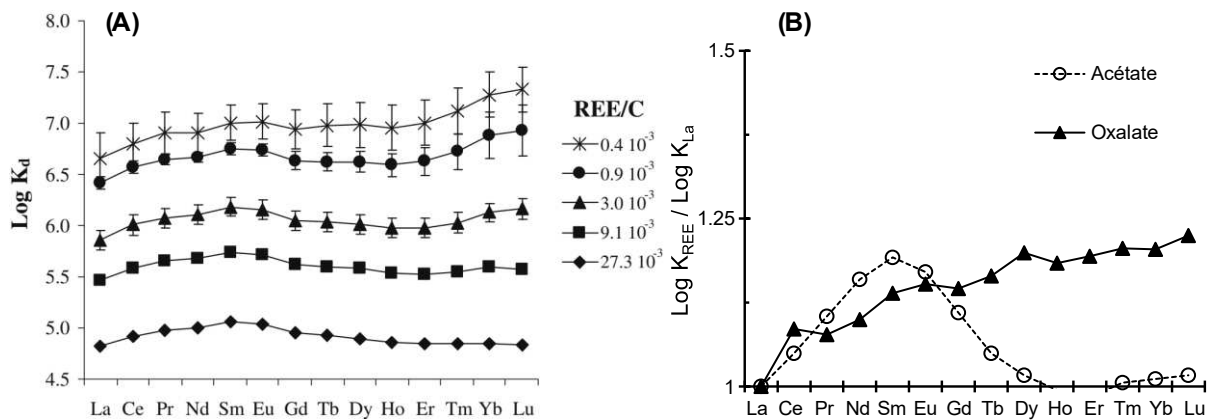


Figure 6. Variation des spectres de REE, (A) coefficients de distribution en fonction du rapport REE/Acide humique (Marsac et al., 2010), et (B) constantes de stabilité normalisées au La avec l'acétate et l'oxalate formant respectivement des complexes monodentés et chélatés (Martell et Smith, 1977).

Objectifs de la these

La présence des NPs dans l'environnement est maintenant admise, et leur quantité est amenée à augmenter. Leur identification, leur caractérisation ainsi que la compréhension de leurs interactions avec les micropolluants métalliques sont donc devenues cruciales. Bien que de nombreuses études portent sur les NPs, trop peu se sont intéressées à développer des stratégies analytiques permettant de les identifier *in-situ*, et la plupart utilisent des modèles de NPs non représentatifs de ceux produits dans l'environnement. De plus, bien que l'interaction entre les NPs et les métaux ait été démontrée, les mécanismes mis en jeu ne sont pas connus.

Pour répondre à ces objectifs, mon doctorat a été structuré en 3 volets :

- **L'identification des NPs dans des échantillons environnementaux,**
- **La production d'un modèle de NPs environnementalement pertinent,**
- **Les interactions entre les métaux et les NPs, étudiées par l'intermédiaire de la « sonde » terres rares et de la modélisation de complexation de surface.**

L'identification des NPs dans des échantillons environnementaux

L'objectif de cette partie est d'identifier la présence de NPs dans une matrice contenant de la MO par Py-GCMS. Les travaux se sont focalisés sur deux polymères, largement produits à l'échelle mondiale, que sont le PS et le PP. Pour cela des pyrogrammes de PS et PP sous forme de MPs et NPs avec et sans MO ont été comparés afin d'identifier les biais analytiques dus à la taille des particules et aux interférences avec la MO. Deux méthodologies ont été testées, une directe, à partir de pyrolyzates propres à chaque polymère et une indirecte, par l'intermédiaire de rapports entre pyrolyzates, notamment pour ceux produits à la fois par le polymère et la MO.

Production d'un modèle de NPs pertinent de l'environnement

L'objectif de cette partie est de produire des NPs proches de ceux produits par photo-oxydation en conditions environnementales. Ces nouveaux modèles ont été produits à partir de plastiques très altérés collectés dans l'environnement. Les MPs et NPs ont ensuite été caractérisés par différentes techniques (taille et forme des particules, fonctions de surface, quantité de sites ionisables, surface spécifique, etc.).

Interactions entre les micropolluants métalliques et les NPs

L'objectif de cette partie est de caractériser les processus mis en jeu dans les interactions entre NPs et métaux. Différents modèles de NPs, dont les nouveaux NPs produits via ce doctorat, ont été utilisés. Dans un premier temps, la 'sonde' terres rares a été utilisée afin de caractériser les mécanismes mis en jeu et notamment les complexes formés. Puis, dans un second temps, les différentes hypothèses ont été testées par modélisation géochimique à l'aide du Pb et d'un ensemble de données expérimentales.

Le manuscrit est construit autour de 4 articles : deux d'ores et déjà acceptés (Environmental Sciences and Technologie, Environmental Science/ Nano), un autre soumis (Environmental Science/ Nano), et un autre qui sera prochainement soumis (Journal of Colloid and Interface Science). Il est composé d'une introduction, de 3 chapitres et se termine par une conclusion générale, reprenant l'ensemble des résultats et des perspectives.

**CHAPITRE I. IDENTIFICATION DES
NANOPLASTIQUES DANS DES
MATRICES
ENVIRONNEMENTALES:
CAS DU POLYSTYRÈNE ET DU
POLYPROPYLENE**

Ce chapitre correspond à un article publié dans la revue Environmental Science & Technology, "Nanoplastics identification in complex environmental matrices: Strategies for polystyrene and polypropylene", Florent Blancho, Mélanie Davranche, Hind El Hadri, Bruno Grassl, Julien Gigault, <https://doi.org/10.1021/acs.est.1c01351>.

Dans ce chapitre, nous nous sommes intéressés à la détection des NPs par Py-GCMS. L'échantillon étant pyrolysé (Py), puis séparé par chromatographie gazeuse (GC) et ensuite détecté spectrométrie de masse (MS).

Résumé

L'identification des NPs dans les matrices environnementales (i.e. fleuve, océan, sol, etc.) reste un challenge analytique. Malgré le nombre important d'études sur les NPs peu d'entre elles se sont intéressées à leur détection dans des matrices complexes. Cela s'explique en partie par leur composition carbonée, la différence des polymères mis en jeu ainsi que leur faible quantité par rapport à la MO en conditions environnementales. La séparation des produits de pyrolyses a permis d'obtenir des réponses analytiques pour les NPs de PP et de PS. Des pyrolyzates spécifiques aux polymères et à leurs fragments d'ion (i.e. m/z) ont été sélectionnés et validés. Dans un second temps, les interférences avec la MO ont été explorées en étudiant des mélanges de NPs et de MO (i.e. algue, matière organique du sol, acide humique) ainsi qu'une suspension de NPs produits à partir de plastiques altérés en conditions environnementales. Cette étude a permis l'identification directe du PP et ce en présence de MO. Les NPs de PS n'ont pu être identifiés de manière directe, en revanche l'évolution de rapport de pyrolyzates a permis de les détecter. Les stratégies présentées dans ce chapitre ouvrent la voie à de nouvelles possibilités de détection et d'identification des NPs pour des matrices environnementales telles que les sols, les particules fines et le vivant.

Abstract

Identification of NPs in complex environmental matrices remains a challenge. Despite the increase in NPs studies, there is a lack of studies dedicated to NPs detection, partially explained by their carbon-based structure, their wide variety of composition, and their low environmental concentrations compared to the natural organic matter. Here, pyrolysis coupled to a GCMS instrumental setup provided a relevant analytical response for PP and PS NPs suspensions. Specific pyrolysis markers and their indicative fragment ions were selected and validated. Possible interferences with environmental matrices were explored by spiking NPs in various organic matter suspensions (i.e., algae, soil natural organic matter, and soil humic acid) and analyzing an environmental suspension of NPs. While a rapid PP NPs identification was validated, PS NPs require preliminary treatment. The here presented strategies open new possibilities to the detection/identification of NPs in environmental matrices such as soil, dust, and biota.

I.1 Introduction

Under environmental conditions, all plastic debris is likely to release many NPs under multiple physicochemical degradation pathways (Andrady, 2011; Gigault et al., 2016; Lambert and Wagner, 2016). While the scientific community is now admitting the occurrence of NPs in the environment, relatively few studies demonstrated their presence (Ter Halle et al., 2017; Davranche et al., 2020; Wahl et al., 2021). When the material reaches the nanoscale, its properties, reactivity, and impact are significantly enhanced, especially for plastic debris due to its considerable heterogeneity in composition (Gigault, 2018; Hartmann et al., 2019; Gigault et al., 2021). The plastic debris regroups an extensive range of materials which complexifies the analytical and environmental challenge. This challenge is even more complex when the size of the plastic debris is under the optical resolution (Gigault, 2018; Gigault et al., 2021). Each plastic family, composition, and size require specific attention and dedicated strategy as performed this last century for a wide range of contaminants.

Among the various plastics produced globally, PP and PS represent approximately 20 to 30% of the total production (Geyer et al., 2017). Polypropylene plastic debris are detected in diverse environmental compartments (Geyer et al., 2017; Plastics Europe, 2017). For instance, Reisser et al. (2013) found approximately 30% PP in plastic debris collected on the Australian sea coast. Brignac et al. (2019) consistently found a significant proportion of PP pieces (i.e., >15%) on beaches, sea surface, and seafloor. In terrestrial environments, PP microplastics (MPs) have been reported in sewage sludge (Okoffo et al., 2020), sediments, and suspended matter in rivers (Dierkes et al., 2019). While PS-based plastics represent more than 96% of the plastic debris investigated in the literature, it represents less than 6% of the plastic found in the environment (Zhao et al., 2019; Wilcox et al., 2020).

At the nanoscale, determining plastic debris occurrence in complex environmental media is highly challenging due to their small size and ability to heteroaggregates with the natural organic matter (NOM) and the inability to physically separate them (NPs vs. NOM) by filtration or other processes (Nguyen et al., 2019). As recently explained, when reaching the nanoscale, the volume of NOM related to the plastics increases exponentially. Therefore, analytical strategies used to characterize microscale cannot be extrapolated to the nanoscale plastic debris.

Among the available analytical methods, pyrolysis coupled to gas chromatography and mass spectrometry proved the presence of polyethylene (PE) NPs in the colloidal fraction of the North Atlantic Ocean gyre (NAOG) (Ter Halle et al., 2017). However, we could not detect

PP markers in the colloid fraction, while this plastic is present in the MPs fraction. Two reasons were invoked: 1) low PP abundance and 2) modification of the pyrolysis products of nanoscale PP. To date, no Py-GCMS pyrogram is provided for colloidal PP in the literature., Potential variations in pyrolysis products at the nanoscale are thus unknown. Polystyrene NPs are identified in NAOG (Ter Halle et al., 2017), coast exposed to the NAOG (Davranche et al., 2020), and contaminated soil (Wahl et al., 2021). However, as for PP under complex environmental conditions, interferences with OM were encountered, especially for their primary direct markers, styrene, and toluene (Dümichen et al., 2015, 2017). While authors are looking for the styrene dimers as proof of the PS presence, as observed for a large fragment of PE, it is less probable to find such pyrolyze products at the nanoscale due to the considerable heterogeneity of the NOM. One way to by-pass such a limitation is to investigate the pyrolyzates ratio to detect the presence of the plastics in NOM (Watteau et al., 2018). Moreover, the problem is even more complicated as, in addition to pyrolyzates interferences, we demonstrated that the NOM also attenuates the global signal (Wahl et al., 2021). A critical preliminary investigation of the possible interferences with NOM has therefore to be performed.

Therefore, this study aims to explore PS and PP NPs identification in the presence of different NOM by Py-GCMS. Two different and complementary strategies are developed and proposed according to the plastics composition and the NOM. Based on a careful investigation of chromatograms in terms of pyrolyzate and retention time. We demonstrate that PP NPs can be directly identified in complex media. However, for PS NPs, we needed to develop a protocol for purifying the environmental sample from NOM to obtain a reliable detection of PS in complex media. The method is finally applied on an environmentally-relevant NPs suspension obtained from plastic debris altered under environmental conditions and covered by NOM. While we use the pyrolysis library to identify PP NPs, PS NPs are detected in the environmental sample according to the relative ratio of its principal pyrolyzates.

I.2 Materials and methods

I.2.1 Samples

Polystyrene and polypropylene pellets were purchased from Sigma Aldrich and were used as reference materials for Py-GCMS and to produce NPs. Natural organic matter standards are purchased from IHSS (International Humic Substances Society): leonardite NOM (LNOM, references 1S104H), leonardite Humic Acid (LHA, reference 1BS104L). LNOM and LHA were solubilized in 1 mol L⁻¹ of NaOH (Sigma Aldrich) (1:10 ratio in g/g) for 24 h. Additionally,

to these NOM standards, fresh organic matter is prepared from Sargasso algae residue (Sainte-Marie Bay, Guadeloupe, France). The organic matter of Sargasso algae (SAWE) was obtained by stirring 1 g of algae in ultrapure water (1:10 ratio in g/g) for 24 h and filtered at 3 μm (Pall) (Stoloff and Silva, 1957). The total organic carbon concentration (TOC) of all the organic matter solutions was quantified by a TOC-analyzer (TOC-V analyzer, Shimadzu).

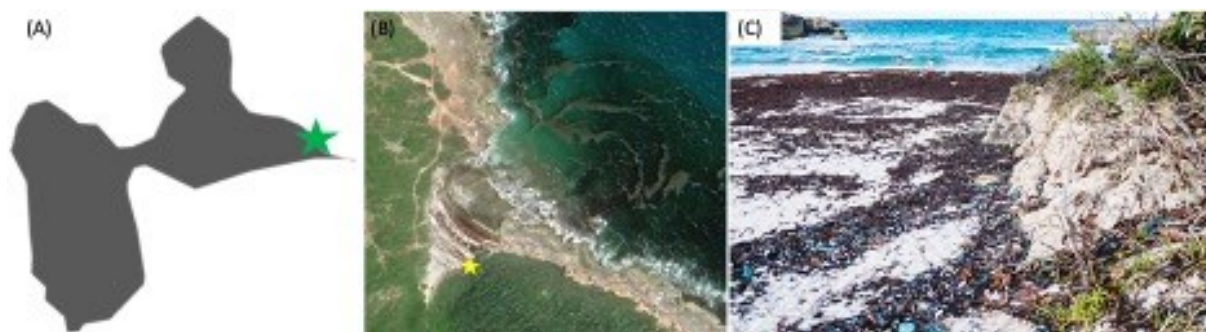


Figure I.1. Sampling area on the French Caribbean Island Guadeloupe; (B) localization of the bay (Sainte Marie) at the GPS coordinate 16°16'24" N-61°14'35" W with the brown line is corresponding to the Sargassum Algae coming from the oceans (CNES); (C) pictures of the sampling site where the plastic debris are identified and mixed with the Sargassum Algae (CNRS, Cyril Fresillon).

I.2.2. Nanoplastics preparation

Polypropylene and polystyrene NPs are produced using a top-down mechanical degradation as previously described (El Hadri et al., 2020). Briefly, plastic pellets were fragmented using a planetary ball mill (Pulverisette 7, Fritsh GmdH) with a 5 or 10 mm diameter zirconium oxide ball. The fragmented PP and PS powders are freeze-dried (Alpha 3-4, Christ). Then, the powders are redispersed in water and filtered at 3 μm (polyethersulfone membrane, Pall) to remove microsized-particles. Additionally, environmentally relevant NPs, namely environmental NPs (e-NPs), were produced from plastic debris collected in the environment (Davranche et al., 2019). Plastic debris were randomly collected on Saint Marie Bay's beach (Guadeloupe, France) in September 2018 (Figure I.1). This beach receives plastic debris and Sargassum Algae (brown line on Figure I.1B and Figure I.1C) from the NAOG (Davranche et al., 2020). Briefly, 100 g of plastic debris was stirred in ultrapure water (1:5 ratio) for 2 days (KS 15A, Edmund Bühler GmbH), sonicated for 5 days (TP 680/DH, Elma GmbH), and finally filtered at 3 μm (PTFE, Pall). To be in the range of analytical ability of the here-used methods and when necessary, the mass of the colloids (analyzed NPs and NOM) was

concentrated using an ultrafiltration system (Amicon, Merck Millipore) equipped with a 20 kDa cut-off membrane (PES, Microdyn NADIR).



Figure I.2. Plastic debris used to produce the e-NPs suspension, showing brown algae residue on its surface

As beached plastics were primarily associated with sand and sargassum algae residues (Figure I.2), a significant amount of natural organic matter is released and dispersed with the NPs produced. To purify the NPs from the NOM, a preliminary degradation study was done on algae suspension using H_2O_2 with and without UV. Algae suspensions were obtained by agitating algae debris with ultrapure water during two days, then the suspensions were filtrated at $3\mu m$ (Pall). According to literature (Alnaizy and Akgerman, 2000; Vilhunen et al., 2010; Nuelle et al., 2014), the oxidation reaction time with H_2O_2 was set to 72h without UV and 5h with UV (UVC, RMR-600, Rayonet). Both reaction times are explained by the slower reaction time of H_2O_2 without UV, than with UV. Figure I.3 present the OM degradation yield relative to the $H_2O_2\%$ with and without UV exposition. The highest OM degradation was reached for $H_2O_2\%=1$ combined with UV. As observed, the coupling H_2O_2/UV efficiency to degrade OM decreased with the increasing H_2O_2 %. the optimized degradation protocol (H_2O_2 1% +UV) was then selected and applied onto the e-NPs OM suspensions.

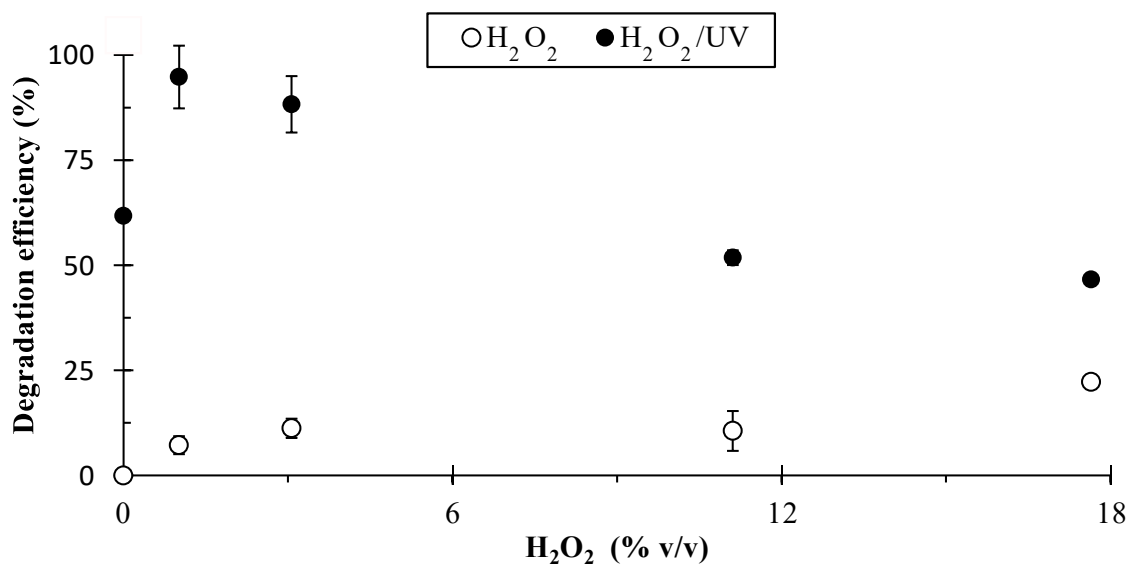


Figure I.3. OM degradation yield (i.e. $\text{TOC}(t)/\text{TOC}(t_0) \times 100$) relative to the $\text{H}_2\text{O}_2\%$ and with (Black point) and without (White point) UV exposition.

I.2.3 Size and shape characterization

The hydrodynamic size distribution of the NPs and e-NPs was determined using optical fiber dynamic light scattering (DLS). Measurements are performed with a VASCO Flex (Cordouan Technologies, France). The size distribution of NPs is determined by fitting the autocorrelation function (ACF) with Padé-Laplace and Sparse Bayesian Learning algorithm (Nyeo and Ansari, 2011; Maguire et al., 2018). Each DLS analysis is carried out with six replicates with an analysis period of 120 s. Only results for replicates with reliable residuals ($r < 0.01$) were accepted. The ACF samples are compared to 200, 500, and 900 nm polystyrene spherical latex nanoparticles (Thermo Scientific). The shape of the NPs is examined using a Jeol JEM 2100 HR electron microscope in transmission mode (TEM) after drying 2.5 μL of suspension onto a carbon grid (Oxford Instrument). Images are acquired with a Gatan Orius SC200D camera, and elemental analysis is performed using an EDX Oxford X-Max 80T detector.

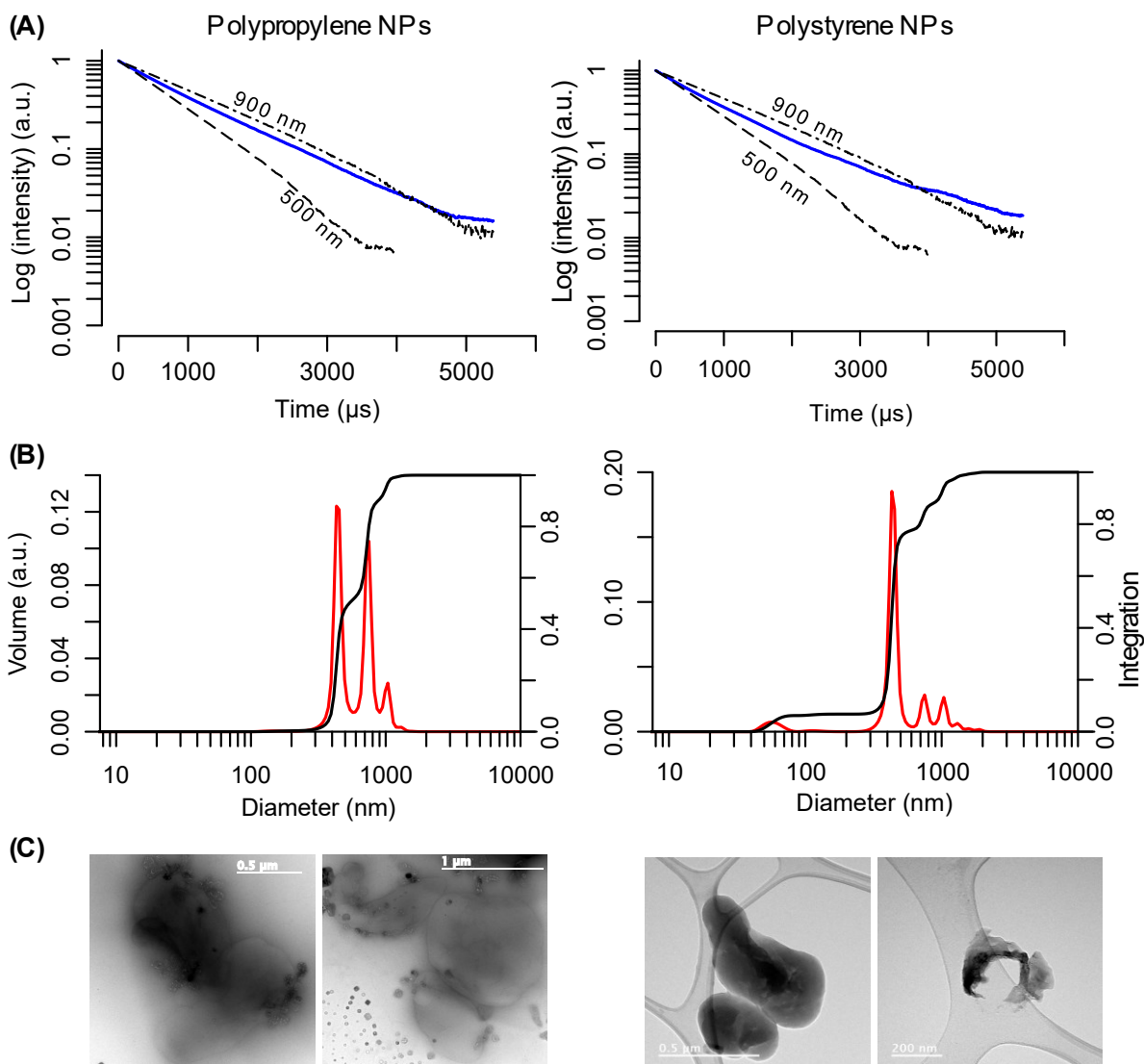


Figure I.4. (A) Log-transformed autocorrelation function (blue) bordered by the 500 and 900 nm polystyrene spherical latex nanoparticles, (B) size distribution, and (C) TEM images for PP and PS NPs.

I.2.4 Nanoplastics molecular identification

NPs suspensions (PP, PS, and e-NPs) and the NOM were analyzed by pyrolysis (PY-3030, Frontier Lab) coupled to gas chromatography and a mass spectrometry detector (Py-GCMS) (5977B, Agilent Technologies). Before Py-GCMS analysis, liquid samples are evaporated at 45°C in an 80 μL pyrolysis cup (Frontier Lab). The mass of prepared NPs was fixed at 2 μgC in the pyrolysis cup. Concerning the NOM, the mass was ranged from 25 to 175 μgC . To assess any polymer contamination during the sample preparation (i.e., drying process), empty pyrolysis cups were systematically added beside regular samples. The optimal GC conditions were fixed according to the method of Dehaut et al. (2016). The pyrolysis was

performed at 600°C. Once pyrolyzed, samples were injected (splitless) into a 30m DB5 capillary column (Agilent Technologies) using helium as the carrier gas. The column temperature was fixed at 50°C for 10 min, increased to 275°C at a rate of 5°C/min, and finally kept at this temperature for 15 min. Separated pyrolysis products were ionized at 70 eV, and their mass spectra were analyzed between m/z 33 to 500. Pyrolyzates signals are compared to the NIST library and personal library builds using plastic pellets described above. Each pyrograms were realized in four replicates. As it is not yet possible to quantify NPs by Py-GCMS, we determined the signal-to-noise ratio (SNR), ranging from 150 to 430, for all performed analyses. Based on the SNR and the mass of NPs (Environmental Protection Agency, 2016), LOD can be estimated from 0.2 to 0.4 mgC L⁻¹.

I.3 Results and Discussions

I.3.1 Nanoscale effects on plastic pyrolysis

The size and shape of PP and PS NPs used in these studies were described in the Figure I.4. For both suspensions, NPs present a different population with $d_H < 1 \mu\text{m}$. It is worth noting that hydrodynamic diameter depends on the geometric size (radius) and the shape of materials (Graf et al., 1992; Liu et al., 2012). Therefore, asymmetrical materials can present different diffusion (transversal and rotational), which results in different apparent populations on the size distribution (Liu et al., 2012). All NPs suspensions present anisotropic and heterogeneous shapes with spherical equivalent sizes less than 1 μm . For PP NPs, fine particles (size > 200nm) were identified as NPs, and opaque particles as inorganic species (< 200nm), as confirmed by EDX analysis (Figure I.5). These species are principally titanium oxide, known to be one of the major plastic additives (Hahladakis et al., 2018). No inorganic species were identified into PS NPs, which is explained by their virgin pellet source.

Based on the PP pyrolysis at a microscale (Figure and Table I.1), four distinctive peaks were pre-selected: the C9 (2,4-dimethyl-1-heptene), the C12 (meso-2,4,6-trimethyl-1-nonene), the C15i (isotactic-2,4,6,8-tetramethyl-1-undecene) and the C15s (syndiotactic-2,4,6,8-tetramethyl-1-undecene). The pyrolyzates C9 and the C15s have already been documented as a PP marker in environmental studies (Ter Halle et al., 2017; Dierkes et al., 2019; Okoffo et al., 2020; Sullivan et al., 2020; Nasa et al., 2020).

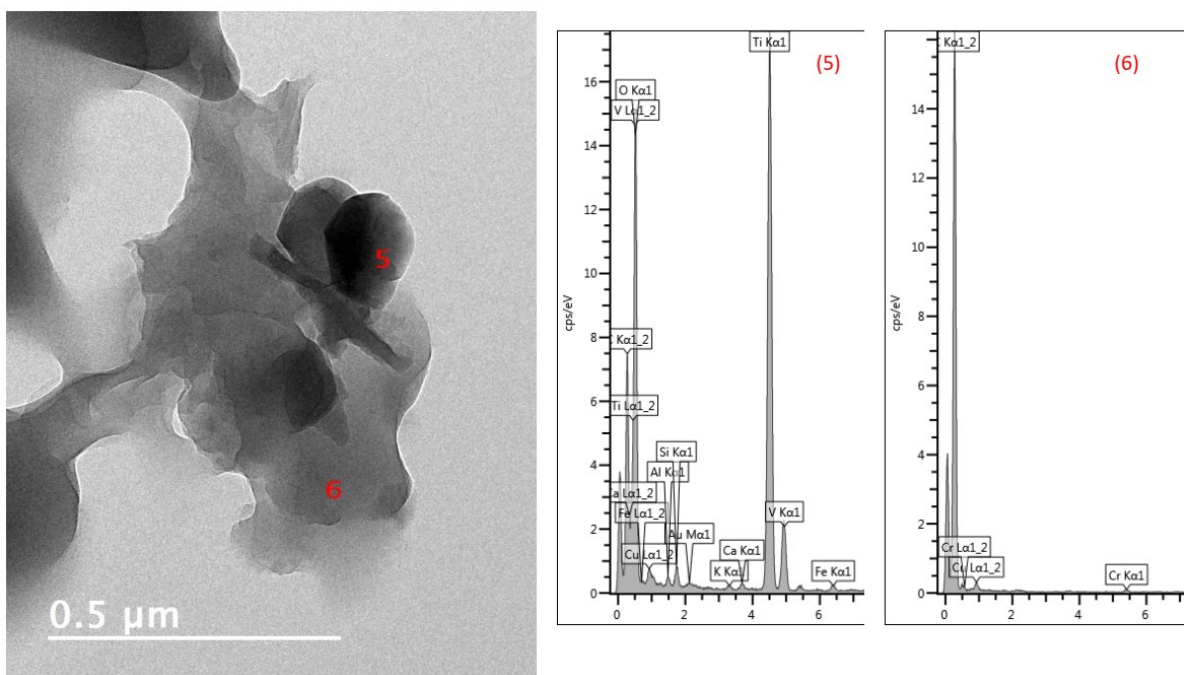


Figure I.5. TEM image, left part and EDX spectra, right part. The Spectra 5 and 6 are related to the named zone 5 and 6 on the TEM image, respectively.

Based on a literature comparison (Fischer and Scholz-Böttcher, 2017; Okoffo et al., 2020), none of these markers were obtained for various NOMs. The pyrograms of PP NPs (TIC, m/z 70 and 69) are plotted in Figure I.6. The m/z 70 pyrogram specifically enhanced the marker C9, whereas the m/z 69 enhanced the other PP pyrolyzates (i.e., C12, C15i, and C15s). The mass spectra of the PP marker pyrolyzates are presented in Figure I.6B. For each pyrolyzate, the mass spectrum showed an important correlation with that presented by Tsuge et al. (2011). As a result, these mass spectra were saved to build an in-lab library for further comparison with other mass spectra. An important piece of auxiliary information extracted from these pyrograms was the retention times of the PP markers (Table I.1).

Peaks are observed at the retention times of all the selected PP markers (Figure I.7A). The mass spectrum of PP NPs obtained at the characteristic retention times (blue bar) were compared with the PP library (red bar). For C9, C12, and both C15 compounds, mass spectra were significantly similar to the library ones (Spectrum Similarity, SS > 0.90). Although these markers are found on both micrometric pellet and NPs pyrolysis, their relative peak areas vary significantly (Table I.1). For PP NPs, the proportion of C12, C15i, and C15s increases by a factor of 2-3 compared to MPs pellets. Based on this result, C9, C12, and C15 compounds are the most relevant for identifying PP at the nanoscale.

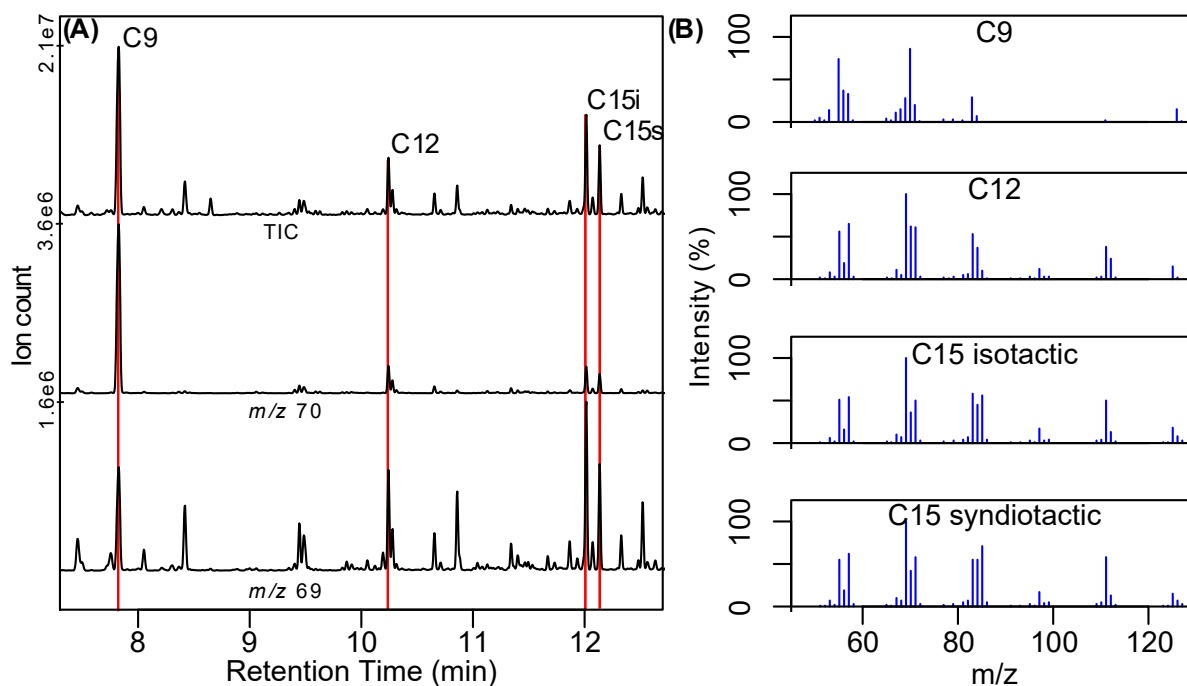


Figure I.6. (A) Polypropylene micropellet pyrograms for TIC, m/z 70 and m/z 69. (B) Mass spectra of pyrolyzates recorded at the PP marker retention times used to build the library.

For PS NPs identification, seven distinctive peaks were pre-selected from the microscale pellet pyrolysis (Figure I.8): toluene, styrene, α -methyl styrene, bibenzyl, styrene dimer, 2-phenyl naphthalene, and styrene trimer. Only two pyrolyzates differ from the pyrolysis of literature and hereafter studied organic matter (Table I.2): styrene dimer and trimer. The m/z 104 pyrogram specifically enhanced the styrene, whereas the m/z 91 pyrogram enhanced the styrene dimer and trimer. Only significant peaks at the styrene and styrene dimer's retention time were studied (Figure I.9). Their mass spectra were similar to the library spectra.

Table I.1. Polypropylene distinctives pyrolyzates and the occurrence in the OM studied and in literature.

Pyrolyzates	Peak (%)	Peak (%)	Area	LHA	LNOM	SAWE	Ref.	RI
	PP	PP NPs	(a.u./ μ gC) PP NPs					
C9	100	100	3.29e5	-	-	-	-This study	855
C12	5.48	10	1.80e4	-	-	-		1084
C15i	3.14	9.58	1.03e4	-	-	-		1312
C15s	2.61	6.53	8.59e4	-	-	-		1330

Oppositely, the styrene trimer mass spectra are noisily due to their low abundance and the limit of detection. From PS MPs to NPs, the proportion of styrene dimer and trimer decreased from 26% to 0.2% and 23% to a negligible area. One hypothesis to explain such result, as we previously observed for PE (Ter Halle et al., 2017), is that the probability of forming a large mass of pyrolyzate (i.e., $m/z > 200$) considerably decreases from the microscale to the nanoscale.

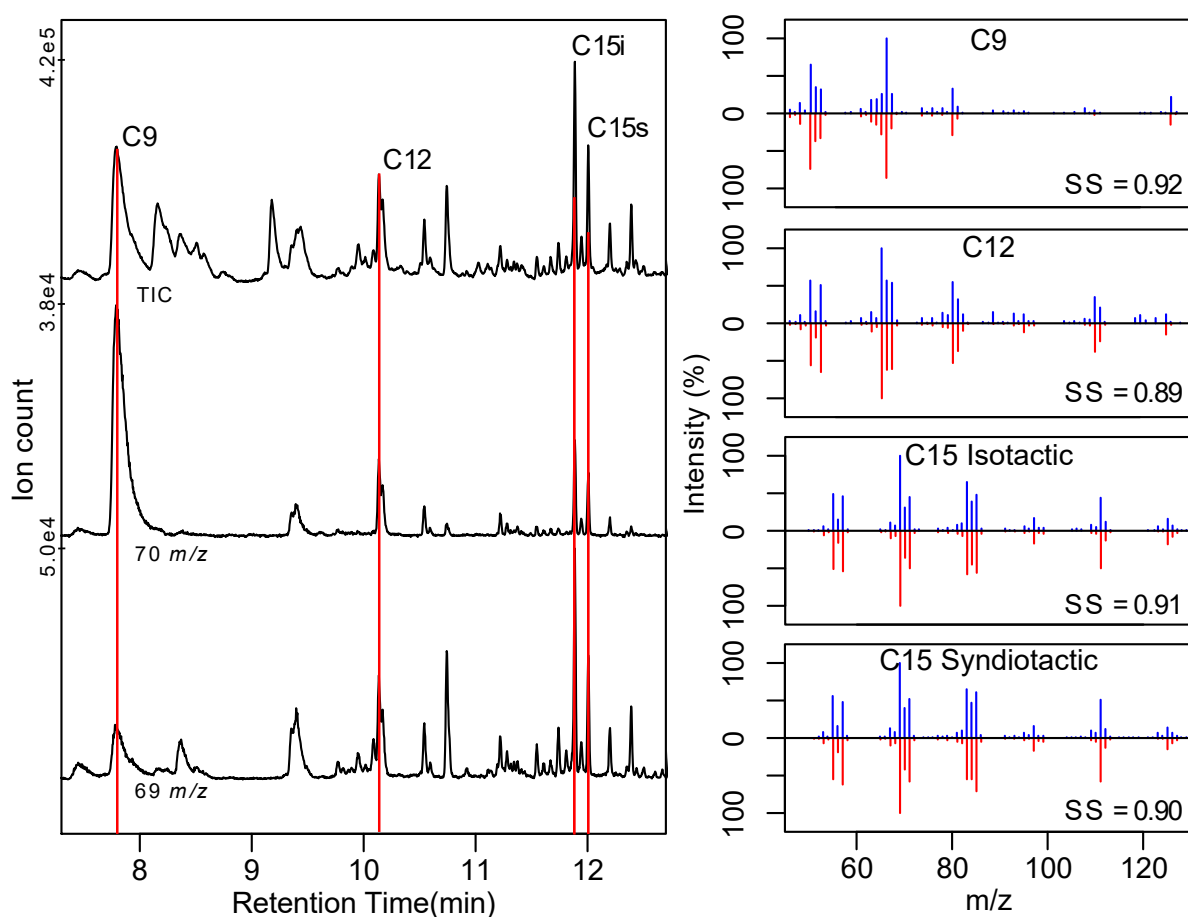


Figure I.7. (A) Polypropylene NPs pyrograms for TIC, m/z 70 and m/z 69. (B) Mass spectra comparison between the MSs of pyrolyzates recorded at the PP marker retention times (blue) and their library MSs (red).

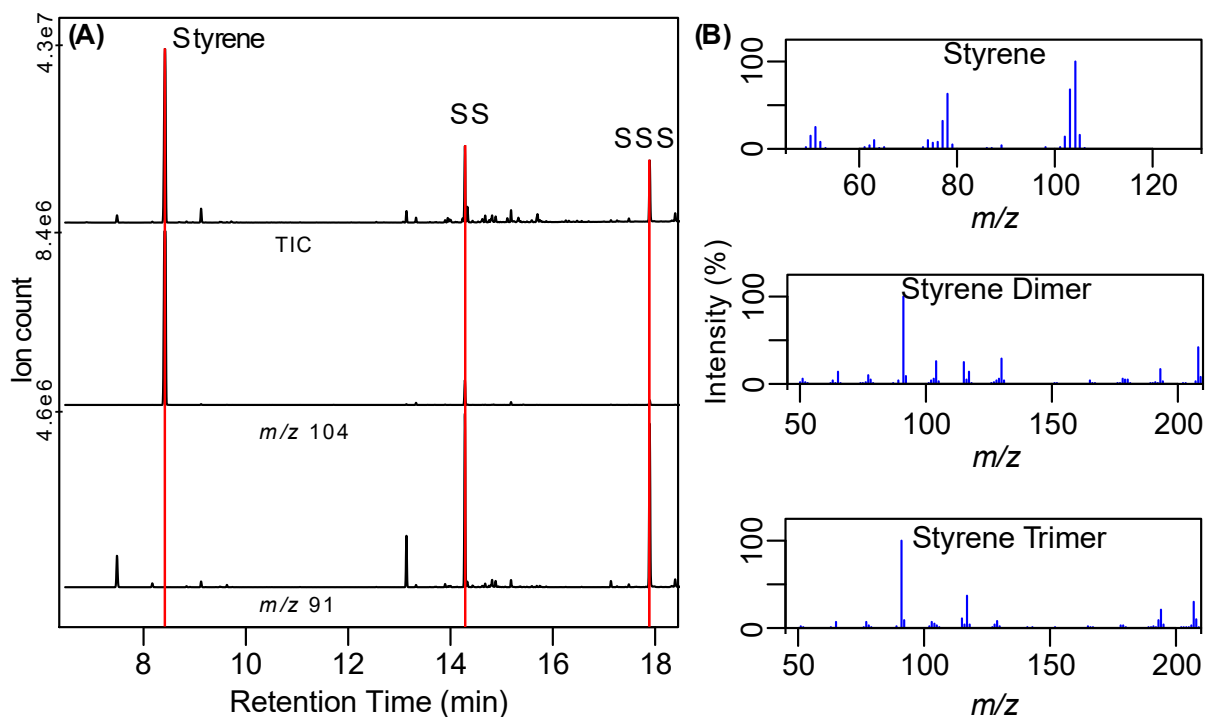


Figure I.8. (A) Polystyrene micropellet pyrograms for TIC, m/z 104 and m/z 91. (B) Mass spectra of pyrolyzates recorded at the PP marker retention times used to build the library.

Since the direct identification of PS NPs is based on both pyrolyzates, the decreasing size from PS MPs to NPs would affect the PS NPs detection in environmental matrices. Regarding their nanoscale, low quantity, and ability to hetero-aggregate with the NOM, the direct identification of PS NPs in environmental matrices seems impossible. Polystyrene identification should thus integrate an indirect identification. An alternative is to determine the absolute pyrolyzate ratio of toluene/styrene (Tol/Sty) (Fabbri et al., 1998; Watteau et al., 2018). This ratio is <0.01 for pristine PS and $> 4-5$ for organic matter (Fabbri et al., 1998; Watteau et al., 2018).

Table I.2. Polystyrene distinctive pyrolyzates and their occurrence in the OM studied and in literature. * Non-isothermal Kovats retention indice.

Pyrolyzates	Peak (%) PS	Peak (%) PS NPs	Area (a.u./ μgC)	LHA	LNOM	SAWE	OM	References	RI
Toluene	2.99	1.85	4.02e5	X	X	X	X	Dignac et al., 2005; Gillam and Wilson, 1985; Kaal et al., 2016; Nierop et al., 2005; Rouches et al., 2017	784
Styrene	100	100	2.17e7	X	X	X	X		916
Benzaldehyde	NA	2.85	6.20e5	X	X	X	X	Carr et al., 2010; Schulten and Sorge, 1995	987
α -methylstyrene	2.27	1.32	2.87e5	X	-	-	X	Fabbri et al., 1998; Dignac et al., 2005; Watteau et al., 2018	1006
Bibenzyl	1.76	0.53	1.15e5	-	-	X	X	S. Wang et al., 2017	1583
Styrene dimer	25.65	0.2	4.35e4	-	-	-	-		1789
2-phenylnaphtalene	3.6	1.41	3.07e5	X	X	X	X	Geng et al., 2019	2083
Styrene trimer	22.8	NA	-	-	-	-	-		2542

I.3.2 Natural organic matter contribution

Although few pyrolyzates are common between PP NPs and NOM, their potential coelution of NOM and PP markers was thus investigating. Polypropylene identification was performed by spiking PP NPs into the three different OM (I.2 section). For the SAWE, the PP/OM ratio (g/g) was set to 0.073, corresponding to 2 μgC of PP and 27.5 μgC of SAWE. For LNOM and LHA, the PP/OM ratio (g/g) was set to 0.011, corresponding to 2 μgC of PP and 175 μgC of OM. Leonardite organic matter pyrograms with and without PP NPs were compared to identify potential coeluted pyrolyzates at the retention times of C9, C12, and both C15 compounds.

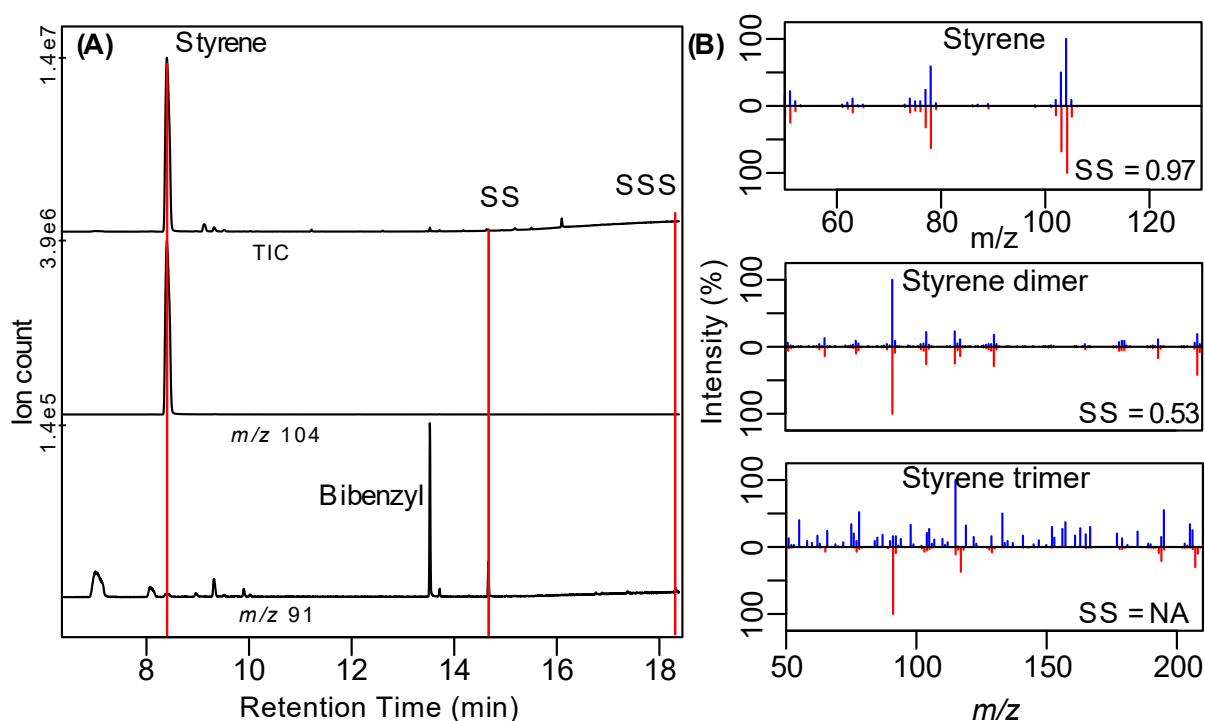


Figure I.9. (A) Polystyrene NPs pyrogram for TIC, m/z 104 and m/z 91. (B) Mass spectra comparison between the MSs of pyrolyzates recorded at the PS marker retention times (blue) and their library MSs (red).

For PP NPs spiked into SAWE, at m/z 70 (Figure I.10A), the pyrogram showed a significant peak at the retention time of C9. At m/z 69, the three other PP markers are observed in the pyrogram (Figure I.10B). Without PP NPs, the mass spectra did not show any similarity with the reference, confirming that SAWE and PP have no homo-pyrolyzate interferences, as previously discussed (Table I.1). The mass spectra for PP NPs spiked into SAWE showed a very high similarity with PP for the following markers: C9, C15i, and C15s (Figure I.10C).

These coeluted SAWE pyrolyzates were thus at too low concentration to interfere. Conversely, the C12 spectra were not similar due to the presence of a coeluted OM pyrolyzates, which contributed to the C12 mass spectrum (Figure I.10C). Therefore, only C12 has coeluted-pyrolyzate interference with SAWE.

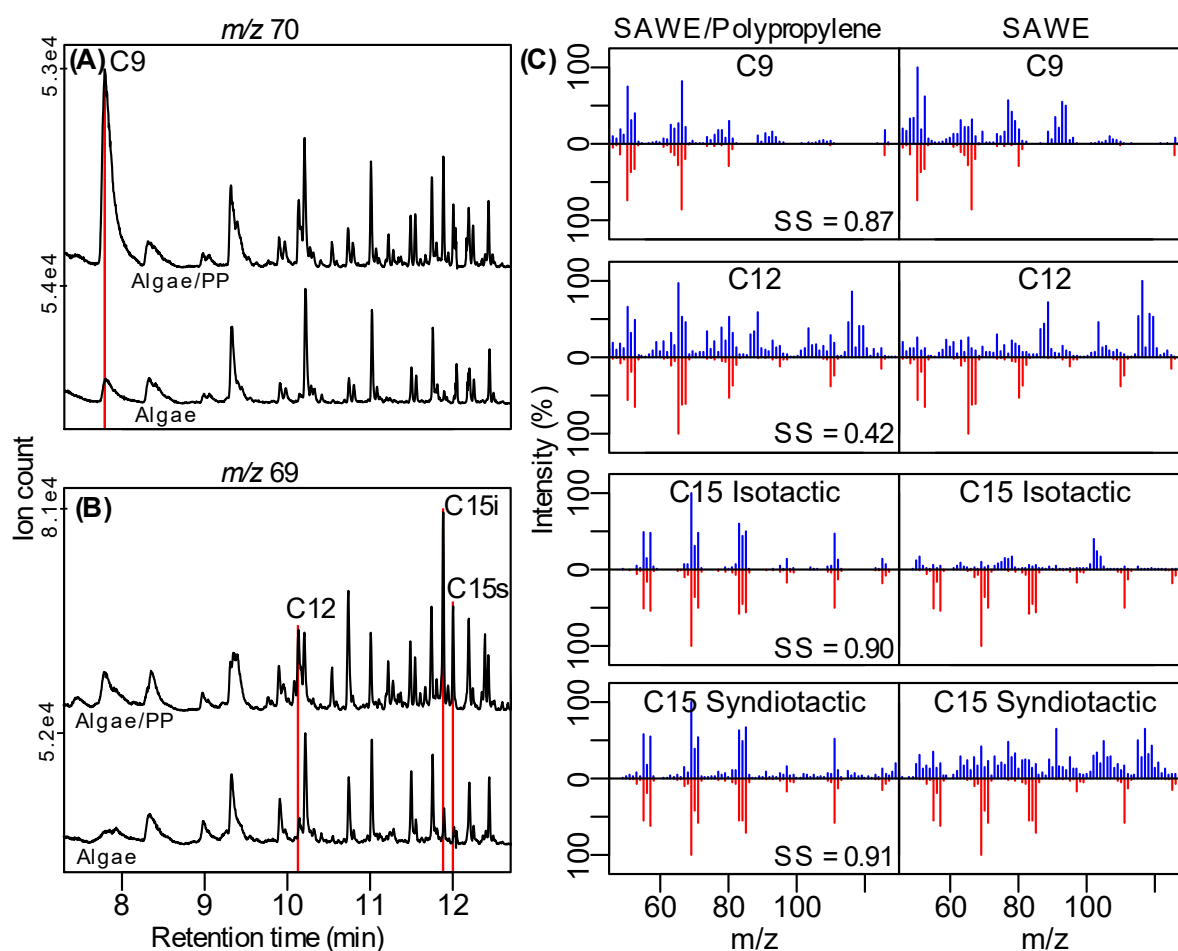


Figure I.10. (A) m/z 70 pyrograms for SAWE without and with PP NPs; (B) m/z 69 pyrograms for SAWE without and with PP NPs; (C) Mass spectra of pyrolyzates recorded at PP marker retention times (blue) and their library MSs (red).

For PP NPs spiked into LNOM (Figure I.11), the m/z 70 and m/z 69 pyrograms showed a significant peak increase for all the PP markers compared to non-spiked LNOM. The peaks at PP retention times remained low compared to those of OM. The LNOM mass spectra with and without PP NPs were different. No homo-pyrolyzate interferences are observed between LNOM and PP. For LHA, a significant peak increase was observed for pyrograms with and without PP NPs at all PP markers' retention times (Figure I.12). The PP markers are thus very distinctive. No mass spectrum similarities are obtained between PP markers and LHA. As

observed for SAWE and NOM, no homo-pyrolyzate interference exists between LHA and PP. With PP NPs, the mass spectra were similar for the PP markers (Figure I.10). No coeluted-pyrolyzate is observed. Thus, PP can be directly identified with all four selected markers.

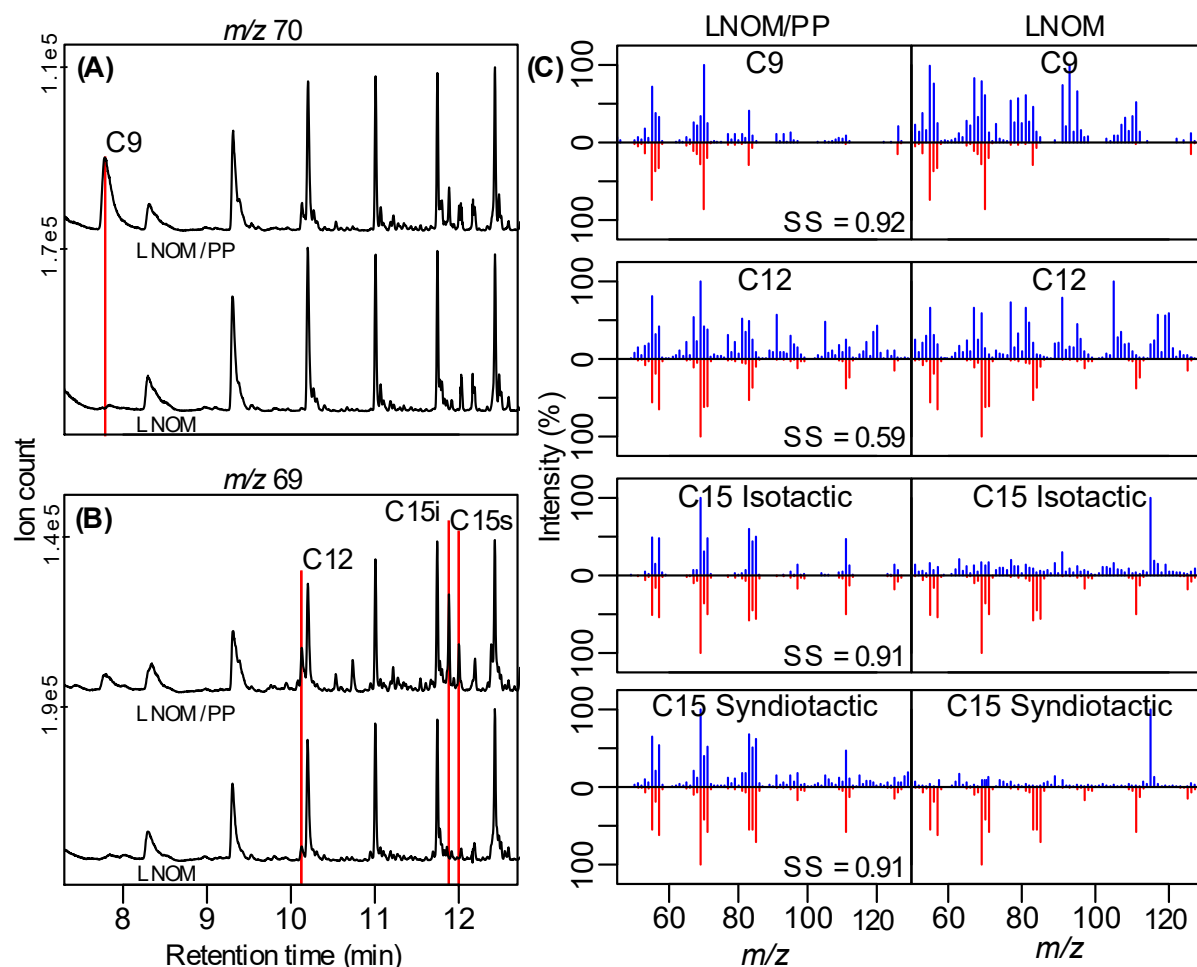


Figure I.11. (A) m/z 70 pyrograms for LNOM without and with PP NPs; (B) m/z 69 pyrograms for LNOM without and with PP NPs; (C) Mass spectra of pyrolyzates recorded at the PP markers retention times (blue) and their library MSs (red).

In summary, coeluted-pyrolyzate interference is identified for C12 for SAWE and NOM. Polypropylene was still identifiable because the three other markers had no interferences. The use of these three PP markers allowed direct PP identification in the three studied OM samples. Concerning the environmental identification of PP, although OM was in excess (e.g., 14 times for SAWE and 100 for LNOM and LHA), all these ratios allowed PP identification. Moreover, the m/z 70 pyrograms show that these ratios could be decreased and that PP identification could be achieved using only the C9 marker. For LNOM and LHA, the PP/OM ratio could be decreased since no peak is present at the retention time of C9 in both OM pyrogram without PP NPs.

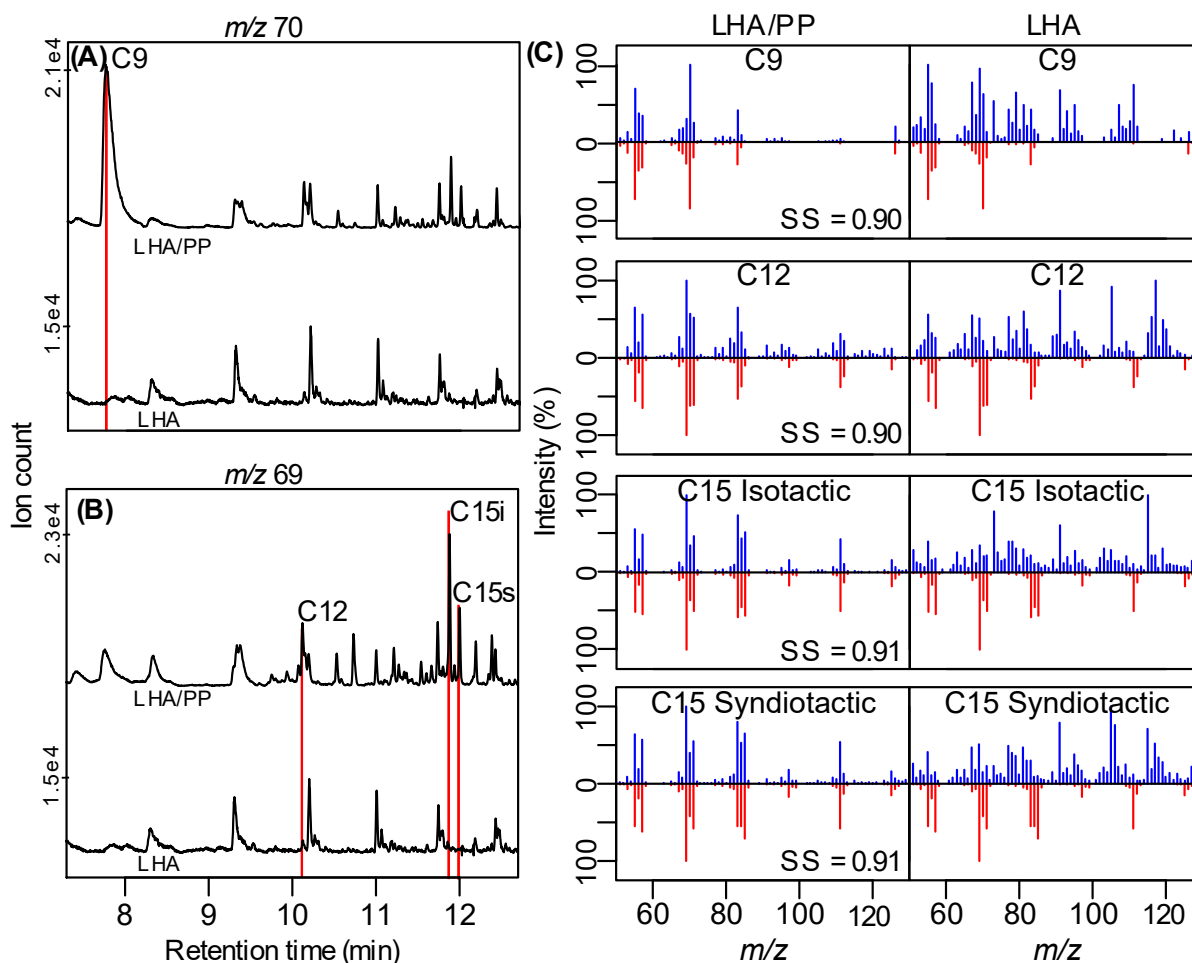


Figure I.12. (A) m/z 70 pyrograms for LHA without and with PP NPs; (B) m/z 69 pyrograms for LNOM without and with PP NPs; (C) Mass spectra of pyrolyzates recorded at the PP marker retention times (blue) and their library MSs (red).

In contrast, the SAWE pyrogram without PP NPs exhibited a peak at the retention time of C9. Therefore, over the PP/OM ratio, the C9 marker could no longer be identified. By setting the limit when the C9 mass peak is equal to 2 times the SAWE coeluted pyrolyzate, it may be difficult to assess the presence of PP in SAWE below a ratio of 0.025 (g/g).

I.4 Application to environmental NPs

To evaluate the ability to identify the NPs composition in complex matrices, we applied the Py-GCMS on e-NPs. These e-NPs were produced from unwashed beached plastics covered by Sargasso algae (e.g., type SAWE). Figure I.13 illustrates the size and shape characterization of the e-NPs obtained by DLS and TEM. The e-NPs have a hydrodynamic diameter ranging from 200 to 500 nm (Figure I.13), lower than the PS and PP NPs. This difference can be described by the advanced oxidation state of the plastic debris sampled in the environment that

more likely produces nanoscale particles. The e-NPs are less size-polydispersed and better separated probably because NOM stabilized them differently according to their size. However, e-NPs present an identical shape to PP and PS NPs (Figure I.13). As for PP NPs, TiO₂ and carbonates were identified. While TiO₂ results from additive, carbonates could result from both additive and natural biotic or abiotic precipitates.

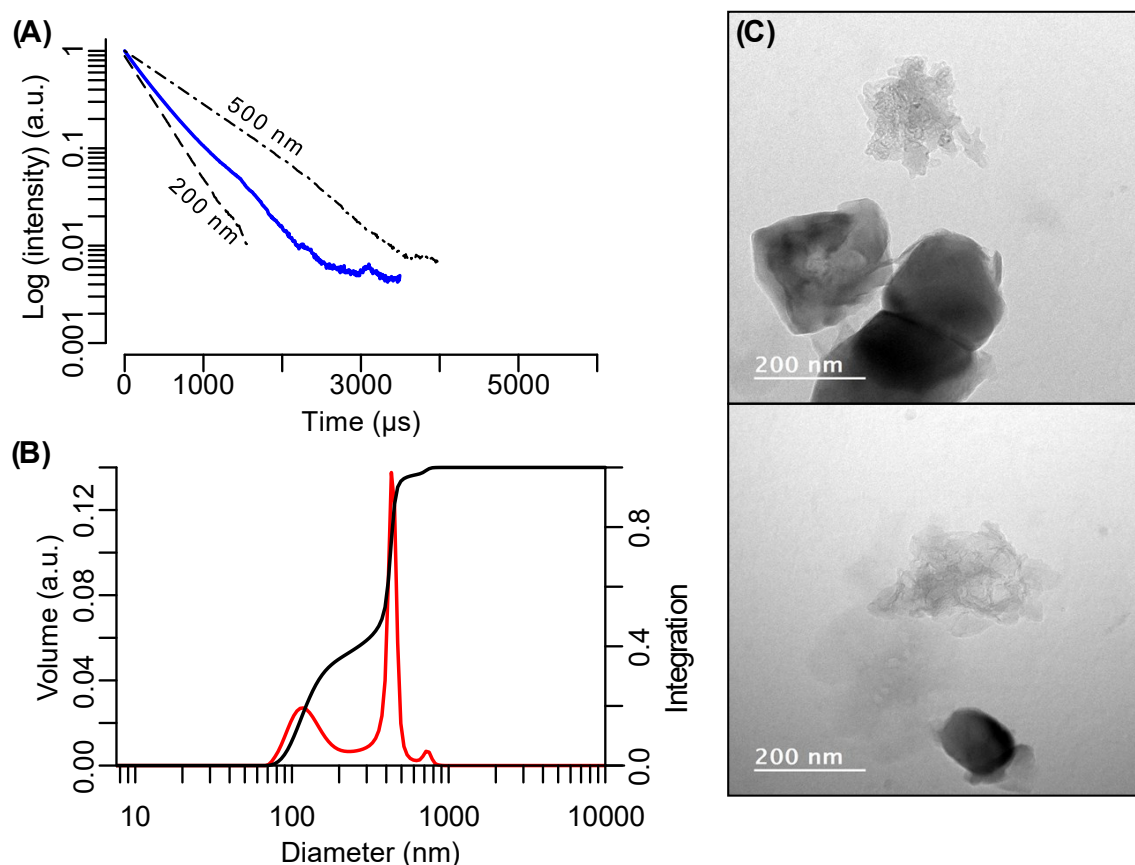


Figure I.13. (A) ACF function of the e-NPs bordered by the 500 and 900 nm polystyrene spherical latex nanoparticles; (B) corresponding size distribution expressed in volume with the associated integration; (C) TEM images of e-NPs.

The direct identification of PP NPs was applied and validated with e-NPs. For e-NPs, on the m/z 70 pyrogram, an important peak occurred at the retention time of C9 (Figure I.14). On the m/z 69 pyrogram, three other high-intensity peaks are distinct at the PP markers' retention time: C12, C15i, and C15s. For all of these peaks, comparisons of their mass spectra with those in the literature showed high similarities ($SS > 0.90$, Figure I.14). Therefore, even if NOM is highly present in the e-NPs suspension, PP is evidenced without further treatments.

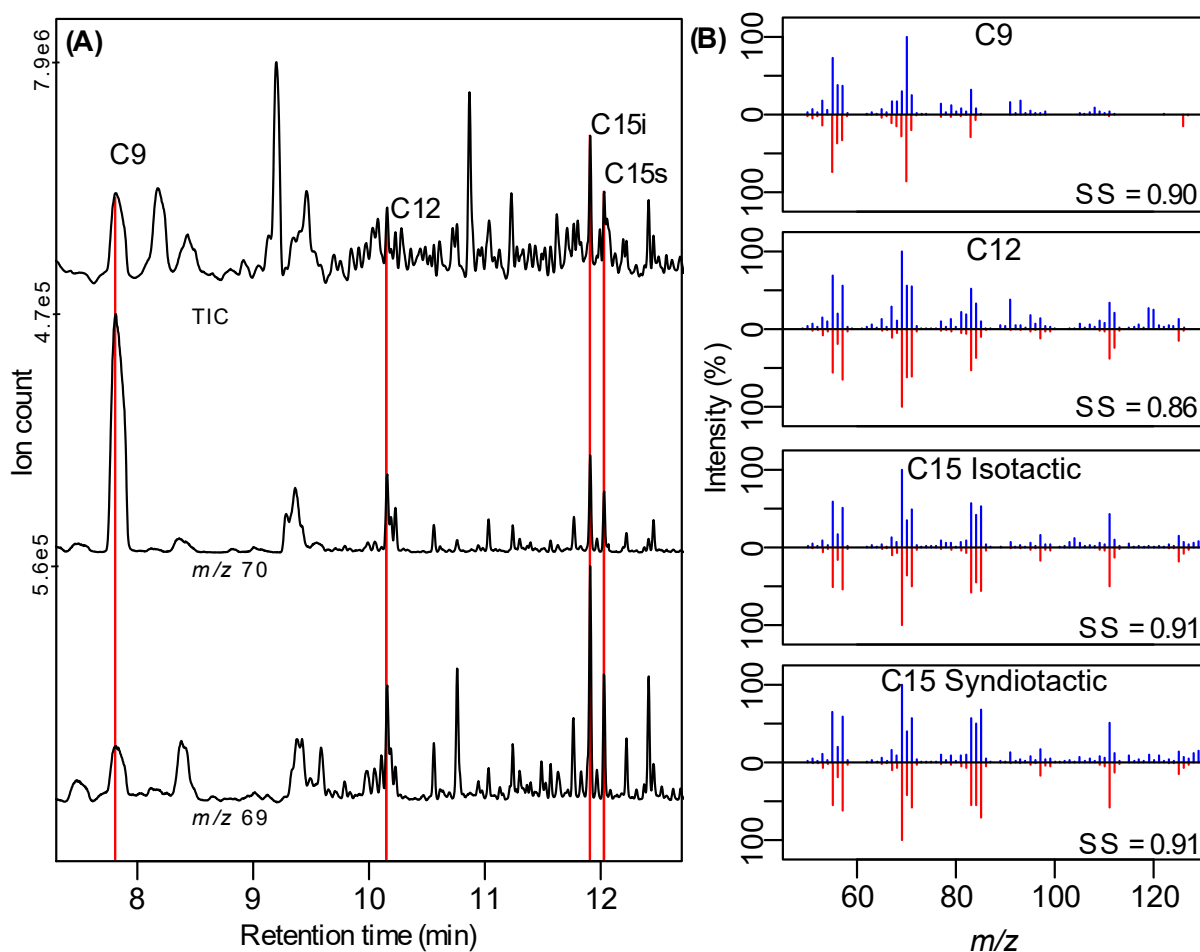


Figure I.14. (A) Environmental-NPs pyrograms for TIC, m/z 70 and m/z 69. (B) Mass spectra comparison between the MSs of pyrolyzates recorded at PS marker retention times (blue) and their library MSs (red).

However, concerning PS in the e-NPs, identifying the styrene dimer and trimer pyrolyzates was not possible, as illustrated by the pyrograms in Figure I.15. Moreover, based on the TIC, a large range of signals and peaks are NOM characteristics without a clear indication of PS. Also, the Tol/Sty ratio obtained for e-NPs ranges from 4 to 5, suggesting that the Styrene signal (m/z 104) can be attributed to NOM rather than PS.

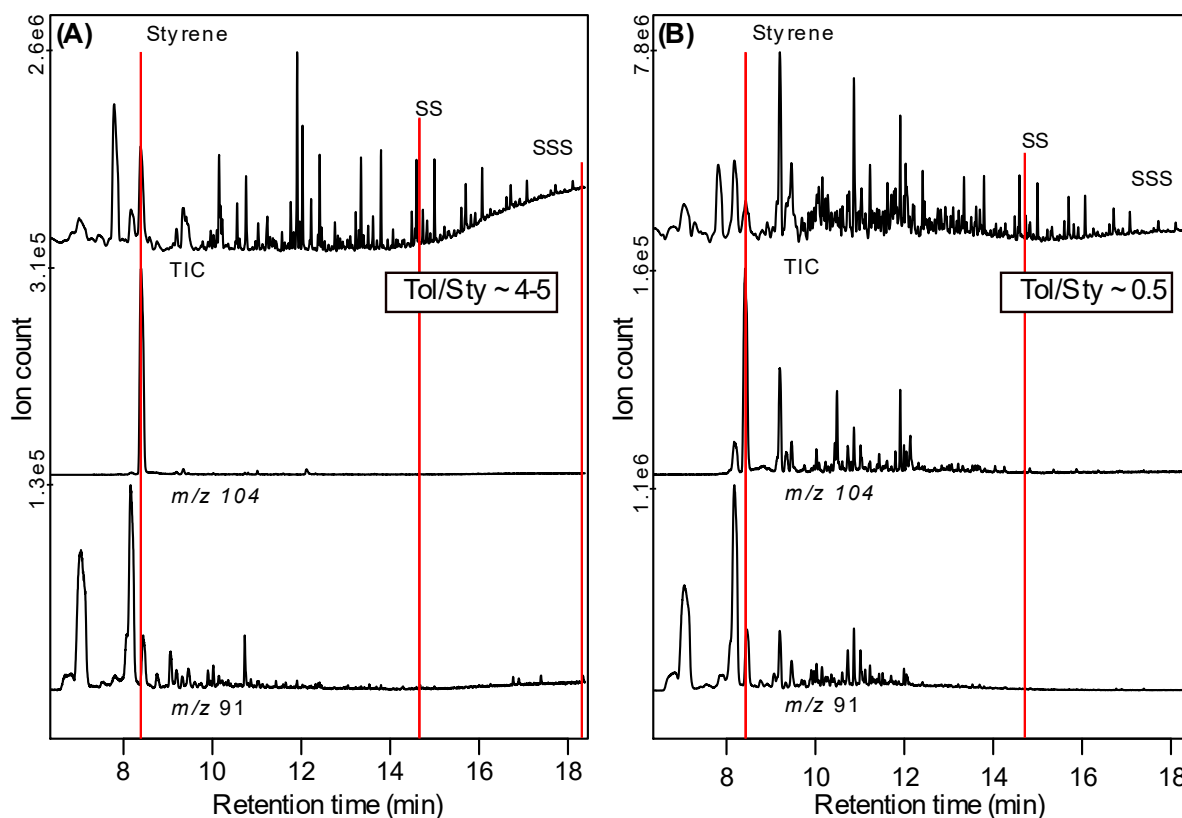


Figure I.15. Environmental-NPs pyrograms for TIC, m/z 104 and m/z 91 (A) before and (B) after H_2O_2/UV purification process.

Therefore, we developed a protocol using H_2O_2 and UV light (Wang et al., 2001, 2006) to selectively degrade NOM without affecting the NPs integrity by testing various experimental conditions. The optimized protocol consists of the H_2O_2 addition at 1% (v/v) in the e-NPs suspension and then exposition to UV light to induce OH radical reaction. This protocol allows the degrading of more than 90% of NOM (Figure I.3). During the H_2O_2/UV processes, the Tol/Sty ratio is followed over time and NOM degradation (Figure I.16). As explained above, at $t=0$, e-NPs had a high Tol/Sty ratio suggesting that the styrene comes from NOM as expected by the large amount of NOM associated with the plastics debris (Fabbri et al., 1998; Dignac et al., 2005). After twenty-four hours of UV, the Tol/Sty ratio decreases to reach a ratio around 0.5, highly similar to the PS NPs' ratio (Figure I.15B). It is worth noting that after e-NPs purification from NOM, the m/z 104 pyrogram presents both a cleaner and twice intense chromatogram with a clear styrene peak ($t_R=8.2$ min). At the same time, the carbon mass significantly decreased with the H_2O_2/UV light action. Such combined observation confirms, after all, the PS occurrence in the e-NPs suspension.

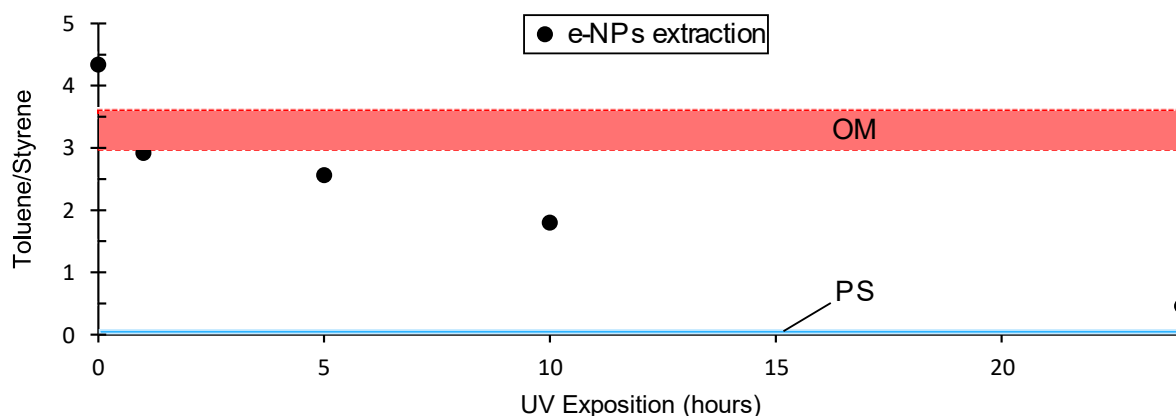


Figure I.16 Toluene/Styrene ratio evolution during the OM degradation applied on the e-NPs suspension. The red zone indicated the Tol/Sty ratio obtained to the different studied NOM. The blue zone indicated the Tol/Sty ratio obtained for the PS microscale pellet and PS NPs.

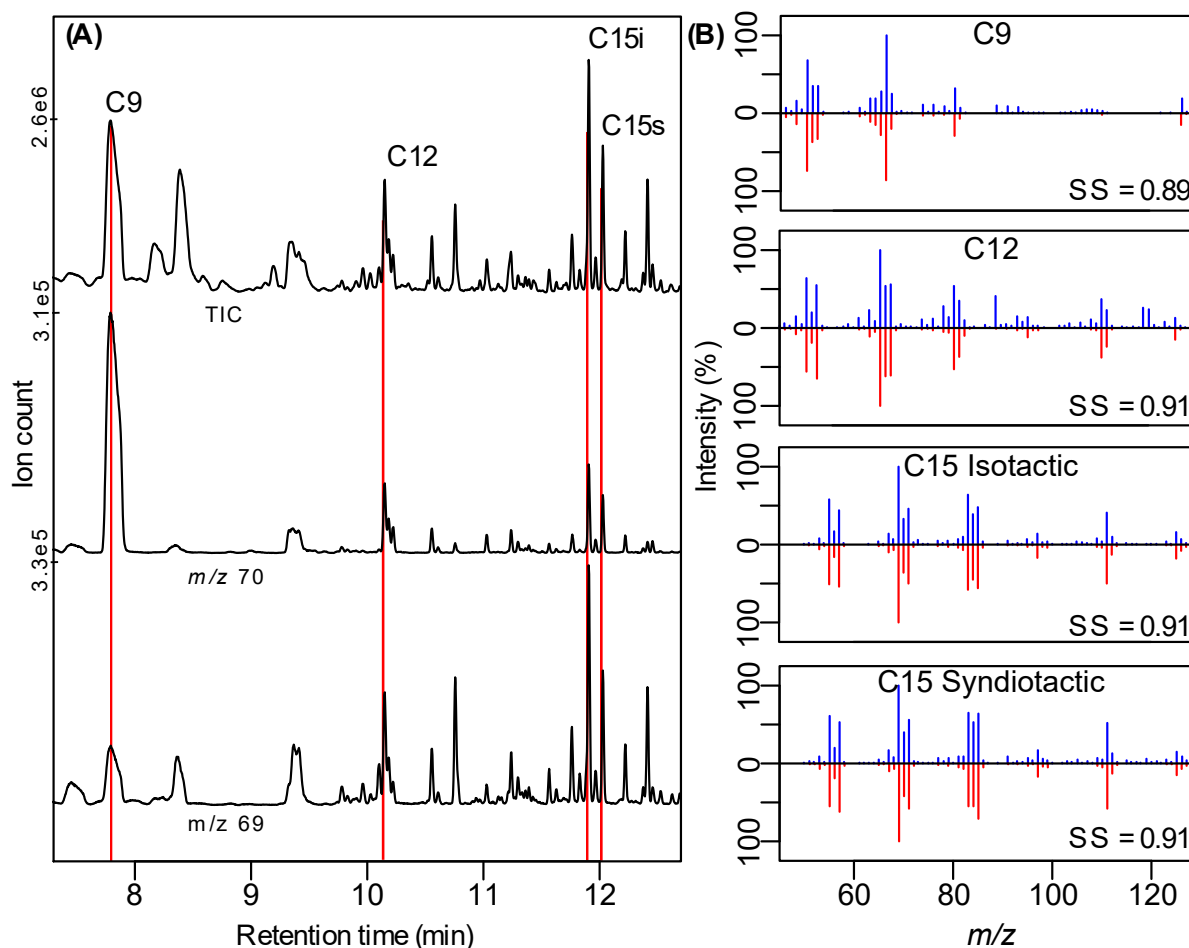


Figure I.17. (A) Environmental-NPs pyrograms for TIC, m/z 70 and m/z 69 after purification with H_2O_2/UV process. (B) Mass spectra comparison between the MSs of pyrolyzates recorded at PS marker retention times (blue) and their library MSs (red).

Additionally, the detection of the styrene is significantly enhanced after the H₂O₂/UV treatment. This result is coherent with: (i) the better sensitivity of the Py-GCMS to detect styrene pyrolyzate for PS vs. NOM since styrene is the principal component of PS; (ii) the NOM effect on the signal attenuation previously demonstrated for styrene for Nps detection in soil (Wahl et al., 2021). Moreover, the major pyrolyzate of PP (i.e., C9, C12, C15i, and s) were still identified (Figure I.17). The combination of both strategies is thus appropriate to detect them in complex environmental matrices.

**CHAPITRE II. PRODUCTION D'UN
MODÈLE DE NANOPLASTIQUES
REPRÉSENTATIF DE
L'ENVIRONNEMENT**

Ce chapitre correspond à un article accepté dans la revue Environmental Science : Nano, “A reliable procedure to obtain environmentally relevant nanoplastic proxies”, Florent Blancho, Mélanie Davranche, Francesco Fumagalli, Giacomo Ceccone, Julien Gigault, <https://doi.org/10.1039/D1EN00395J>

Dans le premier chapitre, nous avons proposé différentes stratégies analytiques afin de permettre la détection des NPs en milieu complexe. Cependant, si de nombreuses études se sont intéressées aux comportements des NPs, elles ont toutes utilisées des modèles dont les propriétés sont éloignées des NPs qui ont pu être observés dans l’environnement. Or, Pradel et al. (2020) ont démontré que la taille et la morphologie de NPs étaient des facteurs de contrôle clés de leur comportement en condition environnementale. **Afin d’approcher au plus près des NPs environnementaux, nous avons décidé de produire des NPs plus proches de ceux rencontrés dans l’environnement.** D’autres études se sont également intéressées à cette problématique. Des NPs ont ainsi été produits à partir de plastiques vierges (El Hadri et al., 2020; Magri et al., 2018). Cependant, leur état d’oxydation n’est pas comparable à celui des NPs produits dans l’environnement et leur représentativité peut être remise en question. Davranche et al. (2019) ont montré qu’il était aussi possible de produire des NPs à partir de débris plastiques altérés, collectés dans l’environnement et donc plus pertinents des NPs produits en condition environnementale. Cependant, ces NPs n’ont pas été caractérisés de manière approfondie.

Dans ce chapitre, nous nous sommes donc intéressés à la production d’un nouveau modèle de NPs de type environnemental. Le protocole s’est inspiré de Davranche et al. (2019) et a été optimisé afin (i) de produire un maximum de NPs et (ii) d’éliminer les traces potentielles de MO. Ensuite, les stratégies de détection directe mises au point dans le chapitre 1 ont été mises à profit afin d’identifier les polymères présents et la méthodologie d’identification directe a été extrapolée au NPs de PE. Enfin, nous avons caractérisés les propriétés physico-chimiques de ces NPs.

Résumé

Disposer de modèles environnementaux de NPs est une priorité. Différents modèles de NPs sont utilisés dans le but de développer des méthodes analytiques ainsi qu’élucider leur comportement dans les systèmes naturels, l’objectif final étant d’arriver à appréhender leur devenir et leur impact dans l’environnement et sur les organismes vivants. Bien que des modèles plus représentatifs des NPs environnementaux aient été proposés, les modèles disponibles ne représentent pas la diversité de leurs propriétés. Un protocole permettant

d'obtenir des NPs proches des NPs environnementaux a ainsi été mis en place. Les NPs sont obtenus à partir de débris plastiques altérés et collectés dans le milieu naturel. Les NPs sont extraits par abrasion mécanique et sonication. Associé à ce protocole de production, une méthode de dégradation des résidus de matière organique initialement présents à la surface des plastiques a été développée. Les suspensions de NPs produites ont une concentration moyenne de 400 mg Carbon L⁻¹. Ces concentrations ont permis de caractériser les propriétés de surface par XPS, analyse BET et titrages potentiométriques. Ces NPs ont des distributions de taille comprises entre 200 et 500 nm, ils ont des formes hétérogènes et sont majoritairement composés de PP et de PE.

Abstract

More environmentally relevant NPs models are urgently needed. Models of environmental plastics are used to develop analytical methods to get an accurate picture of how NPs behave in natural systems, and to generate data on NPs' environmental fate and impact on living organisms. Despite the recent progress in developing models to mimic NPs, the models that are available do not yet show enough diversity to represent the wide heterogeneity in the physical and chemical properties of environmental NPs. In this paper, we report on the strategy we developed to obtain environmentally relevant NPs by mechanical abrasion and sonication of weathered plastics collected from the natural environment (on the beach, and floating in the water). An organic matter degradation protocol was devised to eliminate any potential organic residues that were initially present on the collected plastic samples. The final NPs suspension contains an average of 400 mg carbon L⁻¹, allowing the surface properties to be characterized by XPS, BET analysis, and potentiometric titration. The size distribution of NPs ranges from 200 to 500 nm, with a heterogenous shape and composition (PE and PE) similar to the NPs observed in marine, coastline, and soil systems.

II.1. Introduction

Most plastics are engineered to be mechanically, biologically, and chemically resistant, and therefore they persist forever and are accumulating in the environment (Barnes et al., 2009; Geyer et al., 2017; Horton et al., 2017; Yulan Zhang et al., 2020). The accumulation of mesoplastics (5–25 mm) and microplastics (1–5 mm) in the ocean, resulting from plastic debris degradation, is well documented (Thompson, 2004; Law et al., 2010; Cozar et al., 2014). Plastic debris fragmentation leads to nanoscale particles (nanoplastics, NPs) as plastic debris continues to degrade (Eriksson and Burton, 2003; Gigault et al., 2018, 2016; Reisser et al., 2013). Nanoplastics present specific physical and chemical colloidal properties that micro-scale plastics do not, such as Brownian motion and wavelength interaction (Gigault et al., 2021). Nanoplastics have only recently been identified in the ocean (Ter Halle et al., 2017), coastal areas (Davranche et al., 2020), and soil (Wahl et al., 2021), and from degradation experiments of plastics (Gigault et al., 2016; Lambert and Wagner, 2016). However, there is a lack of knowledge regarding their physicochemical properties, surface reactivity, and ecotoxicological impacts.

Due to their low availability in the environment, NPs cannot be collected sufficiently well to develop standardized characterization methods and ecotoxicology tests in the environment. Since measurement procedures and impact assessments are urgently needed, the main challenge is to find accurate and relevant NPs models. Historically, the ecotoxicology community first used PS latex as a NPs model (Bhattacharya et al., 2010; Wegner et al., 2012; Besseling et al., 2014). However, recent findings have questioned the efficacy this type of model (Gigault et al., 2021). Several alternative models were thus proposed. They were mainly produced by polymerization (Balakrishnan et al., 2019; Mitrano et al., 2019; Pessoni et al., 2019; Rodríguez-Hernández et al., 2019), milling (El Hadri et al., 2020), and other auxiliary methods, such as the laser-based approach (Magri et al., 2018). For NPs impact assessments, some of those models are promising regarding the absence of surfactants (Pessoni et al., 2019), their traceability (Mitrano et al., 2019), and their heterogeneity, size, and shape, which are similar to those observed under environmental conditions (El Hadri et al., 2020). These current NPs models demonstrated that their nanosize allows them to interact with microorganisms or cells (Balakrishnan et al., 2019; Rodríguez-Hernández et al., 2019). However, the justification for using these models for investigating NPs reactivity with contaminants is limited. Their surface functionalization was *a priori* chosen (Pessoni et al., 2019) as no characterization of NPs surface functional groups is available. Finally, recent studies have demonstrated that the

size and shape influence NPs retention in porous media and their stability in aqueous systems (Pradel et al., 2020; Venel et al., 2021).

All of the methods used similar approaches: a polymer or specific monomer is used to produce NPs that are homogeneous in composition and not naturally oxidized. Recently, Davranche et al. (2019) have opened the door to a new way of relevant NPs preparation from the altered surface of MPs collected from natural systems (Davranche et al., 2019). Despite the potential of these NPs from nature, the method was not pushed further, and the resulting NPs were only partially described. Altering the outer layer to produce NPs models seem to be promising since 1) plastics are altered from the outside (surface) to the inside in nature (Ter Halle et al., 2016); 2) their alteration occurs under environmental conditions; and 3) their shape and surface functional groups are expected to be environmentally relevant.

Based on Davranche et al. (2019), the present work proposes a protocol to produce an environmentally relevant model for NPs (e-NPs). Environmental NPs are produced using beached plastic debris (BDs) from the North Atlantic gyre and floating debris (FDs) from the great Pacific garbage patch. Environmental NPs composition, size, and surface properties were characterized by Py-GCMS, DLS, TEM, XPS, BET analysis, and potentiometric titration. Besides the production of an e-NPs model, a method was developed to remove the associated organic matter (OM), using a combined H₂O₂/UV process. These e-NPs open new possibilities for investigating ecotoxicological effects and the environmental fate of plastics.

II.2. Materials and methods

II.2.1. Environmental NPs production and organic matter degradation

Beach plastic debris (BDs) was collected on Saint Marie Bay beach (Guadeloupe, France) in September 2018. Only beach plastics that were less than 10 cm in diameter were collected. After sieving with a 1 cm grid, pieces of plastic debris were manually separated from the beach matrix (i.e., sand and algae residues). Floating plastic debris (FDs) was collected from the North Pacific Garbage Patch in 2015 by Ocean Clean-Up, a non-profit organization dedicated to plastics debris removal from the water system (riverine and oceans) (Royer and Deheyn, 2019; Lieshout et al., 2020).

We used 100 g BDs and 300 g FDs as initial material. The plastic debris was mixed with deionized water (DI) at a 1:5 BDs/DI and 1:2 FDs/DI ratio (wt/wt) in a square bottle and stirred at 250 rpm (Step 1, Figure II.1). The ratio of plastic debris to water was optimized in order to obtain the higher quantity of carbon in the final solution. After 48 h, the suspension was


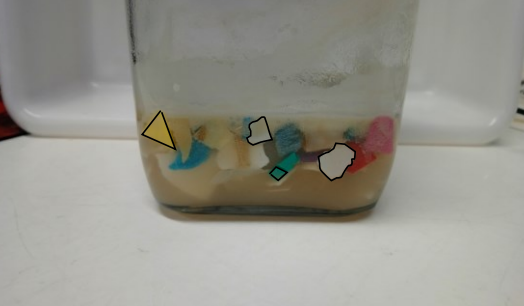
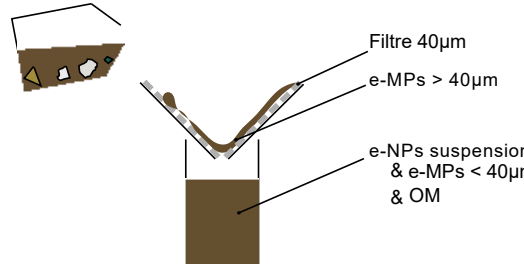

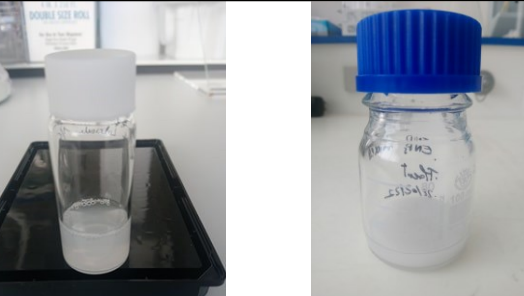
sonicated for 1 hour (Step 2, Figure II.1). Microplastics were then separated from the suspension with a 40 μm cut-off filter (cellulose acetate, VWR) (Step 3, Figure II.1). Organic matter from algae residues (i.e., Sargassum Algae) associated with plastic debris was removed from the suspension using 1% H_2O_2 /UV for 5 hours (see I.2.2). Finally, the e-NPs were collected with a 1.2 μm cut-off filter (Glass fiber, Prat DUMAS) (Step 4, Figure II.1). After the OM oxidation, ultrafiltration (Amicon, Merck Millipore) was used to remove the extra H_2O_2 and concentrate the e-NPs using an ultrafiltration membrane of 20 kDa molecular-weight cut-off (PES, Microdyn NADIR) (Step 5, Figure II.1). Small MPs ($< 1 \text{ mm}$) were retrieved by the 40 μm filter (cellulose acetate, VWR) and called environmental MPs (referred to as e-MPs from now on). The e-NPs OM and e-MPs OM refer to NPs and MPs that have not been purified of organic matter.

II.2.2. Particle size, shape, and surface analysis

The hydrodynamic size of the particles is analyzed using Dynamic Light Scattering (DLS) (VASCO-Flex, Cordouan Technologies). The particle motion is characterized by a correlation of the scattered light intensity according to time and thereby represented by an autocorrelation function (ACF). Originally colloids in solution have an ACF forms by a decreasing exponential function from coherent to incoherent movements. To better illustrated the ACF, this function was normalized and presented on a y-axis logarithm scale. Through this transformation, the ACF of monodisperse standard are composed of a straight line with a negative slope and a curvilinear line including noises. The first part is related to the hydrodynamic radius of the particles and the latest part assured that particles are submitted to Brownian motion as expected for colloids. Note that the ACF of spherical standards were recorded in order to compare it to ACF from sample's particles.

These spherical standards (100, 200, 500 and 900 nm) were purchased from ThermoFisher, and analysed at a concentration of 100 mg L^{-1} without ionic strength. Size distribution were determined by fitting the autocorrelation function with Sparse Bayesian learning algorithms (SBL, Tipping, 2001). SBL algorithm deconvolutes the signal in a way which allow to identify the different population size associated with their distribution. Note that each DLS analyses were carried in 6 replicates with an analyses period of 120s. Only results for replicates with reliable residue ($r < 0.01$) compared to the modeling were accepted. The geometric size and shape of nanoparticles were also examined by transmission electronic microscopy (TEM) (JEM 2100 HR, Jeol). Samples were prepared by drying 2.5 μL of solution

on a carbon grid (Oxford instruments). TEM was operated at 200-kV acceleration voltage with LaB₆ as an electron source.

<p>1. Plastics Selection</p> <p>1.a. Select plastics between 1cm < Plastics < 10 cm with non negligible weathered layer.</p> <p>1.b. Add dionized water (D.I.) at a 1:2 ratio in square bottle.</p>	
<p>2. e-NPs extraction</p> <p>2.a. Let agitate the suspension for 2 days at 250 rpm.</p> <p>2.b. Then apply 1 hour of sonication.</p>	
<p>3. Microplastics separation</p> <p>3.a. Take away microplastics with 40 µm cut-off filter.</p>	
<p>4. OM removing & e-NPs separation</p> <p>4.a. Apply UVC during 5 h prior adding H₂O₂ (1% v/v).</p> <p>4.b. Separate microplastics (<40µm) from e-NPs with a 1.2 µm cut-off.</p> <p>4.c. Remove H₂O₂ by concentrating/diluting* with D.I.the suspension 5 times.</p>	
<p>5. e-NPs concentration</p> <p>5.a. Quantify the total organic carbon</p> <p>5.b. Concentrate the suspension as wanted with an ultrafiltration cell</p>	

* this operation is operated with the ultrafiltration cell

Figure II.1. Workflow of the e-NPs preparation protocol.

The e-NPs were analyzed by X-ray photoelectron spectroscopy (XPS) using an AXIS Ultra-DLD (Kratos Analytical, JRC, ISPRA) at a pressure of less than 8×10^{-9} mbar. The specific surface area (SSA) of the e-NPs was quantified by the BET (Brunnauer Emmet and Teller) method using a Gemini VII instrument (Micromeritics).

The proton-reactive site was determined by potentiometric titration using a Titration unit controlled by the Tiamo software (Metrohm). All solutions were base-titrated under N_2 flux with an NaOH solution of 0.01 M (Honeywell Fluka). Prior analysis, the pH probe was calibrated during the titration of an external acidic solution (1mM HNO_3 , Honeywell Fluka). The ionic strength of all solution was set to 10 mM with $NaNO_3$ (Fisher Scientific) and all titration started below pH 4. The operational determination of the acid/base functional group was done as presented by (Spadini et al., 2018). Briefly, the proton released from the polymer surface, H_{surf} , was related to the pH of the solution (Eq. II.1). Then, the total surface reactivity, H_{tot} , was defined as the H_{surf} released between pH 4 to 8, which implicitly do not take in account deprotonated function group at $pH \leq 4$. Note that, the CO_2 diffusion during the experiment was taken in account by calculating the H_{tot} for a blank solution (i.e. deionized water).

$$[H^+] = [H_{init}] + [H_{base}] + [H_{surf}] + [OH^-] \quad (II.1)$$

Where, $[H^+]$, the free proton concentration, known at every time with the pH probe, $[H_{init}]$, the concentration of the strong acid added to fix the pH to 3 prior the titration, $[H_{surf}]$, is the concentration of the proton released by the surface titrated, the only unknown and $[OH^-]$, the concentration proton released from the water auto-dissociation, at pH 7 $[H^+] = [OH^-]$.

II.2.3. Characterization of e-NPs composition

Total Organic Carbon (TOC) content in grams of carbon per liter was quantified using a TOC-V Shimadzu analyzer (Sugimura and Suzuki 1988). The precision of the TOC measurements was estimated to be $\pm 5\%$ using a standard potassium hydrogen phthalate solution (Sigma Aldrich). Fluorescence spectroscopy was performed with an FL6500 system (Perkin Elmer). Pyrolysis (Pyrolyzer PY-3030 Frontier Lab) coupled to Gas Chromatography-Mass Spectrometry (Py-GCMS) (5977B, Agilent Technologies) was used for plastic identification. Before Py-GCMS analysis, a known volume of samples was evaporated at $45^\circ C$ in an $80\mu L$ pyrolysis cup (Frontier Lab). Pyrolysis was performed at $600^\circ C$, and the gas chromatography temperatures were similar to the literature (Dehaut et al. 2016). Pyrolyzates were separated on a C18 capillary column (DB5, 30m, Agilent Technologies), with helium as the carrier gas. The mass spectra of pyrolyzates were then compared to the NIST/EPA/NIH

library (NIST 14) values, and to our own laboratory library values, including specific polymer pyrolyzates' mass spectra from Blanco et al.,2021b, and from PE (Figure II.2 and Table II.1).

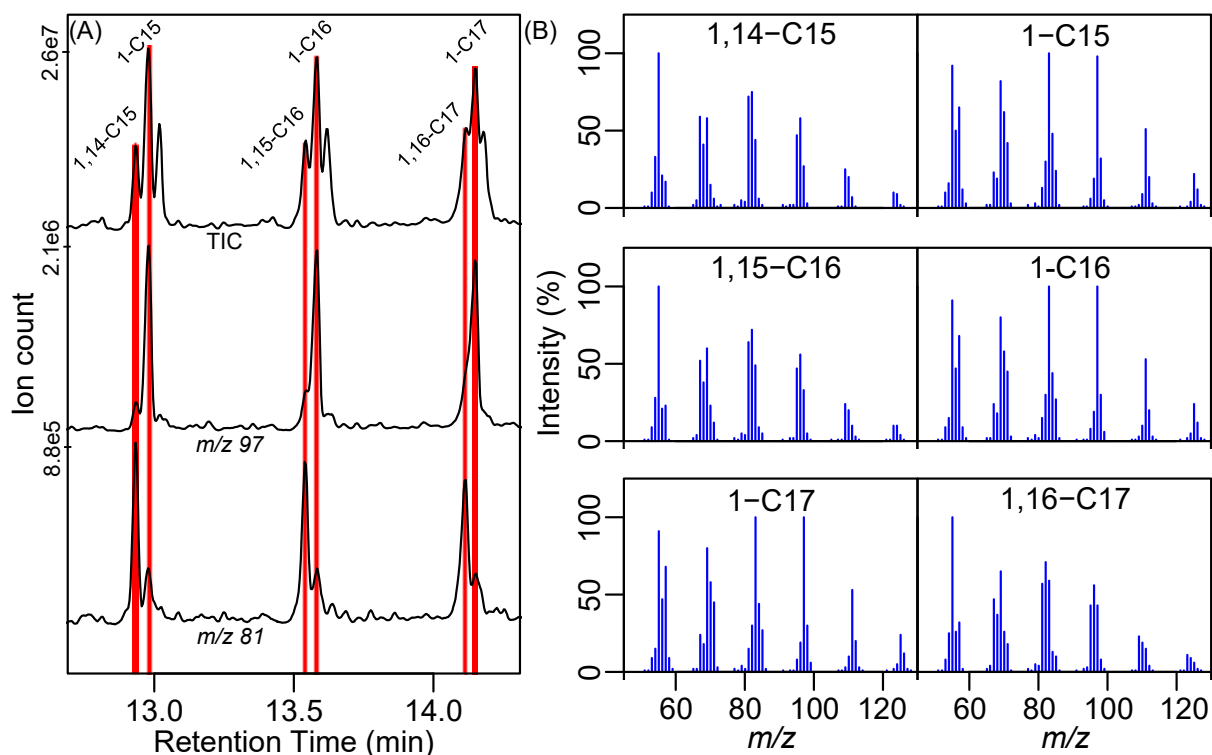


Figure II.2. (A) Polyethylene micropellet pyrograms for TIC, m/z 97 and 81. (B) Mass spectra of pyrolyzates recorded at the PE marker retention times used to build the library. 1,14-C15 for 1,14-pentadecadiene; 1-C15 for pentadecene; 1,15-C16 for 1,15-hexadecadiene; 1-C16 for hexadecene; 1,16-C17 for 1,16-heptadecadiene; 1-C17 for heptadecene.

The quantification of spectrum similarity (SS) was performed using the MSD Chemstation algorithm (Agilent Technologies). The polymer identification was based on non-interferent pyrolyzates (there were no homolog pyrolyzates from OM). Thus, the procedure used to validate the identification of a polymer pyrolyzate was to have a similar Kovats retention index already found from polymer pyrolysis and an SS for at least one specific pyrolyzate > 0.80 . Table II.1 and Table II.2 present the Kovats retention indices calculated for the pyrolyzates used to identify PE and PP polymer, respectively. Besides the polymer identification, Py-GCMS is used to monitor the removal of OM. For this purpose, three OM pyrolyzates were selected after being identified on algae samples with the NIST library ($SS > 0.80$): 2C-Phenol, 2C-2-Cyclopentenone, and Indole (Table II.3). The 2C-phenol has many OM precursors (i.e., non-specific) among peptides, proteins, and lignins. The 2C-2-cyclopentenone has only one precursor: polysaccharides. Molecules that contain N, such as

proteins, can be precursors of indole. Combining these pyrolyzates permits us to follow OM degradation across different components.

Table II.1. Polyethylene pyrolyzates used for its identification. * Indicates pyrolyzates with no interference with OM. ** Non-isothermal Kovats retention indices.

Pyrolyzates	PE pellet sigma	
	RI**	Reference
1,14-C15*	1487	This study
1-C15	1493	
1,15-C16*	1586	
1-C16	1593	
1,16-C17*	1687	
1-C17	1693	

Table II.2. Pyrolyzates used for PP identification. * pyrolyzates with no interference with OM. ** Non-isothermal Kovats retention indices.

Pyrolyzates	PP pellet sigma	
	RI**	Reference
C9*	855	(Blanco et al., 2021b)
C12*	1084	
C15i*	1312	
C15s*	1330	

Table II.3. Pyrolyzates markers for typical OM and their occurrence in major plastic polymers. The table summarize the precursors of these markers found in literature. * Indicates Py-GCMS analysis realized at the laboratory beside literature data.

Specific OM marker	Class	Origin	References	Presence in							
				Algae*	Marine DOC	Riverine DOC	SOM*	PS*	PP*	PVC*	PE
2C-Phenol	Phenol	Unspecific (Peptides, proteins, lignin, tannins, polysaccharides)	Gillam and Wilson 1985; Dignac et al. 2005; Nierop et al. 2005; Kaal et al. 2016	X	X	X	X	-	-	-	-
2C-2-Cyclopentenone	Cyclopentone	Carbohydrates	Nierop et al. 2005; Kaal et al. 2016; Rouches et al. 2017	X	-	X	X	-	-	-	-
Indole	N-containing	Proteins	Kaal et al. 2016; Biller et Ross 2014	X	X	X	-	-	-	-	-
			References	Gillam and Wilson 1985; Ross et al. 2009; Van Heemst et al. 1996; Maddi et al. 2011	Ishiwatari et al., 1995	Christy et al. 1998; Dignac et al. 2005	Huang et al. 1998; Kaal et al. 2016; Nierop et al. 2005	Tsuge et al., 2011			

II.3. Results and Discussion

II.3.1. Water extraction and purification of e-NPs

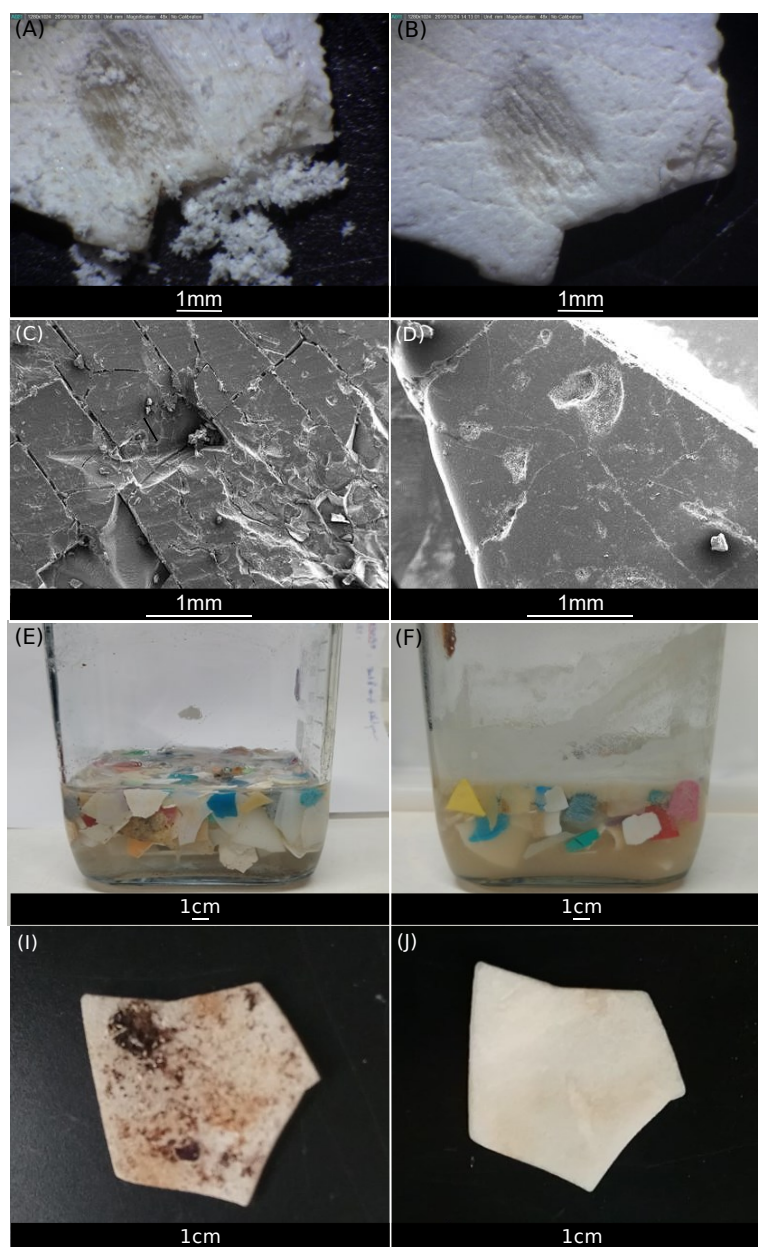


Figure II.3. Microplastics and extraction solution before and after applying the extraction protocol on beach plastics. (A), (B) are photography of the same MPs, in detail (A) is the MPs scratched before applying the protocol revealing the weathered layer at its surface and (B), the MPs after using the protocol; (C) and (D) are TEM observations of MPs, before and after using the protocol, respectively; and (E) and (F) showed the extraction solution before and after applying the protocol; (I) and (J) show a MPs covered by organic materials, before and after using the protocol.

Plastic debris offers an easily extracted altered layer, as shown in Figure II.3A. After water extraction, it showed a polished surface (Figure II.3B), as confirmed by TEM observations (Figure II.3C and Figure II.3D). The resultant suspension of beach plastics is highly turbid, suggesting numerous small particles (see turbidity difference between Figure II.3E and Figure II.3F). After filtration, the organic carbon (OC) content was 71 ± 4.1 and 759 ± 61 mg L⁻¹ for beach plastics and floating plastics, respectively (Figure II.4). This organic carbon includes both e-NPs and natural organic matter from algae residues (Figure II.3I and Figure II.3J).

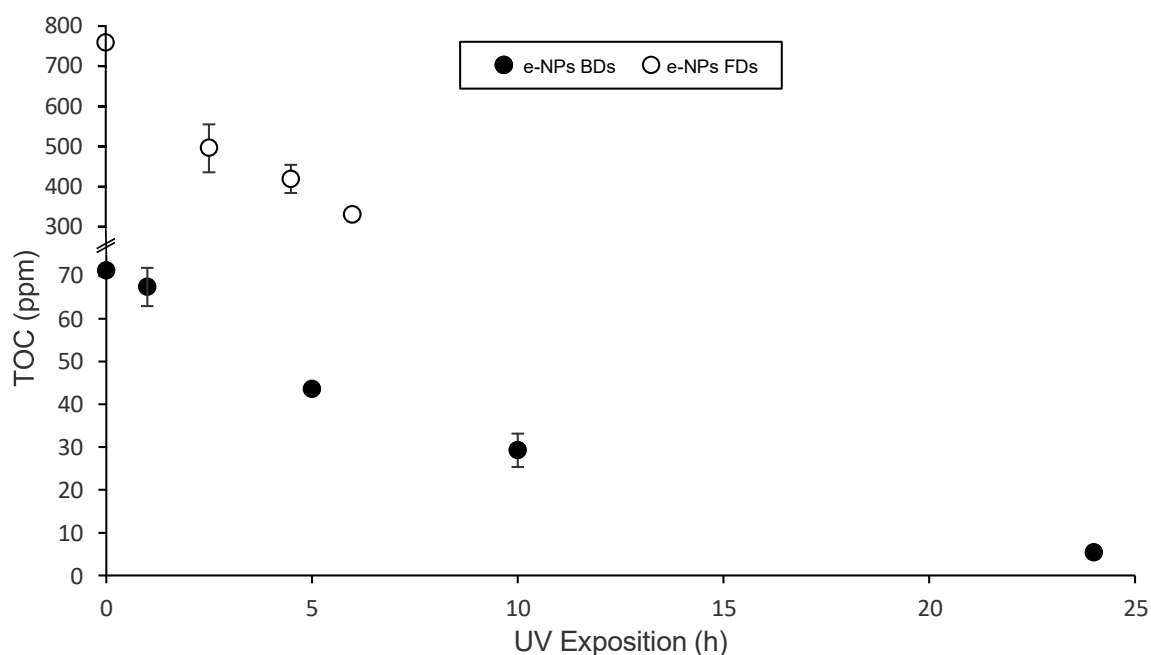


Figure II.4. Evolution of TOC concentration during the application of OM degradation protocol applied on the e-NPs suspension from PDs and BDs extraction, filled dot and unfilled dot, respectively.

To remove OM from the plastic suspension, several protocols using basic, acidic, or oxidizing reagents could be used (Dehaut et al., 2016; Kühn et al., 2017; Hurley et al., 2018). H₂O₂ was shown to be the most efficient for plant matter, notably coupled to a catalyzer such as UV light, TiO₂, or ionic Fe(III)/Fe(II) (Vilhunen et al., 2010; Prata et al., 2019). Using H₂O₂ avoids nanoparticle aggregation, compared to basic or acidic reagents. A preliminary investigation demonstrated that photooxidation at 254 nm with 1% H₂O₂ is mandatory to reach more than 95% degradation (Figure I.3). Alnaizy and Akgerman (2000) also demonstrated that temperature inhibits OM degradation from 90% to 30% if the temperature is decreased from

45°C to 20°C. Therefore, the temperature was set to 37°C (regulated in the UV reactor), pH 7 and 1% H₂O₂. This protocol was applied on both suspensions. After OM degradation, the OC content of the e-NPs suspensions reached 5.4±0.1 mg L⁻¹ and 331±3.1 mg L⁻¹, respectively, for beach and floating debris. Fluorescence spectroscopy and Pyr-GCMS were used to validate the OM degradation. 80% of the OM's initial fluorescent C-peak disappears after 5 h of exposure to H₂O₂/UV (Figure II.5A) (Coble, 1996; Huguet et al., 2009). Py-GCMS analysis of the suspension also provided evidence about the disappearance of the OM pyrolyzates (Figure II.5B). Note that Figure II.5B showed a different efficiency to degrade OM. This may be explained by the order of difference of the initial OC amount. After the concentration step, the concentration reached was 37±1.0 mg L⁻¹ and 2038 ±12 mg L⁻¹, for beach and floating plastics, respectively. Note that the concentration chosen for floating debris was primarily targeted to make the potentiometric titration work.

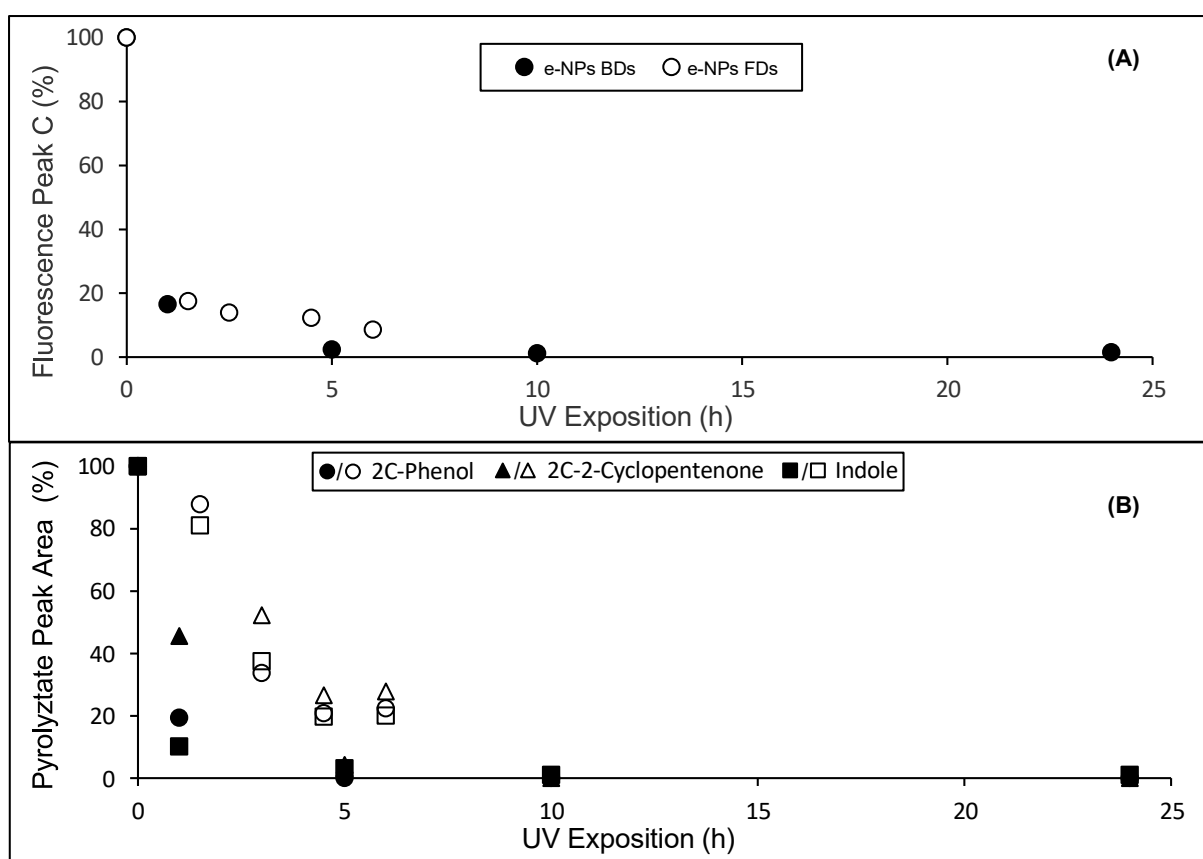


Figure II.5. Evolution of organic tracer during OM degradation protocol applied on the e-NPs suspension from beach plastic and floating plastic extraction, filled dot and unfilled dot, respectively; (A) Fluorescence C Peak, obtained by fluorescence spectroscopy; (B) Pyrolyzates evolution, obtained from Py-GCMS.

II.3.2. Environmental NPs polymer identification

As identified by Dümichen et al. (2015), the pyrolysis of PE produces a class of pyrolyzate with no interferences towards OM pyrolyzates: the alkadienes. These singular markers originate from the scission of long polymer chains, which are not abundant among environmental OM (Table II.1) (Dümichen et al., 2015). For the e-NPs produced from beach debris, none of these PE markers were identified. By contrast, such markers were found for the e-NPs from the floating debris extraction. Three succeeding peaks were identified as alkadienes, as they have similar Kovats retention indices as found in the library, and their spectrum similarities were superior to 0.80 for the m/z 81 pyrogram (Figure II.6A and Table II.4). Moreover, these markers were followed closely by alkene (m/z 97 Figure II.6A) as observed during PE pyrolysis (i.e., Figure II.2). As a consequence, PE polymer is present in the e-NPs from floating debris.

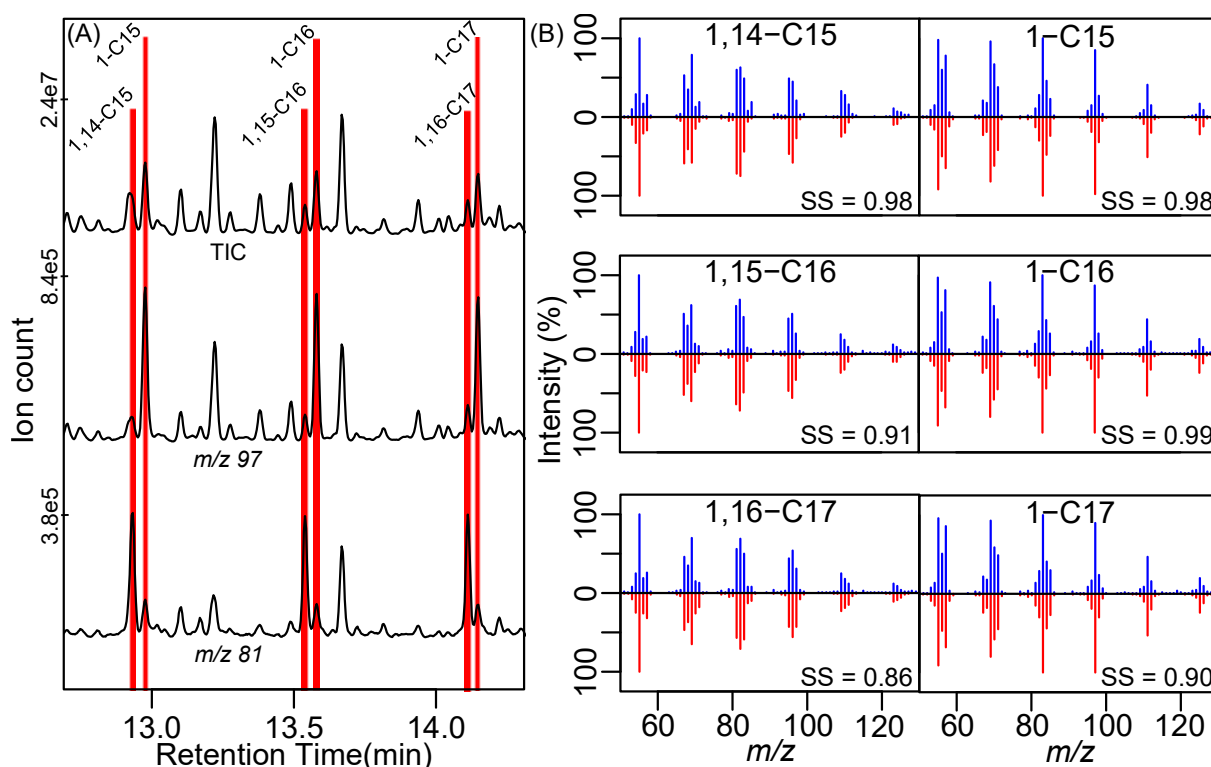


Figure II.6. (A) Environmental-NPs BDs pyrograms for TIC, m/z 97 and m/z 81. (B) Mass spectra comparison between the MSs of pyrolyzates recorded at the PE marker retention times (blue) and their library MSs (red).

The identification of PP succeeds for both suspensions. As already demonstrated for NPs, PP can be identified by the presence of four singular PP pyrolyzates. These 4 PP markers (i.e., C9, C12, C15i, and C15s) were identified in our studies. Indeed, peaks with similar Kovats retention indices showed spectrum similarities > 0.80 (Figure II.7, Figure II.8 and Table II.5). Whether for e-NPs suspension of beach or floating debris, PP-identified markers have a dominant height on the total ion pyrogram (TIP). These “fingerprints” suggest that PP is a dominant component of e-NPs.

Table II.4. Polyethylene pyrolyzates used for its identification. * Indicates pyrolyzates with no interference with OM. ** Non-isothermal Kovats retention indices.

Pyrolyzates	PE pellet sigma		e-NPs PDs		e-NPs BDs	
	RI**	Ref.	RI**	SS	RI**	SS
1,14-C15*	1487	This study	-	-	1485	0.98
1-C15	1493		-	-	1493	0.98
1,15-C16*	1586		-	-	1587	0.91
1-C16	1593		-	-	1594	0.99
1,16-C17*	1687		-	-	1687	0.86
1-C17	1693		-	-	1693	0.90

II.3.3. Size characterization of e-NPs

Both fractions that were less than $1.2 \mu\text{m}$ were characterized by DLS and TEM (Figure II.9). Figure II.9A and Figure II.9D displayed the log-transformed time-correlation function of the intensity of light scattered (ACF) obtained by DLS. Compared to spherical size-standardized nanoparticles (PS latex), e-NPs from beach debris present monomodal suspension (i.e., a straight line), with a hydrodynamic diameter ranging from 200 to 500 nm and centered at 250 nm (Sparse Bayesian learning-based modeling). The e-NPs from floating debris are polymodal with an additional colloidal population at a larger size ($>500 \text{ nm}$). As shown by the SBL modeling, the first population has a hydrodynamic diameter centered at 150 nm, whereas the second is centered around 500 nm. Note that the SBL predicts particle size $>1000 \mu\text{m}$; this

is modeling bias as the ACF does not cross the ACF from the 900 nm microsphere standard. Transmission electronic microscopic observations displayed anisotropic nanoparticles with sizes $<1 \mu\text{m}$ (Figure II.9C and Figure II.9F). The carbon intensity of their EDX signal was significantly higher than the grid, suggesting a polymer composition, 6.5 and 0.9 Cps/eV, respectively. Black cubic particles embedded in the nanoparticle, $<250\text{nm}$, were also observed. Based on EDX (Table II.6), this cubic particle is composed of Ti and O, suggesting TiO_2 . These nanoparticles are a well-known additive of plastics (Deanin, 1975) and were already identified as associated with MPs (Fries et al., 2013).

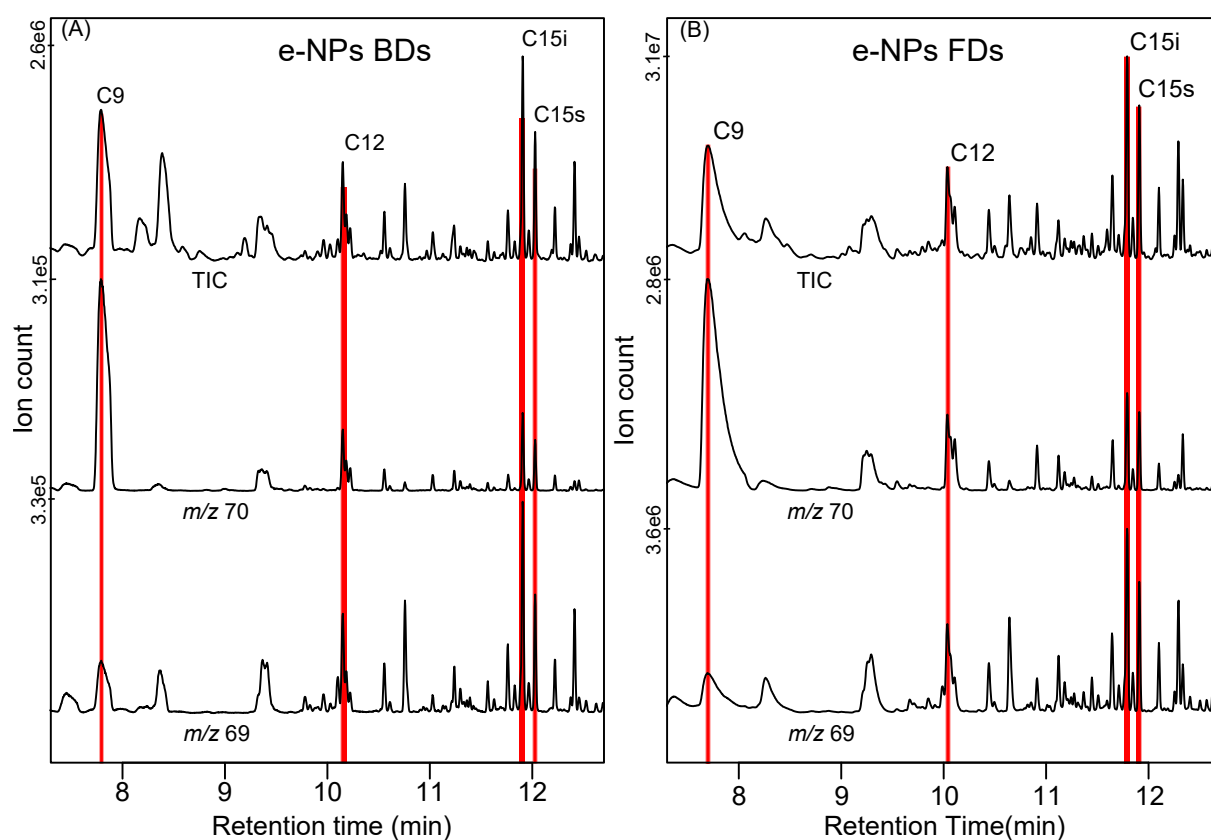


Figure II.7. Total ion count, m/z 70 and 69 e-NPs pyrograms from (A) beach debris and (B) floating debris.

II.3.4. Surface characterization of e-NPs and e-MPs

Overall, the C-C bond is predominant for all samples (> 70%) except for e-NPs OM, where bonds to oxygen are prevalent ($\approx 60\%$) (Figure II.10). Dominant C-O bonds for e-NPs OM can be attributed to the algae residue (Yazdani, 2015; Dobrinčić et al., 2020). Algae are characterized by considerable water-extractable polysaccharides (> 50%), mainly composed of alginate, laminarin, and mannitol (Chee et al., 2011; Oliveira et al., 2014; Yazdani, 2015; Graiff et al., 2016). Therefore, the difference in the carbon bond distribution between e-NPs and the e-NPs OM surface is explained by the molecules' release during the e-NPs extraction. More oxidized carbon bonds characterize the e-NPs than for e-MPs. Moreover, they share similar C=O on their surfaces, whereas O-C=O and C-O bonds are more present on e-NPs. O-C=O (the carboxyl functional group) is interesting as they are known to form complexes with metals (Cannan and Kibrick, 1938).

Table II.5. Pyrolyzates used for PP identification. * Pyrolyzates with no interference with OM. ** Non-isothermal Kovats retention indices.

Pyrolyzates	PP pellet sigma		e-NPs PDs		e-NPs BDs	
	RI**	Reference	RI**	SS	RI**	SS
C9*	855	Blanco et al. 2021	852	0.89	853	0.87
C12*	1084		1086	0.91	1085	0.91
C15i*	1312		1313	0.91	1312	0.91
C15s*	1330		1331	0.91	1330	0.91

During the H₂O₂/UV oxidation, HO• is formed by UV irradiation at 254 nm (Oppenländer, 2003; Santos et al., 2009). These radicals can initiate numerous oxidation reactions, which are otherwise limited to photo-reactive impurities (i.e., chromophores). These impurities are included in the polymers during its early production process (Rånby, 1989; Rabek, 1995). High concentrations of HO• and HO₂• may affect the termination reaction differently than would occur in environmental conditions (Chamas et al., 2020). Even if similar functional groups are expected on e-NPs, their density may vary. As shown by XPS, the C bonds at the surface of e-NPs are not drastically different from e-MPs and e-MPs-OM. This suggests that the H₂O₂/UV oxidation has a limited impact on the e-NPs surface. As H₂O₂ is

transparent to $\lambda > 300$ nm but absorbed the UV radiation at 254 nm, e-NPs were mainly irradiated at $\lambda = 315$ nm wavelength, as H_2O_2 was in excess ($> 0.5\%$ v/v, Table II.7) (Oppenländer, 2003). Since the backbone bond of PP, PS, PVC, and PE polymers do not absorb at 315 nm (Rånby and Rabek, 1989), the direct UV effect on the e-NPs surface is therefore limited to UVB, as observed in the environment.

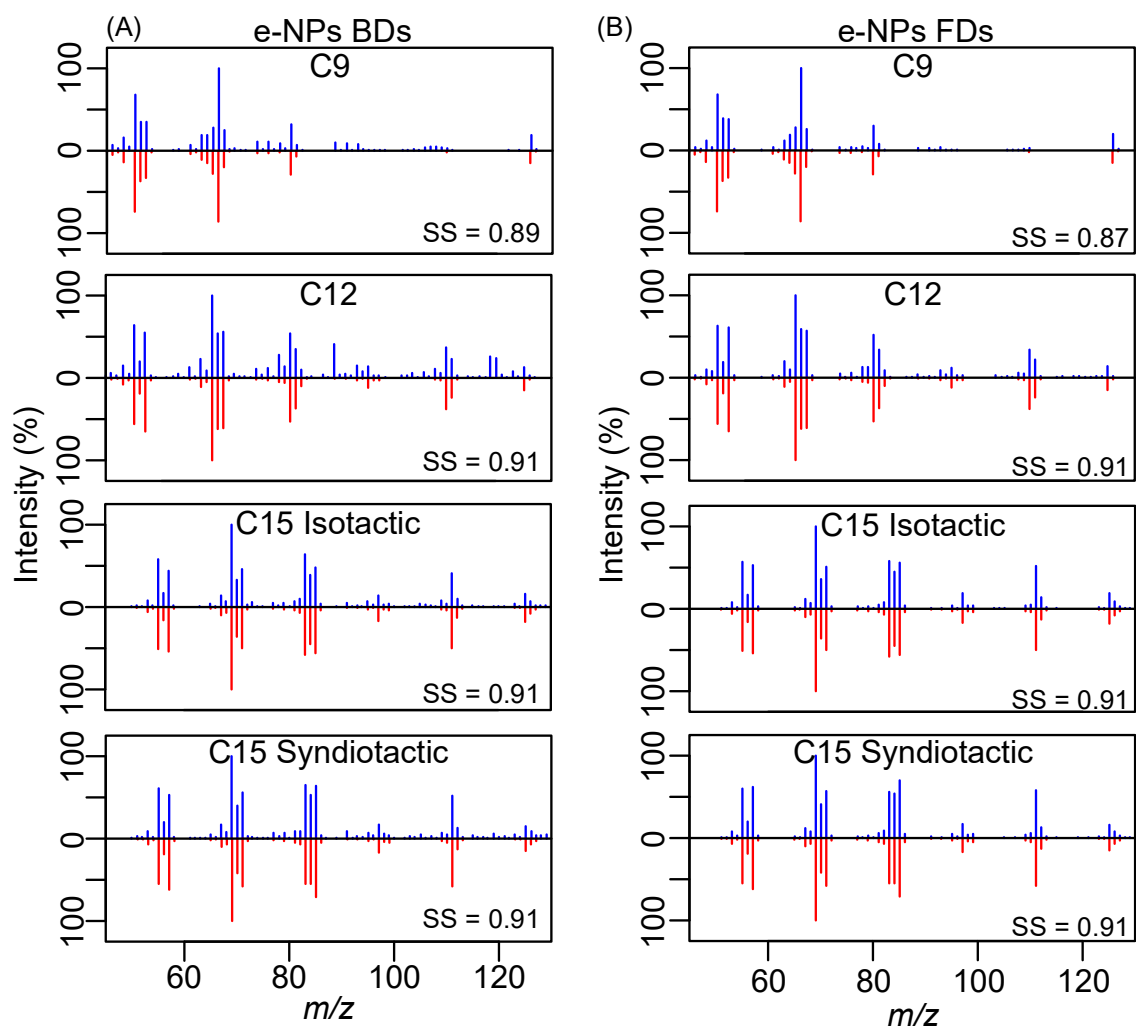


Figure II.8. Mass spectra comparison between the MSs of pyrolyzates recorded at the PP marker retention times (blue) and their library MSs (red) for PDs (A) and (B) BDs, respectively. SS, spectrum similarity calculated with MSD Chemstation algorithm.

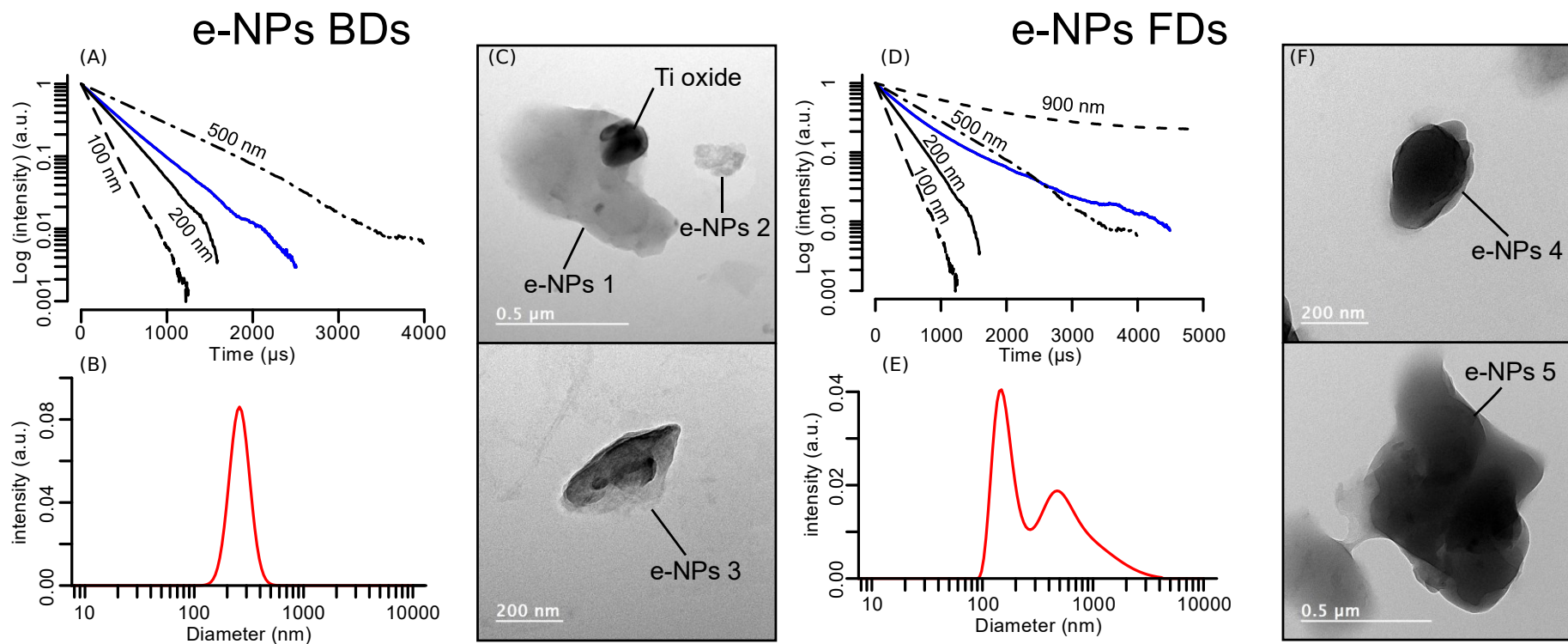


Figure II.9. Size characterization of e-NPs from beach and floating debris types. Log-transformed autocorrelation function (blue) and size nominated spherical nanoparticles of PS (black) (A) and (D) for e-NPs from BDs and FDs, respectively. SBL modeling (red) from the autocorrelation function (B) and I for e-NPs from BDs and FDs, respectively. TEM images (C) and (F) from BDs and FDs, respectively. EDX spectrum and atomic composition of e-NPs 1, Ti oxide and the grid are available in Table II.6.

The surface site on floating e-NPs between pH 4 and 8 was quantified to $0.225 \pm 8.5e^{-3}$ mmol g⁻¹. Among colloids, the e-NPs have proton-reactive sites similar to that of clays, 0.250 mmol g⁻¹, but one order of magnitude lower than ferrihydrite and soil OM, 7.77 and 7 mmol g⁻¹, respectively (Table II.8). The specific surface is determined to equal 12.3 ± 2.4 m² g⁻¹ and the resulting surface site density is calculated to 11.0 ± 0.4 sites m⁻². Such density is close to montmorillonite and ferrihydrite, 6.63 and 10.32 sites nm⁻², respectively. To summarize, the e-NPs surface has carbon-oxygen functions (C-O, C=O, and O-C=O) estimated at $32 \pm 6\%$. Among these oxidized functional groups, $0.225 \pm 8.5e^{-3}$ mmol g⁻¹ were proton-reactive, leading to a surface site density of 13.3 ± 2 sites m⁻². Such proton-reactive sites and site density are similar to the reactive colloidal in the environment pictured by clays and ferrihydrite.

Table II.6. Relative atomic composition obtained from EDX analysis on e-NPs 1 and its embedded black cubic particle.

% Atomic	e-NPs 1	Ti oxide
C	96.60	65.70
O	21.58	21.58
Na	-	-
Al	0.07	0.25
Si	0.63	0.50
S	0.06	0.06
K	-	-
Ca	0.21	0.10
Ti	-	11.80

II.3.5. Implication for environmental NPs and protocol advantages

Nanoplastic characteristics are poorly understood and studied due to the difficulties of sampling enough material under environmental conditions. The production of environmentally relevant NPs models in large quantities is needed to study their environmental fate, behavior, and impact. The production of e-NPs with the proposed protocol allows reached concentration of around 400 mg L⁻¹. These concentrations were enough to characterize their composition and surface properties (Table II.8). Among the functional group present at the surface of e-NPs, ~10% were identified as carboxylic functional groups (i.e., C-O=O bounds) (Figure II.10). These groups explained the proton-reactive sites observed and quantified by potentiometric titration. These results are in accordance with the pH-dependent Pb sorption followed by Davranche et al. 2019. Moreover, as PE and PP carbon skeletons do not include the aromatic cycle, the C-O hydrolyzed bond may be restricted to alcohol functional groups, not known to complex metals (Martell and Smith, 1977). Thus, the sorption capacity of e-NPs may be only

due to carboxylic functional groups. However, although one main functional group may drive metal complexation on the e-NPs, these COOH groups may have diverse pKa values due to the presence and proximity of electron-withdrawing groups (carboxylic, acid, ketone, ester, ether, hydroxyl, etc.) on the aliphatic skeleton of PP and PE (Martell and Smith, 1977; Leenheer et al., 1995).

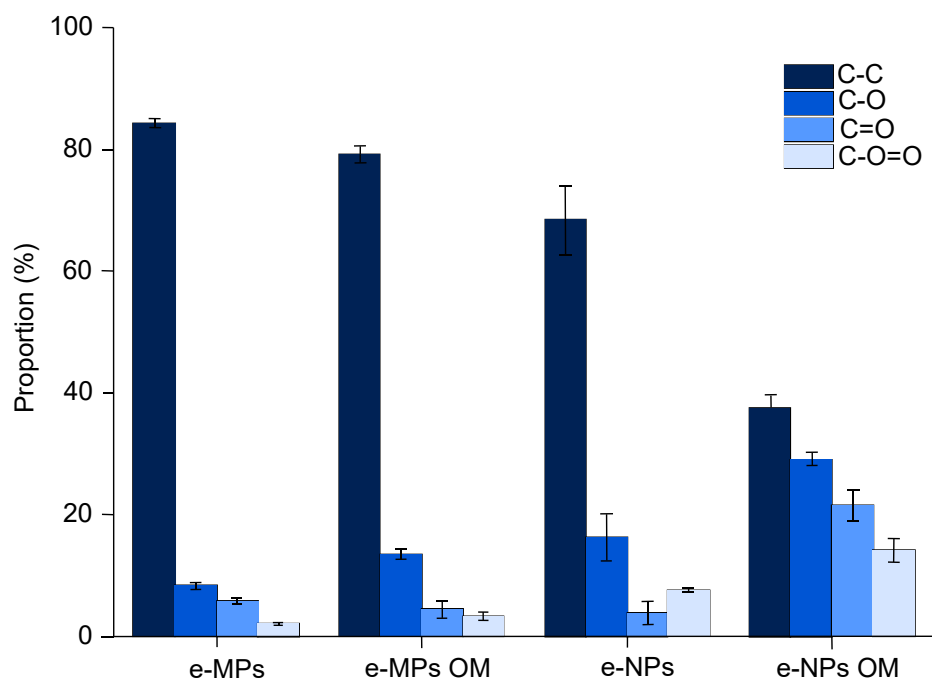


Figure II.10. Atomic bonding distribution from C1s. High-resolution spectra from the e-NPs FDs.

PP and PE were identified as polymers found in the e-NPs. This is in accordance with the polymer composition of plastic pieces found in the sea surface and coastal region (Reisser et al., 2013; Ter Halle et al., 2017; Brignac et al., 2019). Nevertheless, the PE presence seemed limited as it was not detected for the e-NPs from the beached plastic debris. Moreover, the TIP e-NPs pyrograms show the PP fingerprints with a higher proportion (Figure II.7). The higher photooxidation of PP debris certainly explains the observation. Ojeda et al. (2011) observed a higher degradation for PP than for PE after the exact solar light exposition.

Moreover, Fotopoulou and Karapanagioti (2012) observed a significant textural difference between PP and PE plastics. The surface of beached PP was more cracked while PE was more altered. Those cracks may enhance the removal of the PP altered layer and produce more PP e-NPs than the further application of the present protocol may give an interesting response about the polymer sensitivity to form NPs. The surface site density of e-NPs was close to that of inorganic colloids, known to be a strong environmental adsorbent of micropollutants. Therefore, the produced e-NPs are significant sorbents, able to compete with clays and Fe

oxyhydroxides. However, about physicochemical properties, two critical differences can be distinguished between these environmental colloids and e-NPs. First, e-NPs do not bear amphoteric hydroxyl sites as observed on Fe oxyhydroxides. These sites can develop negative and positive charges in response to the pH variations (Stumm, 1987). By contrast, e-NPs proton-reactive sites are driven by oxidized carbon functional groups (Figure II.10). The e-NPs usually had a charge of zero at acidic pH, and were negatively charged at basic pH values. By contrast, clays and Fe oxyhydroxides always bear negative, and negative or positive charges, respectively (Lövgren et al., 1990; Stumm, 1987; Tombácz and Szekeres, 2004). From a colloidal perspective, these properties explain why e-NPs may be stable or unstable, depending on the environmental conditions. As a consequence, in favourable conditions, NPs may accumulate. However, the presence of additives or adsorbed elements may affect the net surface charge of the e-NPs, and it is therefore essential to evaluate this surface potential by direct measurement. Also, these surface functionalities are imperative to mimic the metal reactivity of NPs in the environment. Therefore, this first determination of the e-NPs site density could be integrated to produce free soap NPs with realistic site density at their surface (Pessoni et al., 2019).

Table II.7. H₂O₂ quantification after the UVC exposition of the e-NPs suspension.

UV exposition (hours)	H ₂ O ₂ (% v/v)
0	1
6	0.64

Among the different protocols to produce NPs (Magrì et al., 2018; Mitrano et al., 2019; Pessoni et al., 2019; El Hadri et al., 2020), using the altered layer from weathered plastics provides numerous advantages, including the realistic presence of random additives, an accurate representative shape and surface morphology, and the presence of oxidized functional groups. Among these groups, a non-negligible part was proton-reactive. The first step of the protocol used in this study is non-degradative, and thus, the extracted e-NPs are the closest model for NPs produced by environmental photooxidation. Another advantage is the possibility to form nanoparticles that are environmentally representative of the plastic made in a specific place under specific conditions. Such properties may be essential for ecotoxicological studies. Moreover, the protocol described here provided quantity of e-NPs to further study their physicochemical properties with consumptive techniques and instruments in this study (XPS, MEB, ATR-FTIR, etc.).

Table II.8. Physico-chemical properties of e-NPs and environmental phases.

Sample	Size range (nm)	TOC (mg L ⁻¹)	SSA (m ² g ⁻¹)	H _{surf,tot} (mmol g ⁻¹)	Site density (sites nm ⁻²)	References
e-NPs	120-180 and 600-800	200	12.3±2.4	0.225 ± 8.5e-3	11± 0.4	This study
Soil organic matter	-	-	94-174	7	24-45	de Jonge and Mittelmeijer-Hazeleger, 1996; van Schaik et al., 2010
Ferrihydrite	5	-	350	6	10.32	Villalobos and Antelo, 2011
Ferrihydrite	7	-	650	7.771	7.2	Hiemstra and Van Riemsdijk, 2009
Goethite	400*40	-	40	0.11	1.68	Lövgren et al., 1990
Goethite	500	-	70	0.732	6.3	Villalobos et al., 2009
Gibbsite	200x10	-	29.5	0.133	2.71	Rosenqvist et al., 2002
Montmorillonite	<2000	-	8.5	0.250	17.41	Cadene et al., 2005; Tournassat et al., 2004
Montmorillonite	200	-	45.4	0.500	6.63	Le Forestier et al., 2010; Tombácz and Szekeres, 2004
Kaolinite	< 2000	-	12.10	0.358	17.8	Jeon and Nam, 2019

II.4. Conclusions

Based on previous work, this study proposed to produce an environmentally relevant nanoplastic model (e-NPs). The e-NPs were obtained by mechanical abrasion and sonication of the altered outer layer found on weathered plastic debris. The efficiency of the process in removing organic matter to purify the e-NPs suspension was assessed by fluorescence spectroscopy and Py-GCMS. analysis. The yield reached ~80 to 90% depending on the initial concentration of the e-NPs suspension. Purified e-NPs were further characterized in terms of size, shape, composition, and surface properties. The e-NPs produced in this way had a colloidal behavior in solution, were <1 μm , and had polymorphic shapes as expected for NPs. The e-NPs were composed mainly of PP, but PE was also present. Concerning physicochemical properties, e-NPs were found to contain less than 30% oxidized functional groups (i.e., C=O, C-O, and C-O=O), and a non-negligible proportion were proton-reactive. The density of binding sites on e-NPs was comparable to mineral colloids like clays, which means they are a competing sorbent. The e-NPs are expected to be more stable at high pH values and unstable at low pH, according to the quantity of (de)protonated sites at its surface. Overall, the proposed protocol was successful in producing environmentally relevant NPs. For the first time, we produced a suspension concentration that was sufficient to study NPs' physicochemical properties. These achievements represent substantial progress in NPs model research, and some direct consequences are the further characterizations of the NPs' physicochemical properties, as a better understanding of NPs behavior and their impacts in the environment. Finally, our protocol offers the opportunity to the scientific community interested to the NPs contamination by using this protocol for specific plastic composition that will be pre-selected.

CHAPITRE III. IDENTIFICATION DES MÉCANISMES DE SORPTION

Ce chapitre correspond à 2 articles. Le premier « Metals binding processes on Nanoplastics : Rare earth elements as a probe » soumis dans Environmental Sciences Nano, Florent Blancho, Mélanie Davranche, Adrien Léon, Bruno Grassl, Stéphanie Reynauld, Julien Gigault. Et le 2ème à un article qui sera prochainement soumis dans la revue Journal of Colloid and Interface Science, « Mechanistic description of metal sorption onto Nanoplastics », Florent Blancho, Mélanie Davranche, Adrien Léon, Rémi Marsac, Bruno Grassl, Stéphanie Reynauld, Julien Gigault.

Dans le chapitre 2, nous avons développé un protocole de NPs pertinents de l'environnement. Les analyses XPS ont mises en évidence la présence à leur surface de groupements fonctionnels ionisables de types -COOH dont la concentration approche les 0.3 mmol g^{-1} . Ces sites sont capables d'interagir avec des cations métalliques et sont à l'origine de l'adsorption de métaux comme démontré par Davranche et al. (2019). Bien que l'adsorption des métaux par les NPs ait été démontrée, les mécanismes l'expliquant restent mal contraints.

L'objectif de ce chapitre a donc été de mieux comprendre les processus mis en jeu afin d'estimer la capacité des NPs à adsorber les métaux et d'en déduire leur capacité à agir comme des vecteurs de métaux dans l'environnement. Pour cela nous avons utilisés deux méthodologies, la sonde terres rares et la modélisation géochimique.

L'efficacité de la sonde terres rares à tracer les processus de complexation de surface a été démontrée dans plusieurs études (Pourret et al., 2007; Marsac et al., 2010, 2011). L'utilisation de la sonde terres rares repose sur les fractionnements produits entre chaque terre rare lorsqu'elles sont mises en jeu dans des réactions chimiques. Ces fractionnements sont traduits par des spectres (pattern de terres rares). La variation de la forme des spectres de terres rares, notamment suite à leur complexation par un adsorbant complexe peut permettre de mettre en évidence les sites activés et les complexes formés (Wood, 1993; Tang, 2003; Pourret et al., 2007; Marsac et al., 2010).

Dans la deuxième partie de ce chapitre, nous avons utilisé la modélisation géochimique pour décrire plus en détails les mécanismes et paramétrer les processus. Cette étude a été réalisée avec le Pb, la modélisation des spectres de terres rares restant compliquée à ce stade de connaissance. Cependant, les hypothèses mécanistiques testées dans le modèle reposent sur les mécanismes déduits de la sonde terres rares, c'est-à-dire la formation de complexes monodentés et/ou bidentés. La paramétrisation du modèle est également basée sur l'extrapolation d'un jeu de données expérimentales produites à partir de différents modèles de NPs dont celui produit dans le Chapitre 2. Le modèle a ensuite été validé à l'aide du jeu de données de Davranche et al. (2019) et des données produites pour des NPs à différents degrés d'oxydation.

III.1. Identification des complexes de surface : cas des terres rares

Résumé

La présence de nanoplastiques dans l'océan et les sols démontre une distribution globale dans l'environnement. En raison de leurs propriétés colloïdales, les nanoplastiques pourraient influencer la spéciation des métaux traces dans les matrices naturelles, sujet peu abordé en raison du manque de méthodologie pour évaluer l'association nanoplastiques-métaux dans l'environnement naturel. Pour donner une image globale de cette propriété des nanoplastiques, cette étude vise à utiliser les terres rares (REE) comme sonde chimique pour comprendre les mécanismes d'adsorption des métaux qui pourraient se produire sur les surfaces des nanoplastiques, qui devraient être fortement oxydées dans l'environnement. La comparaison entre les modèles de nanoplastiques pertinents pour l'environnement et les complexes REE-COOH ont démontré que les REE sont adsorbés par des sites COOH sur les nanoplastiques. Ces voies d'adsorption suivent un processus mono-ligand pour les REE légères et bi-ligand pour les complexes REE lourdes, le chélate étant exclu. Nous avons démontré que la denticité des complexes est influencée par le pH, la charge en REE et les ions compétitifs. Les complexes bi-ligands avec les REE lourdes dominent à $\text{pH} > 4.5$ et une faible charge en REE. Cette étude propose une nouvelle approche pour comprendre l'interaction nanoplastiques-métaux et met en évidence les REE comme un puissant traceur des mécanismes de sorption.

Abstract

The nanoplastics presence in the ocean and soil demonstrates their global distribution in the environment. Due to their colloidal properties, nanoplastics could influence trace metal speciation in natural matrices, which has been poorly addressed due to the lack of methodology to assess the nanoplastics -metal association in the natural environment. To give a global picture of this property for nanoplastics, this work aims at using rare earth elements (REE) as a chemical probe to understand metal adsorption mechanisms that could occur onto nanoplastics surfaces, which is expected to be highly oxidized in the environment. Comparison between environmentally relevant nanoplastics' models and REE-COOH complexes patterns demonstrated that REE are adsorbed through the COOH sites onto the nanoplastics. These adsorptions pathways follow a mono-ligand process for light REE and bi-ligand for heavy REE complexes, chelate being excluded. We demonstrated that the denticity of the complexes is influenced by the pH, REE loading, and competitive ions. Bi-ligand complexes with heavy REE dominate at $\text{pH} > 4.5$ and low REE loading. This study is a novel approach in understanding NPs-metals interaction and highlights REE as a powerful tracer of sorption mechanisms.

III.1.1 Introduction

The presence of nanoplastics (NPs) in various environmental compartments, notably ocean, soils, and alpine snows, is now evidenced (Ter Halle et al., 2017; Materić et al., 2020; Wahl et al., 2021). When released in the environment, plastics waste fragments into plastic particles of various sizes, mainly through mechanical abrasion and photo/thermo-oxidation (Lambert et al., 2013; da Costa et al., 2016; Dawson et al., 2018; Mattsson et al., 2018). Nanoplastics are particles < 1000 nm with heterogeneous shapes and charged surfaces (Gigault et al., 2018). Nanoplastics act as colloids, and regarding their nanometric size, they are expected to have a high specific surface area (SSA), leading to a considerable surface reactivity for micropollutants (Orts-Gil et al., 2013; Mattsson et al., 2018; Yu et al., 2019; Davranche et al., 2019; Gigault et al., 2021). Recent ecotoxicological studies showed the release of organic and inorganic pollutants associated with NPs in living organisms, namely the "trojan horse effect" (Chen et al., 2017; Rist and Hartmann, 2018; Baudrimont et al., 2020).

However, information and data are scarce for inorganic pollutants, notably metal interactions with NPs. Nevertheless, metals are used mainly in the plastic formulation as color pigments or provide specific properties to plastics (Piringer and Baner, 2008; Flick, 2013). These metals are trapped in the polymer structure. Although their diffusion within plastic polymer bodies is possible, this process is slow and expects to release very few amounts of metal (Piringer and Baner, 2008; Town et al., 2018; Turner and Filella, 2021). However, when plastics are photodegraded and subsequently fragmented as micro- and nanoplastics, their metal loading is also released. Catrouillet et al., 2021, showed that most metal adsorbed on the altered surface layers of microplastics came from the metal additives used to form the plastic. Since this altered layer is also the source of NPs released in the environment, it can be hypothesized that metal and NPs interact from their release.

Moreover, it is not excluded that metal is initially present in the environment (such as in landfills), and NPs can interact independently of their release. Davranche et al., 2019, demonstrated that Pb(II) is associated with NPs principally by surface complexation and intraparticle diffusion. However, this study focused only on the Pb(II) uptake and did not evaluate the sorption mechanisms. At the same time, ATR-FTIR and XPS analysis evidenced that O-containing functions (Kalogerakis et al., 2017; J. Wang et al., 2017; Q. Wang et al., 2020) and carboxylic sites are present on the surface of NPs and the altered surface of microplastics sampled in the environment (Blancho et al., 2021a; Tang et al., 2021). Tang et al., 2021, suggested that –COOH is the principal functional group at the MPs surface associated

with metals. And yet, compared to microplastics, it was demonstrated that the NPs reactive surface site density could reach 11 sites nm⁻², higher than goethite (Bargar et al., 1997; Ponthieu et al., 2006; Blancho et al., 2021a). It is, therefore, crucial to determine how NPs properties could affect the fate and behavior of trace metals.

Several techniques exist to characterize the complexes formed between metals and solids. One of the most resolved is the X-ray absorption (XAS, etc.), which was successfully used to investigate the metal complexation by minerals and colloids (Bargar et al., 1997; Fitts et al., 1999; Sverjensky, 2006; Yano and Yachandra, 2009). But such a technique is challenging to operate for accurate determination of the speciation. One interesting strategy is to use geochemical proxies as a probe for sorption studies. Rare earth elements (REE) represent a group of chemical elements with coherent chemical properties that allow their use as a fingerprint of sources and biogeochemical processes (de Baar et al., 1991; McLennan, 1994; Pourret et al., 2007; Marsac et al., 2010; Davranche et al., 2011; Noack et al., 2014). Their chemical properties present systematic changes along with the range of their atomic number, resulting in typical distribution patterns (Taylor and McLennan, 1988). For natural organic matter (OM), REE patterns have successfully described the metal-binding mechanisms. They are notably sensitive to the number of chemical bindings or ligands surrounding REE and can therefore provide information on the complex denticity (Byrne and Li, 1995; Wood, 1993; Marsac et al., 2011).

This work aims at evaluating the ability of REE to determine the adsorption mechanism of trace metals occurring at the NPs' surface. Rare earth elements were used as a probe to characterize the NPs functional groups that control the sorption and complexes formed between metal and NPs. Rare earth elements adsorption isotherm and pH-adsorption edge were performed with REE and three NPs models, 1) the commonly used carboxylate polystyrene nano-beads (PSL), and 2) an environmentally-relevant NPs produced following (Blancho et al., 2021a). Experimental REE patterns were compared to literature REE ligands patterns to decipher the occurring mechanisms.

III.1.2. Materials and methods

III.1.2.1. Nanoplastics models and characterization

Nanoplastics models were 200 nm, carboxylate polystyrene Latex nanoparticles (Polysciences Europe), PSL_{surfactant}, 380 nm free soap Polystyrene latex nanoparticles, PSL_{free}

(Pessoni et al., 2019). The third model is environmentally-relevant NPs produced from altered plastics debris collected in the Environment, e-NPs (Blancho et al., 2021a).

The hydrodynamic radius, H_r , of the NPs was determined using Dynamic Light Scattering (DLS) (VASCO Flex's, Cordouan Technologies) for suspensions concentrated at 10 ppm without Ionic Strength (IS). The geometric shape of NPs was observed by transmission electronic microscopy (TEM) (JEM 2100 HR, Jeol). Transmission electronic microscopy was operated at 200-kV acceleration voltage with a LaB_6 as electron source, the point and line resolution are of 2.3 Å and 1.4 Å, respectively. Particles were photographed with a Gatan Orius SC200D camera, and elemental analysis was performed using an EDX Oxford X-Max 80T detector.

The specific surface area (SSA) of NPs was determined by the BET method (Brunnauer Emmet and Teller) for e-NPs while it was extrapolated from the particle diameter for PSLs (Table III.1.1). The BET analyses were carried out using with a Gemini VII instrument (Micromeritics) for e-NPs and m-NPs while extrapolated from the particle diameter for the spherical PSL. The determined SSA are reported in the Table III.1.1.

Table III.1.1: Specific surface area of the studied NPs

NPs	SSA ($m^2 g^{-1}$)
PSL _{surfactant}	28.84
PSL _{free}	15.18
e-NPs	11.9

III.1.2.2. Surface charge modelling

The surface charge was assessed by potentiometric titration using a Titrano unit controlled by the Tiamo software (Metrohm). All solutions were titrated with 0.01 M NaOH (Honeywell Fluka), under a N_2 flux. Prior titration, the pH probe was calibrated on a concentration scale using 1mM HNO_3 . Titration were performed at 10, 100 and 1000 mM of $NaNO_3$ as IS and started below pH 4 by adding a fixed volume of 100mM HNO_3 . The determination of the protonable groups was performed as describe by Spadini et al., 2018. Briefly, the proton released from the surface, H_{surf} , was related to the pH of the solution (Eq. S1). The total surface site concentration $H_{s\ tot}$, was defined as the released H_{surf} between pH 4 and 8.0 for the highest IS. Due to early site deprotonation, there is an initial charge at the NPs surface, noted H_0 . This H_0 is IS dependent and was estimated by modelling calculations. This

calculated H_0 was thus added to H_{surf} . The CO_2 diffusion during the titration was taken in account using the $H_{s\ tot}$ of the ultrapure water (Blank).

$$[H^+] = [H_{init}] + [H_{base}] + [H_{surf}] + [OH^-] \quad (III.1.1)$$

With, $[H^+]$, the free proton concentration, (M), $[H_{init}]$, the concentration of acid added to fix the pH below pH 4 (M), $[H_{base}]$, the concentration of base added during the titration (M), positive when base is used and negative when acid is used, $[H_{surf}]$, the concentration of the released H^+ , the only unknown (M) and $[OH^-]$, the concentration of the H^+ released from the water auto-protolyze, at pH 7 (M).

The NPs surface charge was determined by calculation using PHREEQC implemented by the SIT thermodynamic database.

III.1.2.3. Adsorption experiments

Adsorption isotherms of REE by NPs were carried out for REE/NPs ratios from 0.025 to 1 mg g⁻¹ Carbon. The stock solution of REE was the REE standard CCS-1 solution (Inorganic Venture) that contained equal concentrations of REE, Sc, U, Th, and Y. The concentration of NPs was fixed at 50 and 25 ppm for both PSLs and the e-NPs, respectively, regarding the low amount of produced e-NPs. The ionic strength (IS) was fixed at 5 mM with NaNO₃ (Fisher Scientific). After adding REE, the pH of the suspension was adjusted to 5 with HNO₃ and/or NaOH (0.1 to 1 mol L⁻¹). At equilibrium, the suspensions were filtered at 0.2 μm (PES syringe filter, Sartorius) for both PSLs and 30 kD for e-NPs (PES ultrafiltration cells, Sartorius). The equilibrium time was estimated from previous kinetic experiments to 48h for all NPs. Dynamic light scattering previously checked the absence of nanoparticles in the filtrate (VASCO Flex, Cordouan Technologies). After filtration, all samples were acidified at 2% HNO₃ for ICP-MS analysis.

The pH-adsorption edge experiments were carried out with REE concentration at 0.1 and 0.35 mg g C⁻¹ for both PSLs and e-NPs, respectively. The pH was fixed at pH 3, 4.5, 5, 5.5, 6, and 7 with HNO₃ or NaOH. At equilibrium, the suspensions were filtered at 0.2 μm (PES, Sartorius) for both PSLs and 30 kDa for e-NPs (PES ultrafiltration cells, Sartorius). After filtration, all samples were acidified at 2% HNO₃ for ICP-MS measurements.

III.1.2.4. Chemical Analysis

The REE concentrations were measured using a Quadrupole ICP-MS (Agilent Technologies 7700X). Before metal quantification, calibration curves were performed and validated using certified material references (SLRS-6, National Research Council). A rhodium solution was used as an internal standard to correct the instrumental drift and potential matrix effects. The average limit of REE quantification was determined at 0.4 ± 0.02 ppt (AFNOR Certification). Moreover, as the upper limit of the REE calibration curve was 5 ppb, if necessary, samples were diluted not to exceed this value. Chemical blanks were consistently below the limit of quantification and were thus neglected. The total organic carbon concentration (TOC) of all the NPs suspensions was quantified by a TOC-analyzer (TOC-V analyzer, Shimadzu). The precision of the DOC measurements was estimated to be $\pm 5\%$ using a standard potassium hydrogen phthalate solution (Sigma Aldrich).

III.1.3. Results and discussion

III.1.3.1. Nanoplastics properties

For PSLs, DLS indicated, as expected, a monodisperse suspension (i.e. straight Log-transformed ACF) (Figure III.1.1). As a result, no uncontrolled aggregation occurred. Their Hr were considered as equal to 200 nm for the PSL_{surfactant} (NIST CMRs) and 380 nm for the PSL_{free} (Pessoni et al., 2019).

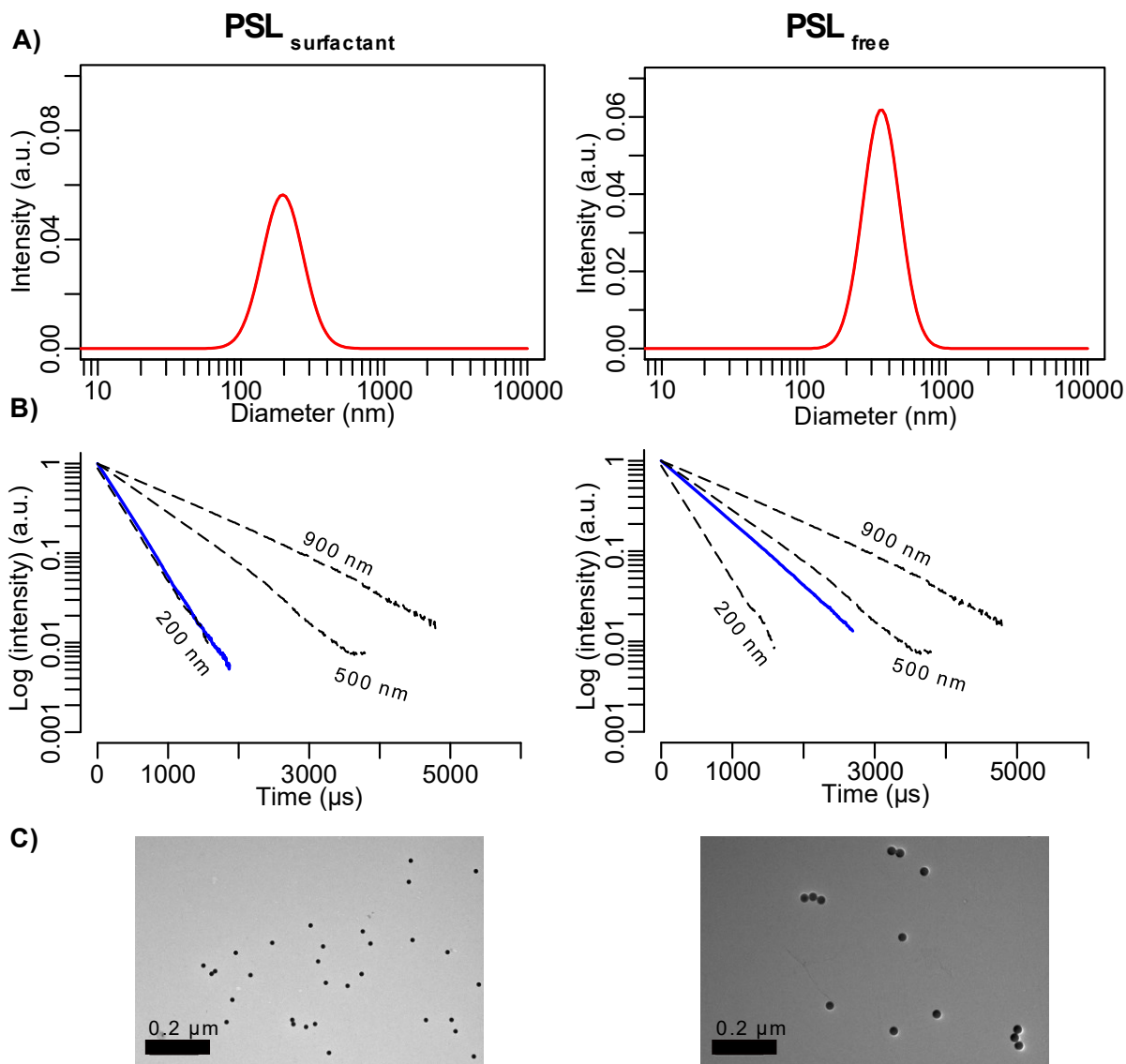


Figure III.1.1. Size characterization of PSL models. A) Population size from SBL modeling. B) Log-transformed time-ACF of the intensity of light scattered compared to CMRs standards. C) TEM pictures from the suspensions.

For e-NPs, both log-transformed slopes of the autocorrelation function (ACF) were inferior to the 900 nm of the CMRs standard (Blue line, Figure III.1.2A), indicating that Hr was inferior to 900 nm. Moreover, their log-transformed ACF were not straight compared to the CMRs indicating polymodal suspensions. This result is coherent with the bimodal distribution proposed by the Sparse Bayesian Learning, SBL, based-modelling of the ACF (Figure III.1.2B), the first and second population size have an average Hr of 226 ± 36 and 376 ± 64 nm.

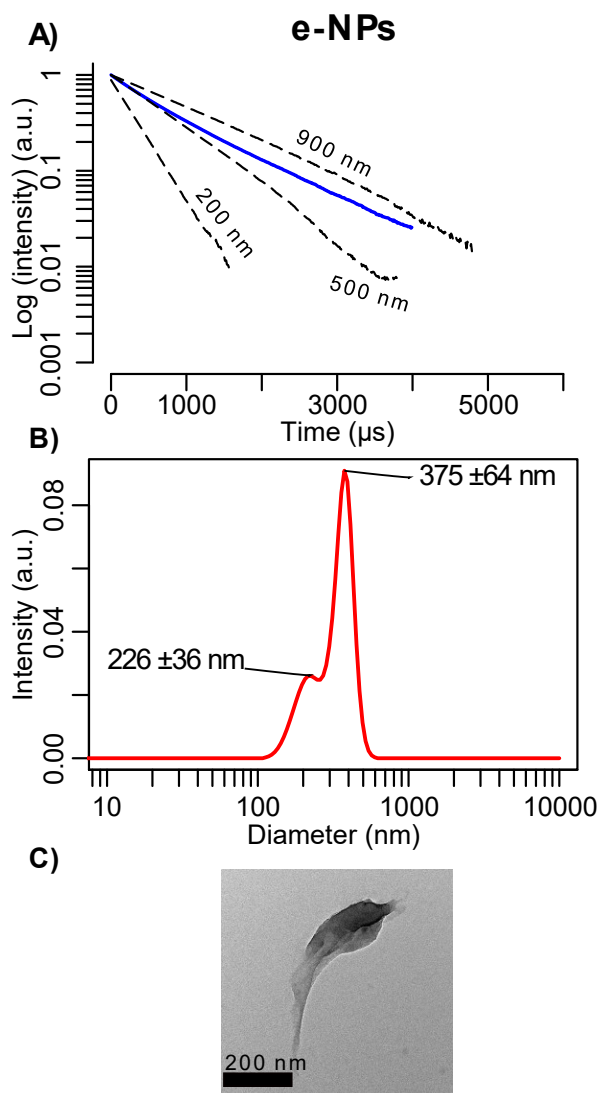


Figure III.1.2. Size characterization the e-NPs model. A) Log-transformed time-ACF of the intensity of light scattered compare to CMRs standards. B) Population size from SBL modeling. C) TEM pictures from the suspensions.

Potentiometric titrations allowed to determine the amount of ionizable function relative to the pH onto PSL surface. In Figure III.2.3. was plotted the $H_s(\text{pH})$ evolution corrected from H_0 (pH 4) at three IS for PSLs, e-NPs and m-NPs. As expected, the dissociation of the surface group increased with the increasing pH (Eq. 3). The IS promoted the deprotonation of surface group by decreasing the diffuse layer length and thus shielding the electrostatic impact of Ψ_0 (Pfeiffer et al., 2014). Titrations at 1M IS showed a typical sigmoidal curve (Connors, 1990; Chen et al., 2021). These titration curve indicates that the whole ionizable group was dissociated between pH 4 and 8. The total surface ionizable group, $H_{s \text{ tot}}$, was considered to be equal to the concentration of the deprotonated group at pH 8, as a plateau was reached for both PSLs. The $H_{s \text{ tot}}$ was determined as $0.316 \pm 2 \cdot 10^{-3}$ and $0.086 \pm 2 \cdot 10^{-3} \text{ mmol g}^{-1}$ for the PSL_{surfactant} and PSL

free, respectively. According to the SSA, the site density was 6.60 and 3.41 sites nm^{-2} for PSL_{surfactant} and PSL_{free}, respectively. The $H_{s\text{ tot}}$ and site density are higher for PSL_{surfactant}.

For e-NPs, the 1M titration curves were not sigmoidal and showed the same increase after pH 7.5 (Figure III.1.3) avoiding the $H_{s\text{ tot}}$ determination (no plateau was reached). However, the total concentration of surface site could be estimated (value obtained for the highest, ≈ 8.5) as $\geq 0.282 \pm 4 \cdot 10^{-4}$. According to the SSA, the site density was ≥ 14.3 sites nm^{-2} . The $H_{s\text{ tot}}$ and site density are higher for PSL_{surfactant}.

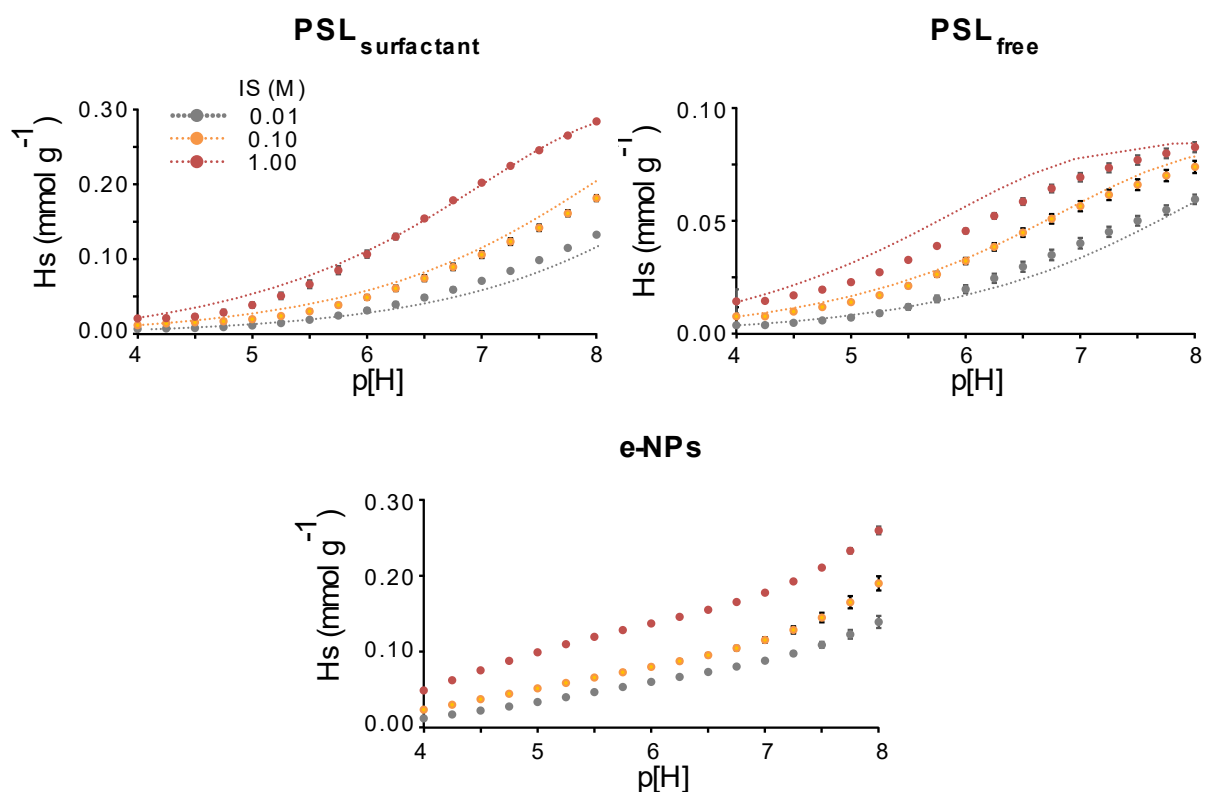


Figure III.1.3. Evolution of the H_s with the $p[H]$ for both PSLs and e-NPs at 3 IS: 0.01, 0.10, 1.00 M. Symbols correspond to experimental data and dotted lines to calculated data.

III.1.3.2. PSL with surfactant, PSL_{surfactant}

Adsorption isotherms showed that $[REE]_{\text{ads}}$ increased with the increasing $[REE]_{\text{free}}$ to reach a strict asymptotic plateau indicating a surface site saturation (Figure III.1.4A). The maximum adsorption concentrations were 0.06 and 0.13 mg g^{-1} for La, Eu, and Lu. The adsorption increased thus from La, Eu to Lu demonstrating that light REE (LREE) are lesser adsorbed at the PSL_{surfactant} surface than the middle (MREE) or heavy REE (HREE). The

isotherm shape did not vary, suggesting a similar adsorption mechanism for all REE. The corresponding REE-NPs binding patterns exhibited an MREE downward concavity supported by the La/Sm ratio variations (from 0.93 at REE/NPs = 0.025 to 0.9 from REE/NPs = 1, Figure III.1.5). This feature is specific to the REE binding by carboxylic groups –COOH (Davranche et al., 2005; Marsac et al., 2010; Pourret et al., 2007; Tang and Johannesson, 2003; Wood, 1993) (Figure III.1.4B) and was expected for the PSL_{surfactant} since carboxylated. The La/Lu ratios varied regularly from 0.94 to 0.89. The increasing REE/NPs ratios suggested a slight HREE adsorption increase than the other REE, increasing REE/NPs ratios (Figure III.1.5).

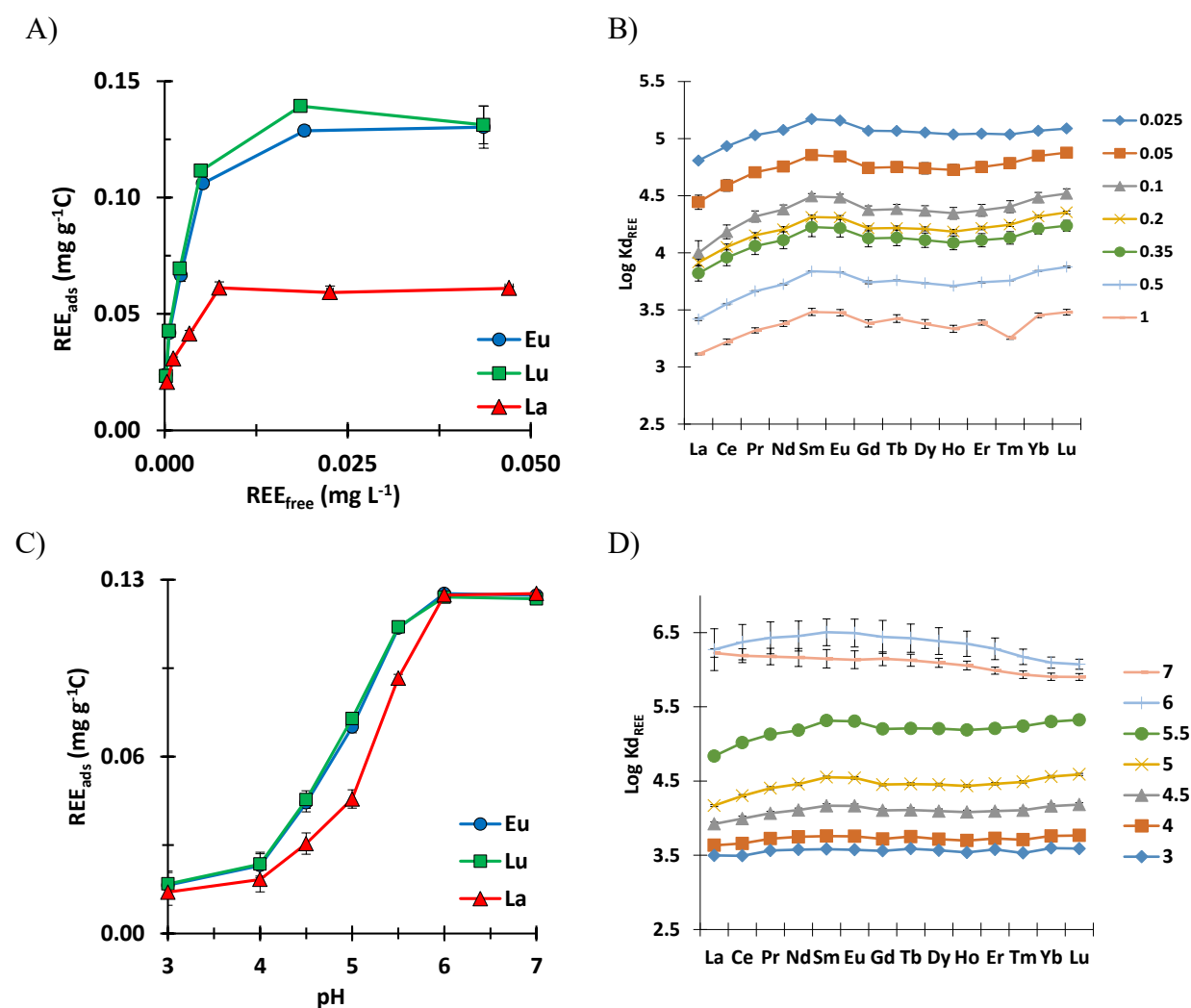


Figure III.1.4. A) Adsorption isotherm of REE onto PSL surfactant for REE/NPs varying from 0.05 to 1 and pH = 6.5, B) REE patterns (log K_d) corresponding to each point of the adsorption isotherm, C) REE adsorption relative to the pH at REE/NPs = 0.1 mg g⁻¹ for pH varying from 3 to 7, D) REE patterns (log K_d) corresponding to each point of the pH-adsorption-edge. Error bars correspond to the SD of the triplicates.

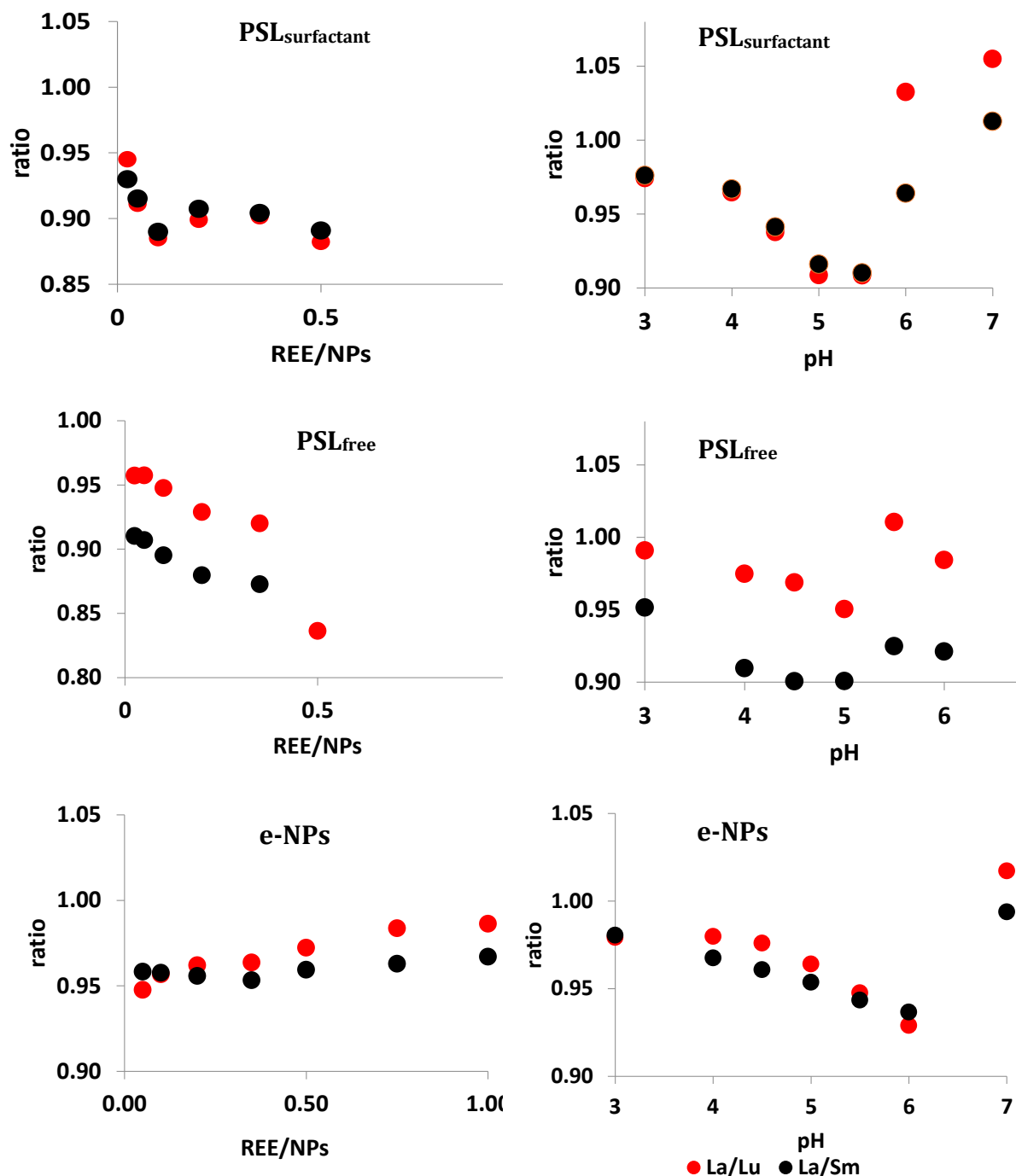


Figure III.1.5. Evolution of the La/Lu and La/Sm of the REE pattern obtained relative to the REE/NPs ratio and pH for both PSLs and e-NPs.

Figure III.1.4C illustrates adsorbed La, Eu, and Lu relative to pH. It shows that the adsorption process was strongly dependent on pH. Adsorption thus occurred through ionizable binding sites. Except for near-total adsorption from pH 6, adsorption decreased from Eu>Lu>La, MREE being the most adsorbed REE. The corresponding REE patterns were flat at low pH, not enough REEs were adsorbed to obtain a significant REE fractionation (La/Lu=

0.97 and La/Sm= 0.97 at pH 3, Figure III.1.5) (Figure III.1.4D). At intermediary pH, an MREE downward concavity (La/Sm = 0.94 to 0.91 between pH 4 to 5.5) and a small HREE adsorption increase (La/Lu= 0.94 to 0.91 between pH 4 to 5.5, Figure III.1.5) were observed on the REE patterns. The MREE enrichment resulted from the preferential MREE binding to the –COOH groups. REE patterns were flatter at high pH, decreasing from La to Lu (La/Lu = 1.05 at pH 7, Figure III.1.5). In such a pH condition, around 99.99 % of REE were adsorbed, and fractionations between REE were small, except for HREE partly maintained in solution by carbonate from pH 6.

III.1.3.3. PSL without surfactant, PSL_{free}

For PSL_{free}, adsorption isotherm showed that [REE]_{ads} increased with the [REE]_{free} until [La]_{ads} = 0.04 mg g⁻¹ C at [La]_{free} ≈ 0.003 mg L⁻¹, [Eu]_{ads} = 0.1 mg g⁻¹ C at [Eu]_{free} ≈ 0.013 mg L⁻¹ and [Lu]_{ads} = 0.08 mg g⁻¹ C at [Lu]_{free} ≈ 0.014 mg L⁻¹ (Figure III.1.6A). Adsorption was lower than PSL_{surfactant} due to PSL_{free} lower site density, 3.4 sites nm⁻² against 6.6 sites nm⁻² for PSL_{surfactant}. Adsorption was higher for Eu>Lu>La. Middle REEs were thus the most adsorbed. The [REE]_{ads} decreased without reaching any plateau. No site saturation occurred. The [REE]_{ads} decrease occurred in response to the REE competition with Y, U, Sc, Th, which are simultaneously present in the stock solution used to perform the adsorption experiments. This competition occurred for the PSL_{free} due to its small surface site density. This competition had a higher impact on La than on Lu and Eu adsorption since occurring from [La]_{free} ≈ 0.003 mg L⁻¹ against 0.013 mg L⁻¹ and 0.014 mg L⁻¹ for Eu and Lu, respectively. As for carboxylated PSL_{surfactant}, REE-NPs binding patterns exhibit an MREE downward concavity specific to the REE binding with carboxylic groups (Figure III.1.6B). Moreover, the La/Lu and the La/Sm ratio decreased continuously from 0.97 to 0.84 and 0.91 to 0.79, respectively, with the increasing REE/NPs suggesting a regular depletion of La (Figure III.1.5 and Figure III.1.6B). This decrease might be explained by the increasing competition between the LREE and Y, U, Sc, and Th for the PSL_{free} binding sites with the increasing elements loading onto PSL_{free}.

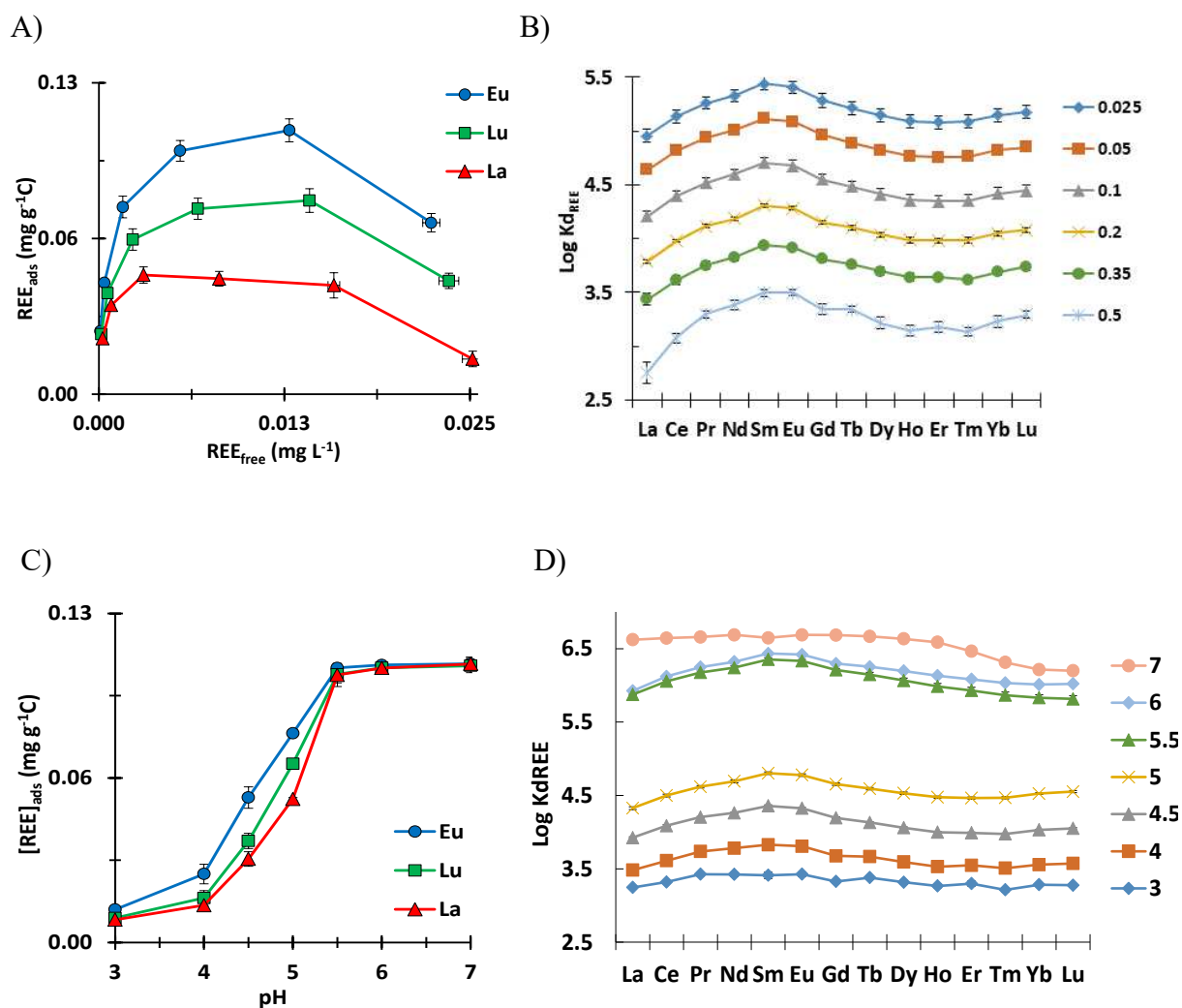


Figure III.1.6. A) Adsorption isotherm of REE onto PSL_{free} for REE/NPs varying from 0.05 to 1 and pH = 6.5, B) REE patterns (log Kd) corresponding to each point of the adsorption isotherm, C) REE adsorption relative to the pH at REE/NPs = 0.1 mg g⁻¹ for pH varying from 3 to 7, D) REE patterns (log Kd) corresponding to each point of the pH-adsorption-edge. Error bars correspond to the SD of the triplicates.

Adsorption of La, Eu, and Lu relative to pH was plotted in Figure III.1.6C. The [REE]_{ads} increased with the increasing pH, indicating adsorption occurred via ionizable binding sites. Adsorption decreased from Eu>Lu>La, MREE being the most adsorbed. Not enough REEs were adsorbed at low pH to obtain a significant REE fractionation (Figure III.1.6D). At intermediary pH, an MREE downward concavity was developed (La/Sm = 0.92 and 0.90 at pH 3 and 5, respectively, Figure III.1.5). The MREE enrichment resulted from the preferential MREE binding to the -COOH groups. The La/Lu ratio decreased from 0.97 to 0.95 between

pH 3 to 5 until reaching 1.1 at pH 7, suggesting a slight HREE enrichment at intermediary pHs (Figure III.1.5). By contrast, at pH 7, the REE pattern was depleted in HREE in response to HREE preferential complexation by carbonate in solution.

III.1.3.4. Environmentally relevant NPs, e-NPS

For e-NPs, $[REE]_{ads}$ continuously increased with the $[REE]_{free}$, no plateau, namely site saturation, was reached, suggesting a heterogeneous adsorption process relative to the REE/NPs ratios.

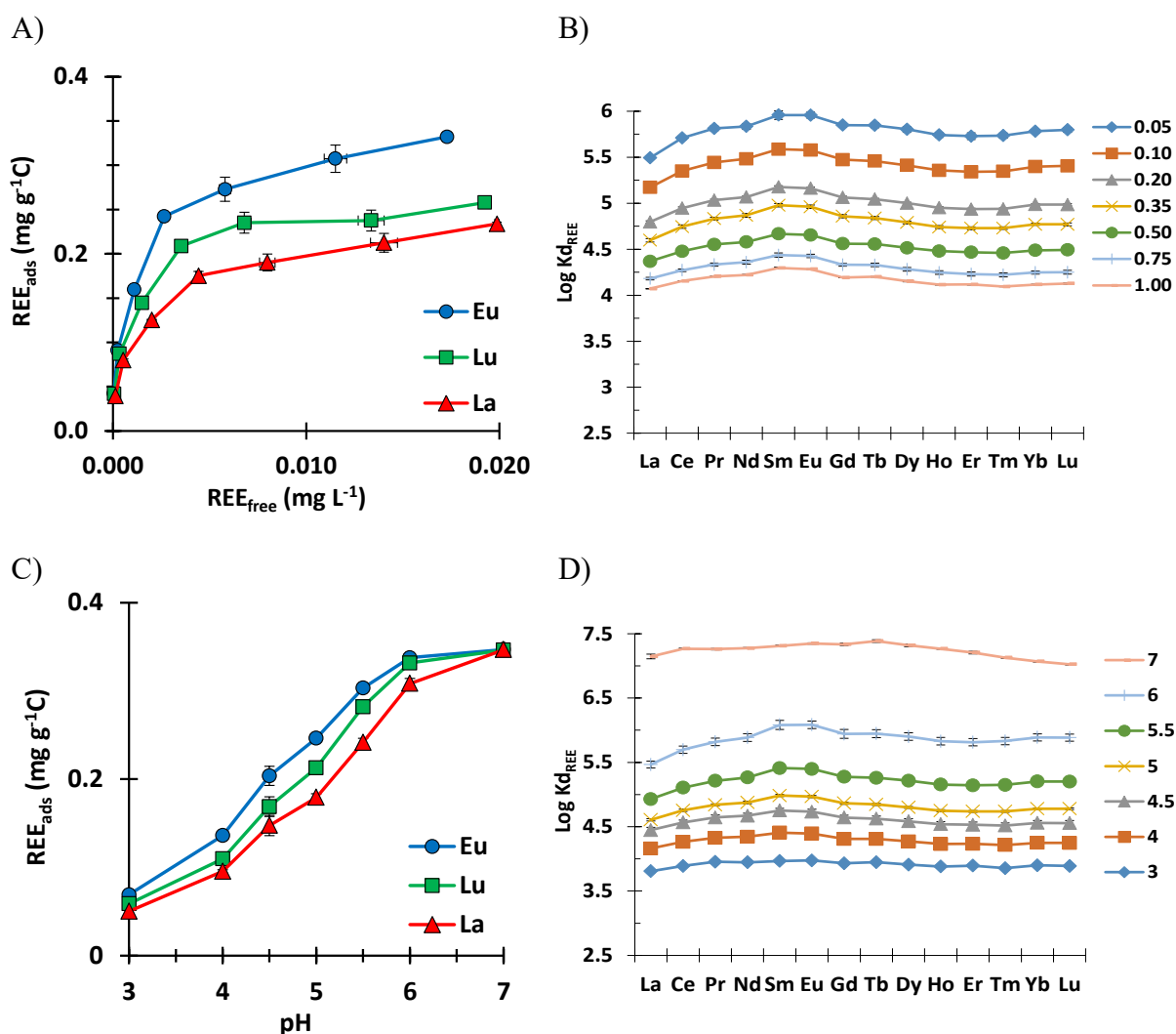


Figure III.1.7. A) Adsorption isotherm of REE onto e-NPs for REE/NPs varying from 0.05 to 1 and pH = 6.5, B) REE patterns (log Kd) corresponding to each point of the adsorption isotherm, C) REE adsorption relative to the pH at REE/NPs = 0.35 mg g⁻¹ for pH varying from 3 to 7, D) REE patterns (log Kd) corresponding to each point of the pH-adsorption-edge. Error bars correspond to the SD of the triplicates

The adsorbed amount of all REEs was higher than for both PSLs, while the adsorption followed the same order, $\text{Eu} > \text{Lu} > \text{La}$, indicating that MREE were the most adsorbed. This higher adsorption, as well as the heterogeneous adsorption process, could be the result of the higher site density of the e-NPs (>13.6 sites nm^{-2}) as compared to both PSLs (6.6 and 3.2 sites nm^{-2} for $\text{PSL}_{\text{surfactant}}$ and PSL_{free} , respectively). This highest site density allowed more REE adsorb and probably formed different complexes. The corresponding REE patterns exhibited the highest log Kd at high REE/NPs ratios than PSL (Figure III.1.7B). The La/Sm ratios varied from 0.95 to 0.97 in response to developing an MREE downward concavity corresponding to the REE binding to $-\text{COOH}$ sites (Figure III.1.5). However, by contrast with both PSLs, the La/Sm ratio increased with the decreasing ratio (Figure III.1.5). This result can be due to both La adsorption decreases or Sm adsorption increases, namely an MREE downward concavity variation. The La/Lu ratios also continuously increased from 0.95 to 0.99, with the decreasing REE/NPs ratios indicating an increase of the HREE adsorption or a decrease of the LREE adsorption (Figure III.1.5).

The $[\text{REE}]_{\text{ads}}$ increased with the increasing pH (Figure III.1.7C). The adsorption was thus pH-dependent and occurred onto ionizable sites. The amount of adsorbed REE was higher than for both PSLs, not only for each pH but also relative to the pH, notably at lower pHs. At $\text{pH} = 4$, 3.6% of REE were adsorbed for e-NPs against 0.4% and 0.2 % for $\text{PSL}_{\text{surfactant}}$ and PSL_{free} , respectively. These results suggest that binding sites of the highest energy existed, and strong complexes were formed at the surface of the e-NPs. For the corresponding REE-NPs binding patterns, the La/Sm ratios continuously decreased until pH 6, developing an MREE downward concavity. The La/Lu ratios also decreased with the pH increase due to the HREE's higher adsorption (Figure III.1.5). From pH 6.5, both ratios were close to 1, indicating a flat REE pattern and showing that e-NPs were more competitive to carbonate than both PSLs towards REE complexation.

These results suggest that e-NPs are the strongest adsorbent than both PSLs, which have binding sites of various energy and/or can form different complexes with REE and compete with carbonate for REE binding.

III.1.3.5. REE pattern deciphering

To obtain more information on the REE-NPs complexes, the present REE patterns were compared to the REE patterns binding with various $-\text{COOH}$ ligands. The impact of the

denticity and the ligand numbers were also compared to obtain information on the complex formed onto the NPs surface.

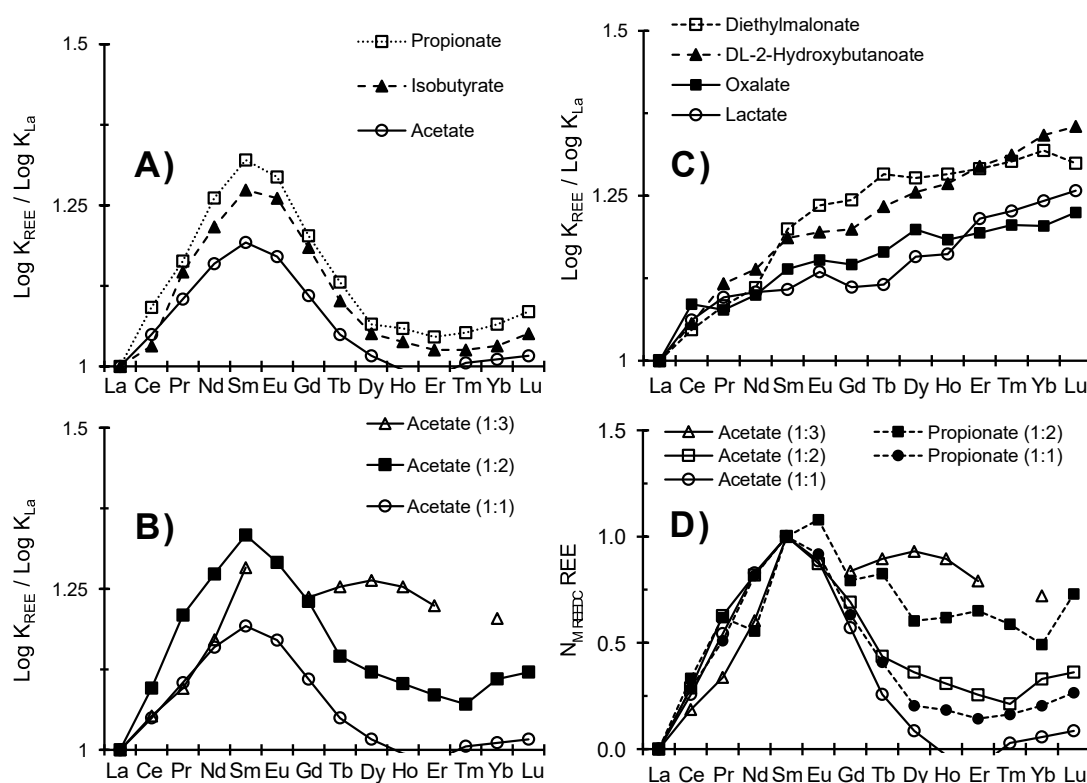


Figure III.1.8. Log K_{REE} patterns normalized to log K_{La} for (A) monocarboxylic acids (1:1), (B) for REE monodentate complexes with oxo carboxylic and dicarboxylic acid, (C) for 1:1, 1:2, and 1:3 REE-acetate complexes, and (D) N_{MREEDC} REE patterns of REE-acetate, 1:1, 1:2, 1:3 complexes and REE-propionate 1:1, 1:2 complexes.

Patterns exhibit an increasing MREE downward concavity with the increasing ligands number (Figure III.1.8C). For mono-ligands and multi-ligands complexes between REE and carboxylates (i.e., acetate and propionate), log K patterns exhibit an MREE downward concavity with a maximum binding for Sm as a slight HREE increase, as observed for the experimental REE patterns (Figure III.1.8A). Log K patterns for chelates formed between REE and dicarboxylic (oxalate, diethyl malonate, etc.) or hydroxycarboxylic ligands (i.e., lactate, hydroxybutanoate) exhibit an enrichment from La to Lu (Figure III.1.8B) but no significant MREE downward concavity by contrast with the experimental REE-NPs patterns, avoiding the potential formation of chelate complexes between REE and all NPs models. Experimental REE patterns were thus only compared to the REE patterns of 1:1, 1:2, and 1:3 REE-COOH ligands, namely acetate and propionate. However, as previously shown from the experimental datasets,

state on a potential HREE increase/decrease on the REE patterns is not trivial regarding the variation of the MREE downward concavity. The same remark can be made for the REE-acetate and REE-propionate patterns. To counter this effect, the REE patterns were normalized to the MREE downward concavity as:

$$N_{\text{MREEDC REE}} = \log(\text{REE}/\text{La}) / \log(\text{Sm}/\text{La}) \quad (\text{III.1.2})$$

This normalization (N_{MREEDC}) allowed us to observe an increase of the HREE compared to the other REE with the ligand numbers on the REE patterns (Figure III.1.8D).

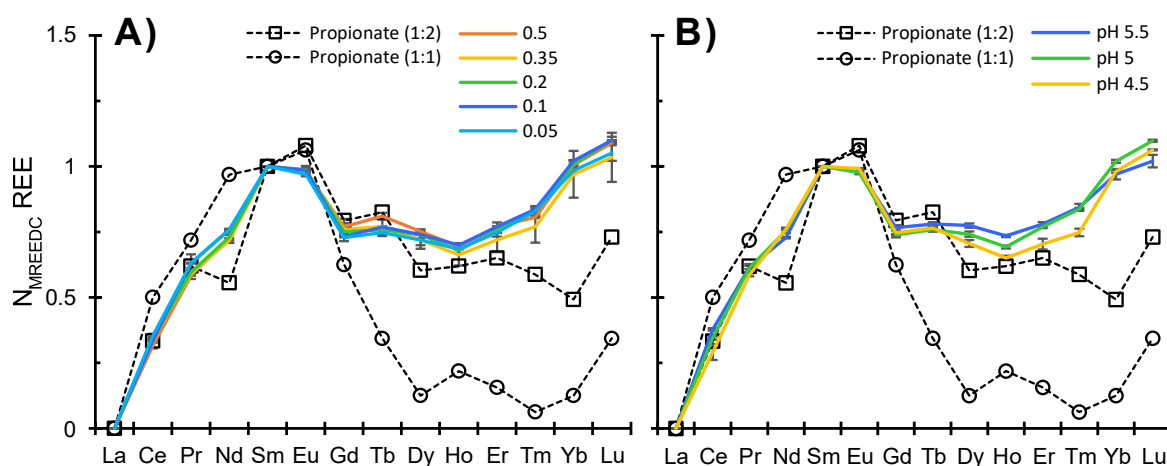


Figure III.1.9. Comparison of REE- $\text{PSL}_{\text{surfactant}}$ patterns normalized to the MREE downward concavity (A) relative to the REE/NPs ratios and (B) relative to pH with the 1:1 and 1:3 REE-propionate complexes patterns normalized to the MREE downward concavity. Error bars correspond to the SD of the triplicates.

For $\text{PSL}_{\text{surfactant}}$, the N_{MREEDC} normalized REE patterns did not evolve with the REE/NPs ratios or pH (Figure III.1.9). Moreover, experimental REE patterns were close in shape to that of the REE-Propionate 1:2 complex suggesting the formation of bi-ligand complexes between REE and 2 $-\text{COOH}$ surface sites of the $\text{PSL}_{\text{surfactant}}$. This bi-ligand complex predominated as no significant variations of the HREE adsorption were observed.

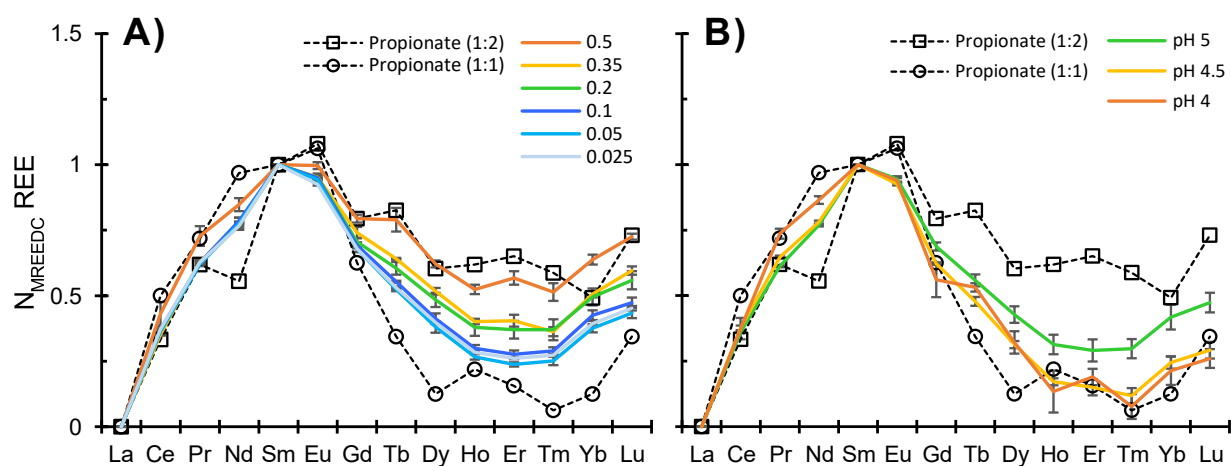


Figure III.1.10. Comparison of REE-PSL_{free} patterns normalized to the MREE downward concavity (A) relative to the REE/NPs ratios and (B) relative to pH with the 1:1 and 1:3 REE-propionate complexes patterns normalized to the MREE downward concavity. Error bars correspond to the SD of the triplicates.

For the PSL_{free}, the N_{MREEDC} REE patterns exhibited an increase of HREE with the REE/NPs ratios up to 0.5 mg g⁻¹C (Figure III.1.10A). The N_{MREEDC} REE patterns were comprised between the 1:1 and 1.2 REE-propionate complexes, suggesting an evolution of the binding number and the complexes formed between HREE and PSL_{free}. A simple comparison of the normalized patterns suggested that mono-ligand complexes were formed at low REE/NPs ratios (low REE loading) although the high availability of the binding site. By contrast, bi-ligand complexes were formed at high REE/NPs ratios (high REE loading) although with lower availability of the binding site. Relative to the pH, normalized REE patterns showed that the pH increases also promoted the formation of bi-ligand complexes in response to the deprotonated sites' increasing availability. Both results were incoherent and antagonist. Variations of the REE pattern did not correspond to an HREE adsorption increase but an LREE adsorption decrease (Figure III.1.6A and B). At high REE/NPs ratios, adsorption isotherms and REE patterns showed that competition with Y, U, Sc, and Th was more pronounced for LREE than for HREE (Figure III.1.6A and B). Detailed observation of the REE patterns variation with the REE/NPs ratio clearly showed an LREE decrease at high REE/NPs ratios (Figure III.1.6B). Therefore, the REE pattern variation can be interpreted as forming strong bi-ligand complexes for HREE that limit competition. At the same time, LREE formed weak mono-ligand complexes unable to maintain the LREE at the PSL_{free} surface. This process can be observed here because of the low site density of the PSL_{free} and the resulting competition with Y, U, Sc, and Th.

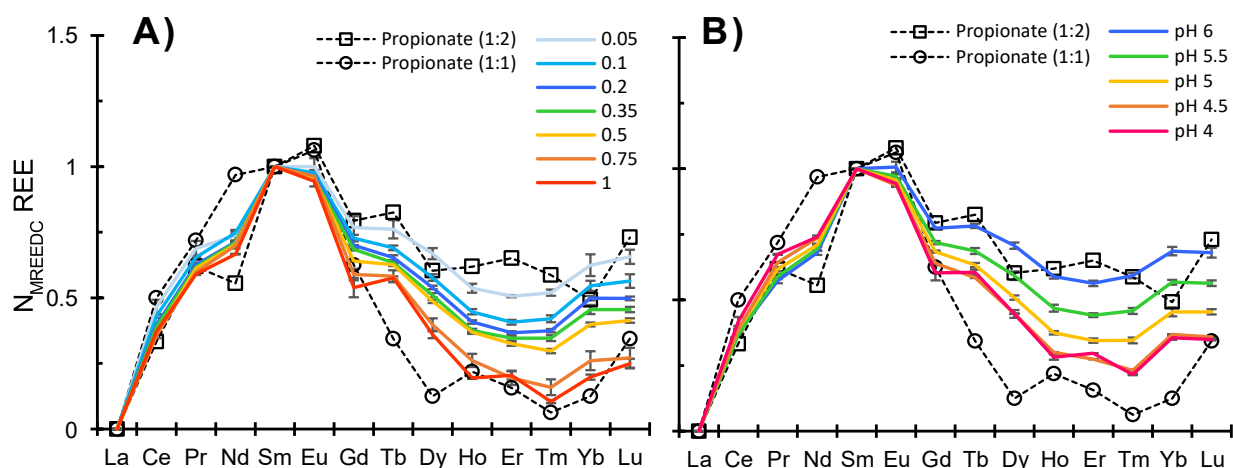


Figure III.1.11. Comparison of REE-e-NPs patterns normalized to the MREE downward concavity (A) relative to the REE/NPs ratios and (B) relative to pH with the 1:1 and 1:3 REE-propionate complexes patterns normalized to the MREE downward concavity. Error bars correspond to the SD of the triplicates.

For the e-NPs, the N_{MREEDC} REE patterns showed a decrease with the increasing REE/NPs ratios (Figure III.1.11A), highlighting the complexes' denticity evolution. These REE pattern variations showed that bi-ligand complexes were formed at low REE/NPs ratios (low loading). In contrast, they formed mono-ligands complexes at high REE/NPs ratios (high loading), as previously observed by Marsac et al., 2010, for humic acid. Between pH 5 and 6, REE pattern variations demonstrated that more bi-ligand complexes occurred in coherence with the increasing number of ionized sites at the e-NPs. However, the N_{MREEDC} REE patterns did not evolve between pH 4 and 4.5, suggesting that bi-ligand complexes' contribution was insignificant under pH 4.

To summarize, REE adsorption onto NPs is driven by their binding to carboxylic sites present or developed at the NPs surface (Figure III.1.9. and III.1.11). The REE pattern variations could be attributed to the complex denticity. A MREE downward concavity was developed for all REE patterns, excluding the formation of chelate complexes at the NPs surface. Rare earth elements are bound as REE-COOH mono and bi-ligand complexes. The low site density of the PSL free combined with the resulting intense competition with Y, U, Sc, and Th, highlight that LREE forms a weaker mono-ligand complex while HREE forms stronger bi-ligand complexes. The mono-ligand complexes dominated all REE at high REE/NPs and low pH (low availability of the binding sites). In contrast, the bi-ligand complexes dominated HREE at low REE/NPs and high pH (high availability of the binding sites). These results are in

concordance with Marsac et al. (Marsac et al., 2010, 2011, 2012, 2013) for REE binding with humic acid.

III.1.3.6. Implications for environmental NPs behavior

The present result demonstrates that REEs are bound onto the NPs surface via COOH groups. These surface sites are present onto PSLs because of their production protocol and onto e-NPs by their degradation route (photo-oxidation) under environmental conditions. The REE binding to NPs appeared strongly dependent on pH. The natural water pH is ranged from 6 to 9 (Mattson, 1999; Jiang et al., 2019) and the pKa of the COOH group varies between 4 and 5.5 (Martell and Smith, 1977). Therefore, COOH groups are deprotonated and strongly available for metal binding under natural conditions. The REE complexes formed at the surface of e-NPs could vary between monodentate and bidentate complexes relative to the REE and the REE/e-NPs ratio and pH. For $\text{pH} > 4.5$ and low REE/e-NPs ratio, as under environmental conditions, REE are mainly bound to e-NPs as bi-ligands complexes, notably HREE. The stability constant of bi-ligands complexes is higher than mono-ligand complexes indicating that e-NPs can strongly adsorb REE and mainly HREE from the environment. Contrary to the formation of bi-ligands, results showed that chelate could not be formed on the e-NPs surface with REE, probably due to geometric constraints (low flexibility of the e-NPs structure, distances between –COOH groups) and site density. Therefore, it can be extrapolated that REEs act as cationic bridges between 2 e-NPs and thus influence the homo-aggregation of e-NPs (Figure III.1.12) at high pH and REE/e-NPs ratios. Further study has to be performed to confirm such aggregation that can confirm the presence of bi-ligands complexes.

Moreover, once adsorbed onto e-NPs, REE (and more generally metals) can penetrate living organisms. The prevailing pH conditions and as previously observed for PSL_{surfactants} (Abdolahpur Monikh et al., 2021), can be released into the living organisms following a Trojan horse effect. However, this release will be controlled by the strength of the complexes. For REE, the present results clearly show that LREE (domination of mono-ligands complexes) will be more released than HREE (bi-ligands complexes).

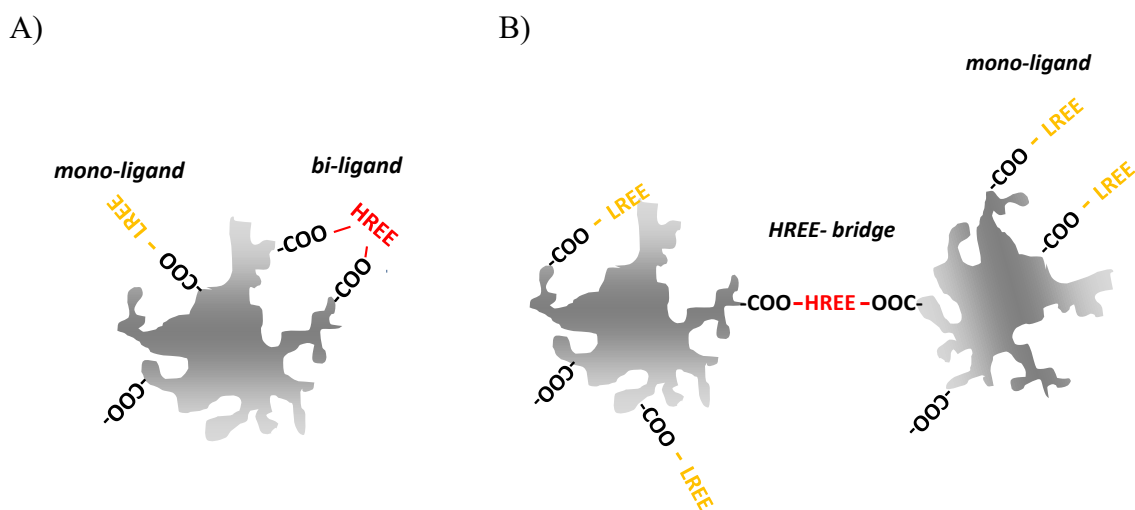


Figure III.1.12. Possible complexes formed between LREE, HREE, and e-NPs, A) simple HREE Bi-ligand complex onto 1 e-NPs and B) HREE bi-ligand complex between 2 e-NPs acting as a cationic bridge and potentially resulting in e-NPs homo-aggregation.

III.1.4. Conclusions

Rare-earth element adsorption experiments were carried out to investigate trace metal-NPs interactions. For the studied NPs models, an MREE downward concavity was developed on the REE-NPs binding patterns corresponding to the sorption of REE onto -COOH groups. Under environmental conditions, -COOH sites are produced in response to the photo-oxidation of the plastics debris. A detailed study of the adsorption isotherm and REE patterns variations with the REE/NPs ratios and pH combined to the competition between REE and other ions demonstrated that LREE were mainly bound as mono-ligands complexes. At the same time, HREE specifically formed bi-ligands complexes with NPs. The binding sites ' availability influences the proportion of mono and bi-ligands, influenced by the pH and the REE/NPS ratio. Under environmental conditions (pH >4.5 and low REE concentrations), bi-ligands complexes are thus expected to be dominant, notably for HREE. These results provide exciting information and constraint, valuable for further investigations, notably the thermodynamic modeling of metal-NPs binding mechanisms.

III.2. Modélisation thermodynamique de la sorption de Pb(II)

Résumé

Bien que la présence des NPs dans l'environnement soit attestée, peu d'études se consacrent à déterminer leurs interactions avec les métaux. Cependant, avant d'être en mesure de connaître leurs associations possibles dans l'environnement, il est crucial de décrire les mécanismes de sorption dans des environnements contrôlés et pour des modèles de NPs pertinents. Récemment, nous avons développé un modèle représentatif des NPs environnementaux, permettant d'étudier les interactions métaux-NPs. Grâce à des expérimentations de sorption entre le Pb(II) et ces NPs, nous avons développé un modèle de sorption qui décrit leurs interactions ainsi que leurs capacités maximales de sorption. Parmi les différents scénarios de sorption testés, les résultats suggèrent que le Pb s'adsorbe à la surface des NPs via des sites carboxyliques en formant des complexes monodentés. L'extrapolation des constantes de stabilité ainsi que les hypothèses de sorption retenues ont pu être validées à l'aide d'une relation linéaire d'énergie libre. Les capacités d'adsorption des NPs sont dépendantes de leur état d'oxydation, qui contrôle leur densité de site carboxylique. L'affinité forte des NPs envers les métaux suggère qu'ils peuvent être des vecteurs de métaux, ce qui augmente le risque environnemental concernant les deux parties, plastiques et métaux.

Abstract

While NPs in the environment are now admitted, relatively very few data exist on their interactions with trace metals. Before evaluating this possible association in the real environment, it is crucial to understand the processes in such interaction in a reliable environment with a representative model. Recently, we developed an environmental NPs models offering new opportunities to study metal-NPs interaction. Using Pb(II) and these news NPs models as proxies for adsorption experiments, we developed a sorption model to describe surface complexation as well as predict relevant NPs sorption capacities. Modeling hypotheses suggested that Pb is adsorbed onto NPs through carboxylic sites, mainly as monodentate complexes. Linear free energy relation validates the extrapolated stability constants and binding hypothesis. Nanoplastics' adsorption capacities are dependent on their oxidation state, which controls their carboxylic sites density and subsequent metal adsorption capacity. This strong affinity metal-NPs suggested that NPs could act as vectors of metals, increasing the environmental risk exposure concerning both plastics and metals.

III.2.1. Introduction

Plastic pollution is one of the significant challenges of the Anthropocene. Plastics benefit society in innumerable ways, and their production has drastically increased over the last century. This has resulted in a dramatic generation of plastic wastes in the world. Moreover, their alteration in the environment, mainly by photo-oxidation and abrasion (Lambert et al., 2013; da Costa et al., 2016; Dawson et al., 2018; Meides et al., 2021) produces NPs (Ter Halle et al., 2017; Materić et al., 2020; Wahl et al., 2021). Nanoplastics are particles < 1000 nm with open and heterogeneous shapes, non-homogeneous charged surfaces, and behaving as colloids (Gigault et al., 2018). Nanoplastics are thus potentially highly reactive, especially to trace metals, and can potentially control their speciation (Davranche et al., 2019; Gigault et al., 2021). Moreover, NPs, like colloids, are mobile and can therefore control the transport of associated metals. The interactions of metals with NPs could also increase metal bioavailability. Nanoplastics ingested by organisms could release their related micropollutants according to the physicochemical conditions (Chen et al., 2017; Jiang et al., 2019). Metal binding by NPs could thus be a critical process for their (eco)toxicological risk assessment.

However, there is a lack of information on the mechanisms that control the NPs micropollutants binding, notably for metals. While detecting NPs at ultra-trace level is highly challenging, collecting NPs and detecting trace metals associated with the NPs or collected is even more complex. Therefore, one relevant strategy is to produce NPs models that mimic the physical and chemical features of the NPs observed and detected in some environments. Three preparation methodologies are proposed : controlled emulsion-polymerization of spherical nanoparticles with or without functionalized surface (Mitrano et al., 2019; Pessoni et al., 2019); mechanical degradation of pristine polymer pellets resulting in NPs with heterogeneous shape and functional surface sites (Magri et al., 2018; El Hadri et al., 2020); mechanical abrasion of highly altered plastics debris sampled in the environment, resulting in NPs with heterogeneous shape and functional surface sites (Blancho et al., 2021a).

While the first NPs model is interesting for instrumental calibration because of their controlled size, shape, and binding sites density (Pessoni et al., 2019; Mitrano et al., 2019), these models are not environmentally relevant, notably in shape and size-polydispersity (Gigault et al., 2021). By contrast, NPs produced by mechanical degradation (polymer pellets and altered plastics debris), are polydispersed in size with heterogeneous and open shapes as observed for environmental NPs (Gigault et al., 2018; El Hadri et al., 2020; Blanco et al., 2021a). However, there are significant differences between NPs produced from polymer pellets

and plastic debris since they are not submitted to surface photo-oxidation, which could strongly influence their site density and thus their trace metal reactivity. Finally, for the first method, surfactants and initiators are used for the production and colloidal stability. Their presence could also strongly influence the produced NPs models' properties and behavior (e.g., SDS, KPS, etc.) (Pikuda et al., 2018).

Recently, the possibility of environmentally relevant models (e-NPs) to bind metal (Pb) via surface complexation and intraparticle diffusion has been demonstrated (Davranche et al., 2019). While the NPs-metals interaction is still under-investigated, data on microplastics have recently been published. Brennecke et al. (2016) showed that Cu and Zn released from antifouling paint were adsorbed by PS pellets and in higher concentration by polyvinyl chloride (PVC) pellets. Turner and Holmes (2015) demonstrated that MPs adsorb metals relative to pH and that altered polymer pellets, collected on beaches, have higher metal affinity than virgin pellets. They explained these results by altering the surface that produced functional sites or the presence of organic materials. Tang et al. (2021) from nylon MPs collected from the environment showed surface complexation and intraparticle diffusion-controlled Ni, Cu, and Zn adsorption onto MPs. They also highlighted the importance of the O-containing group in controlling the adsorption of metals. Recently artificial neural networks calculations suggested that aged MPs have a higher affinity for metals than virgin MPs and that the sorption capacity depends on the initial metal concentrations.

Interestingly, the model also predicted that the sorption capacity of Cd, Pb, and Zn by MPs was higher in the river than in the ocean in response to its salinity (Guo and Wang, 2021). Regarding their nanosized and colloidal behavior, all these results cannot be however extrapolated for NPs. For example, minerals and biofilms are not expected to be formed at their surface. Nevertheless, the impact of the alteration and the role of surface O-containing groups can be considered reliable for NPs. Thus, using rare earth elements (REE) as a mechanism probe, Blancho et al., (Submitted) demonstrated that metal cations are bound to NPs (PSL or environmentally relevant NPs models) via surface carboxylic sites. For environmentally relevant NPs models, these –COOH sites, as O-containing groups, are developed subsequently to their photo-oxidation. Plastic photo-oxidation produces free radicals, initiating and propagating reactions. Their termination incorporates oxygenated function (Rånby and Rabek, 1989; Rabek, 1995) at the surface of the plastics.

If –COOH binding sites seem to control the metal sorption onto MPs and NPs. The sorption mechanism is not fully understood. More importantly, the key parameters are not identified and quantified. Consequently, it is currently not possible to predict metal flow

transfer by NPs in the environment. However, a recent study from Blancho et al., (Submitted) suggested that trivalent metals, namely REE, formed mono and multidentate complexes with the –COOH sites of various NPs models (PSL nano-beads and environmentally-relevant models) relative to the REE loading. Such information can help design an NPs surface complexation model by constraining binding scenarios. Geochemical modeling can be viewed as a predictive way to estimate speciation or test mechanistic hypotheses.

Therefore, this work aims to characterize and quantify the adsorption mechanisms between lead (Pb) and various NPs models. For this purpose, we established experimental datasets from adsorption experiments under different physicochemical conditions (concentration, pH). Finally, the datasets were used to test various binding scenarios and extrapolate sorption parameters. The model was finally validated using experimental datasets from the literature.

III.2.2. Materials and methods

III.2.2.1. NPs properties

The used NPs models are : (i) carboxylated PS Latex nanoparticle of 200 nm size and conditioned with surfactants, named PSL_{surfactant} (Polysciences); (ii) “free soap” carboxylated PS Latex nanoparticle of 380 nm size, PSL_{free}, the PS9 from Pessoni et al. (2019) (iii) polymorph and polysized nanoparticles produced from the milling of PS pellets, m-NPs, following the protocol of El Hadri et al. (2020) and (iv) plastics nanoparticles produced from the altered layer of plastics debris collected in the environment, e-NPs, as described in Blancho et al. (2021).

The hydrodynamic radius (Hr) of the NPs was determined using Dynamic Light Scattering (DLS) (VASCO Flex's, Cordouan Technologies) for suspensions at 10 ppm without Ionic Strength (IS). The shape of NPs was examined by transmission electronic microscopy (TEM) (JEM 2100 HR, Jeol). Transmission electronic microscopy was operated at 200-kV acceleration voltage with a LaB₆ as electron source, the point and line resolution are of 2.3 Å and 1.4 Å, respectively. Particles were photographed with a Gatan Orius SC200D camera, and elemental analysis was performed using an EDX Oxford X-Max 80T detector. The specific surface area (SSA) of NPs was determined by the BET method (Brunnauer Emmet and Teller) for e-NPs and m-NPs while extrapolated from the particle diameter for PSLs (Table III.2.1). The BET analysis was carried out with a Gemini VII instrument (Micromeritics).

The surface charge was assessed by potentiometric titration using a Titration unit controlled by the Tiamo software (Metrohm). All solutions were titrated with 0.01 M NaOH (Honeywell Fluka), under a N₂ flux. Prior titration, the pH probe was calibrated on a concentration scale using 1mM HNO₃. Titration were performed at 10, 100 and 1000 mM of NaNO₃ as IS and started below pH 4 by adding a fixed volume of 100mM HNO₃. The determination of the protonable groups was performed as describe by Spadini et al. (2018). Briefly, the proton released from the surface, H_{surf}, was related to the pH of the solution (Eq. III.2.1). The total surface site concentration H_{tot}, was defined as the released H_{surf} between pH 4 and 8.0 for the highest IS. Due to early site deprotonation, there is an initial charge at the NPs surface, noted H₀. This H₀ is IS dependent and was estimated by modeling calculations. This calculated H₀ was thus added to H_{surf}. The CO₂ diffusion during the titration was taken in account using the H_{tot} of the ultrapure water (Blank).

$$[H^+] = [H_{init}] + [H_{base}] + [H_{surf}] + [OH^-] \quad (III.2.1)$$

With, [H⁺], the free proton concentration, (M), [H_{init}], the concentration of acid added to fix the pH below pH 4 (M), [H_{base}], the concentration of base added during the titration (M), positive when base is used and negative when acid is used, [H_{surf}], the concentration of the released H⁺, the only unknown (M) and [OH⁻], the concentration of the H⁺ released from the water auto-protolyze, at pH 7 (M).

III.2.2.2. Adsorption experiments

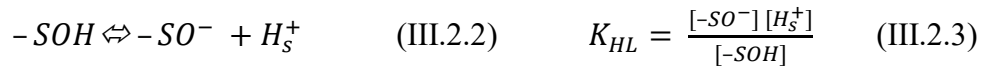
Adsorption isotherms were carried out for Pb(II)/NPs ratios between 0.5 and 100 mg.g⁻¹ of carbon. The concentration of NPs was fixed at 50 and 25 mg L⁻¹ for the PSLs, and e-NPs and m-NPs, respectively. Note that the concentration of NPs is in gC L⁻¹. Mass concentration was preferred rather than particle number as it can be directly measured. The ionic strength was fixed with 5 mmol L⁻¹ of NaNO₃. After adding Pb(II) to NPs suspensions, the pH was adjusted to 5.5 with HNO₃ and NaOH at various molarities. The equilibrium time was estimated at 2 and 10 h from previous kinetic experiments for PSLs, and e-NPs and m-NPs, respectively. At equilibrium, suspensions were filtered at 0.2µm (filter syringe, PES, Sartorius) for the PSLs and 30 kD (filtration cell, PES, Sartorius) for the e-NPs and m-NPs. After filtration, all samples were acidified at 2% HNO₃ for the ICPMS analysis. The pH-adsorption edge experiments were performed with Pb(II) concentration at 2.5 and 25 mg g⁻¹C for the PSLs, and e-NPs and m-NPs, respectively. The pH range was investigated from 2 to 7 using HNO₃ or NaOH.

III.2.2.3. Chemical Analysis

Lead concentrations were measured with a Quadrupole ICP-MS (Agilent Technologies 7700X). Calibration curves were performed and validated using certified material references (SLRS-6, National Research Council). A rhodium solution was used as an internal standard to correct the instrumental drift and potential matrix effects. The limit of Pb quantification was determined at 0.0038 ppb. Moreover, as the upper limit of the Pb(II) calibration curve was 5 ppb, samples were diluted if necessary. The NPs concentrations were monitored with the carbon concentration using a Total Organic Carbon (TOC) analyzer (TOC-V Shimadzu).

III.2.2.4. Modeling

The modeling approach used the extrapolations of the experimental datasets based on a combination of geochemical (PHREEQC version 2) and extrapolation (PhreePlot) programs (Parkhurst and Appelo, 1999; Kinniburgh and Cooper, 2011). PhreePlot was designed to fit experimental datasets using the speciation program PHREEQC. The model combination was used to extrapolate the intrinsic acidity (pK_a) and stability ($\log K$) constants. The binding parameters are optimized by a modified Marquardt-Levenberg procedure (Powell, 1965). The surface charge of the NPs was conceptualized as resulting from the ionizable surface groups (i.e., OH, $-\text{COOH}$, etc.), overall represented as $-\text{SOH}$. Their dissociation was defined as conforming to the mass-action law:



The permanent charge due to lattice defect was neglected for PSL, as latex, and not considered e-NPs and m-NPs as amorphous. As a result, the total net particle charge, σ_P , is restricted to equation III.2.4.

$$\sigma_P = \sigma_H + \sigma_{IS} \quad (\text{III.2.4})$$

with σ_H , charge involved by the H^+ association/dissociation on ionizable groups and σ_{IS} , the charge of inner-sphere complex.

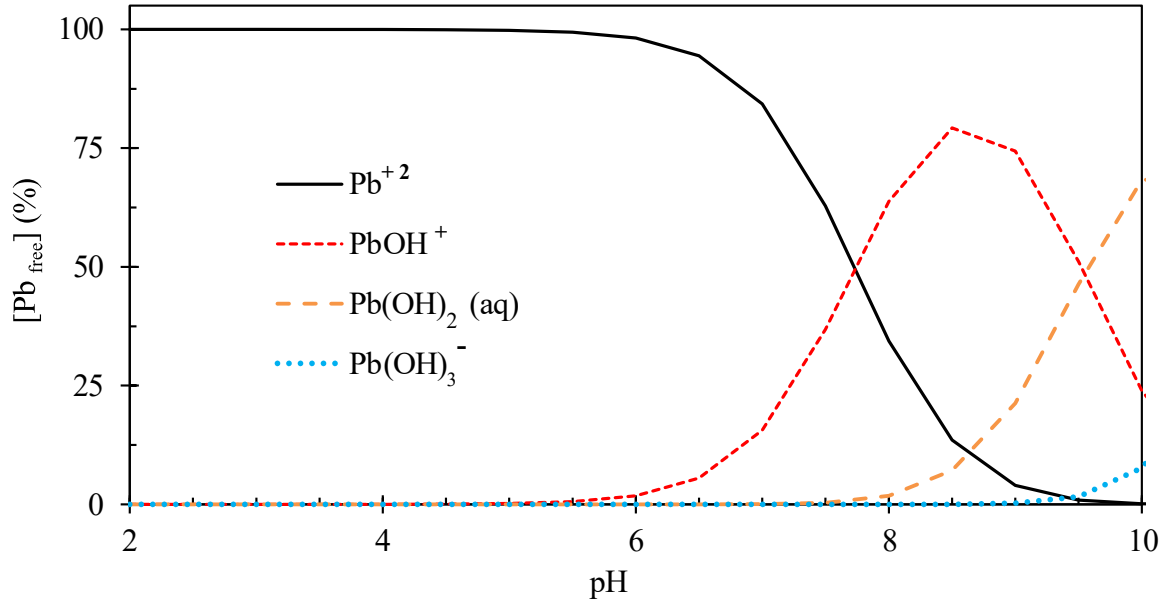
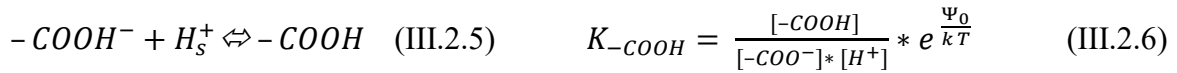


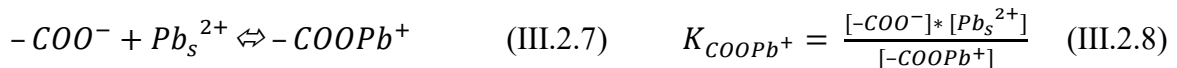
Figure III.2.1. Pb(II) speciation function of pH.

The electrostatic energy term (i.e., coulombic interaction) was considered using a Diffuse Layer Model (DLM). Blancho et al. (Submitted) demonstrated that the sorption of trivalent cations was driven by $-\text{COOH}$ on both PSLs and e-NPs models. As a result, for all NPs, the surface charge is explained and restricted to the presence of $-\text{COOH}$ sites (Eq. III.2.5).

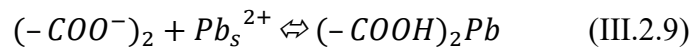


With Ψ_0 , the surface potential energy (J), k , Boltzman constant (J K^{-1}) and T , Temperature (K).

The Pb(II) adsorption onto NPs models is restricted to ionic Pb^{2+} . The dominant species in the studied pH range (Figure III.2.1). Blancho et al. (Submitted) demonstrated that trivalent cations form monodentate and bidentate complexes with $-\text{COOH}$ at the NPs surface. For this reason, the Pb sorption was modeled under two scenarios based on different sorption hypotheses. The first scenario explains the Pb sorption by monodentate complex only (Eq. III.2.7) and the second by both monodentate and bidentate complexes (Eq. III.2.7 and III.2.9). The best scenario was selected based on RMSE values.



To constraint the model, the $\log K_{\text{COO}_2\text{Pb}^+}$ are related to $\log K_{\text{COOPb}^+}$ as described in model VI (Eq. III.2.8) (Tipping, 2002).



$$K_{\text{COO}_2\text{Pb}} = \frac{[(-\text{COO}^-)_2] * [\text{Pb}_s^{2+}]}{[-\text{COO}_2\text{Pb}]} = (K_{\text{COOPb}^+})^2 \quad (\text{III.2.10})$$

Table III.2.1. NPs properties and characteristics

NPs	rH (nm)	SSA (m ² g ⁻¹)	Hs ^{tot} (mmol g ⁻¹)	Site density (site nm ⁻²)	pKa *	RMSE **
PSL _{surfactant}	200 ± 20	28.84	0.316 ± 2e ⁻³	6.60	4.60 ± 0.01	3.2e ⁻⁵
PSL _{free}	380 ± 20	15.18	0.086 ± 2e ⁻³	3.41	4.07 ± 0.02	1.7e ⁻⁵
e-NPS	226 ± 36 354 ± 75	12.5	≥ 0.282 ± 4e ⁻⁴	≥ 13.6	4.76*	-
m-NPS	175 ± 36 452 ± 80	28.85	≥ 0.037 ± 1e ⁻⁴	≥ 1.19	4.76*	-

*, fixed to the acetate pKa (Martell and Smith, 1977).

** , RMSE calculated from the pKa extrapolation.

Table III.2.1 summarizes the used DLM parameters. According to the DLM and for pH 5.5, the maximum Pb(II) adsorption capacity, $Q_{\max \text{ Pb}}$ (mg g⁻¹C), was selected once the isotherm plateau was reached, namely when $\Delta[\text{Pb}]_{\text{ads}}$, did not excess 1% for a $\Delta[\text{Pb}]_{\text{free}}$ set to 10% (Eq. III.2.11).

$$\Delta P b_{\text{ads}} = \frac{[P b_{\text{ads}}(P b_{\text{free}} * 1.1) - P b_{\text{ads}}(P b_{\text{free}})]}{P b_{\text{ads}}(P b_{\text{free}} * 1.1)} * 100 \quad (\text{III.2.11})$$

III.2.3. Results and Discussion

III.2.3.1. Nanoplastics characterization

Both log-transformed slopes of the autocorrelation function (ACF) were to <900 nm, Hr of the CMRs standard (Blue line, Figure III.2.2A). The log-transformed ACF were not straight compare to CMRs indicating polymodal suspensions which is coherent with the bimodal distribution proposed by the Sparse Bayesian Learning, SBL, based-modeling of the ACF (Figure III.2.2B). The first and second population size were particles with an average hydrodynamic radius of 226 ± 36 and 376 ± 64 nm for the e-NPs, and 179 ± 36 and 452 ± 80 nm for the m-NPs. The TEM observations showed anisotropic NPs (Figure III.2.2C), in coherence with previous studies of Blancho et al. (2021) and El Hadri et al. (2020).

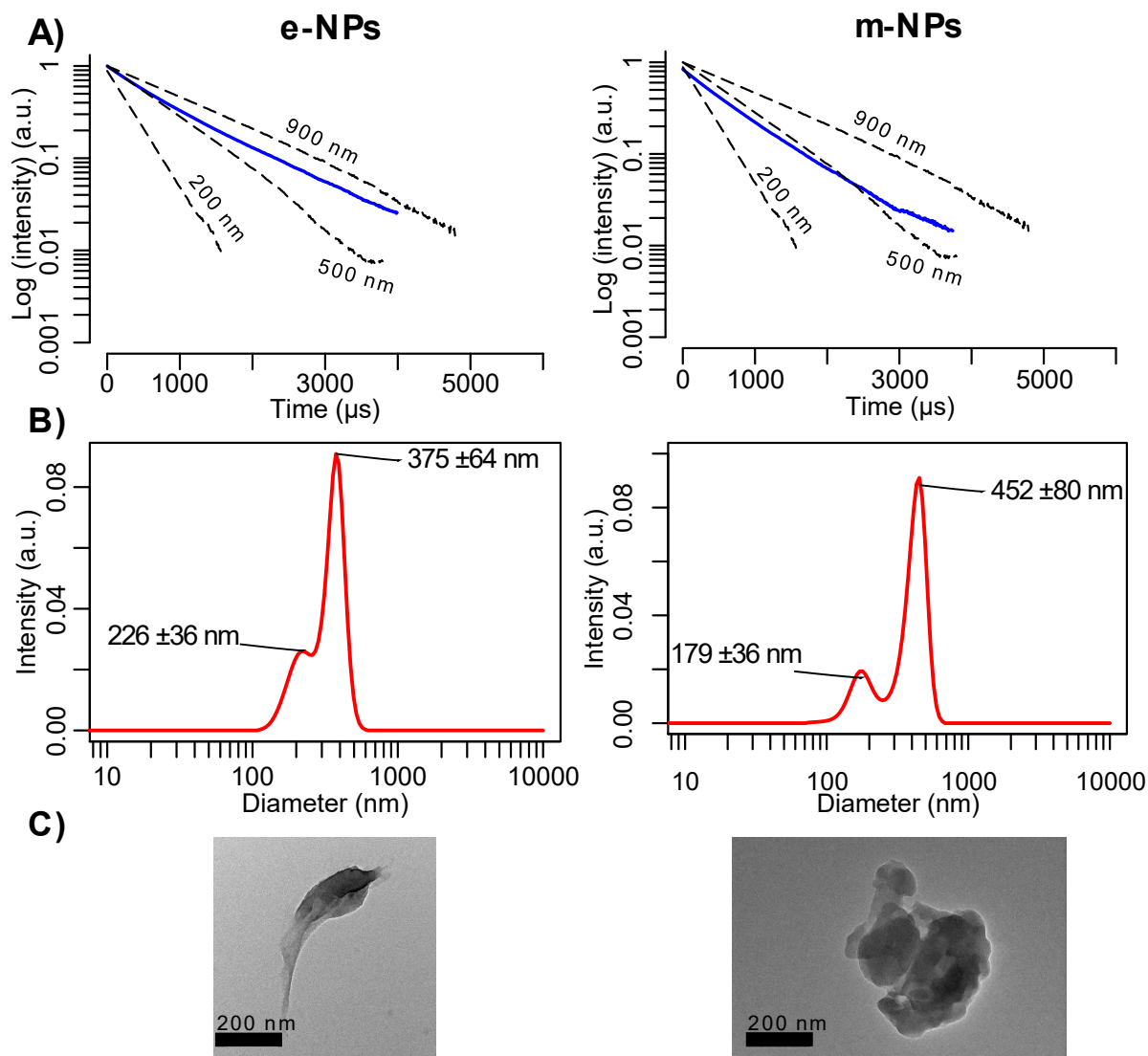


Figure III.2.2. Size characterization of e-NPs and m-NPs models. A) Log-transformed time-ACF of the intensity of light scattered compare to CMRs standards. B) Population size from SBL modeling. C) TEM pictures from the suspensions.

For PSLs, DLS indicated, as expected, a monodisperse suspension (i.e. straight Log-transformed ACF) (Figure III.1.1). As a result, no uncontrolled aggregation occurred. Their Hr was described as equal to 200 nm for the PSL_{surfactant} (NIST CMRs) and 380 nm for the PSL_{free} (Pessoni et al., 2019).

III.2.3.2. Surface charge modeling and pKa extrapolation

The NPs surface charge was determined by calculation using PHREEQC implemented by the SIT thermodynamic database. Potentiometric titrations allowed to determine the amount of ionizable function relative to the pH onto PSL surface. In Figure III.2.3 was plotted the

Hs(pH) evolution corrected from H_0 (pH 4) at three IS for PSLs, e-NPs and m-NPs. As expected, the dissociation of the surface group increased with the increasing pH (Eq. III.2.6). The IS promoted the deprotonation of surface group by decreasing the diffuse layer length and thus shielding the electrostatic impact of Ψ_0 (Pfeiffer et al., 2014). Titrations at 1M IS showed a typical sigmoidal curve (Chen et al., 2021; Connors, 1990). These titration curve indicates that the whole ionizable group was dissociated between pH 4 and 8. The total surface ionizable group, Hs_{tot} , was considered to be equal to the concentration of the deprotonated group at pH 8, as a plateau was reached for both PSLs. The Hs_{tot} was determined equal to $0.316 \pm 2 \cdot 10^{-3}$ and $0.086 \pm 2 \cdot 10^{-3} \text{ mmol g}^{-1}$ for the PSL_{surfactant} and PSL_{free}, respectively. According to the SSA, the site density was 6.60 and 3.41 sites nm^{-2} for PSL_{surfactant} and PSL_{free}, respectively. The Hs_{tot} and site density are higher for PSL_{surfactant}.

The extrapolation of the datasets using PHREEQC (DLM model) allowed to calculate intrinsic pKa values for PSL models (Table III.2.1). Calculated pKa for both PSL are closed to the pKa of acetate, $pK_a = 4.76$ (Martell and Smith, 1977). The acid used by Pessoni et al. (2018) for polymerization was the acrylic acid. Lützenkirchen et al. (2011), determined a pKa for poly(acrylic acid) of 4.05 with a DLM which is coherent with the extrapolated pKa of the PSL_{free}. The acid used during polymerization of PSL_{surfactant} was not precise. However, acid containing a long radical, such as methacrylic acid, could explain the different pKa between both PSL (De Stefano et al., 2000; Ibarra-Montaña et al., 2015).

For e-NPs and m-NPS, the 1M titration curves were not sigmoidal and showed the same increase after pH 7.5 (Figure III.2.3) avoiding the Hs_{tot} determination (no plateau was reached). However, the total concentration of surface site could be estimated (value obtained for the highest, ≈ 8.5) as $\geq 0.282 \pm 4 \cdot 10^{-4}$ and $\geq 0.037 \pm 1 \cdot 10^{-4} \text{ mmol g}^{-1}$ for e-NPs and m-NPs, respectively. The suspension concentration for titration were > 5 and 8 g L^{-1} for e-NPs and m-NPs respectively. At pH titration < 4 , strong aggregation was observed for e-NPs and m-NPs while no aggregation occurred for PSLs. Hesleitner et al. (1987) demonstrated that for titrations, aggregation induces a delay in the H^+ dissociation from the surface sites preventing the pKa determination. Therefore, the pKa for e-NPs and m-NPs were fixed to the $pK_{a \text{ acetate}}$ of 4.76 (Martell and Smith, 1977).

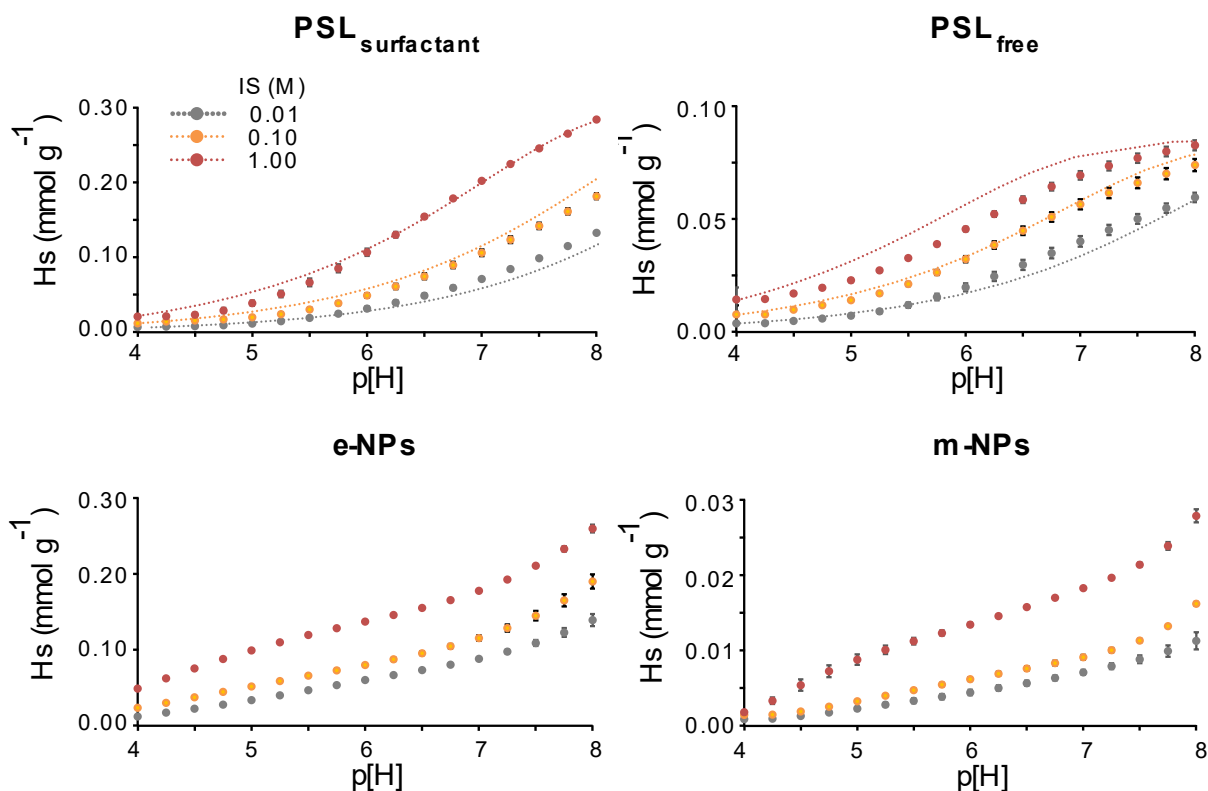


Figure III.2.3. Evolution of the Hs with the pH for both PSLs, e-NPs and m-NPs at 3 IS: 0.01, 0.10, 1.00 M. Symbols correspond to experimental data and dotted lines to calculated data.

III.2.3.3. Pb(II) adsorption by NPs

Experimental and calculated Pb(II) adsorption isotherms and pH-adsorption edge were plotted in Figure III.2.4. Adsorption isotherms were concave, suggesting a progressive saturation of the binding sites (Figure III.2.4A). However, no plateau appeared, suggesting that site saturation wasn't reached or the multilayer or heterogeneous process controlled the adsorption. Significant adsorption capacity variations were obtained between PSLs. For $[\text{Pb}]_{\text{free}} = 2\text{ ppm}$, $[\text{Pb}]_{\text{ads}}$ was ≈ 15 and $1.5\text{ mg g}^{-1}\text{C}$ for $\text{PSL}_{\text{surfactant}}$ and PSL_{free} , respectively. This difference is consistent with the $-\text{COOH}$ sites density (Table III.2.1). For PSLs, Pb(II) adsorption increased with pH. Less than 5 % of $[\text{Pb}]_{\text{tot}}$ was adsorbed at $\text{pH} \leq 4$ against 85 % at $\text{pH} \geq 7$ (Figure III.2.4B). For e-NPs and m-NPs, at $[\text{Pb}]_{\text{free}} = 0.4\text{ ppm}$, $[\text{Pb}]_{\text{ads}}$ were ≈ 7.5 and $2.25\text{ mg g}^{-1}\text{C}$, respectively (Figure III.2.4A). These adsorbed concentrations were coherent with the total ionizable sites density, H_{stot} (Table III.2.1). The adsorption was also strongly dependant on pH. Less than 15 % of $[\text{Pb}]_{\text{tot}}$ was adsorbed for $\text{pH} \leq 4$ against 90 % at pH 7. The

pH-dependence of the adsorbed concentration highlights the competition between H^+ and $Pb(II)$ for their adsorption onto NPs surfaces (Table III.2.1).

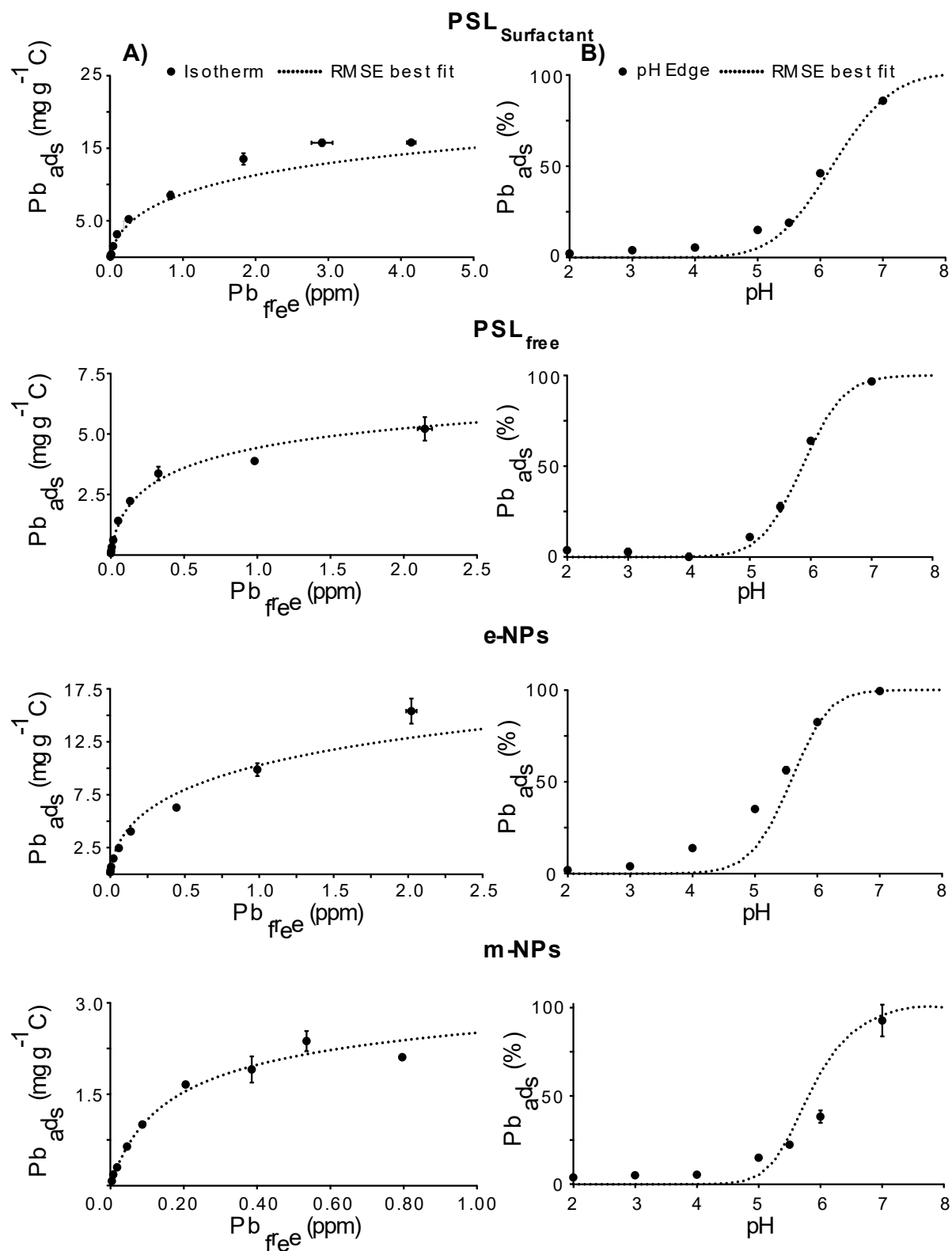


Figure III.2.4. Evolution of the experimental (black points) and calculated (dotted lines) concentrations of adsorbed $Pb(II)$ by NPs, (A) adsorption isotherms, and (B) pH adsorption edges.

III.2.3.4. Pb(II) adsorption modeling

Two scenarios were tested 1) formation of monodentate and 2) formation of both monodentate and bidentate complexes as suggested in Blancho et al. (Submitted). For PSLs and e-NPs, the calculated root-mean-square error (RMSE) was lower for the monodentate model, LM (Table III.2.2). The calculated $\log K_{\text{COOPb}^+}$ were 2.33 ± 0.09 and 2.21 ± 0.03 for PSL_{surfactant} and PSL_{free}, respectively. These values are in coherence with the acetate ($\text{CH}_3\text{-COO}^-$) $\log K_{\text{HL}} = 2.68$ (Martell and Smith, 1977) (Table III.2.3). For the e-NPs, the calculated $\log K_{\text{COOPb}^+}$ was 2.84 ± 0.05 . To validate these values, extrapolated $\log K_{\text{COOH}}$ and $\log K_{\text{COOPb}^+}$ were compared with a linear free energy relation, LFER, relating the protonation constants of various R-COOH ligands, $\log K_{\text{COOH}}$, with their corresponding monodentate stability constant, $\log K_{\text{COOPb}^+}$ (Figure III.2.5). The extrapolated $\log K_{\text{COOH}}$ and $\log K_{\text{COOPb}^+}$ followed the LFER (Figure III.2.5), validating the extrapolated values. Therefore, the hypothesis of Pb(II) binding as a monodentate complex with NPs carboxylic sites was validated for PSLs and e-NPs (Table III.2.3).

Table III.2.2. RMSE obtained for both modeling hypotheses, in bold the lowest value for each NPs model.

NPs	Modeling hypothesis	RMSE
PSL _{surfactant}	ML	0.062
	ML + ML ₂	0.064
PSL _{free}	ML	0.022
	ML + ML ₂	0.023
e-NPs	ML	0.042
	ML + ML ₂	0.045
m-NPs	ML	0.050
	ML + ML ₂	0.030

For the m-NPs, both scenarios were also tested. The lower RMSE was obtained for both monodentate and bidentate complexes hypothesis (Table III.2.2). The calculated $\log K_{\text{COOPb}^+}$ and $\log K_{\text{COO}_2\text{Pb}^+}$ were 2.50 and 4.99. Here, the bidentate $\log K$ was related to the monodentate $\log K$ ($\log K_{\text{COO}_2\text{Pb}^+} = 2 \log K_{\text{-COOPb}^+}$ (Eq. III.2.10, Tipping, 2002)). Therefore, only the monodentate $\log K$ was discussed here. The calculated $\log K_{\text{-COOPb}^+}$ was 2.50 close to the Pb(II)-acetate $\log K = 2.68$ in Martell and Smith (1977) (Table III.2.3) and the value estimated from the LFER $\log K = 2.58$ (Figure III.2.5).

Although, monodentate complexes are dominant for all NPs, bidentate complexes were surprisingly suggested for the m-NPs. Indeed, m-NPs had a lower site density (Table III.2.1).

The milling procedure induces plastics rupture and radical reaction able to include O-containing functions (Sohma, 1989). Moreover, these functions are located on plastic fractures, resulting in local high site density and thus the formation of a multidentate complex. For the e-NPs, the model's formation of a multidentate complex with Pb was not suggested, although occurring for trivalent REE (Blanco et al., Submitted). In this study, the heterogeneity of site density was also argued to explain the presence of the multidentate complex. However, the potential local increases of the site density seem insufficient to allow the formation of the bidentate complexes for divalent cations such as Pb.

Table III.2.3. Calculated binding parameters and the corresponding RMSE from this study and in the literature

NPs	Formed complex	HL (%)	Log K _{COOPb+}	Log K _{COO2Pb+}	Q _{max} (mg g ⁻¹)	RMSE	References
PSL _{surfactant}	ML	100	2.33 ± 0.09	-	20.0	0.022	This study
PSL _{free}	ML	100	2.21 ± 0.03	-	5.15	0.062	This study
e-NPs	ML	100	2.84 ± 0.05	-	18.5	0.042	This study
m-NPs	ML + ML ₂	64.3 ± 0.03	2.50 ± 0.03	4.99	2.32	0.030	This study
Acetate	ML	100	2.68	-	-	-	Martell and Smith 1977
HFO					350	-	Dzombak and Morel 1990; Reich et al. 2010
Goethite					112	-	Komárek et al., 2018
Hematite	-	-	-	-	6.2	-	Komárek et al., 2018
Montmorillonite	-	-	-	-	10.4	-	Wu et al., 2003
Loamy sand soil	-	-	-	-	2.2	-	Fonseca et al., 2009

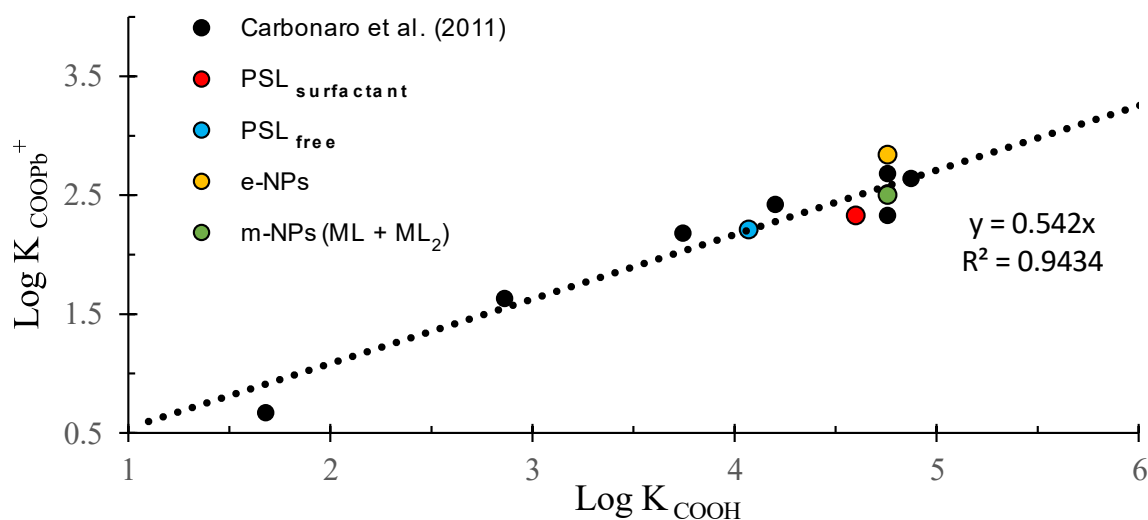


Figure III.2.5. LFER of $\text{Log } K_{\text{COOPb}^+}$ against $\text{log } K_{\text{COOH}}$ for various carboxylic ligands (Adapted from Carbonaro and Di Toro, 2007).

To further validate the binding parameters determined for e-NPs, they were tested to reproduce Davranche et al. (2019) datasets. Their NPs were produced using a similar protocol to Blanco et al. (2021) without OM degradation. As the binding site density was unknown for the e-NPs produced by Davranche et al. (2019), this parameter was fitted. Modeling calculations determined a $-\text{COOH}$ total concentration of $0.112 \pm 0.007 \text{ mmol g}^{-1}$, in the order of magnitude of the e-NPs. The obtained RMSE were in the same order of magnitude as for all other NPs (Table III.2.3). However, the calculated $[\text{Pb}]_{\text{ads}}$ were overestimated for $[\text{Pb}]_{\text{free}} < 3 \text{ ppm}$ (Figure III.2.6A). For the pH-adsorption edge, $[\text{Pb}]_{\text{ads}}$ were underestimated for $\text{pH} < 7$ (Figure III.2.6B). As previously explained, natural organic matter (NOM) was present in the NPs produced by Davranche et al. (2019). This NOM could influence the amount of Pb adsorbed by NPs by complexing Pb, competing with NPs, or forming hetero-aggregates with NPs. The formation of hetero-aggregates could modify the NPs binding site' density and influence the concentration of adsorbed Pb. However, at high Pb concentration and pH (Figure III.2.6), $[\text{Pb}]_{\text{ads}}$ were well predicted, indicating no hetero-aggregation occurred. Pradel et al. (2021) demonstrated that the source of NOM was a major parameter of the hetero-aggregation. They showed that hetero-aggregate could be formed with alginate but not with charged OM such as humic acid.

e-NPs OM (Davranche et al., 2019)

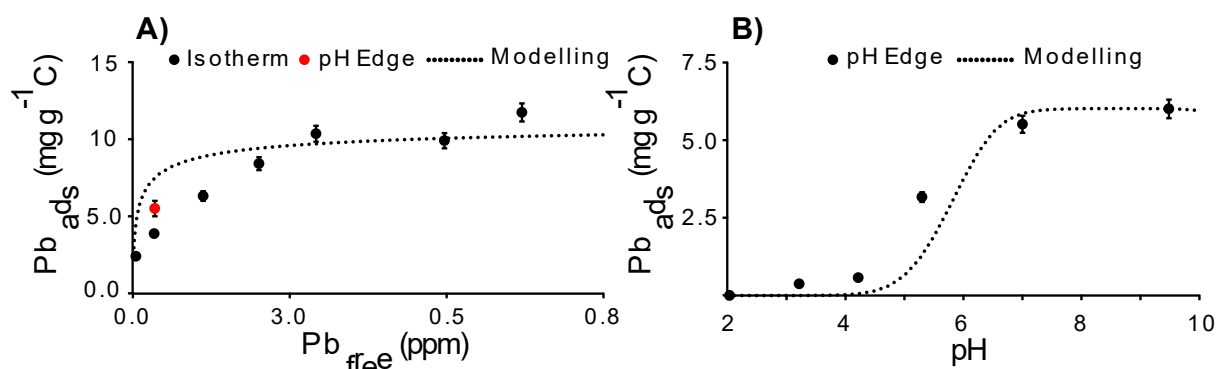


Figure III.2.6. Evolution of the experimental (black points) and calculated (dotted lines) concentrations of adsorbed Pb(II) by NPs, (A) Adsorption isotherm, (B) pH adsorption edge from Davranche et al. (2019).

III.2.3.5. Impact of photo-oxidation on the NPs sorption capacity

The model was used to investigate the impact of photo-oxidation on the surface reactivity of m-NPs after UVC exposure. At pH = 5.5 for a Pb/NPs ratio of 2.5 mg g⁻¹C, the photo-oxidized m-NPs, m-NPs-UV, adsorbed 66% of Pb against 24% for m-NPs. This significant difference might be explained by an increase of the -COOH density at the surface of m-NPs-UV. To test this hypothesis, the model and optimized binding parameters were used to calculate the COOH total site density ($H_{s_{tot}}$) from a dataset of Pb-m-NPs-UV adsorption. The average -COOH total site concentration ($H_{s_{tot}}$) was calculated at 0.227 ± 0.080 mmol g⁻¹, which is 6 times higher than for m-NPs. Modeling calculations demonstrated that the surface reactivity of NPs strongly dependent on their oxidation state. Thus, photo-oxidation has a stronger impact on the NPs surface reactivity than mechanical abrasion.

Finally, the calculated -COOH total concentration of m-NPs-UV was similar to that of e-NPs (Figure III.2.7). The e-NPs were typical photo-oxidized NPs since produced from plastic debris collected at the ocean surface. Therefore, the present results suggested that photo-oxidation of m-NPs can make NPs of equivalent reactivity to e-NPs.

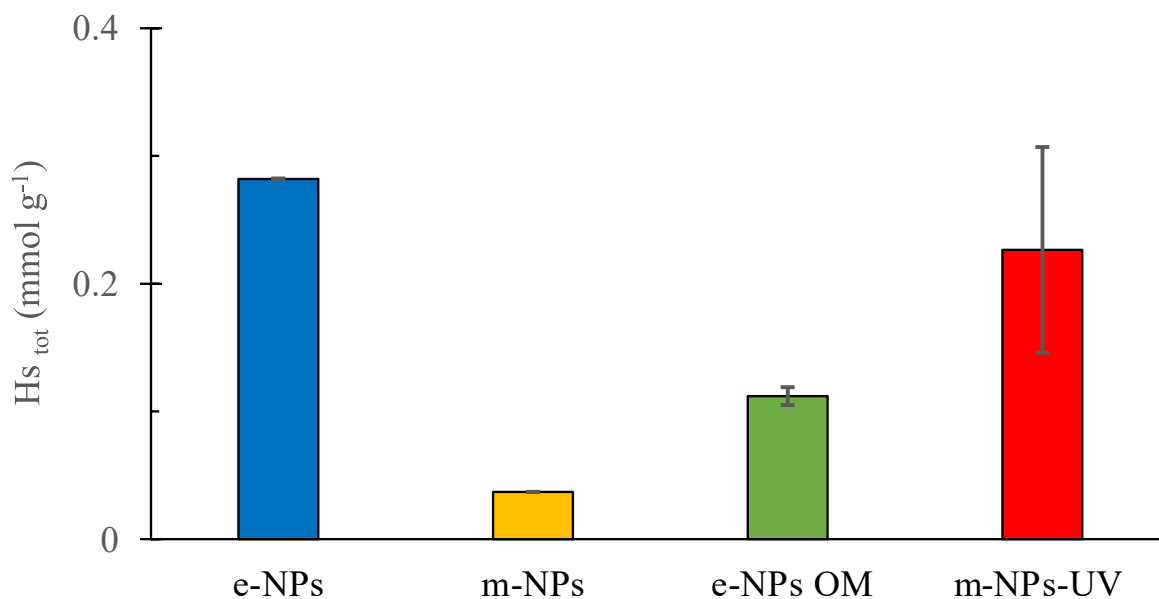


Figure III.2.7. Total surface –COOH concentration, or Total ionizable site concentration (Hs_{tot}), of NPs.

III.2.3.6. Environmental implications

Model calculations suggested that the monodentate complex is the dominant complex formed between Pb and NPs, notably for the most environmentally relevant, e-NPs. The average $\log K_{COO_2Pb^{2+}}$ was 2.47 ± 0.27 , two orders smaller than the $\log K$ for Pb with ferrous hydroxide (HFO), $\log K_{HFOPb^{2+}} = 4.65$ (Dzombak and Morel, 1990). Ferrous oxyhydroxides are ubiquitous and known to be strong adsorbents of metals (Dzombak and Morel, 1990; Stumm and Morgan, 2012). Therefore, NPs seem to not compete with HFO for Pb sorption, except in specific areas where plastics debris is in high amounts, such as landfills or in agricultural soils that received plastics mulches. For e-NPs, $Q_{max Pb}$ was equal to $18.5 \text{ mg g}^{-1}C$, one order lower than HFO and goethite (Table III.2.3). Nanoplastics could only impact divalent metals speciation for $pH > 4.5$ in environments where other binding phases (i.e., HFO or OM) are in low concentration.

The metal valence seems to influence the denticity of the complex formed at the NPs surface. Blancho et al. (Submitted) suggested, that, for trivalent REE, bidentate complex occurred with e-NPs while, here, only monodentate was expected to be formed for the divalent Pb. If NPs cannot compete with HFO for Pb binding, by contrast, it could be the case for trivalent ions. Liu et al. (2017) estimated, indeed, that $\log K$ REE-HFO was equal to 1.68, 2.90, and 3.47, for La, Eu and Lu against 2.82, 3.64, and 3.16 for the corresponding Lu, Eu, and Lu

bidentate $\log K$ REE-(Acetate)₂. The formation of the bidentate complex was confirmed for the m-NPs. The denticity of the complex could then vary with the NPs degradation pathways.

Lead can also be present in the plastics matrices as additives. Catrouillet et al. (2021) calculated a median concentration of Pb into MPs at around 0.3 mg Kg⁻¹c, namely 6500-fold lower than the Pb potentially adsorbed by e-NPs. Authors suggested that the Pb adsorbed on the altered surface of MPs was originated from Pb used as additives rather than from the environment. Lead is expected to be released during the polymer photo-oxidation and then partly adsorbed on the altered layer of the MPs that will further be altered as NPs. Although this adsorption by NPs partially prevents the release of the metal, it could also promote their transfer as a colloidal phase in ecosystems and living organisms. Finally, UV exposition increased the density of the NPs –COO⁻ binding sites. Metal adsorption by photo-oxidized NPs is thus expected to increase with the residence time of NPs in the environment (i.e., ocean and freshwater). Therefore, plastics represent a new source of metals that can be transported in the environment when their degradation products reach the nanosized and behave as colloids.

III.2.4. Conclusions

For the first time, a surface complexation model was designed to describe and predict the Pb adsorption by NPs. Following the previous study, two binding hypotheses were tested to explain Pb adsorption by NPs. Lead adsorption is dominated by carboxyl monodentate complexes for all NPs models, although bidentate occurred for the milled NPs models. The extrapolated $\log K$ was coherent with the $\log K$ Pb(II)-COOCH₃ values from the literature, validating the established NPs adsorption model. Metal-NPs interactions depend on the metal valency. Divalent ion (Pb) forms monodentate complexes, while trivalent metals such as REE form bidentate complexes. Milled NPs are less metal reactive than strongly NPs photo-oxidized under environmental conditions. These results highlighted the influence of NPs degradation route on the NPs binding sites density and thus surface reactivity. Although the results suggested that NPs are not a strong competitor of natural adsorbents, multi-component sorption may be studied within environmental conditions to better define the associated metal to NPs in the environment. Moreover, metal competitions have to be studied in detail to identify metals having the highest affinity for NPs. Such studies may include a mechanistic approach in order to complete the sorption models proposed in this study and to test its reliability to predict metals sorption in a more complex matrix.

CONCLUSIONS ET PERSPECTIVES

IV.1 Conclusions

La présence de NPs dans les différents compartiments environnementaux soulève de nombreuses questions quant à leurs comportements, leurs transports, leur accumulation, leurs interactions avec les métaux, etc. L'état des connaissances sur ces questions reste limité, ce travail de doctorat s'est donc attaché à étudier certaines de ces problématiques telles que la détection des NPs, l'étude de leurs propriétés physico-chimiques et de leurs interactions avec les éléments traces métalliques. Les recherches menées ont été organisées en trois volets. La première partie a été consacrée à l'identification des NPs en milieux complexes. La deuxième a porté sur la production d'un modèle de NPs ainsi que sa caractérisation. Enfin, la dernière partie s'est intéressée à la réactivité des NPs vis-à-vis des micropolluants métalliques.

IV.1.1. Détection de nanoplastiques

La détection des NPs dans le milieu naturel est complexe (Cai et al., 2021). Actuellement, plusieurs techniques analytiques sont capables de les identifier (XPS, ATR-FTIR, pince Raman, Py-GCMS, etc.), en revanche, ces techniques doivent être optimisées. Dans la première partie de cette thèse de doctorat, nous nous sommes intéressés aux capacités analytiques de la Py-GCMS, et à son optimisation en termes de détection. Plus spécifiquement, cette première étude s'est intéressée à la détection du PP et du PS, deux polymères produits et utilisés à l'échelle mondiale. Les résultats majeurs de cette étude sont :

La quantité des produits de pyrolyse varie entre les MPs et NPs. Pour le PS, la proportion d'aire des pics de dimère et trimère de styrène varie respectivement de 26 à 0.2 % et de 23 % à une quantité négligeable par rapport au pic principal (Styrène). Pour le PP, la proportion d'aire du C15i varie de 3 à 10 %, par rapport au C9. Pour le PS, ces variations diminuent la limite de détection des produits de pyrolyse n'ayant pas d'interférences avec la MO. Il est donc indispensable d'obtenir des pyrogrammes des polymères spécifiques aux NPs et de limiter les analogies avec les MPs.

L'identification directe des NPs de PP est possible en présence de MO. De nombreux produits de pyrolyse du PP n'ont pas d'interférences avec la MO. Dans cette première étude, 4 produits de pyrolyses ont été retenus pour l'identification des NPs de PP et validés en présence de MO.

L'identification indirecte des NPs de PS est possible grâce au rapport Toluène/ Styrène. Le rapport Toluène/Styrène de la MO est ≥ 5 alors que pour le PS, il est ≥ 0.1 (Fabbri, 2001; Tsuge et al., 2011). La variation de ce rapport entre le pôle MO et celui du PS a donc permis de

d'identifier la présence de NPs de PS dans un échantillon de NPs produit à partir de plastiques altérés.

IV.1.2. Production d'un modèle représentatif des NPs environnementaux

Les modèles de NPs actuels sont essentiellement des PSLs dont les propriétés correspondent peu à la définition et aux observations faites des NPs environnementaux (Gigault et al., 2018). Dans cette deuxième étude, je me suis donc intéressé à la production d'un modèle de NPs environnementalement pertinent. Pour cela, j'ai optimisé le protocole proposé par Davranche et al. (2019), basé sur l'abrasion mécanique de plastiques altérés en conditions environnementales. Ces plastiques avaient pour origine le gyre Atlantique et Pacifique Nord et ont donc été soumis à une photo-oxydation en conditions environnementales. Le modèle produit a été nommé e-NPs, pour « environmental nanoplastics ». Les principaux résultats sont décrits ci-dessous :

La surface altérée des plastiques permet de produire un modèle proche des NPs environnementaux, appelé e-NPs. Les nanoparticules produites sont polydispersées et leurs formes sont ouvertes, asymétriques et hétérogènes comme observé par Gigault et al. (2018). Malgré leurs formes, les NPs ne présentent pas de pores inférieurs à 2 nm. **Ils sont composés majoritairement de PP et de PE**, et sur la base des pics obtenus par Py-GCMS, le PP semble être dominant. **Environ 30% des groupements fonctionnels présents à la surface des e-NPs incluent des atomes d'oxygène.** Les titrages potentiométriques ont mis en évidence **la présence de groupes ionisables à hauteur de $0.23 \cdot 10^{-3} \text{ mol g}^{-1}$.** La présence de ces fonctions est cohérente avec leurs capacités d'adsorption observées par Davranche et al. (2019). **Leur densité de site est également comparable à celle de la ferrihydrite, $\approx 10 \text{ sites nm}^{-2}$.**

IV.1.3. Identification des mécanismes d'adsorption des métaux par les e-NPS

Davranche et al. (2019) a démontré que l'adsorption de Pb par les e-NPs, se fait par complexation de surface et diffusion intraparticulaire. Cependant, la nature de ces sites ainsi que les complexes formés ne sont pas connus. Pour pallier ce manque de connaissance, j'ai utilisé le groupe des Terres Rares comme « sonde » des processus d'adsorption des métaux par les NPs. En effet, les Terres Rares sont un groupe d'éléments chimique très particulier. Le couplage des quantités adsorbées à la variation des spectres de terres rares permettent d'obtenir

des informations sur la nature des sites activés par la complexation de surface et le type de complexes formés (Marsac et al., 2010, 2011).

Les spectres de REE obtenus par adsorption des REE par les e-NPS et les PSLs ont montré que l'adsorption est contrôlée par des sites carboxyliques. Pour les PSLs, ce contrôle était attendu puisqu'ils sont carboxylatés. **En revanche, et pour la première fois, ces résultats prouvent que ce sont bien des sites carboxyliques qui contrôlent l'adsorption des métaux à la surface des NPs, produits à partir de conditions environnementales.** Les variations des spectres de terre rares et leur comparaison, avec des spectres de complexation REE-COOH en solution, ont montré **une hétérogénéité des complexes formés, distribués entre complexe monodenté et bidenté.** Les spectres REE-e-NPs indiquent que les complexes bidentés sont dominants pour les rapports REE/NPs faibles et à pH élevé. En revanche, pour les PSL « free soap », les spectres indiquent la présence de tels complexes pour des rapports REE/NPs élevés et à pH acide. Leur faible densité de site induit une forte compétition entre ions, mêmes aux faibles ratios REE/NPs. Cette compétition met en évidence les complexes bidentés, en effet, ce sont les seuls à pouvoir se former en présence de Th, U et de Sc, également présents en solution. Pour les PSL « surfactant », les spectres correspondent à la formation d'un complexe bidenté uniquement.

Pour les e-NPs, l'hétérogénéité des complexes formés s'explique par une photo-oxydation inhomogène de la surface qui augmente localement la densité de site de surface et permet la formation de complexes multidentés. Pour les PSL « free soap », la compétition entre ions montre que les complexes bidentés sont anecdotiques à leur surface. Pour les PSL « surfactant », les complexes bidentés sont dominants en réponse à la forte densité de site du modèle, estimée à 6.6 sites nm⁻², contre 3.4 sites nm⁻² pour les PSL « free soap ».

Si l'utilisation des REE a permis de déterminer la nature des sites réactifs et les types de complexes possiblement formés à la surface des différents modèles de NPs, cette étude n'a pas permise de paramétrer les mécanismes de sorption. Ce paramétrage est en général obtenu par la modélisation de données expérimentales. Cependant, il est très complexe d'établir un tel modèle avec autant d'éléments (18). Pour cela, j'ai choisi pour une première approche de réaliser cette modélisation avec 1 seul cation, ici le Pb.

Les données physico-chimiques d'entrée du modèle ont été produites lors de ce travail et collectées dans la littérature. Les constantes de stabilité des complexes Pb-NPs ont été extrapolées à partir des données expérimentales d'adsorption du Pb avec les différents modèles de NPs étudiés. Différentes hypothèses mécanistiques ont été testées, à savoir, une

complexation par les sites carboxyliques avec et sans complexes multidentés. Cette approche mécanistique a montré que :

La complexation est dominée par les sites carboxyliques. Les complexes formés sont **uniquement monodentés pour les PSLs et les e-NPs alors que les m-NPs (abrasion) forment jusqu'à 25% de complexes bidentés avec le Pb, dans les conditions expérimentales utilisées.** Une distribution inhomogène des sites à la surface des NPs, suite à leur broyage, pourrait expliquer ce résultat. De fait, bien que leur densité de site soit faible, elle pourrait localement être plus élevée, facilitant la formation de complexe bidenté avec des ions divalents. Enfin, cette étude montre que l'adsorption est très dépendante du nombre de sites de surface, eux-mêmes contrôlés par la photo-oxydation subit par les plastiques.

Ces travaux de doctorat ont répondu à un certain nombre de questions sur la détection, les propriétés physico-chimiques et la réactivité des NPs vis-à-vis des micropolluants métalliques. Le premier volet a montré que la détection de certains polymères était possible en présence de matière organique, ce qui ouvre de nombreuses perspectives quant à leurs études dans des milieux complexes tels que les sols, les sédiments et même les organismes vivants. En revanche, bien que ces résultats soient prometteurs, un certain nombre de points doivent être discutés, optimisés et/ou complétés (voir perspectives). Le deuxième volet a permis de mettre au point un protocole simple de production d'e-NPs bien plus représentatif des NPs observés dans l'environnement que les modèles utilisés actuellement. Les propriétés et les quantités produites de ces e-NPs ouvrent un champ immense de nouvelles possibilités d'études tant en terme technique (imagerie, spectroscopie, etc.) que scientifique (comportement physico-chimique, écotoxicologique, etc.).

Enfin, le dernier volet a montré que les NPs ont une forte réactivité vis-à-vis des métaux, ils sont capables de former des complexes via les sites carboxyliques développés à leur surface par photo-oxydations des polymères. La denticité des complexes est contrôlée par la valence des métaux, les trivalents formant des complexes bidentés et les divalents des complexes monodentés, et par la densité de sites carboxyliques, c'est-à-dire par l'état d'altération des NPs. Ces résultats ne sont pas sans conséquences et montrent que les métaux divalents seront moins fortement complexés par les NPs que les plurivalents et donc potentiellement plus facilement remobilisés (libérés) en fonction des variations des conditions physicochimiques dans l'environnement et au sein des organismes vivants. Récemment, Catrouillet et al. (2021) ont suggéré que les métaux adsorbés dans la couche altérée des MPs avaient en majorité pour origine les métaux utilisés comme additifs dans la formulation des plastiques. Ces métaux

seraient libérés de la matrice par leur altération et seraient aussitôt adsorbés par la couche altérée de surface. Ces résultats suggèrent que les métaux adsorbés à la surface des NPs dans l'environnement seraient adsorbés bien avant leur libération dans l'environnement.

IV.2. Perspectives

Ces résultats représentent une avancée significative dans notre connaissance du comportement des NPs, mais ils soulèvent eux-mêmes, un certain nombre de questions qui permettent de proposer de nouvelles perspectives d'étude.

IV.2.1. Identification/détection des NPs

Les pyrogrammes des NPs ne sont pas disponibles dans la littérature alors qu'ils sont indispensables puisque la taille des particules influence la quantité de pyrolyzates produits (Blanco et al., 2021b). Pour certains échantillons, la détection des NPs nécessite une étape chronophage de dégradation de la MO en suspension. Dümichen et al. (2017) ont montré qu'une partie non négligeable de la MO était pyrolysée à 400°C alors que la dégradation des polymères débute à des températures supérieures à 400°C (e.g. PA, PE, PET, PP). Il serait donc intéressant de séparer la pyrolyse pour éliminer, dans un premier temps la MO, puis ensuite pyrolyser les NPs. Pour le PS, ce protocole permettrait de valider l'utilisation du rapport Toluène/Styrène. Si la dégradation de la MO à 400°C n'est pas suffisante, il serait également intéressant d'acquérir des données par TGA-GC/MS. En effet, la pyrolyse à température croissante d'un composant organique à une signature singulière. L'évolution des produits de pyrolyse identifiés en fonction de la température, et de leurs rapports, pourraient permettre de détecter la présence de NPs.

Il est également primordial de quantifier les NPs. Sur ce point, la Py-GCMS ne semble pas appropriée bien que ce soit le cas pour les MPs (Fischer and Scholz-Böttcher, 2019, 2017). Pour cela, la décomposition thermique des NPs en CO₂ pourrait être une piste intéressante, après élimination de la MO. Lai et al. (2021) ont démontré qu'il était possible de dégrader séparément la MO des MPs. De plus, leur méthodologie dispose d'une limite de détection suffisamment basse pour être appliquée aux NPs, i.e. $\approx 2 \mu\text{g}$ comme en Py-GCMS.

IV.2.2. Modèles de NPs

Des variantes du protocole développé pour produire les e-NPs peuvent être envisagées. Elles produiront des e-NPs aux propriétés différentes :

1/ Des e-NPs composés d'un unique polymère. Il est possible de produire des e-NPs à partir d'un seul débris plastique (Figure IV.2.1). Cette option est intéressante puisque qu'elle permettrait d'étudier séparément les propriétés physico-chimiques des différents polymères.



Figure IV.2.1. Bouée plastique de PE photo-oxydée en condition environnementale.

2/ Des e-NPs à partir de plastiques altérés en laboratoire. Des chambres de simulation permettent d'altérer des plastiques en conditions proches des conditions environnementales (Rabek, 1995). Produire des e-NPs à partir de plastique vierge permettrait d'obtenir des NPs sans additifs. Ce genre de modèle répondrait aux problématiques des écotoxicologues. Il semble en effet primordial de réaliser des études d'écotoxicologie pour des NPs avec et sans additifs afin de discriminer l'impact de l'un et de l'autre.

3/ Des e-NPs à partir des plastiques contenant du Pd puis altérés en laboratoire. Ce type de NPs permettrait d'utiliser des e-NPs dans des études de transport grâce au Pd qui faciliterait leur traçage (Mitrano et al., 2019).

Concernant le protocole présenté dans notre étude, les différents polymères composant les e-NPs doivent encore être quantifiés. D'après les pyrogrammes obtenus, les e-NPs produits sont composés majoritairement de PE et PP, en revanche leur proportion reste inconnue. Aux vues des quantités produites, il est envisageable de réaliser des analyses quantitatives par exemple par ATR-FTIR. La déconvolution des spectres ATR-FTIR devrait permettre de quantifier ensuite la proportion relative des polymères qui composent les NPs. Les quantités d'additifs minéraux dans les e-NPs doivent encore être déterminées. Des analyses de perte au

feu permettraient de quantifier leur proportion. Enfin, il serait intéressant de s'affranchir de l'étape de dégradation de la MO par UV/H₂O₂. Bien que l'oxydation de surface semble faible, des réactions radicalaires peuvent se produire à la surface des e-NPs.

IV.2.3. Interaction entre métaux et NPs

Ce travail de doctorat a permis de mieux définir les interactions entre les métaux et les NPs. La complexation se produit via des sites carboxyliques, cependant, la denticité des complexes formés doit être confirmée à l'aide par exemple de l'absorption des rayons-X. Ces informations permettront aussi de contraindre le modèle de sorption développé dans ce travail de doctorat.

IV.2.3. Caractérisation et transformation des NPs dans l'environnement

La caractérisation et l'étude du comportement des NPs n'en est qu'à ses débuts. Un certain nombre de paramètres indispensables à la compréhension et à la paramétrisation de leur réactivité de surface restent à déterminer. Ainsi, les constantes de déprotonation des groupements ionisables, pKa, doivent être extrapolées à partir de données expérimentales. En effet, dans notre dernière étude, nous ne sommes pas parvenus à les obtenir. Bien que la valeur fixée pour la conception du modèle de complexation soit cohérente, cette constante doit être déterminée expérimentalement. Les constantes de déprotonation sont des données clés car elles permettent de prédire en fonction des conditions géochimiques, 1) la réactivité métaux-NPs lorsqu'elles sont associées aux constantes de stabilité et 2) le potentiel de surface des NPs.

De plus, la densité de site à la surface des NPs est un autre paramètre clé car il conditionne les interactions métal-NPs et influence leurs stabilités colloïdales. Bien que ce travail de doctorat ait permis de déterminer des densités de sites pour certains NPs, les paramètres qui l'influencent n'ont pas été étudiés, notamment la photo-oxydation, taille des particules, etc... Cai et al. (2018) ont montré que l'oxydation de surface des MPs augmente en fonction de l'exposition aux UV mais aussi que leurs surfaces sont de plus en plus rugueuses, augmentant ainsi leur surface spécifique (Fotopoulou and Karapanagioti, 2012). Qu'en est-il de la densité de site ? Atteint-elle un plateau, pour une surface et une photo-oxydation donnée ?

La description des propriétés physico-chimiques des NPs dans leur ensemble fait partie intégrante d'un projet de recherche à plus long terme qui viserait à caractériser et modéliser les interactions métaux-NPs, phases réactives-NPs (MO, HFO, etc) dans le but de prédire la stabilité des NPs et de leurs agrégats. Il est en effet possible d'intégrer les données de potentiel

déterminées à l'aide d'un Four Layer Model, FLM (Charmas et al., 1995), dans le modèle DLVO. Un modèle de ce type a récemment été proposé par Gil-Díaz et al. (2021) nommé SINFONIA, il est donc possible d'appliquer cette approche aux NPs. Une telle approche couplée aux travaux de Galli et al. (2020) semble être en mesure de prédire un des paramètres clé de la stabilité colloïdale, la concentration critique de coagulation (CCC), et ce en fonction des conditions géochimiques et des propriétés des NPs. Bien que cette intégration représente actuellement un challenge surtout pour les hétéro-agrégats (NPs-OM, NPs-HFO), il est primordial d'y parvenir. Actuellement, de nombreuses études étudient la stabilité colloïdale des NPs sans pour autant bien connaître leurs propriétés physico-chimiques, mais aussi et surtout en ne les intégrant pas dans un modèle mécanistique. De fait, les CCC décrites ne permettent pas d'être extrapolées à un autre pH, un autre ion, etc. Il est important de faire cette jonction entre les modèles de complexation de surface d'un côté et la stabilité colloïdale de l'autre.

De ce projet de recherche à long terme, plusieurs sous-objectifs peuvent d'ores et déjà être réalisés. Dans un premier temps, les interactions entre cations majeurs et NPs pourraient être étudiées afin de paramétrer le FLM du modèle SINFONIA. En effet, il est connu que les ions majeurs, via le contrôle de la force ionique, compressent la couche diffuse et influencent la stabilité colloïdale des NPs. Cependant, les cations majeurs peuvent aussi former des complexes de sphères externes avec les surfaces chargées négativement, influençant aussi la stabilité des colloïdes. Lorsque les interactions entre cations majeurs (ex. Na^+ et Ca^{2+}), et NPs seront paramétrées, l'utilisation de LFER devra être envisagée et testée afin d'obtenir ces données pour les autres cations majeurs. Une fois paramétré, SINFONIA pourra estimer les CCC de différents modèles de NPs en fonction des conditions géochimiques (Galli et al., 2020; Gil-Díaz et al., 2021). Ces estimations pourront être comparées au CCC déterminées expérimentalement dans la littérature (Singh et al., 2019; El Hadri et al., 2020; Shams et al., 2020; X. Wang et al., 2020; Liu et al., 2021; Pradel et al., 2021).

Il est tout aussi primordial d'étudier les interactions avec les autres phases réactives de l'environnement. Dans un premier temps, les interactions seront étudiées dans des systèmes à deux composants afin de restreindre la complexité des hétéro-agrégats formés. L'étude des interactions avec la MO et les hydroxydes de Fer sera privilégiée car ils sont tous deux très présents dans l'environnement. Les modalités d'agrégation seront étudiées pour des conditions géochimiques variées. Concernant les NPs et la MO, comme ces deux surfaces sont chargées négativement, leur interaction est possible par l'intermédiaire de pont cationique (Dong et al., 2021), c'est cette interaction qui doit être étudiée et paramétrée en première. Aux pH

environnementaux, compris entre 5 et 8, la surface des HFO est positive. Une interaction directe entre NPs et HFO est donc prévisible et a déjà été observée (Yangyang Zhang et al., 2020). Que ce soit pour la MO ou HFO, ces études doivent permettre de décrire les paramètres mécanistiques contrôlant leurs agrégations et elles doivent aussi permettre de prédire les CCC en fonction des conditions géochimiques.

LISTE DES ABREVIATIONS, DES SIGLES ET DES ACRONYMES

ACF	Autocorrelation function
ATR-FTIR	Attenuated total reflectance - Fourier-transform infrared spectroscopy
BDs	Beached plastic debris
BET	Brunauer Emmett et Teller theory
CCC	Concentration critique de coagulation
CMRs	Certified material references
C9	2,4-dimethyl-1-heptene
C12	Meso-2,4,6-trimethyl-1-nonene
C15i	Isotactic-2,4,6,8-tetramethyl-1-undecene
C15s	Syndiotactic-2,4,6,8-tetramethyl-1-undecene
DLM	Diffuse Layer Model
DLS	Dynamic light scattering
DOC	Dissolved organic carbon
EDX	Energy-dispersive X-ray spectroscopy
e-MPs	Environmental microplastics
e-NPs	Environmental nanoplastics
EPA	Environmental Protection Agency
EPS	Extracellular polymeric substances
EXAFS	Extended X-ray absorption fine structure
FDs	Floating debris
FI	Force ionique
FLM	Four layers model
GC	Gas chromatography
HFO	Hydrous ferric oxide
HREE	High rare earth elements
ICP-MS	Inductively coupled plasma mass spectrometry
IHP	Inner Helmholtz plane
IS	Ionic strength

KPS Potassium persulfate
LHA Leonardite humic acid
LFER Linear free energy relation
LNOM Leonardite natural organic matter
LOD Limit of detection
LREE Light rare earth elements
MEB Microscopie électronique à balayage
MO Matière organique
MPs Microplastiques
MS Mass spectrometer
MSs Mass spectrum
NAOG North Atlantic Ocean Gyre
NIH National Institutes of Health
NIST National Institute of Standards and Technology
N_{MREEDC} Middle rare earth elements downward concavity normalization
NOM Natural organic matter
NPs Nanoplastiques
OC Organic carbon
OHP *Outer* Helmholtz plane
OM Organic matter
PE Polyéthylène
PES Polyéther sulfones
PP Polypropylène
PS Polystyrène
PSL Polystyrene latex nanoparticle
PVC Polychlorure de vinyle
Py Pyrolysis
Py-GCMS Pyrolysis gas chromatography mass spectrometry
REE Rare earth element
RI Retention index
RMSE Root Mean Square Error
RPE Résonance paramagnétique électronique
SAWE Sargasso algae water extractable
SBL Sparse Bayesian Learning algorithms

SDS Sodium dodecyl sulfate
SNR Signal-to-noise ratio
SOM Soil organic matter
SS Spectrum similarity
SSA Specific surface area
TEM Transmission electron microscopy
TGA-GCMS Thermogravimetric analysis combined with gas chromatography and mass spectrometry
TIC Total ion count
TIP Total ion pyrogram
TOC Total organic carbon
Tol/Sty Ratio toluene/styrene
UV Ultraviolet
XANES X-ray Absorption Near Edge Structure
XAS X-ray absorption spectroscopy
XPS X-ray photoelectron spectroscopy

LISTE DES FIGURES

Figure	Page
INTRODUCTION GENERALE	
Figure 1. Production globale de plastique primaire et de déchets en millions de tonnes. Adapté d'après Geyer et Al. 2017.....	2
Figure 2. Nombre d'articles publiés par an traitant des NPs (recherche faite sous Scopus pour le terme "Nanoplastics" dans le titre, l'abstract et les mots clés).	4
Figure 3. Rapport de volume MO/NPs en fonction du rayon des NPs pour une couche de MO constante (Gigault et al., 2021).	6
Figure 4. Image TEM de (a) Nanoplastiques environnementaux et (b) des modèles de NPs obtenus par polymérisation (Gigault et al., 2018).	8
Figure 5. Modèle de Stern, décrivant l'évolution du potentiel de charge d'une surface, Ψ_0 , en fonction de la distance et des interactions avec les ions; IHP et OHP représentant, respectivement, les complexes de sphère interne et externe. Illustration d'après Zhang and Zhao (2009).....	11
Figure 6. Variation des spectres de REE, (A) coefficients de distribution en fonction du rapport REE/Acide humique (Marsac et al., 2010), et (B) constantes de stabilité normalisées au La avec l'acétate et l'oxalate formant respectivement des complexes monodentés et chélatés (Martell et Smith, 1977).....	13
CHAPITRE I	
Figure I.1. Sampling area on the French Caribbean Island Guadeloupe; (B) localization of the bay (Sainte Marie) at the GPS coordinate 16°16'24" N-61°14'35" W with the brown line is corresponding to the Sargassum Algae coming from the oceans (CNES); (C) pictures of the sampling site where the plastic debris are identified and mixed with the Sargassum Algae (CNRS, Cyril Fresillon).	20
Figure I.2. Plastic debris used to produce the e-NPs suspension, showing brown algae residue on its surface	21
Figure I.3. OM degradation yield (i.e. $\text{TOC}(t)/\text{TOC}(t_0)*100$) relative to the $\text{H}_2\text{O}_2\%$ and with (Black point) and without (White point) UV exposition.....	22
Figure I.4. (A) Log-transformed autocorrelation function (blue) bordered by the 500 and 900 nm polystyrene spherical latex nanoparticles, (B) size distribution, and (C) TEM images for PP and PS NPs.	23

Figure I.5. TEM image, left part and EDX spectra, right part. The Spectra 5 and 6 are related to the named zone 5 and 6 on the TEM image, respectively.....	25
Figure I.6. (A) Polypropylene micropellet pyrograms for TIC, m/z 70 and m/z 69. (B) Mass spectra of pyrolyzates recorded at the PP marker retention times used to build the library.	26
Figure I.7. (A) Polypropylene NPs pyrograms for TIC, m/z 70 and m/z 69. (B) Mass spectra comparison between the MSs of pyrolyzates recorded at the PP marker retention times (blue) and their library MSs (red).	27
Figure I.8. (A) Polystyrene micropellet pyrograms for TIC, m/z 104 and m/z 91. (B) Mass spectra of pyrolyzates recorded at the PP marker retention times used to build the library.	28
Figure I.9. (A) Polystyrene NPs pyrogram for TIC, m/z 104 and m/z 91. (B) Mass spectra comparison between the MSs of pyrolyzates recorded at the PS marker retention times (blue) and their library MSs (red).	30
Figure I.10. (A) m/z 70 pyrograms for SAWE without and with PP NPs; (B) m/z 69 pyrograms for SAWE without and with PP NPs; (C) Mass spectra of pyrolyzates recorded at PP marker retention times (blue) and their library MSs (red).....	31
Figure I.11. (A) m/z 70 pyrograms for L NOM without and with PP NPs; (B) m/z 69 pyrograms for L NOM without and with PP NPs; (C) Mass spectra of pyrolyzates recorded at the PP markers retention times (blue) and their library MSs (red).	32
Figure I.12. (A) m/z 70 pyrograms for LHA without and with PP NPs; (B) m/z 69 pyrograms for L NOM without and with PP NPs; (C) Mass spectra of pyrolyzates recorded at the PP marker retention times (blue) and their library MSs (red).	33
Figure I.13. (A) ACF function of the e-NPs bordered by the 500 and 900 nm polystyrene spherical latex nanoparticles; (B) corresponding size distribution expressed in volume with the associated integration; (C) TEM images of e-NPs.	34
Figure I.14. (A) Environmental-NPs pyrograms for TIC, m/z 70 and m/z 69. (B) Mass spectra comparison between the MSs of pyrolyzates recorded at PS marker retention times (blue) and their library MSs (red).....	35
Figure I.15. Environmental-NPs pyrograms for TIC, m/z 104 and m/z 91 (A) before and (B) after H_2O_2 /UV purification process.	36
Figure I.16. Toluene/Styrene ratio evolution during the OM degradation applied on the e-NPs suspension. The red zone indicated the Tol/Sty ratio obtained to the different studied NOM. The blue zone indicated the Tol/Sty ratio obtained for the PS microscale pellet and PS NPs.....	37

Figure I.17. (A) Environmental-NPs pyrograms for TIC, m/z 70 and m/z 69 after purification with H ₂ O ₂ /UV process. (B) Mass spectra comparison between the MSs of pyrolyzates recorded at PS marker retention times (blue) and their library MSs (red).....	37
---	----

CHAPITRE II

Figure II.1. Workflow of the e-NPs preparation protocol.....	45
--	----

Figure II.2. (A) Polyethylene micropellet pyrograms for TIC, m/z 97 and 81. (B) Mass spectra of pyrolyzates recorded at the PE marker retention times used to build the library. 1,14-C15 for 1,14-pentadecadiene; 1-C15 for pentadecene; 1,15-C16 for 1,15-hexadecadiene; 1-C16 for hexadecene; 1,16-C17 for 1,16-heptadecadiene; 1-C17 for heptadecene.....	47
---	----

Figure II.3. Microplastics and extraction solution before and after applying the extraction protocol on beach plastics. (A), (B) are photography of the same MPs, in detail (A) is the MPs scratched before applying the protocol revealing the weathered layer at its surface and (B), the MPs after using the protocol; (C) and (D) are TEM observations of MPs, before and after using the protocol, respectively; and (E) and (F) showed the extraction solution before and after applying the protocol; (I) and (J) show a MPs covered by organic materials, before and after using the protocol.	50
---	----

Figure II.4. Evolution of TOC concentration during the application of OM degradation protocol applied on the e-NPs suspension from PDs and BDs extraction, filled dot and unfilled dot, respectively.	51
--	----

Figure II.5. Evolution of organic tracer during OM degradation protocol applied on the e-NPs suspension from beach plastic and floating plastic extraction, filled dot and unfilled dot, respectively; (A) Fluorescence C Peak, obtained by fluorescence spectroscopy; (B) Pyrolyzates evolution, obtained from Py-GCMS.....	52
--	----

Figure II.6. (A) Environmental-NPs BDs pyrograms for TIC, m/z 97 and m/z 81. (B) Mass spectra comparison between the MSs of pyrolyzates recorded at the PE marker retention times (blue) and their library MSs (red).....	53
---	----

Figure II.7 Total ion count, m/z 70 and 69 e-NPs pyrograms from (A) beach debris and (B) floating debris.	55
--	----

Figure II.8. Mass spectra comparison between the MSs of pyrolyzates recorded at the PP marker retention times (blue) and their library MSs (red) for PDs (A) and (B) BDs, respectively. SS, spectrum similarity calculated with MSD Chemstation algorithm.	57
---	----

Figure II.9. Size characterization of e-NPs from beach and floating debris types. Log-transformed autocorrelation function (blue) and size nominated spherical nanoparticles of PS (black) (A) and (D) for e-NPs from BDs and FDs, respectively. SBL modeling (red) from the autocorrelation function (B) and	
---	--

I for e-NPs from BDs and FDs, respectively. TEM images (C) and (F) from BDs and FDs, respectively. EDX spectrum and atomic composition of e-NPs 1, Ti oxide and the grid are available in Table II.6. 58

Figure II.10. Atomic bonding distribution from C1S. High-resolution spectra from the e-NPs FDs. 60

CHAPITRE III

Figure III.1.1. Size characterization of PSL models. A) Population size from SBL modeling. B) Log-transformed time-ACF of the intensity of light scattered compare to CMRs standards. C) TEM pictures from the suspensions..... 72

Figure III.1.2. Size characterization the e-NPs model. A) Log-transformed time-ACF of the intensity of light scattered compare to CMRs standards. B) Population size from SBL modeling. C) TEM pictures from the suspensions..... 73

Figure III.1.3. Evolution of the Hs with the pH for both PSLs and e-NPs at 3 IS: 0.01, 0.10, 1.00 M. Symbols correspond to experimental data and dotted lines to calculated data. 74

Figure III.1.4. A) Adsorption isotherm of REE onto PSL surfactant for REE/NPs varying from 0.05 to 1 and pH = 6.5, B) REE patterns (log Kd) corresponding to each point of the adsorption isotherm, C) REE adsorption relative to the pH at REE/NPs = 0.1 mg g⁻¹ for pH varying from 3 to 7, D) REE patterns (log Kd) corresponding to each point of the pH-adsorption-edge. Error bars correspond to the SD of the triplicates. 75

Figure III.1.5. Evolution of the La/Lu and La/Sm of the REE pattern obtained relative to the REE/NPs ratio and pH for both PSLs and e-NPs..... 76

Figure III.1.6. A) Adsorption isotherm of REE onto PSL_{free} for REE/NPs varying from 0.05 to 1 and pH = 6.5, B) REE patterns (log Kd) corresponding to each point of the adsorption isotherm, C) REE adsorption relative to the pH at REE/NPs = 0.1 mg g⁻¹ for pH varying from 3 to 7, D) REE patterns (log Kd) corresponding to each point of the pH-adsorption-edge. Error bars correspond to the SD of the triplicates..... 78

Figure III.1.7. A) Adsorption isotherm of REE onto e-NPs for REE/NPs varying from 0.05 to 1 and pH = 6.5, B) REE patterns (log Kd) corresponding to each point of the adsorption isotherm, C) REE adsorption relative to the pH at REE/NPs = 0.35 mg g⁻¹ for pH varying from 3 to 7, D) REE patterns (log Kd) corresponding to each point of the pH-adsorption-edge. Error bars correspond to the SD of the triplicates 79

Figure III.1.8. Log K_{REE} patterns normalized to log K_{La} for (A) monocarboxylic acids (1:1), (B) for REE monodentate complexes with oxo carboxylic and dicarboxylic acid, (C) for 1:1, 1:2, and 1:3 REE-acetate complexes, and

(D) N_{MREEDC} REE patterns of REE-acetate, 1:1, 1:2, 1:3 complexes and REE-propionate 1:1, 1:2 complexes.....	81
Figure III.1.9. Comparison of REE-PSL _{surfactant} patterns normalized to the MREE downward concavity (A) relative to the REE/NPs ratios and (B) relative to pH with the 1:1 and 1:3 REE-propionate complexes patterns normalized to the MREE downward concavity. Error bars correspond to the SD of the triplicates.	82
Figure III.1.10. Comparison of REE-PSL _{free} patterns normalized to the MREE downward concavity (A) relative to the REE/NPs ratios and (B) relative to pH with the 1:1 and 1:3 REE-propionate complexes patterns normalized to the MREE downward concavity. Error bars correspond to the SD of the triplicates	83
Figure III.1.11. Comparison of REE-e-NPs patterns normalized to the MREE downward concavity (A) relative to the REE/NPs ratios and (B) relative to pH with the 1:1 and 1:3 REE-propionate complexes patterns normalized to the MREE downward concavity. Error bars correspond to the SD of the triplicates.	84
Figure III.1.12. Possible complexes formed between LREE, HREE, and e-NPs, A) simple HREE Bi-ligand complex onto 1 e-NPs and B) HREE bi-ligand complex between 2 e-NPs acting as a cationic bridge and potentially resulting in e-NPs homo-aggregation.....	86
Figure III.2.1. Pb(II) speciation function of pH.	93
Figure III.2.2. Size characterization of e-NPs and m-NPs models. A) Log-transformed time-ACF of the intensity of light scattered compare to CMRs standards. B) Population size from SBL modeling. C) TEM pictures from the suspensions.....	95
Figure III.2.3. Evolution of the Hs with the pH for both PSLs, e-NPs and m-NPs at 3 IS: 0.01, 0.10, 1.00 M. Symbols correspond to experimental data and dotted lines to calculated data.	97
Figure III.2.4. Evolution of the experimental (black points) and calculated (dotted lines) concentrations of adsorbed Pb(II) by NPs, (A) adsorption isotherms, and (B) pH adsorption edges.	98
Figure III.2.5. LFER of Log K_{COOPb^+} against log K_{COOH} for various carboxylic ligands (Adapted from Carbonaro and Di Toro, 2007).	101
Figure III.2.6. Evolution of the experimental (black points) and calculated (dotted lines) concentrations of adsorbed Pb(II) by NPs, (A) Adsorption isotherm, (B) pH adsorption edge from Davranche et al. (2019).....	102
Figure III.2.7. Total surface –COOH concentration, or Total ionizable site concentration (Hs tot), of NPs.....	103

CONCLUSIONS ET PERSPECTIVES

Figure IV.2.1. Bouée plastique de PE photo-oxydée en condition environnementale.... 111

LISTE DES TABLEAUX

Table	Page
INTRODUCTION GENERALE	
Table 1. Paramètres de surface nécessaires et disponibles pour la conception d'un modèle de complexation de surface métaux/NPs.....	12
CHAPITRE I	
Table I.1. Polypropylene distinctives pyrolyzates and the occurrence in the OM studied and in literature.	26
Table I.2. Polystyrene distinctive pyrolyzates and their occurrence in the OM studied and in literature. * Non-isothermal Kovats retention indice.	29
CHAPITRE II	
Table II.1. Polyethylene pyrolyzates used for its identification. * Indicates pyrolyzates with no interference with OM. ** Non-isothermal Kovats retention indices.	48
Table II.2. Pyrolyzates used for PP identification. * pyrolyzates with no interference with OM. ** Non-isothermal Kovats retention indices.	48
Table II.3. Pyrolyzates markers for typical OM and their occurrence in major plastic polymers. The table summarize the precursors of these markers found in literature. * Indicates Py-GCMS analysis realized at the laboratory beside literature data.	49
Table II.4. Polyethylene pyrolyzates used for its identification. * Indicates pyrolyzates with no interference with OM. ** Non-isothermal Kovats retention indices.	54
Table II.5. Pyrolyzates used for PP identification. * Pyrolyzates with no interference with OM. ** Non-isothermal Kovats retention indices.	56
Table II.6. Relative atomic composition obtained from EDX analysis on e-NPs 1 and its embedded black cubic particle.	59
Table II.7. H ₂ O ₂ quantification after the UVC exposition of the e-NPs suspension.	61
Table II.8. Physico-chemical properties of e-NPs and environmental phases.	62
CHAPITRE III	
Table III.1.1. Specific surface area of the studied NPs	69
Table III.2.1. NPs properties and characteristics	94

Table III.2.2. RMSE obtained for both modeling hypotheses, in bold the lowest value for each NPs model.	99
Table III.2.3. Calculated binding parameters and the corresponding RMSE from this study and in the literature	100

REFERENCES

- Abdolahpur Monikh, F., Chupani, L., Vijver, M.G., Peijnenburg, W.J.G.M., 2021. Parental and trophic transfer of nanoscale plastic debris in an assembled aquatic food chain as a function of particle size. *Environmental Pollution* 269, 116066. <https://doi.org/10.1016/j.envpol.2020.116066>
- Acevedo-Trejos, E., Brandt, G., Bruggeman, J., Merico, A., 2015. Mechanisms shaping size structure and functional diversity of phytoplankton communities in the ocean. *Sci Rep* 5, 8918. <https://doi.org/10.1038/srep08918>
- Ahmad, J.U., Goni, Md.A., 2010. Heavy metal contamination in water, soil, and vegetables of the industrial areas in Dhaka, Bangladesh. *Environ Monit Assess* 166, 347–357. <https://doi.org/10.1007/s10661-009-1006-6>
- Alimi, O.S., Farner Budarz, J., Hernandez, L.M., Tufenkji, N., 2018. Microplastics and Nanoplastics in Aquatic Environments: Aggregation, Deposition, and Enhanced Contaminant Transport. *Environmental Science & Technology* 52, 1704–1724. <https://doi.org/10.1021/acs.est.7b05559>
- Allen, S., Allen, D., Phoenix, V.R., Le Roux, G., Durántez Jiménez, P., Simonneau, A., Binet, S., Galop, D., 2019. Atmospheric transport and deposition of microplastics in a remote mountain catchment. *Nat. Geosci.* 12, 339–344. <https://doi.org/10.1038/s41561-019-0335-5>
- Alnaizy, R., Akgerman, A., 2000. Advanced oxidation of phenolic compounds. *Advances in Environmental Research* 4, 233–244. [https://doi.org/10.1016/S1093-0191\(00\)00024-1](https://doi.org/10.1016/S1093-0191(00)00024-1)
- Andrady, A.L., 2011. Microplastics in the marine environment. *Marine Pollution Bulletin* 62, 1596–1605. <https://doi.org/10.1016/j.marpolbul.2011.05.030>
- Andrady, A.L. (Ed.), 2003. *Plastics and the environment*. Wiley-Interscience, Hoboken, N.J.
- Balakrishnan, G., Déniel, M., Nicolai, T., Chassenieux, C., Lagarde, F., 2019. Towards more realistic reference microplastics and nanoplastics: preparation of polyethylene micro/nanoparticles with a biosurfactant. *Environmental Science: Nano* 6, 315–324. <https://doi.org/10.1039/C8EN01005F>
- Bargar, J.R., Brown, G.E., Parks, G.A., 1997. Surface complexation of Pb(II) at oxide-water interfaces: I. XAFS and bond-valence determination of mononuclear and polynuclear Pb(II) sorption products on aluminum oxides. *Geochimica et Cosmochimica Acta* 61, 2617–2637. [https://doi.org/10.1016/S0016-7037\(97\)00124-5](https://doi.org/10.1016/S0016-7037(97)00124-5)
- Barnes, D.K.A., Galgani, F., Thompson, R.C., Barlaz, M., 2009. Accumulation and fragmentation of plastic debris in global environments. *Phil. Trans. R. Soc. B* 364, 1985–1998. <https://doi.org/10.1098/rstb.2008.0205>
- Baudrimont, M., Arini, A., Guégan, C., Venel, Z., Gigault, J., Pedrono, B., Prunier, J., Maurice, L., Ter Halle, A., Feurtet-Mazel, A., 2020. Ecotoxicity of polyethylene nanoplastics from the North Atlantic oceanic gyre on freshwater and marine organisms (microalgae and filter-feeding bivalves). *Environ Sci Pollut Res* 27, 3746–3755. <https://doi.org/10.1007/s11356-019-04668-3>
- Bellingeri, A., Bergami, E., Grassi, G., Faleri, C., Redondo-Hasselerharm, P., Koelmans, A.A., Corsi, I., 2019. Combined effects of nanoplastics and copper on the freshwater alga *Raphidocelis subcapitata*. *Aquatic Toxicology* 210, 179–187. <https://doi.org/10.1016/j.aquatox.2019.02.022>

- Bergami, E., Krupinski Emerenciano, A., González-Aravena, M., Cárdenas, C.A., Hernández, P., Silva, J.R.M.C., Corsi, I., 2019. Polystyrene nanoparticles affect the innate immune system of the Antarctic sea urchin *Sterechinus neumayeri*. *Polar Biology* 42, 743–757. <https://doi.org/10.1007/s00300-019-02468-6>
- Besseling, E., Redondo-Hasselerharm, P., Foekema, E.M., Koelmans, A.A., 2019. Quantifying ecological risks of aquatic micro- and nanoplastic. *Critical Reviews in Environmental Science and Technology* 49, 32–80. <https://doi.org/10.1080/10643389.2018.1531688>
- Besseling, E., Wang, B., Lüring, M., Koelmans, A.A., 2014. Nanoplastic affects growth of *S. obliquus* and reproduction of *D. magna*. *Environmental Science and Technology* 48, 12336–12343. <https://doi.org/10.1021/es503001d>
- Bhattacharya, P., Lin, S., Turner, J.P., Ke, P.C., 2010. Physical Adsorption of Charged Plastic Nanoparticles Affects Algal Photosynthesis. *The Journal of Physical Chemistry C* 114, 16556–16561. <https://doi.org/10.1021/jp1054759>
- Bianco, A., Sordello, F., Ehn, M., Vione, D., Passananti, M., 2020. Degradation of nanoplastics in the environment: Reactivity and impact on atmospheric and surface waters. *Science of The Total Environment* 742, 140413. <https://doi.org/10.1016/j.scitotenv.2020.140413>
- Biller, P., Ross, A.B., 2014. Pyrolysis GC–MS as a novel analysis technique to determine the biochemical composition of microalgae. *Algal Research* 6, 91–97. <https://doi.org/10.1016/j.algal.2014.09.009>
- Blanco, F., Davranche, M., Fumagalli, F., Ceccone, G., Gigault, J., 2021a. A reliable procedure to obtain environmentally relevant nanoplastic proxies. *ES nano*.
- Blanco, F., Davranche, M., Hadri, H.E., Grassl, B., Gigault, J., 2021b. Nanoplastics Identification in Complex Environmental Matrices: Strategies for Polystyrene and Polypropylene. *Environ. Sci. Technol.* [acs.est.1c01351](https://doi.org/10.1021/acs.est.1c01351). <https://doi.org/10.1021/acs.est.1c01351>
- Blanco, F., Davranche, M., Léon, A., Grassl, B., Reynaud, S., Gigault, J., Submitted. Metals binding processes on Nanoplastics : Rare earth elements as a probe. *Environ. Sci.: Nano*.
- Brachner, A., Fragouli, D., Duarte, I.F., Farias, P.M.A., Dembski, S., Ghosh, M., Barisic, I., Zdziebło, D., Vanoirbeek, J., Schwabl, P., Neuhaus, W., 2020. Assessment of Human Health Risks Posed by Nano-and Microplastics Is Currently Not Feasible. *IJERPH* 17, 8832. <https://doi.org/10.3390/ijerph17238832>
- Brennecke, D., Duarte, B., Paiva, F., Caçador, I., Canning-Clode, J., 2016. Microplastics as vector for heavy metal contamination from the marine environment. *Estuarine, Coastal and Shelf Science* 178, 189–195. <https://doi.org/10.1016/j.ecss.2015.12.003>
- Brignac, K.C., Jung, M.R., King, C., Royer, S.-J., Blickley, L., Lamson, M.R., Potemra, J.T., Lynch, J.M., 2019. Marine Debris Polymers on Main Hawaiian Island Beaches, Sea Surface, and Seafloor. *Environ. Sci. Technol.* 53, 12218–12226. <https://doi.org/10.1021/acs.est.9b03561>
- Browne, M.A., Dissanayake, A., Galloway, T.S., Lowe, D.M., Thompson, R.C., 2008. Ingested Microscopic Plastic Translocates to the Circulatory System of the Mussel, *Mytilus edulis* (L.). *Environ. Sci. Technol.* 42, 5026–5031. <https://doi.org/10.1021/es800249a>
- Byrne, R.H., Li, B., 1995. Comparative complexation behavior of the rare earths. *Geochimica et Cosmochimica Acta* 59, 4575–4589. [https://doi.org/10.1016/0016-7037\(95\)00303-7](https://doi.org/10.1016/0016-7037(95)00303-7)
- Cadene, A., Durand-Vidal, S., Turq, P., Brendle, J., 2005. Study of individual Na-montmorillonite particles size, morphology, and apparent charge. *Journal of Colloid and Interface Science* 285, 719–730. <https://doi.org/10.1016/j.jcis.2004.12.016>

- Cai, H., Xu, E.G., Du, F., Li, R., Liu, J., Shi, H., 2021. Analysis of environmental nanoplastics: Progress and challenges. *Chemical Engineering Journal* 410, 128208. <https://doi.org/10.1016/j.cej.2020.128208>
- Cai, L., Wang, J., Peng, J., Wu, Z., Tan, X., 2018. Observation of the degradation of three types of plastic pellets exposed to UV irradiation in three different environments. *Science of The Total Environment* 628–629, 740–747. <https://doi.org/10.1016/j.scitotenv.2018.02.079>
- Cannan, R.K., Kibrick, A., 1938. Complex Formation between Carboxylic Acids and Divalent Metal Cations. *J. Am. Chem. Soc.* 60, 2314–2320. <https://doi.org/10.1021/ja01277a012>
- Carbonaro, R.F., Di Toro, D.M., 2007. Linear free energy relationships for metal–ligand complexation: Monodentate binding to negatively-charged oxygen donor atoms. *Geochimica et Cosmochimica Acta* 71, 3958–3968. <https://doi.org/10.1016/j.gca.2007.06.005>
- Carr, A.S., Boom, A., Chase, B.M., Roberts, D.L., Roberts, Z.E., 2010. Molecular fingerprinting of wetland organic matter using pyrolysis-GC/MS: an example from the southern Cape coastline of South Africa. *Journal of Paleolimnology* 44, 947–961. <https://doi.org/10.1007/s10933-010-9466-9>
- Catrouillet, C., Davranche, M., Khatib, I., Fauny, C., Wahl, A., Gigault, J., 2021. Metals in microplastics: determining which are additive, adsorbed, and bioavailable. *Environ. Sci.: Processes Impacts* 23, 553–558. <https://doi.org/10.1039/D1EM00017A>
- Chamas, A., Moon, H., Zheng, J., Qiu, Y., Tabassum, T., Jang, J.H., Abu-Omar, M., Scott, S.L., Suh, S., 2020. Degradation Rates of Plastics in the Environment. *ACS Sustainable Chem. Eng.* 8, 3494–3511. <https://doi.org/10.1021/acssuschemeng.9b06635>
- Charmas, R., Piasecki, W., Rudzinski, W., 1995. Four Layer Complexation Model for Ion Adsorption at Electrolyte/Oxide Interface: Theoretical Foundations. *Langmuir* 11, 3199–3210. <https://doi.org/10.1021/la00008a053>
- Chee, S.-Y., Wong, P.-K., Wong, C.-L., 2011. Extraction and characterisation of alginate from brown seaweeds (Fucales, Phaeophyceae) collected from Port Dickson, Peninsular Malaysia. *J Appl Phycol* 23, 191–196. <https://doi.org/10.1007/s10811-010-9533-7>
- Chen, J., Hu, J., Xu, Y., Krasny, R., Geng, W., 2021. Computing Protein pKas Using the TABI Poisson–Boltzmann Solver. *J. Comput. Biophys. Chem.* 20, 175–187. <https://doi.org/10.1142/S2737416520420065>
- Chen, Q., Yin, D., Jia, Y., Schiwiy, S., Legradi, J., Yang, S., Hollert, H., 2017. Enhanced uptake of BPA in the presence of nanoplastics can lead to neurotoxic effects in adult zebrafish. *Science of The Total Environment* 609, 1312–1321. <https://doi.org/10.1016/j.scitotenv.2017.07.144>
- Christy, A.A., Bruchet, A., Rybacki, D., 1998. CHARACTERIZATION OF NATURAL ORGANIC MATTER BY PYROLYSWGC-MS 9.
- Coble, P.G., 1996. Characterization of marine and terrestrial DOM in seawater using excitation-emission matrix spectroscopy. *Marine Chemistry* 51, 325–346. [https://doi.org/10.1016/0304-4203\(95\)00062-3](https://doi.org/10.1016/0304-4203(95)00062-3)
- Connors, K.A., 1990. *Chemical kinetics: the study of reaction rates in solution*. VCH, New York, N.Y.

- Cozar, A., Echevarria, F., Gonzalez-Gordillo, J.I., Irigoien, X., Ubeda, B., Hernandez-Leon, S., Palma, A.T., Navarro, S., Garcia-de-Lomas, J., Ruiz, A., Fernandez-de-Puelles, M.L., Duarte, C.M., 2014. Plastic debris in the open ocean. *Proceedings of the National Academy of Sciences* 111, 10239–10244. <https://doi.org/10.1073/pnas.1314705111>
- da Costa, J.P., Santos, P.S.M., Duarte, A.C., Rocha-Santos, T., 2016. (Nano)plastics in the environment – Sources, fates and effects. *Science of The Total Environment* 566–567, 15–26. <https://doi.org/10.1016/j.scitotenv.2016.05.041>
- Davranche, M., Grybos, M., Gruau, G., Pédrot, M., Dia, A., Marsac, R., 2011. Rare earth element patterns: A tool for identifying trace metal sources during wetland soil reduction. *Chemical Geology* 284, 127–137. <https://doi.org/10.1016/j.chemgeo.2011.02.014>
- Davranche, M., Lory, C., Juge, C.L., Blancho, F., Dia, A., Grassl, B., El Hadri, H., Pascal, P.-Y., Gigault, J., 2020. Nanoplastics on the Coast Exposed to the North Atlantic Gyre: Evidence and Traceability. *NanoImpact* 100262. <https://doi.org/10.1016/j.impact.2020.100262>.
- Davranche, M., Pourret, O., Gruau, G., Dia, A., Le Coz-Bouhnik, M., 2005. Adsorption of REE(III)-humate complexes onto MnO₂: Experimental evidence for cerium anomaly and lanthanide tetrad effect suppression. *Geochimica et Cosmochimica Acta* 69, 4825–4835. <https://doi.org/10.1016/j.gca.2005.06.005>
- Davranche, M., Veclin, C., Pierson-Wickmann, A.-C., El Hadri, H., Grassl, B., Roweczyk, L., Dia, A., Ter Halle, A., Blancho, F., Reynaud, S., Gigault, J., 2019. Are nanoplastics able to bind significant amount of metals? The lead example. *Environmental Pollution* 249, 940–948. <https://doi.org/10.1016/j.envpol.2019.03.087>
- Dawson, A.L., Kawaguchi, S., King, C.K., Townsend, K.A., King, R., Huston, W.M., Bengtson Nash, S.M., 2018. Turning microplastics into nanoplastics through digestive fragmentation by Antarctic krill. *Nature Communications* 9. <https://doi.org/10.1038/s41467-018-03465-9>
- de Baar, H.J.W., Schijf, J., Byrne, R.H., 1991. Solution chemistry of the rare earth elements in seawater. *European Journal of Solid State and Inorganic Chemistry*, 357–373.
- de Jonge, H., Mittelmeijer-Hazeleger, M.C., 1996. Adsorption of CO₂ and N₂ on Soil Organic Matter: Nature of Porosity, Surface Area, and Diffusion Mechanisms. *Environ. Sci. Technol.* 30, 408–413. <https://doi.org/10.1021/es950043t>
- De Stefano, C., Gianguzza, A., Piazzese, D., Sammartano, S., 2000. Polyacrylate Protonation in Various Aqueous Ionic Media at Different Temperatures and Ionic Strengths. *J. Chem. Eng. Data* 45, 876–881. <https://doi.org/10.1021/je0000219>
- Deanin, R.D., 1975. Additives in plastics. *Environmental Health Perspectives* 11, 35–39. <https://doi.org/10.1289/ehp.751135>
- Dehaut, A., Cassone, A.-L., Frère, L., Hermabessiere, L., Himber, C., Rinnert, E., Rivière, G., Lambert, C., Soudant, P., Huvet, A., Duflos, G., Paul-Pont, I., 2016. Microplastics in seafood: Benchmark protocol for their extraction and characterization. *Environmental Pollution* 215, 223–233. <https://doi.org/10.1016/j.envpol.2016.05.018>
- Della Torre, C., Bergami, E., Salvati, A., Faleri, C., Cirino, P., Dawson, K.A., Corsi, I., 2014. Accumulation and Embryotoxicity of Polystyrene Nanoparticles at Early Stage of Development of Sea Urchin Embryos *Paracentrotus lividus*. *Environmental Science & Technology* 48, 12302–12311. <https://doi.org/10.1021/es502569w>
- Dierkes, G., Lauschke, T., Becher, S., Schumacher, H., Földi, C., Ternes, T., 2019. Quantification of microplastics in environmental samples via pressurized liquid extraction and pyrolysis-gas chromatography. *Anal Bioanal Chem* 411, 6959–6968. <https://doi.org/10.1007/s00216-019-02066-9>

- Dignac, M.-F., Houot, S., Francou, C., Derenne, S., 2005. Pyrolytic study of compost and waste organic matter. *Organic Geochemistry* 36, 1054–1071. <https://doi.org/10.1016/j.orggeochem.2005.02.007>
- Dobrinčić, A., Balbino, S., Zorić, Z., Pedisić, S., Bursać Kovačević, D., Elez Garofulić, I., Dragović-Uzelac, V., 2020. Advanced Technologies for the Extraction of Marine Brown Algal Polysaccharides. *Marine Drugs* 18, 168. <https://doi.org/10.3390/md18030168>
- Dong, S., Cai, W., Xia, J., Sheng, L., Wang, W., Liu, H., 2021. Aggregation kinetics of fragmental PET nanoplastics in aqueous environment: Complex roles of electrolytes, pH and humic acid. *Environmental Pollution* 268, 115828. <https://doi.org/10.1016/j.envpol.2020.115828>
- Dong, Y., Gao, M., Qiu, W., Song, Z., 2020. Adsorption of arsenite to polystyrene microplastics in the presence of humus. *Environ. Sci.: Processes Impacts* 22, 2388–2397. <https://doi.org/10.1039/D0EM00324G>
- Dümichen, E., Barthel, A.-K., Braun, U., Bannick, C.G., Brand, K., Jekel, M., Senz, R., 2015. Analysis of polyethylene microplastics in environmental samples, using a thermal decomposition method. *Water Research* 85, 451–457. <https://doi.org/10.1016/j.watres.2015.09.002>
- Dümichen, E., Eisentraut, P., Bannick, C.G., Barthel, A.-K., Senz, R., Braun, U., 2017. Fast identification of microplastics in complex environmental samples by a thermal degradation method. *Chemosphere* 174, 572–584. <https://doi.org/10.1016/j.chemosphere.2017.02.010>
- Dzombak, D.A., Morel, F.M.M., 1990. Surface complexation modeling: hydrous ferric oxide. Wiley, New York.
- El Hadri, H., Gigault, J., Maxit, B., Grassl, B., Reynaud, S., 2020. Nanoplastic from mechanically degraded primary and secondary microplastics for environmental assessments. *NanoImpact* 17, 100206. <https://doi.org/10.1016/j.impact.2019.100206>
- Environmental Protection Agency, 2016. Definition and Procedure for the Determination of the Method Detection Limit, Revision 2 (No. EPA 821-R-16-006).
- Eriksson, C., Burton, H., 2003. Origins and Biological Accumulation of Small Plastic Particles in Fur Seals from Macquarie Island. *AMBIO: A Journal of the Human Environment* 32, 380–384. <https://doi.org/10.1579/0044-7447-32.6.380>
- Fabbri, D., 2001. Use of pyrolysis-gas chromatography/mass spectrometry to study environmental pollution caused by synthetic polymers: a case study: the Ravenna Lagoon. *Journal of Analytical and Applied Pyrolysis* 58–59, 361–370. [https://doi.org/10.1016/S0165-2370\(00\)00170-4](https://doi.org/10.1016/S0165-2370(00)00170-4)
- Fabbri, D., Trombini, C., Vassura, I., 1998. Analysis of Polystyrene in Polluted Sediments by Pyrolysis--Gas Chromatography--Mass Spectrometry. *Journal of Chromatographic Science* 36, 600–604. <https://doi.org/10.1093/chromsci/36.12.600>
- Fischer, M., Scholz-Böttcher, B.M., 2019. Microplastics analysis in environmental samples – recent pyrolysis-gas chromatography-mass spectrometry method improvements to increase the reliability of mass-related data. *Anal. Methods* 11, 2489–2497. <https://doi.org/10.1039/C9AY00600A>
- Fischer, M., Scholz-Böttcher, B.M., 2017. Simultaneous Trace Identification and Quantification of Common Types of Microplastics in Environmental Samples by Pyrolysis-Gas Chromatography–Mass Spectrometry. *Environ. Sci. Technol.* 51, 5052–5060. <https://doi.org/10.1021/acs.est.6b06362>

- Fitts, J.P., Trainor, T.P., Grolimund, D., Bargar, J.R., Parks, G.A., Brown, G.E., 1999. Grazing-incidence XAFS investigations of Cu(II) sorption products at α -Al₂O₃ – water and α -SiO₂ –water interfaces. *J Synchrotron Rad* 6, 627–629. <https://doi.org/10.1107/S0909049599001375>
- Flick, E.W., 2013. *Plastics Additives, Volume 1: An Industry Guide*. Elsevier.
- Fonseca, B., Maio, H., Quintelas, C., Teixeira, A., Tavares, T., 2009. Retention of Cr(VI) and Pb(II) on a loamy sand soil. *Chemical Engineering Journal* 152, 212–219. <https://doi.org/10.1016/j.cej.2009.04.045>
- Fotopoulou, K.N., Karapanagioti, H.K., 2012. Surface properties of beached plastic pellets. *Marine Environmental Research* 81, 70–77. <https://doi.org/10.1016/j.marenvres.2012.08.010>
- Fries, E., Dekiff, J.H., Willmeyer, J., Nuelle, M.-T., Ebert, M., Remy, D., 2013. Identification of polymer types and additives in marine microplastic particles using pyrolysis-GC/MS and scanning electron microscopy. *Environmental Science: Processes & Impacts* 15, 1949. <https://doi.org/10.1039/c3em00214d>
- Galli, M., Saringer, S., Szilagyi, I., Trefalt, G., 2020. A Simple Method to Determine Critical Coagulation Concentration from Electrophoretic Mobility. *Colloids and Interfaces* 4, 20. <https://doi.org/10.3390/colloids4020020>
- Geng, J., Cheng, S., Fang, H., Pei, J., Xu, M., Lu, M., Yang, Y., Cao, Z., Li, Y., 2019. Different Molecular Characterization of Soil Particulate Fractions under N Deposition in a Subtropical Forest. *Forests* 10, 914. <https://doi.org/10.3390/f10100914>
- Gewert, B., Plassmann, M.M., MacLeod, M., 2015. Pathways for degradation of plastic polymers floating in the marine environment.
- Geyer, R., Jambeck, J.R., Law, K.L., 2017. Production, use, and fate of all plastics ever made. *Science Advances* 3, e1700782. <https://doi.org/10.1126/sciadv.1700782>
- Gigault, J., 2018. Current opinion: What is a nanoplastic? *Environ. Pollut* 235, 1030–1034.
- Gigault, J., El Hadri, H., Nguyen, B., Grassl, B., Roweczyk, L., Tufenkji, N., Feng, S., Wiesner, M., 2021. Nanoplastics are neither microplastics nor engineered nanoparticles. *Nat. Nanotechnol.* 16, 501–507. <https://doi.org/10.1038/s41565-021-00886-4>
- Gigault, J., Halle, A. ter, Baudrimont, M., Pascal, P.-Y., Gauffre, F., Phi, T.-L., El Hadri, H., Grassl, B., Reynaud, S., 2018. Current opinion: What is a nanoplastic? *Environmental Pollution* 235, 1030–1034. <https://doi.org/10.1016/j.envpol.2018.01.024>
- Gigault, J., Pedrono, B., Maxit, B., Ter Halle, A., 2016. Marine plastic litter: The unanalyzed nano-fraction. *Environmental Science: Nano* 3, 346–350. <https://doi.org/10.1039/c6en00008h>
- Gil-Díaz, T., Jara-Heredia, D., Heberling, F., Lützenkirchen, J., Link, J., Sowoidnich, T., Ludwig, H.-M., Haist, M., Schäfer, T., 2021. Charge regulated solid-liquid interfaces interacting on the nanoscale: Benchmarking of a generalized speciation code (SINFONIA). *Advances in Colloid and Interface Science* 294, 102469. <https://doi.org/10.1016/j.cis.2021.102469>
- Gillam, A.H., Wilson, M.A., 1985. Pyrolysis-GC-MS and NMR studies of dissolved seawater humic substances and isolates of a marine diatom. *Organic Geochemistry* 8, 15–25. [https://doi.org/10.1016/0146-6380\(85\)90046-4](https://doi.org/10.1016/0146-6380(85)90046-4)
- Gong, Y.-K., Nakashima, K., Xu, R., 2001. A Novel Method To Determine Effective Charge of Polystyrene Latex Particles in Aqueous Dispersion. *Langmuir* 17, 2889–2892. <https://doi.org/10.1021/la001483n>

- Graf, C., Deggelmann, M., Hagenbüchle, M., Johner, C., Kramer, H., Krause, R., Weber, R., 1992. Dynamic Light Scattering by Aqueous Solutions of Rod-Like FD-Virus Particles, in: Chen, S.-H., Huang, J.S., Tartaglia, P. (Eds.), *Structure and Dynamics of Strongly Interacting Colloids and Supramolecular Aggregates in Solution*, NATO ASI Series. Springer Netherlands, Dordrecht, pp. 827–830. https://doi.org/10.1007/978-94-011-2540-6_46
- Graiff, A., Ruth, W., Kragl, U., Karsten, U., 2016. Chemical characterization and quantification of the brown algal storage compound laminarin — A new methodological approach. *J Appl Phycol* 28, 533–543. <https://doi.org/10.1007/s10811-015-0563-z>
- Guo, X., Wang, J., 2021. Projecting the sorption capacity of heavy metal ions onto microplastics in global aquatic environments using artificial neural networks. *Journal of Hazardous Materials* 402, 123709. <https://doi.org/10.1016/j.jhazmat.2020.123709>
- Guo, X., Wang, J., 2019. The phenomenological mass transfer kinetics model for Sr²⁺ sorption onto spheroids primary microplastics. *Environmental Pollution* 250, 737–745. <https://doi.org/10.1016/j.envpol.2019.04.091>
- Gustafsson, J., 2010. Visual MINTEQ, version 3.0: a window version of MINTEQA2, version 4.0.
- Hahladakis, J.N., Velis, C.A., Weber, R., Iacovidou, E., Purnell, P., 2018. An overview of chemical additives present in plastics: Migration, release, fate and environmental impact during their use, disposal and recycling. *Journal of Hazardous Materials* 344, 179–199. <https://doi.org/10.1016/j.jhazmat.2017.10.014>
- Hartmann, N.B., Hüffer, T., Thompson, R.C., Hassellöv, M., Verschoor, A., Daugaard, A.E., Rist, S., Karlsson, T., Brennholt, N., Cole, M., Herrling, M.P., Hess, M.C., Ivleva, N.P., Lusher, A.L., Wagner, M., 2019. Are We Speaking the Same Language? Recommendations for a Definition and Categorization Framework for Plastic Debris. *Environ. Sci. Technol.* 53, 1039–1047. <https://doi.org/10.1021/acs.est.8b05297>
- Hesleitner, P., Babic, D., Kallay, N., Matijevic, E., 1987. Adsorption at solid/solution interfaces. 3. Surface charge and potential of colloidal hematite. *Langmuir* 3, 815–820. <https://doi.org/10.1021/la00077a041>
- Hiemstra, T., Van Riemsdijk, W.H., 2009. A surface structural model for ferrihydrite I: Sites related to primary charge, molar mass, and mass density. *Geochimica et Cosmochimica Acta* 73, 4423–4436. <https://doi.org/10.1016/j.gca.2009.04.032>
- Horton, A.A., Walton, A., Spurgeon, D.J., Lahive, E., Svendsen, C., 2017. Microplastics in freshwater and terrestrial environments: Evaluating the current understanding to identify the knowledge gaps and future research priorities. *Science of the Total Environment* 586, 127–141. <https://doi.org/10.1016/j.scitotenv.2017.01.190>
- Huang, Y., Eglinton, G., Van Der Hage, E.R.E., Boon, J.J., Bol, R., Ineson, P., 1998. Dissolved organic matter and its parent organic matter in grass upland soil horizons studied by analytical pyrolysis techniques. *European Journal of Soil Science* 49, 1–15. <https://doi.org/10.1046/j.1365-2389.1998.00141.x>
- Huguet, A., Vacher, L., Relexans, S., Saubusse, S., Froidefond, J.M., Parlanti, E., 2009. Properties of fluorescent dissolved organic matter in the Gironde Estuary. *Organic Geochemistry* 40, 706–719. <https://doi.org/10.1016/j.orggeochem.2009.03.002>
- Hurley, R.R., Lusher, A.L., Olsen, M., Nizzetto, L., 2018. Validation of a Method for Extracting Microplastics from Complex, Organic-Rich, Environmental Matrices. *Environmental Science & Technology* 52, 7409–7417. <https://doi.org/10.1021/acs.est.8b01517>

- Ibarra-Montaño, E.L., Rodríguez-Laguna, N., Aníbal Sánchez-Hernández, A., Rojas-Hernández, A., 2015. Determination of pKa Values for Acrylic, Methacrylic and Itaconic Acids by ¹H and ¹³C NMR in Deuterated Water. *J. Appl. Sol. Chem. Model.* 4, 7–18. <https://doi.org/10.6000/1929-5030.2015.04.01.2>
- Ishiwatari, R., Yamamoto, S., Handa, N., 1995. Characterization of sinking particles in the ocean by pyrolysis-gas chromatography/mass spectrometry. *Journal of Analytical and Applied Pyrolysis* 32, 75–89. [https://doi.org/10.1016/0165-2370\(94\)00874-Z](https://doi.org/10.1016/0165-2370(94)00874-Z)
- Jambeck, J.R., Geyer, R., Wilcox, C., Siegler, T.R., Perryman, M., Andrady, A., Narayan, R., Law, K.L., 2015. Plastic waste inputs from land into the ocean 5.
- Jeon, I., Nam, K., 2019. Change in the site density and surface acidity of clay minerals by acid or alkali spills and its effect on pH buffering capacity. *Sci Rep* 9, 9878. <https://doi.org/10.1038/s41598-019-46175-y>
- Jiang, L.-Q., Carter, B.R., Feely, R.A., Lauvset, S.K., Olsen, A., 2019. Surface ocean pH and buffer capacity: past, present and future. *Sci Rep* 9, 18624. <https://doi.org/10.1038/s41598-019-55039-4>
- Jiang, X., Tian, L., Ma, Y., Ji, R., 2019. Quantifying the bioaccumulation of nanoplastics and PAHs in the clamworm *Perinereis aibuhitensis*. *Science of The Total Environment* 655, 591–597. <https://doi.org/10.1016/j.scitotenv.2018.11.227>
- Kaal, J., Wagner, S., Jaffé, R., 2016. Molecular properties of ultrafiltered dissolved organic matter and dissolved black carbon in headwater streams as determined by pyrolysis-GC-MS. *Journal of Analytical and Applied Pyrolysis* 118, 181–191. <https://doi.org/10.1016/j.jaap.2016.02.003>
- Kalogerakis, N., Karkanorachaki, K., Kalogerakis, G.C., Triantafyllidi, E.I., Gotsis, A.D., Partsinevelos, P., Fava, F., 2017. Microplastics Generation: Onset of Fragmentation of Polyethylene Films in Marine Environment Mesocosms. *Frontiers in Marine Science* 4. <https://doi.org/10.3389/fmars.2017.00084>
- Kashiwada, S., 2006. Distribution of Nanoparticles in the See-through Medaka (*Oryzias latipes*). *Environmental Health Perspectives* 114, 1697–1702. <https://doi.org/10.1289/ehp.9209>
- Kelly, T., Matos, G., 2005. Data Series (Data Series), *Data Series*.
- Kinniburgh, D., Cooper, D., 2011. PhreePlot: Creating graphical output with PHREEQC.
- Koelmans, A.A., Diepens, N.J., Velzeboer, I., Besseling, E., Quik, J.T.K., van de Meent, D., 2015. Guidance for the prognostic risk assessment of nanomaterials in aquatic ecosystems. *Science of The Total Environment* 535, 141–149. <https://doi.org/10.1016/j.scitotenv.2015.02.032>
- Komárek, M., Antelo, J., Králová, M., Veselská, V., Číhalová, S., Chrastný, V., Ettler, V., Filip, J., Yu, Q., Fein, J.B., Koretsky, C.M., 2018. Revisiting models of Cd, Cu, Pb and Zn adsorption onto Fe(III) oxides. *Chemical Geology* 493, 189–198. <https://doi.org/10.1016/j.chemgeo.2018.05.036>
- Koziara, J.M., Lockman, P.R., Allen, D.D., Mumper, R.J., 2003. *In Situ* Blood–Brain Barrier Transport of Nanoparticles. *Pharm Res* 20, 1772–1778. <https://doi.org/10.1023/B:PHAM.0000003374.58641.62>
- Kühn, S., van Werven, B., van Oyen, A., Meijboom, A., Bravo Rebolledo, E.L., van Franeker, J.A., 2017. The use of potassium hydroxide (KOH) solution as a suitable approach to isolate plastics ingested by marine organisms. *Marine Pollution Bulletin* 115, 86–90. <https://doi.org/10.1016/j.marpolbul.2016.11.034>
- Lai, Y., Sheng, X., Dong, L., Li, P., Li, Q., Yu, S., Zhou, Q., Liu, J., 2021. Digestive Elimination of Coexisting Microplastics for Determination of Particulate Black Carbon in Environmental Waters. *Anal. Chem.* 93, 11184–11190. <https://doi.org/10.1021/acs.analchem.1c01727>

- Lambert, S., Sinclair, C.J., Bradley, E.L., Boxall, A.B.A., 2013. Effects of environmental conditions on latex degradation in aquatic systems. *Science of The Total Environment* 447, 225–234. <https://doi.org/10.1016/j.scitotenv.2012.12.067>
- Lambert, S., Wagner, M., 2016. Characterisation of Nanoplastics during the Degradation of Polystyrene. *Chemosphere* 145, 265–268. <https://doi.org/10.1016/j.chemosphere.2015.11.078>.
- Law, K.L., Moret-Ferguson, S., Maximenko, N.A., Proskurowski, G., Peacock, E.E., Hafner, J., Reddy, C.M., 2010. Plastic Accumulation in the North Atlantic Subtropical Gyre. *Science* 329, 1185–1188. <https://doi.org/10.1126/science.1192321>
- Le Forestier, L., Muller, F., Villieras, F., Pelletier, M., 2010. Textural and hydration properties of a synthetic montmorillonite compared with a natural Na-exchanged clay analogue. *Applied Clay Science* 48, 18–25. <https://doi.org/10.1016/j.clay.2009.11.038>
- Leenheer, J.A., Wershaw, R.L., Reddy, M.M., 1995. Strong-Acid, Carboxyl-Group Structures in Fulvic Acid from the Suwannee River, Georgia. 1. Minor Structures. *Environ. Sci. Technol.* 29, 393–398. <https://doi.org/10.1021/es00002a015>
- Lieshout, C., Oeveren, K., Emmerik, T., Postma, E., 2020. Automated River Plastic Monitoring Using Deep Learning and Cameras. *Earth and Space Science* 7. <https://doi.org/10.1029/2019EA000960>
- Liu, H., Pierre-Pierre, N., Huo, Q., 2012. Dynamic light scattering for gold nanorod size characterization and study of nanorod–protein interactions. *Gold Bull* 45, 187–195. <https://doi.org/10.1007/s13404-012-0067-4>
- Liu, H., Pourret, O., Guo, H., Bonhoure, J., 2017. Rare earth elements sorption to iron oxyhydroxide: Model development and application to groundwater. *Applied Geochemistry* 87, 158–166. <https://doi.org/10.1016/j.apgeochem.2017.10.020>
- Liu, L., Song, J., Zhang, M., Jiang, W., 2021. Aggregation and Deposition Kinetics of Polystyrene Microplastics and Nanoplastics in Aquatic Environment. *Bull Environ Contam Toxicol.* <https://doi.org/10.1007/s00128-021-03239-y>
- Lofts, S., Tipping, E., 1998. An assemblage model for cation binding by natural particulate matter. *Geochimica et Cosmochimica Acta* 62, 2609–2625. [https://doi.org/10.1016/S0016-7037\(98\)00183-5](https://doi.org/10.1016/S0016-7037(98)00183-5)
- Lövgren, L., Sjöberg, S., Schindler, P.W., 1990. Acid/base reactions and Al(III) complexation at the surface of goethite. *Geochimica et Cosmochimica Acta* 54, 1301–1306. [https://doi.org/10.1016/0016-7037\(90\)90154-D](https://doi.org/10.1016/0016-7037(90)90154-D)
- Luan, H., Vadas, T.M., 2015. Size characterization of dissolved metals and organic matter in source waters to streams in developed landscapes. *Environmental Pollution* 197, 76–83. <https://doi.org/10.1016/j.envpol.2014.12.004>
- Lützenkirchen, J., van Male, J., Leermakers, F., Sjöberg, S., 2011. Comparison of Various Models to Describe the Charge–pH Dependence of Poly(acrylic acid). *J. Chem. Eng. Data* 56, 1602–1612. <https://doi.org/10.1021/je101253q>
- Maddi, B., Viamajala, S., Varanasi, S., 2011. Comparative study of pyrolysis of algal biomass from natural lake blooms with lignocellulosic biomass. *Bioresource Technology* 102, 11018–11026. <https://doi.org/10.1016/j.biortech.2011.09.055>
- Magri, D., Sánchez-Moreno, P., Caputo, G., Gatto, F., Veronesi, M., Bardi, G., Catelani, T., Guarnieri, D., Athanassiou, A., Pompa, P.P., Fragouli, D., 2018. Laser Ablation as a Versatile Tool To Mimic Polyethylene Terephthalate Nanoplastic Pollutants: Characterization and Toxicology Assessment. *ACS Nano* 12, 7690–7700. <https://doi.org/10.1021/acsnano.8b01331>
- Maguire, C.M., Rösslein, M., Wick, P., Prina-Mello, A., 2018. Characterisation of particles in solution – a perspective on light scattering and comparative technologies. *Sci Technol Adv Mater* 19, 732–745. <https://doi.org/10.1080/14686996.2018.1517587>

- Marsac, R., Davranche, M., Gruau, G., Bouhnik-Le Coz, M., Dia, A., 2011. An improved description of the interactions between rare earth elements and humic acids by modeling: PHREEQC-Model VI coupling. *Geochimica et Cosmochimica Acta* 75, 5625–5637. <https://doi.org/10.1016/j.gca.2011.07.009>
- Marsac, R., Davranche, M., Gruau, G., Dia, A., 2010. Metal loading effect on rare earth element binding to humic acid: Experimental and modelling evidence. *Geochimica et Cosmochimica Acta* 74, 1749–1761. <https://doi.org/10.1016/j.gca.2009.12.006>
- Marsac, R., Davranche, M., Gruau, G., Dia, A., Bouhnik-Le Coz, M., 2012. Aluminium competitive effect on rare earth elements binding to humic acid. *Geochimica et Cosmochimica Acta* 89, 1–9. <https://doi.org/10.1016/j.gca.2012.04.028>
- Marsac, R., Davranche, M., Gruau, G., Dia, A., Pédrot, M., Le Coz-Bouhnik, M., Briant, N., 2013. Effects of Fe competition on REE binding to humic acid: Origin of REE pattern variability in organic waters. *Chemical Geology* 342, 119–127. <https://doi.org/10.1016/j.chemgeo.2013.01.020>
- Martell, A.E., Smith, R.M., 1977. *Other Organic Ligands*. Springer US, Boston, MA. <https://doi.org/10.1007/978-1-4757-1568-2>
- Martin, J.-M., Dai, M.-H., Cauwet, G., 1995. Significance of colloids in the biogeochemical cycling of organic carbon and trace metals in the Venice Lagoon (Italy). *Limnol. Oceanogr.* 40, 119–131. <https://doi.org/10.4319/lo.1995.40.1.0119>
- Materić, D., Kasper-Giebl, A., Kau, D., Anten, M., Greilinger, M., Ludewig, E., van Sebille, E., Röckmann, T., Holzinger, R., 2020. Micro- and Nanoplastics in Alpine Snow: A New Method for Chemical Identification and (Semi)Quantification in the Nanogram Range. *Environ. Sci. Technol.* 54, 2353–2359. <https://doi.org/10.1021/acs.est.9b07540>
- Materić, D., Peacock, M., Dean, J., Futter, M., Maximov, T., Moldan, F., Röckmann, T., Holzinger, R., 2021. Presence of nanoplastics in rural and remote surface waters (preprint). In Review. <https://doi.org/10.21203/rs.3.rs-548844/v1>
- Mattson, M.D., 1999. Acid lakes and rivers, in: *Environmental Geology, Encyclopedia of Earth Science*. Kluwer Academic Publishers, Dordrecht, pp. 6–9. https://doi.org/10.1007/1-4020-4494-1_4
- Mattsson, K., Jovic, S., Doverbratt, I., Hansson, L.-A., 2018. Nanoplastics in the Aquatic Environment, in: *Microplastic Contamination in Aquatic Environments*. Elsevier, pp. 379–399. <https://doi.org/10.1016/B978-0-12-813747-5.00013-8>
- McLennan, S.M., 1994. Rare earth element geochemistry and the “tetrad” effect. *Geochimica et Cosmochimica Acta* 58, 2025–2033. [https://doi.org/10.1016/0016-7037\(94\)90282-8](https://doi.org/10.1016/0016-7037(94)90282-8)
- Meides, N., Menzel, T., Poetzschner, B., Löder, M.G.J., Mansfeld, U., Strohriegl, P., Altstaedt, V., Senker, J., 2021. Reconstructing the Environmental Degradation of Polystyrene by Accelerated Weathering. *Environ. Sci. Technol.* 55, 7930–7938. <https://doi.org/10.1021/acs.est.0c07718>
- Min, K., Cuiffi, J.D., Mathers, R.T., 2020. Ranking environmental degradation trends of plastic marine debris based on physical properties and molecular structure. *Nat Commun* 11, 727. <https://doi.org/10.1038/s41467-020-14538-z>
- Mitrano, D.M., Beltzung, A., Frehland, S., Schmiedgruber, M., Cingolani, A., Schmidt, F., 2019. Synthesis of metal-doped nanoplastics and their utility to investigate fate and behaviour in complex environmental systems. *Nature Nanotechnology* 14, 362–368. <https://doi.org/10.1038/s41565-018-0360-3>
- Nasa, J.L., Biale, G., Ferriani, B., Trevisan, R., Colombini, M.P., Modugno, F., 2020. Plastics in Heritage Science: Analytical Pyrolysis Techniques Applied to Objects of Design. *Molecules* 25, 1705. <https://doi.org/10.3390/molecules25071705>

- Nguyen, B., Claveau-Mallet, D., Hernandez, L.M., Xu, E.G., Farner, J.M., Tufenkji, N., 2019. Separation and Analysis of Microplastics and Nanoplastics in Complex Environmental Samples. *Acc. Chem. Res.* 52, 858–866. <https://doi.org/10.1021/acs.accounts.8b00602>
- Nierop, K.G.J., van Bergen, P.F., Buurman, P., van Lagen, B., 2005. NaOH and Na₄P₂O₇ extractable organic matter in two allophanic volcanic ash soils of the Azores Islands—a pyrolysis GC/MS study. *Geoderma* 127, 36–51. <https://doi.org/10.1016/j.geoderma.2004.11.003>
- Noack, C.W., Dzombak, D.A., Karamalidis, A.K., 2014. Rare Earth Element Distributions and Trends in Natural Waters with a Focus on Groundwater. *Environ. Sci. Technol.* 48, 4317–4326. <https://doi.org/10.1021/es4053895>
- Nuelle, M.-T., Dekiff, J.H., Remy, D., Fries, E., 2014. A new analytical approach for monitoring microplastics in marine sediments. *Environmental Pollution* 184, 161–169. <https://doi.org/10.1016/j.envpol.2013.07.027>
- Nyeo, S.-L., Ansari, R.R., 2011. Sparse Bayesian learning for the Laplace transform inversion in dynamic light scattering. *Journal of Computational and Applied Mathematics* 235, 2861–2872. <https://doi.org/10.1016/j.cam.2010.12.008>
- Ojeda, T., Freitas, A., Birck, K., Dalmolin, E., Jacques, R., Bento, F., Camargo, F., 2011. Degradability of linear polyolefins under natural weathering. *Polymer Degradation and Stability* 96, 703–707. <https://doi.org/10.1016/j.polymdegradstab.2010.12.004>
- Okoffo, E.D., Ribeiro, F., O'Brien, J.W., O'Brien, S., Tschärke, B.J., Gallen, M., Samanipour, S., Mueller, J.F., Thomas, K.V., 2020. Identification and quantification of selected plastics in biosolids by pressurized liquid extraction combined with double-shot pyrolysis gas chromatography–mass spectrometry. *Science of The Total Environment* 715, 136924. <https://doi.org/10.1016/j.scitotenv.2020.136924>
- Oliveira, R.C., Hammer, P., Guibal, E., Taulemesse, J.-M., Garcia, O., 2014. Characterization of metal–biomass interactions in the lanthanum(III) biosorption on *Sargassum* sp. using SEM/EDX, FTIR, and XPS: Preliminary studies. *Chemical Engineering Journal* 239, 381–391. <https://doi.org/10.1016/j.cej.2013.11.042>
- Oppenländer, T., 2003. Photochemical Purification of Water and Air 387.
- Orts-Gil, G., Natte, K., Österle, W., 2013. Multi-parametric reference nanomaterials for toxicology: state of the art, future challenges and potential candidates. *RSC Adv.* 3, 18202. <https://doi.org/10.1039/c3ra42112k>
- Pankow, J.F., 2018. Aquatic chemistry concepts.
- Parkhurst, D.L., Appelo, C.A.J., 1999. User's guide to PHREEQC (Version 2): A computer program for speciation, batch-reaction, one-dimensional transport, and inverse geochemical calculations. <https://doi.org/10.3133/wri994259>
- Pessoni, L., Veclin, C., El Hadri, H., Cugnet, C., Davranche, M., Pierson-Wickmann, A.-C., Gigault, J., Grassl, B., Reynaud, S., 2019. Soap- and metal-free polystyrene latex particles as a nanoplastic model. *Environ. Sci.: Nano* 6, 2253–2258. <https://doi.org/10.1039/C9EN00384C>
- Pfeiffer, C., Rehbock, C., Hühn, D., Carrillo-Carrion, C., de Aberasturi, D.J., Merk, V., Barcikowski, S., Parak, W.J., 2014. Interaction of colloidal nanoparticles with their local environment: the (ionic) nanoenvironment around nanoparticles is different from bulk and determines the physico-chemical properties of the nanoparticles. *J. R. Soc. Interface.* 11, 20130931. <https://doi.org/10.1098/rsif.2013.0931>
- Pikuda, O., Xu, E.G., Berk, D., Tufenkji, N., 2018. Toxicity Assessments of Micro- and Nanoplastics Can Be Confounded by Preservatives in Commercial Formulations. *Environmental Science & Technology Letters* 6, 21–25. <https://doi.org/10.1021/acs.estlett.8b00614>

- Piringer, O.G., Baner, A.L., 2008. *Plastic Packaging: Interactions with Food and Pharmaceuticals*. John Wiley & Sons.
- Plastics Europe, 2017. *Plastics – the facts 2017*. (PlasticsEurope, Brussels, Belgium, 2017).
- Ponthieu, M., Juillot, F., Hiemstra, T., van Riemsdijk, W.H., Benedetti, M.F., 2006. Metal ion binding to iron oxides. *Geochimica et Cosmochimica Acta* 70, 2679–2698. <https://doi.org/10.1016/j.gca.2006.02.021>
- Pourret, O., Davranche, M., Gruau, G., Dia, A., 2007. Rare earth elements complexation with humic acid. *Chemical Geology* 243, 128–141. <https://doi.org/10.1016/j.chemgeo.2007.05.018>
- Powell, M.J.D., 1965. A Method for Minimizing a Sum of Squares of Non-Linear Functions Without Calculating Derivatives. *The Computer Journal* 7, 303–307. <https://doi.org/10.1093/comjnl/7.4.303>
- Pradel, A., Ferreres, S., Veclin, C., El Hadri, H., Gautier, M., Grassl, B., Gigault, J., 2021. Stabilization of Fragmental Polystyrene Nanoplastic by Natural Organic Matter: Insight into Mechanisms. *ACS EST Water* 1, 1198–1208. <https://doi.org/10.1021/acsestwater.0c00283>
- Pradel, A., Hadri, H. el, Desmet, C., Ponti, J., Reynaud, S., Grassl, B., Gigault, J., 2020. Deposition of environmentally relevant nanoplastic models in sand during transport experiments. *Chemosphere* 255, 126912. <https://doi.org/10.1016/j.chemosphere.2020.126912>
- Prata, J.C., da Costa, J.P., Girão, A.V., Lopes, I., Duarte, A.C., Rocha-Santos, T., 2019. Identifying a quick and efficient method of removing organic matter without damaging microplastic samples. *Science of The Total Environment* 686, 131–139. <https://doi.org/10.1016/j.scitotenv.2019.05.456>
- Rabek, Jan.F., 1995. *Polymer Photodegradation*. Springer Netherlands, Dordrecht. <https://doi.org/10.1007/978-94-011-1274-1>
- Rånby, B., 1989. Photodegradation and photo-oxidation of synthetic polymers. *Journal of Analytical and Applied Pyrolysis* 15, 237–247. [https://doi.org/10.1016/0165-2370\(89\)85037-5](https://doi.org/10.1016/0165-2370(89)85037-5)
- Rånby, B., Rabek, J.F., 1989. Photodegradation of Polymer Materials, in: *Comprehensive Polymer Science and Supplements*. Elsevier, pp. 253–283. <https://doi.org/10.1016/B978-0-08-096701-1.00230-5>
- Reich, T.J., Das, S., Koretsky, C.M., Lund, T.J., Landry, C.J., 2010. Surface complexation modeling of Pb(II) adsorption on mixtures of hydrous ferric oxide, quartz and kaolinite. *Chemical Geology* 275, 262–271. <https://doi.org/10.1016/j.chemgeo.2010.05.017>
- Reisser, J., Shaw, J., Wilcox, C., Hardesty, B.D., Proietti, M., Thums, M., Pattiaratchi, C., 2013. Marine Plastic Pollution in Waters around Australia: Characteristics, Concentrations, and Pathways. *PLoS ONE* 8, e80466. <https://doi.org/10.1371/journal.pone.0080466>
- Rist, S., Hartmann, N.B., 2018. Aquatic Ecotoxicity of Microplastics and Nanoplastics: Lessons Learned from Engineered Nanomaterials, in: Wagner, M., Lambert, S. (Eds.), *Freshwater Microplastics, The Handbook of Environmental Chemistry*. Springer International Publishing, Cham, pp. 25–49. https://doi.org/10.1007/978-3-319-61615-5_2
- Rochman, C.M., Hentschel, B.T., Teh, S.J., 2014. Long-Term Sorption of Metals Is Similar among Plastic Types: Implications for Plastic Debris in Aquatic Environments. *PLoS ONE* 9, e85433. <https://doi.org/10.1371/journal.pone.0085433>

- Rodríguez-Hernández, A.G., Muñoz-Tabares, J.A., Aguilar-Guzmán, J.C., Vazquez-Duhalt, R., 2019. A novel and simple method for polyethylene terephthalate (PET) nanoparticle production. *Environ. Sci.: Nano* 6, 2031–2036. <https://doi.org/10.1039/C9EN00365G>
- Rosenqvist, J., Persson, P., Sjöberg, S., 2002. Protonation and Charging of Nanosized Gibbsite ($\alpha\text{-Al}(\text{OH})_3$) Particles in Aqueous Suspension. *Langmuir* 18, 4598–4604. <https://doi.org/10.1021/la015753t>
- Ross, A.B., Anastasakis, K., Kubacki, M., Jones, J.M., 2009. Investigation of the pyrolysis behaviour of brown algae before and after pre-treatment using PY-GC/MS and TGA. *Journal of Analytical and Applied Pyrolysis* 85, 3–10. <https://doi.org/10.1016/j.jaap.2008.11.004>
- Rouches, E., Dignac, M.-F., Zhou, S., Carrere, H., 2017. Pyrolysis-GC-MS to assess the fungal pretreatment efficiency for wheat straw anaerobic digestion. *Journal of Analytical and Applied Pyrolysis* 123, 409–418. <https://doi.org/10.1016/j.jaap.2016.10.012>
- Royer, S.-J., Deheyn, D.D., 2019. The Technological Challenges of Dealing With Plastics in the Environment. *mar technol soc j* 53, 13–20. <https://doi.org/10.4031/MTSJ.53.5.3>
- Santé Publique France, 2021. Etude de santé sur l'environnement, la biosurveillance, l'activité physique et la nutrition (ESTEBAN) [WWW Document]. URL <https://www.santepubliquefrance.fr/etudes-et-enquetes/esteban> (accessed 10.5.21).
- Santos, L.C., Poli, A.L., Cavalheiro, C.C.S., Neumann, M.G., 2009. The UV/H₂O₂ - photodegradation of poly(ethyleneglycol) and model compounds. *J. Braz. Chem. Soc.* 20, 1467–1472. <https://doi.org/10.1590/S0103-50532009000800012>
- Schulten, H.-R., Sorge, C., 1995. Pyrolysis methylation—mass spectrometry of whole soils. *Eur J Soil Science* 46, 567–579. <https://doi.org/10.1111/j.1365-2389.1995.tb01353.x>
- Scott, P.G., 1972. Plastics packaging and coastal pollution. *International Journal of Environmental Studies* 3, 35–36. <https://doi.org/10.1080/00207237208709489>
- Shams, M., Alam, I., Chowdhury, I., 2020. Aggregation and stability of nanoscale plastics in aquatic environment. *Water Research* 171, 115401. <https://doi.org/10.1016/j.watres.2019.115401>
- Singh, N., Tiwari, E., Khandelwal, N., Darbha, G.K., 2019. Understanding the stability of nanoplastics in aqueous environments: effect of ionic strength, temperature, dissolved organic matter, clay, and heavy metals. *Environ. Sci.: Nano* 6, 2968–2976. <https://doi.org/10.1039/C9EN00557A>
- Sohma, J., 1989. Mechanochemical Degradation, in: *Comprehensive Polymer Science and Supplements*. Elsevier, pp. 621–644. <https://doi.org/10.1016/B978-0-08-096701-1.00203-2>
- Song, Y.K., Hong, S.H., Jang, M., Han, G.M., Jung, S.W., Shim, W.J., 2017. Combined Effects of UV Exposure Duration and Mechanical Abrasion on Microplastic Fragmentation by Polymer Type. *Environ. Sci. Technol.* 51, 4368–4376. <https://doi.org/10.1021/acs.est.6b06155>
- Spadini, L., Navel, A., Martins, J.M.F., Vince, E., Lamy, I., 2018. Soil aggregates: a scale to investigate the densities of metal and proton reactive sites of organic matter and clay phases in soil. *Eur J Soil Sci* 69, 953–961. <https://doi.org/10.1111/ejss.12695>
- Steffen, W., Broadgate, W., Deutsch, L., Gaffney, O., Ludwig, C., 2015. The trajectory of the Anthropocene: The Great Acceleration. *The Anthropocene Review* 2, 81–98. <https://doi.org/10.1177/2053019614564785>
- Stoloff, L., Silva, P., 1957. An attempt to determine possible taxonomic significance of the properties of water extractable polysaccharides in red algae. *Econ Bot* 11, 327–330. <https://doi.org/10.1007/BF02903813>

- Stumm, W. (Ed.), 1987. *Aquatic surface chemistry: chemical processes at the particle-water interface*, Environmental science and technology. Wiley, New York.
- Stumm, W., Morgan, J.J., 2012. *Aquatic Chemistry: Chemical Equilibria and Rates in Natural Waters*. Wiley, Hoboken.
- Sugimura, Y., Suzuki, Y., 1988. A high-temperature catalytic oxidation method for the determination of non-volatile dissolved organic carbon in seawater by direct injection of a liquid sample. *Marine Chemistry* 24, 105–131. [https://doi.org/10.1016/0304-4203\(88\)90043-6](https://doi.org/10.1016/0304-4203(88)90043-6)
- Sullivan, G.L., Gallardo, J.D., Jones, E.W., Holliman, P.J., Watson, T.M., Sarp, S., 2020. Detection of trace sub-micron (nano) plastics in water samples using pyrolysis-gas chromatography time of flight mass spectrometry (PY-GCToF). *Chemosphere* 249, 126179. <https://doi.org/10.1016/j.chemosphere.2020.126179>
- Sverjensky, D.A., 2006. Prediction of the speciation of alkaline earths adsorbed on mineral surfaces in salt solutions. *Geochimica et Cosmochimica Acta* 70, 2427–2453. <https://doi.org/10.1016/j.gca.2006.01.006>
- Takahashi, Y., Châtellier, X., Hattori, K.H., Kato, K., Fortin, D., 2005. Adsorption of rare earth elements onto bacterial cell walls and its implication for REE sorption onto natural microbial mats. *Chemical Geology* 219, 53–67. <https://doi.org/10.1016/j.chemgeo.2005.02.009>
- Talleg, K., Blard, O., González-Fernández, C., Brotons, G., Berchel, M., Soudant, P., Huvet, A., Paul-Pont, I., 2019. Surface functionalization determines behavior of nanoplastic solutions in model aquatic environments. *Chemosphere* 225, 639–646. <https://doi.org/10.1016/j.chemosphere.2019.03.077>
- Tang, J., Johannesson, K.H., 2003. Speciation of rare earth elements in natural terrestrial waters: assessing the role of dissolved organic matter from the modeling approach. *Geochimica et Cosmochimica Acta* 67, 2321–2339. [https://doi.org/10.1016/S0016-7037\(02\)01413-8](https://doi.org/10.1016/S0016-7037(02)01413-8)
- Tang, S., Lin, L., Wang, X., Yu, A., Sun, X., 2021. Interfacial interactions between collected nylon microplastics and three divalent metal ions (Cu(II), Ni(II), Zn(II)) in aqueous solutions. *Journal of Hazardous Materials* 403, 123548. <https://doi.org/10.1016/j.jhazmat.2020.123548>
- Tang, W.Z., 2003. *Physicochemical Treatment of Hazardous Wastes*, 0 ed. CRC Press. <https://doi.org/10.1201/9780203506219>
- Tauer, K., Deckwer, R., 1998. Polymer end groups in persulfate-initiated styrene emulsion polymerization. *Acta Polym.* 6.
- Taylor, S.R., McLennan, S.M., 1988. Chapter 79 The significance of the rare earths in geochemistry and cosmochemistry, in: *Handbook on the Physics and Chemistry of Rare Earths*. Elsevier, pp. 485–578. [https://doi.org/10.1016/S0168-1273\(88\)11011-8](https://doi.org/10.1016/S0168-1273(88)11011-8)
- Ter Halle, A., Jeanneau, L., Martignac, M., Jardé, E., Pedrono, B., Brach, L., Gigault, J., 2017. Nanoplastic in the North Atlantic Subtropical Gyre. *Environmental Science & Technology* 51, 13689–13697. <https://doi.org/10.1021/acs.est.7b03667>
- ter Halle, A., Ladirat, L., Gendre, X., Goudouneche, D., Pusineri, C., Routaboul, C., Tenailleau, C., Duployer, B., Perez, E., 2016. Understanding the Fragmentation Pattern of Marine Plastic Debris. *Environmental Science & Technology* 50, 5668–5675. <https://doi.org/10.1021/acs.est.6b00594>
- Thompson, R.C., 2004. Lost at Sea: Where Is All the Plastic? *Science* 304, 838–838. <https://doi.org/10.1126/science.1094559>
- Tipping, E., 2002. *Cation Binding by Humic Substances*. Cambridge University Press: 201.

- Tipping, E., 1994. WHAMC—A chemical equilibrium model and computer code for waters, sediments, and soils incorporating a discrete site/electrostatic model of ion-binding by humic substances. *Computers & Geosciences* 20, 973–1023. [https://doi.org/10.1016/0098-3004\(94\)90038-8](https://doi.org/10.1016/0098-3004(94)90038-8)
- Tipping, M.E., 2001. Sparse Bayesian Learning and the Relevance Vector Machine. *Journal of Machine Learning Research* Volume 1, P211-244.
- Tombácz, E., Szekeres, M., 2004. Colloidal behavior of aqueous montmorillonite suspensions: the specific role of pH in the presence of indifferent electrolytes. *Applied Clay Science* 27, 75–94. <https://doi.org/10.1016/j.clay.2004.01.001>
- Tournassat, C., Greneche, J.-M., Tisserand, D., Charlet, L., 2004. The titration of clay minerals. *Journal of Colloid and Interface Science* 273, 224–233. <https://doi.org/10.1016/j.jcis.2003.11.021>
- Town, R.M., van Leeuwen, H.P., Blust, R., 2018. Biochemodynamic Features of Metal Ions Bound by Micro- and Nano-Plastics in Aquatic Media. *Frontiers in Chemistry* 6, 627. <https://doi.org/10.3389/fchem.2018.00627>
- Tsuge, S., Ohtani, H., Watanabe, C., 2011. *Pyrolysis-GC/MS data book of synthetic polymers: pyrograms, thermograms and MS of pyrolyzates*, 1st ed. ed. Elsevier, Amsterdam ; Boston.
- Turner, A., Filella, M., 2021. Hazardous metal additives in plastics and their environmental impacts. *Environment International* 156, 106622. <https://doi.org/10.1016/j.envint.2021.106622>
- Turner, A., Holmes, L.A., 2015. Adsorption of trace metals by microplastic pellets in fresh water. *Environ. Chem.* 12, 600. <https://doi.org/10.1071/EN14143>
- van den Hul, H.J., Vanderhoff, J.W., 1970. Inferences on the mechanism of emulsion polymerisation of styrene from characterisation of the polymer end-groups. *Brit. Poly. J.* 2, 121–127. <https://doi.org/10.1002/pi.4980020205>
- Van Heemst, J.D.H., Peulve, S., De Leeuw, J.W., 1996. Novel algal polyphenolic biomacromolecules as significant contributors to resistant fractions of marine dissolved and particulate organic matter. *Organic Geochemistry* 24, 629–640. [https://doi.org/10.1016/0146-6380\(96\)00054-X](https://doi.org/10.1016/0146-6380(96)00054-X)
- van Schaik, J.W.J., Kleja, D.B., Gustafsson, J.P., 2010. Acid–base and copper-binding properties of three organic matter fractions isolated from a forest floor soil solution. *Geochimica et Cosmochimica Acta* 74, 1391–1406. <https://doi.org/10.1016/j.gca.2009.11.007>
- Vega, F.A., Weng, L., 2013. Speciation of heavy metals in River Rhine. *Water Research* 47, 363–372. <https://doi.org/10.1016/j.watres.2012.10.012>
- Venel, Z., Tabuteau, H., Pradel, A., Pascal, P.-Y., Grassl, B., El Hadri, H., Baudrimont, M., Gigault, J., 2021. Environmental Fate Modeling of Nanoplastics in a Salinity Gradient Using a Lab-on-a-Chip: Where Does the Nanoscale Fraction of Plastic Debris Accumulate? *Environ. Sci. Technol.* [acs.est.0c07545](https://doi.org/10.1021/acs.est.0c07545). <https://doi.org/10.1021/acs.est.0c07545>
- Vilhunen, S., Vilve, M., Vepsäläinen, M., Sillanpää, M., 2010. Removal of organic matter from a variety of water matrices by UV photolysis and UV/H₂O₂ method. *Journal of Hazardous Materials* 179, 776–782. <https://doi.org/10.1016/j.jhazmat.2010.03.070>
- Villalobos, M., Antelo, J., 2011. A UNIFIED SURFACE STRUCTURAL MODEL FOR FERRIHYDRITE: PROTON CHARGE, ELECTROLYTE BINDING, AND ARSENATE ADSORPTION 13.

- Villalobos, M., Cheney, M.A., Alcaraz-Cienfuegos, J., 2009. Goethite surface reactivity: II. A microscopic site-density model that describes its surface area-normalized variability. *Journal of Colloid and Interface Science* 336, 412–422. <https://doi.org/10.1016/j.jcis.2009.04.052>
- Wahl, A., Le Juge, C., Davranche, M., El Hadri, H., Grassl, B., Reynaud, S., Gigault, J., 2021. Nanoplastic occurrence in a soil amended with plastic debris. *Chemosphere* 262, 127784. <https://doi.org/10.1016/j.chemosphere.2020.127784>
- Wang, G.-S., Liao, C.-H., Chen, H.-W., Yang, H.-C., 2006. Characteristics of Natural Organic Matter Degradation in Water by UV/H₂O₂ Treatment. *Environmental Technology* 27, 277–287. <https://doi.org/10.1080/09593332708618638>
- Wang, G.-S., Liao, C.-H., Wu, F.-J., 2001. Photodegradation of humic acids in the presence of hydrogen peroxide. *Chemosphere* 42, 379–387. [https://doi.org/10.1016/S0045-6535\(00\)00153-3](https://doi.org/10.1016/S0045-6535(00)00153-3)
- Wang, J., Peng, J., Tan, Z., Gao, Y., Zhan, Z., Chen, Q., Cai, L., 2017. Microplastics in the surface sediments from the Beijiang River littoral zone: Composition, abundance, surface textures and interaction with heavy metals. *Chemosphere* 171, 248–258. <https://doi.org/10.1016/j.chemosphere.2016.12.074>
- Wang, Q., Zhang, Y., Wangjin, X., Wang, Y., Meng, G., Chen, Y., 2020. The adsorption behavior of metals in aqueous solution by microplastics effected by UV radiation. *Journal of Environmental Sciences* 87, 272–280. <https://doi.org/10.1016/j.jes.2019.07.006>
- Wang, S., Dai, G., Yang, H., Luo, Z., 2017. Lignocellulosic biomass pyrolysis mechanism: A state-of-the-art review. *Progress in Energy and Combustion Science* 62, 33–86. <https://doi.org/10.1016/j.pecs.2017.05.004>
- Wang, X., Li, Y., Zhao, J., Xia, X., Shi, X., Duan, J., Zhang, W., 2020. UV-induced aggregation of polystyrene nanoplastics: effects of radicals, surface functional groups and electrolyte. *Environ. Sci.: Nano* 7, 3914–3926. <https://doi.org/10.1039/D0EN00518E>
- Watteau, F., Dignac, M.-F., Bouchard, A., Revallier, A., Houot, S., 2018. Microplastic Detection in Soil Amended With Municipal Solid Waste Composts as Revealed by Transmission Electronic Microscopy and Pyrolysis/GC/MS. *Front. Sustain. Food Syst.* 2, 81. <https://doi.org/10.3389/fsufs.2018.00081>
- Wegner, A., Besseling, E., Foekema, E.M., Kamermans, P., Koelmans, A.A., 2012. Effects of nanopolystyrene on the feeding behavior of the blue mussel (*Mytilus edulis* L.). *Environmental Toxicology and Chemistry* 31, 2490–2497. <https://doi.org/10.1002/etc.1984>
- Welden, N.A., Cowie, P.R., 2017. Degradation of common polymer ropes in a sublittoral marine environment. *Marine Pollution Bulletin* 118, 248–253. <https://doi.org/10.1016/j.marpolbul.2017.02.072>
- Wilcox, C., Hardesty, B.D., Law, K.L., 2020. Abundance of Floating Plastic Particles Is Increasing in the Western North Atlantic Ocean. *Environ. Sci. Technol.* 54, 790–796. <https://doi.org/10.1021/acs.est.9b04812>
- Wood, S.A., 1993. The aqueous geochemistry of the rare-earth elements: Critical stability constants for complexes with simple carboxylic acids at 25°C and 1 bar and their application to nuclear waste management. *Engineering Geology* 34, 229–259. [https://doi.org/10.1016/0013-7952\(93\)90092-Q](https://doi.org/10.1016/0013-7952(93)90092-Q)
- Worm, B., Lotze, H.K., Jubinville, I., Wilcox, C., Jambeck, J., 2017. Plastic as a Persistent Marine Pollutant. *Annu. Rev. Environ. Resour.* 42, 1–26. <https://doi.org/10.1146/annurev-environ-102016-060700>

- Wu, Z., Gu, Z., Wang, X., Evans, L., Guo, H., 2003. Effects of organic acids on adsorption of lead onto montmorillonite, goethite and humic acid. *Environmental Pollution* 121, 469–475. [https://doi.org/10.1016/S0269-7491\(02\)00272-5](https://doi.org/10.1016/S0269-7491(02)00272-5)
- Xu, G., Cheng, H., Jones, R., Feng, Y., Gong, K., Li, K., Fang, X., Tahir, M.A., Valev, V.K., Zhang, L., 2020. Surface-Enhanced Raman Spectroscopy Facilitates the Detection of Microplastics <1 μm in the Environment. *Environ. Sci. Technol.* 54, 15594–15603. <https://doi.org/10.1021/acs.est.0c02317>
- Yano, J., Yachandra, V.K., 2009. X-ray absorption spectroscopy. *Photosynth Res* 102, 241–254. <https://doi.org/10.1007/s11120-009-9473-8>
- Yazdani, P., 2015. Characterization of *Nizimuddinina zanardini* macroalgae biomass composition and its potential for biofuel production. *Bioresource Technology* 7.
- Yu, F., Yang, C., Zhu, Z., Bai, X., Ma, J., 2019. Adsorption behavior of organic pollutants and metals on micro/nanoplastics in the aquatic environment. *Science of The Total Environment* 694, 133643. <https://doi.org/10.1016/j.scitotenv.2019.133643>
- Zettler, E.R., Mincer, T.J., Amaral-Zettler, L.A., 2013. Life in the “Plastisphere”: Microbial Communities on Plastic Marine Debris. *Environmental Science & Technology* 47, 7137–7146. <https://doi.org/10.1021/es401288x>
- Zhang, L.L., Zhao, X.S., 2009. Carbon-based materials as supercapacitor electrodes. *Chem. Soc. Rev.* 38, 2520. <https://doi.org/10.1039/b813846j>
- Zhang, S., Xu, Y., Wu, M., Mao, X., Yao, Y., Shen, Q., Zhang, M., 2021. Geogenic enrichment of potentially toxic metals in agricultural soils derived from black shale in northwest Zhejiang, China: Pathways to and risks from associated crops. *Ecotoxicology and Environmental Safety* 215, 112102. <https://doi.org/10.1016/j.ecoenv.2021.112102>
- Zhang, Yulan, Kang, S., Allen, S., Allen, D., Gao, T., Sillanpää, M., 2020. Atmospheric microplastics: A review on current status and perspectives. *Earth-Science Reviews* 203, 103118. <https://doi.org/10.1016/j.earscirev.2020.103118>
- Zhang, Yangyang, Luo, Y., Guo, X., Xia, T., Wang, T., Jia, H., Zhu, L., 2020. Charge mediated interaction of polystyrene nanoplastic (PSNP) with minerals in aqueous phase. *Water Research* 178, 115861. <https://doi.org/10.1016/j.watres.2020.115861>
- Zhao, Y.-B., Gao, P.-P., Ni, H.-G., 2019. A Chemical Time Bomb: Future Risks of Microplastics. *Water Air Soil Pollut* 230, 268. <https://doi.org/10.1007/s11270-019-4320-9>

Titre : Identification, production et caractérisation de nanoplastiques environnementaux par l'utilisation d'outils géochimiques et de nanométrie.

Mots clés : Nanoplastiques, identification, caractérisation, interactions métal-NPs, modélisation

Résumé : L'utilisation des plastiques s'est accompagnée d'un rejet massif de déchets plastiques dans l'environnement. Leur altération par photo-oxydation produit des nanoplastiques (NPs) dont les caractéristiques et les propriétés en font des vecteurs potentiellement importants de métaux. Etant difficiles à échantillonner dans l'environnement, leur étude a été jusqu'à présent réalisée à l'aide de modèles non représentatifs de l'environnement. Il est donc primordial de produire des modèles de NPs plus pertinents afin de mieux appréhender leur comportement et leur impact sur les polluants métalliques.

La Py-GCMS permet d'identifier les NPs de polypropylène en présence de matière organique comme dans les matrices environnementales. L'abrasion mécanique des couches d'altération des plastiques photo-oxydés dans l'environnement, nous a permis de produire un modèle plus représentatif.

Ces modèles de NPs présentent à leur surface des fonctions capables de complexer les métaux et de contrôler leur stabilité colloïdale. L'utilisation des terres rares et la modélisation thermodynamique, nous a permis de démontrer que l'adsorption des métaux est contrôlée par la formation de complexes mono ou bidentés avec les sites carboxyliques de surface. La formation des complexes mono ou bidentés dépend de la valence des métaux étudiés et des conditions physicochimiques du milieu. Plus globalement, la réactivité des NPs dépend de leur état d'oxydation qui contrôle leur densité de site de surface.

De par leurs propriétés de sorption, les NPs peuvent être des acteurs clés de la dynamique des métaux dans des zones polluées par les plastiques comme par exemple: les sols agricoles amendés en déchets plastiques et les décharges.

Title : Identification, production and characterization of environmental nanoplastics using geochemical and nanometrology tools.

Keywords : Nanoplastics, identification, characterization, metal-NPs interactions, modeling

Abstract: The use of plastics has been accompanied by a massive release of plastic waste into the environment. Their alteration by photo-oxidation produces nanoplastics (NPs), whose characteristics and properties make them potentially important metal vectors. Being difficult to sample in the environment, their study has been carried out with models not representative of environmental NPs. It is therefore essential to produce more relevant NPs models in order to better understand their behavior and impact on metal pollutants.

Py-GCMS allows the identification of polypropylene nanoparticles in the presence of organic matter as in environmental matrices. The mechanical abrasion of the weathering layers of photo-oxidized plastics in the environment allowed us to produce a more representative model.

These NPs models present on their surface functions complexing metals and controlling their colloidal stability. The use of rare earths and thermodynamic modeling, allowed us to demonstrate that the metal adsorption of metals is controlled by the formation of mono- or bidentate complexes with the surface carboxylic sites. The formation of mono- or bidentate complexes depends on the valence of the metals studied and the physicochemical conditions of the medium. More globally, the reactivity of NPs depends on their oxidation state which controls their surface site density.

Due to their sorption properties, NPs can be key players in the dynamics of metals in areas polluted by plastics such as: agricultural soils amended with plastic waste and landfills.